

Walter Schottky Institut  
Zentralinstitut für physikalische Grundlagen der Halbleiterelektronik  
der  
Technischen Universität München

# **Group III-Nitrides for Bio- and Electrochemical Sensors**

**Georg Steinhoff**

Vollständiger Abdruck der von der Fakultät für Physik der Technischen Universität München  
zur Erlangung des akademischen Grades eines

**Doktors der Naturwissenschaften**

(Dr. rer. nat.)

genehmigten Dissertation.

Vorsitzender:

Univ.-Prof. Dr. R. Netz

Prüfer der Dissertation:

1. Univ.-Prof. Dr. M. Stutzmann
2. Univ.-Prof. Dr. J. Barth

Die Dissertation wurde am 06.03.2008 bei der Technischen Universität München eingereicht  
und durch die Fakultät für Physik am 14.07.2008 angenommen.



## Zusammenfassung

In der vorliegenden Arbeit werden grundlegende Eigenschaften der Gruppe III-Nitride im Hinblick auf eine Realisierung von Feldeffekt-Sensoren für die biochemische Analytik und die Messung elektrophysiologischer Signale in wässrigen Lösungen untersucht.

Als Signalwandler wurden Feldeffekttransistoren und Transistorarrays mit elektrolytischem Gate auf Basis von AlGa<sub>N</sub>/Ga<sub>N</sub> Heterostrukturen analysiert. Die spektrale Rauschleistungsdichte dieser Transistoren bei niedrigen Frequenzen zwischen 1 Hz und 1 kHz zeigte einen  $1/f$  Verlauf mit einem Hooge-Parameter von  $5 \times 10^{-3}$ . Die nicht optimierte Kontakttechnologie der Gruppe III-Nitride führte dabei jedoch zu großen Variationen im Niederfrequenzrauschen. Die rauschärmsten getesteten Transistoren wiesen am Arbeitspunkt ein äquivalentes Gateeingangsspannungsrauschen von 25  $\mu$ V im doppelten Scheitelwert auf, etwa eine Größenordnung niedriger als bei gewöhnlichen Silizium-basierten Transistoren mit elektrolytischem Gate und vergleichbar zu komplexen “buried-channel” Transistorstrukturen.

Die elektrochemischen Eigenschaften der AlGa<sub>N</sub>/Elektrolyt Grenzfläche wurden mittels Impedanzspektroskopie und zyklischer Voltammetrie analysiert. Eine Beschreibung der elektrischen Grenzflächeneigenschaften war durch einfache Ersatzschaltkreise idealer Elemente möglich. Die relativen energetischen Positionen der Ga<sub>N</sub> Valenz- und Leitungsbandkante am Interface und der Redoxniveaus im Elektrolyten sind gegenüber Variation der externen Biasspannungen nahezu unveränderlich und konnte aus den Flachbandspannungen für n-Typ ( $V_{fb} = -1.12$  V) und p-Typ Ga<sub>N</sub> ( $V_{fb} = 2.27$  V) zu  $E_{C,S} = 0.91$  eV und  $E_{V,S} = -2.69$  eV relativ zum Redoxniveau der Standard-Wasserstoffelektrode bestimmt werden. Dabei wurde die Flachbandspannung aus Mott-Schottky Diagrammen der Raumladungszonenkapazität ermittelt, die wiederum aus den Impedanzspektren extrahiert wurde. Die Abhängigkeit der Flachbandspannung von der Dotierungsdichte lässt sich durch den kapazitiven Beitrag einer zusätzlichen Schicht an der Oberfläche ( $C_L \approx 2 \mu\text{F cm}^{-2}$ ) erklären. Chemische Analysen der Ga<sub>N</sub>-Oberfläche mit XPS zeigten die Bildung eines natürlichen Oberflächenoxids bei Lagerung an Atmosphäre. Für die untersuchten Al<sub>*x*</sub>Ga<sub>1-*x*</sub>N-Elektroden ( $x_{Al} = 0 - 0.5$ ) war die Lage der Valenzbandkante an der Grenzfläche zum Elektrolyten unabhängig von der Al-Konzentration.

Die Abhängigkeit des Oberflächenpotentials von natürlich und thermisch oxidierten Ga<sub>N</sub>-Oberflächen wurde mit Hilfe von Ga<sub>N</sub>/AlGa<sub>N</sub>/Ga<sub>N</sub> bzw. Ga<sub>N</sub>:Si/Ga<sub>N</sub>:Mg Feldeffekttransistoren untersucht und wies eine lineare Abhängigkeit vom pH-Wert des Elektrolyten auf. Die hohe lineare pH-Sensitivität ist mit 56 mV/*pH* nahe am theoretischen Nernstschen Limit und wurde im Rahmen des Site-Binding Modells für oxidische Oberflächen diskutiert. Die untersuchten Ga<sub>N</sub>/AlGa<sub>N</sub>/Ga<sub>N</sub> Transistoren wiesen ohne Optimierung des Schichtaufbaus oder der Gate-Geometrie bereits eine Auflösung besser als 0.05 pH auf. Für Ionenkonzentrationen

zwischen  $10^{-5}$  M und  $2 \times 10^{-3}$  M war bei pH 7 nur eine geringe Quersensitivität auf  $K^+$ ,  $Na^+$ ,  $Ca^{2+}$  oder  $Cl^-$  festzustellen.

Des Weiteren konnte die Deposition von fluiden und stabilen Lipidmembranen auf der Oberfläche von hydrophilen AlGaN-Elektroden nachgewiesen werden. Die laterale Beweglichkeit der Lipide in der Membran wurde mit Hilfe von Photobleichexperimenten an fluoreszenzmarkierten Lipiddoppelschichten untersucht und ist ausreichend, um die Selbstheilung von Membrandefekten während der Bildung der Membran zu ermöglichen. Anionische Lipidmembranen zeigten dabei eine deutlich geringere laterale Beweglichkeit als zwitterionische oder kationische Membranen. Der beobachtete Trend ( $D_{kationisch} > D_{zwitterionisch} > D_{anionisch}$ ) war unabhängig von der Oberflächenladung des Substrats.

Die Bildung von Lipidmembranen auf planaren GaN-Elektroden wurde durch die sequentielle Aufnahme von Impedanzspektren untersucht. Dabei konnten die elektrischen Membraneigenschaften mit Hilfe des Ersatzschaltbilds eines idealen parallelen RC-Glieds approximiert werden. Der Membranwiderstand war nach Ausbildung der Lipiddoppelschicht im Bereich von etwa  $1 \text{ k}\Omega \text{ cm}^2$ . Dies entspricht einer relativen Flächendefektdichte von weniger als  $10^{-7}$ . Eine Abhängigkeit des Membranwiderstands von der Präparationsmethode oder der Oberflächenrauigkeit konnte nicht festgestellt werden. Es wurde gezeigt, dass die beobachtete Abnahme der Membrankapazität während der Ausbildung der Membran durch eine Homogenisierung von anfangs geclustertem Cholesterin verursacht werden kann. Der Endwert war mit  $0.7 \mu\text{F cm}^{-2}$  vergleichbar zur Kapazität von identischen Lipidmembranen auf p-Silizium Elektroden. Eine mögliche Erklärung für den vergleichsweise niedrigen Membranwiderstand ist die Existenz von lokalen "Pinning Zentren" aufgrund eines inhomogenen Oberflächenoxids. Diese Vermutung wurde durch die Ergebnisse aus dynamischen Kontaktwinkelmessungen unterstützt.

Die Anbindung organischer Silanmoleküle stellt einen weiteren Weg zur Biofunktionalisierung von hydroxylierten GaN-Oberflächen dar. Der Silanisierungsprozess mit ODTMS oder APTES führte dabei zur Ausbildung von selbstorganisierenden Monolagen. Die elektrischen Eigenschaften einer ODTMS-Monolage wurden durch Impedanzspektroskopie zu  $C_{silane} = 2 \mu\text{F cm}^{-2}$  und  $R_{silane} > 1 \text{ M}\Omega \text{ cm}^2$  bestimmt. Die relative Oberflächenbedeckung betrug  $92\% \pm 2\%$ . APTES-funktionalisierte GaN-Oberflächen ermöglichen aufgrund der reaktiven Amino-Gruppe eine anschließende Anbindung von funktionalen Proteinen wie z.B. Enzymen oder DNA. Erste enzymfunktionalisierte Feldeffekt-Sensoren auf Basis von AlGaN/GaN Transistoren zur Detektion von Penicillin und Harnstoff in wässrigen Lösungen wurden bereits realisiert.

Ferner konnte die elektrische Kopplung von AlGaN/GaN Transistoren mit lebenden Zellsystemen gezeigt werden. Dabei wurden erstmals elektrophysiologische Zellsignale mit nicht in Siliziumtechnologie hergestellten Feldeffektsensoren detektiert. Die untersuchten Herzmuskelzellen von Rattenembryonen wurden direkt auf der Gate-Oberfläche des AlGaN/GaN FET-Arrays kultiviert und bildeten nach 4 – 6 Tagen ein konfluentes Synzytium, das gleichmäßige spontane Kontraktionen zeigte. Extrazelluläre Aktionspotentiale von etwa 1 mV wurden über Änderungen des Transistorkanalstroms detektiert.

# Contents

<b>Zusammenfassung</b>	<b>i</b>
<b>1. Introduction</b>	<b>1</b>
1.1. Biosensor Concepts . . . . .	3
1.1.1. Biological Recognition Reactions . . . . .	3
1.1.2. Semiconductor Transducer Devices . . . . .	5
1.2. Scope of this Work . . . . .	8
<b>2. Experimental Methods</b>	<b>10</b>
2.1. Surface Analytical Methods . . . . .	10
2.1.1. X-Ray Photoelectron Spectroscopy . . . . .	10
2.1.2. Contact Angle Measurements . . . . .	13
2.2. Electrochemical Techniques . . . . .	15
2.2.1. Electrochemical Measurement Setup . . . . .	15
2.2.2. Buffer Solutions . . . . .	16
2.2.3. Impedance Spectroscopy . . . . .	17
2.2.4. Cyclic Voltammetry . . . . .	22
2.2.5. Photoelectrochemical Measurement Setup . . . . .	22
2.3. Optical Techniques . . . . .	23
2.3.1. Fluorescence Microscopy . . . . .	23
2.3.2. Continuous Bleaching . . . . .	24
<b>3. Structure and Processing of the III-Nitride based Transducer Devices</b>	<b>27</b>
3.1. Layer Structure of the Transducer Devices . . . . .	27

3.1.1.	Transistor Structures . . . . .	27
3.1.2.	Electrode Structures . . . . .	28
3.2.	Surface Treatments . . . . .	29
3.2.1.	Thermal Oxidation . . . . .	29
3.2.2.	Chemical Surface Treatment . . . . .	32
3.3.	Processing and Packaging of the Transducer Devices . . . . .	34
3.3.1.	Single SGFET Devices . . . . .	34
3.3.2.	SGFET Arrays . . . . .	35
3.3.3.	Electrode Transducers . . . . .	36
<b>4.</b>	<b>Electronic Characteristics of AlGaN/GaN SGFETs</b>	<b>38</b>
4.1.	Transistor Characteristics . . . . .	39
4.2.	Low Frequency Noise . . . . .	41
<b>5.</b>	<b>Physical Chemistry of the GaN/Electrolyte Interface</b>	<b>49</b>
5.1.	The Semiconductor/Electrolyte Interface . . . . .	49
5.1.1.	Electronic Energy Levels in Semiconductors . . . . .	50
5.1.2.	Electronic Energy Levels in Liquids . . . . .	52
5.1.3.	Potential and Charge Distribution at the Semiconductor/Electrolyte Interface . . . . .	57
5.1.4.	Charge Transfer Processes . . . . .	69
5.1.5.	Illumination of the Semiconductor/Electrolyte Junction . . . . .	71
5.1.6.	Surface States . . . . .	72
5.1.7.	Electrochemical Reactions at the GaN/Electrolyte Interface . . . . .	73
5.2.	Chemical Characterization of the GaN Surface . . . . .	74
5.3.	Electrochemical and Photoelectrochemical Characterization . . . . .	79
5.3.1.	Impedance Spectroscopy Analysis of GaN Electrodes and Determina- tion of the Flatband Voltage . . . . .	80
5.3.2.	Photoelectrochemical Characterization of GaN Electrodes . . . . .	87

---

5.3.3.	Comparison of MOCVD and PAMBE Grown GaN Electrodes with Different Doping Densities . . . . .	90
5.3.4.	Determination of the Energetic Levels of the Band Edges at the GaN/ Electrolyte Interface . . . . .	92
5.3.5.	Energetic Position of the Band Edges at the AlGaN/ Electrolyte Interface	96
5.3.6.	Influence of Different Buffer Solutions and Redox Ions on the Flatband Voltage . . . . .	99
5.3.7.	Charge Transfer over the GaN/ Electrolyte Interface . . . . .	100
5.3.8.	Summary . . . . .	104
5.4.	Ion-Sensitivity of GaN Surfaces . . . . .	105
5.4.1.	Ion-Sensitivity of GaN Surfaces Measured by III-Nitride Based Field Effect Transistors . . . . .	107
5.4.2.	Site-Binding Model of the Oxide/ Electrolyte Interface . . . . .	112
<b>6.</b>	<b>Biofunctionalization of III-Nitride Transducer Devices</b>	<b>118</b>
6.1.	Supported Lipid Bilayer Membranes . . . . .	118
6.1.1.	Preparation of Supported Membranes . . . . .	121
6.1.2.	Optical Characterization of Supported Membranes on III-Nitrides . . . . .	123
6.1.3.	Electrical Characterization of Supported Membranes and Membrane Formation on GaN . . . . .	128
6.2.	Organic Functionalization of GaN by Silane Monolayers . . . . .	142
6.2.1.	Silanization of GaN Surfaces . . . . .	144
6.2.2.	Electrical Characterization of Silane Monolayers on GaN . . . . .	145
6.3.	The Cell-Transistor Hybrid System . . . . .	151
6.3.1.	Preparation of Cardiac Myocyte Cells . . . . .	153
6.3.2.	Recording of Action Potentials . . . . .	153
<b>7.</b>	<b>Summary and Outlook</b>	<b>157</b>
<b>A.</b>	<b>Appendix</b>	<b>162</b>
A.1.	Abbreviations . . . . .	162

## Contents

---

A.2. Lipids . . . . .	164
A.3. The Semiconductor Space Charge Layer . . . . .	165
A.4. Site-Binding Model . . . . .	168
A.5. Equivalent Circuits . . . . .	170



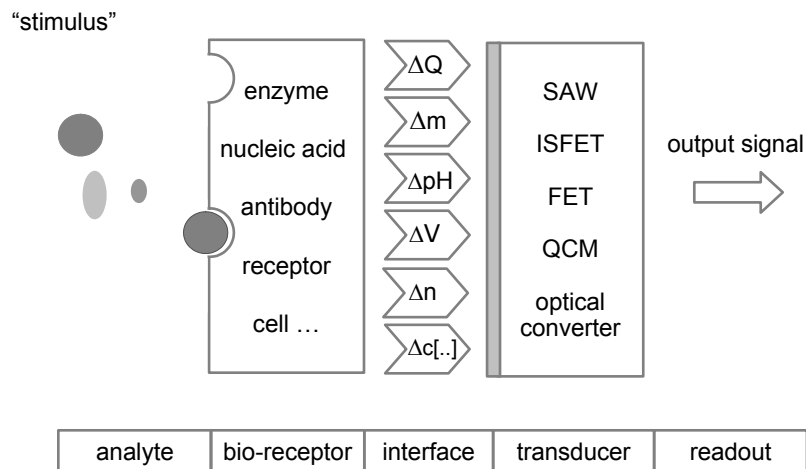
# 1. Introduction

Fast, specific and inexpensive analytical detection methods are demanded in various sectors of today's society, as clinical diagnostics and patients home care, in-line monitoring of processes in the food or pharmaceutical industry, screening and development of new drugs, or waste water analysis. The traditional methods provided by analytical chemistry cannot fulfill this demand, as they are time-consuming and require expensive equipment and reagents to achieve high selectivity and low detection limits. Biological recognition events are highly selective and allow a sensitive and specific detection of analytes on a molecular level. Over the last decades, a variety of sensing principles based on biological receptors and physicochemical transducers has been developed, and the interdisciplinary and rapidly growing field of biosensors was established [Bilitewski & Turner, 2000], [Eggins, 2002].

In general, a biosensor is an analytical device comprising a biological recognition element directly connected to a physicochemical transducer, which converts the biological or biochemical response mostly into an electrical output signal [Thevenot, 1999]. The first functional biosensor was the blood glucose meter developed by Updike and Hicks [Updike & Hicks, 1967], which was based on the enzyme electrode proposed by Clark and Lyons in 1962 [Clark & Lyons, 1962]. Using such an electrode modified with the enzyme glucose oxidase (GOD), the glucose concentration could be measured amperometrically by detecting the oxygen consumption during the GOD mediated oxidation of glucose. An enhanced version of the early blood glucose meter is the most common and successful example of a biosensor so far. Since the introduction of the blood glucose meter, many biosensors based on different biological receptors and transducer concepts have been developed, benefiting from the rapid progress in bio- and microtechnology.

The detection of an analyte by a biosensor can be described by two consecutive steps, as illustrated in Figure 1.1:

**Detection** The analyte reacts with the biological recognition element immobilized on the sensor surface, either by selective binding to the bioreceptor or by catalytic conversion mediated by the bioreceptor. Examples for sensitive biological elements include single molecules, or molecular complexes like enzymes, antigens and antibodies, nucleic acids, cell receptors as well as larger organic complexes like whole cells, tissues or microorganisms. The selective interaction between analyte and bioreceptor determines the sensitivity and specificity of the biosensor.



**Figure 1.1.:** Functional principle of a biosensor. Possible signal transducers are for example surface acoustic wave devices (SAWs), field-effect transistors (FETs), ion-sensitive field-effect transistors (ISFETs), a quartz crystal microbalance (QCM), or optical converters.

The biochemical recognition of the target molecule by the bioreceptor causes a physical or chemical response at the surface of the transducer - a change in mass, refractive index, charge or ionic concentration.

**Transduction** The physical or chemical change caused by the interaction of the analyte with the bioreceptor is converted by the transducer mostly into an electric signal, which is amplified and processed by standard measurement electronics. Optical, electrochemical, or piezoelectric transducers are preferentially utilized for the signal conversion. In general, the transducer element is not selective.

Traditional bioanalytical methods routinely employ reporter molecules, such as fluorescent labels and radio- or redox active markers for a transduction of the biological recognition. However, label molecules often interfere with the biological functions. Label-free techniques omit the preparatory labeling steps and in many cases are suitable for continuous monitoring of assays and the analysis of binding events. Examples for label-free detection principles are given in the following.

## 1.1. Biosensor Concepts

### 1.1.1. Biological Recognition Reactions

The selectivity of biological sensing mechanisms is enabled by the specific affinity of the analyte molecule and the biological receptor. The recognition event is a specific interaction of the complementary molecular structures of analyte and receptor, according to the key-lock or induced-fit principle [Alberts, 2002]. In general, biological sensing reactions can be divided into two groups: biocomplexing recognition events and biocatalytic recognition reactions [Thevenot, 1999].

In sensors based on biocomplexing recognition, interaction of the bioreceptor immobilized on the sensor surface with the analyte molecule leads to the formation of a complex. After the recognition event, an equilibrium response is reached and no further analyte is consumed. Biocomplex-based biosensors generally do not allow a continuous monitoring of the analyte concentration and are often restricted to single-use. In some cases, the sensor surface can be regenerated and functionalized by a new layer of bioreceptors. Commonly employed biocomplexing recognition reactions are:

**DNA hybridization** Single-stranded oligonucleotide receptor molecules immobilized on the sensor surface interact with target DNA in case of complementary base pair sequences, resulting in a DNA double-strand. If probe and target molecule mismatch, hybridization does not occur. After incubation, unbound DNA strands of the assay solution are washed from the sensor surface. For identification of the DNA hybridization, the target DNA is commonly labeled with a fluorescence marker and the recognition event is detected optically by means of a fluorescence microscope or an optical scanner [Schna, 2000]. An alternative concept, the electrochemical redox-cycle technique, uses target DNA tagged by an enzyme label. As a transducer element, interdigitated gold electrodes with a spacing in the order of a few  $\mu\text{m}$  are used. After incubation of the sample solution and the removal of unbound DNA, a chemical substrate is applied to the sensor surface, which is converted into a redox active compound by the enzyme. The redox-currents between the two gold electrodes are a direct measure for the density of hybridized DNA [Bard, 1986], [Schienle, 2004].

Detection of the intrinsic charge associated with DNA strands by a field-effect device enables the verification of DNA hybridization without labeling of the target oligonucleotide. Corresponding experiments have been performed utilizing silicon-based capacitors as well as silicon and diamond field-effect transistors (FETs) as transducer devices and potentiometric detection of nucleic acid sequences was demonstrated [Fritz, 2002], [Uslu, 2004], [Song, 2006].

**Antibody-antigen interaction** Immunochemical tests are among the standard analytical methods in most medical laboratories. They are based upon the specific interaction of an antibody and the respective antigen. The presence or concentration of either antigen or antibody

in the assay is evaluated. The corresponding antibody or antigen serving as bioreceptor is produced by biotechnological methods. One reaction partner - the analyte - binds to the ligand immobilized on the surface of a microtiter plate or the sensor chip. Transduction of the binding event can be realized by various methods: The enzyme-linked immunosorbent assay (ELISA) uses a second antibody which couples to antigen-antibody complexes and is labeled with an enzyme. A probe substrate is applied to the surface which is converted by the enzyme to elicit a chromogenic or fluorescent signal, then analyzed by optical devices. Immunosensors based on surface plasmon resonance (SPR) [Myszka, 1997], [van Regenmortel, 1998] or quartz crystal microbalance (QCM) transducers [Kösslinger, 1995] operate without labels and measure the change in refractive index or mass that accompanies the antibody-antigen reaction at the sensor surface. Thus, the binding process can be visualized as a function of time and no influence on the binding properties is expected due to the label-free reactants. Further, immunosensors based on amperometric transduction [Hart, 1997] or ion-sensitive field-effect transducers have been realized [Katz & Willner, 2003].

Biocomplexing recognition reactions generally exhibit very large affinity constants and the analyte remains bound to the receptor after the recognition event. In contrast, biocatalytic recognition elements convert the analyte and return to their initial state after the recognition. Commonly used biocatalytic recognition elements are:

**Enzymes** Enzymes immobilized on the sensor surface bind the analyte and convert it catalytically [Michaelis & Menten, 1913]. After releasing the products, the enzymes return to their initial state. In enzyme based biosensors, either the products of the catalytic reaction or involved co-substrates are analyzed electrochemically. Ion-sensitive electrodes sensitive to  $H^+$ ,  $NH_4^+$ ,  $CN^-$ ,  $CO_2$ , or  $O_2$  are frequently utilized as transducer devices, according to the enzyme electrode proposed by Clark and Lyons [Clark & Lyons, 1962]. Caras and Janata introduced an enzyme based potentiometric biosensor based on an ion-sensitive field-effect transistor (ISFET) device with a layer of enzyme molecules immobilized on the gate surface, the enzyme-modified field-effect transistor (EnFET) [Caras & Janata, 1980]. Analyte concentrations of urea, glucose or penicillin have been successfully measured by Si-based EnFET devices [Kharitonov, 2000], [Poghossian, 2001], [Pijanowska, 2003]. The penicillin EnFET for example measures the pH change on the sensor surface as a result of the catalytic conversion of penicillin to penicilloic acid by the immobilized penicillinase enzymes [Poghossian, 2001].

**Cells and cell networks** Utilizing cells or cell networks as biological recognition elements, functional information - information about the effect of a chemical stimulus on a living system - rather than analytical information can be obtained. The biological recognition event - binding of the ligand to a receptor in the plasma cell membrane - is then amplified by second messenger pathways of the cell and the cellular response is detected. Cell based biosensors are mainly used to screen analytes for physiological effects, for example drug screening in the pharmaceutical industry, environmental monitoring or alarm systems responding to cytotoxic agents [Gross, 1985], [Pancrazio, 1998], [Wolf, 1998], [Yeung, 2001]. Either the electrical

cell activity [Pancrazio, 1998], [Yeung, 2001] or the cell metabolism is monitored to detect the cellular response associate with chemical stimuli. The metabolic activity of living cells is monitored mainly by means of the oxygen consumption or the extracellular acidification rate - the excretion rate of acidic by-products of metabolism [Parce, 1989], [McConnell, 1992], [Owicki & Parce, 1992], [Baumann, 1999].

### 1.1.2 Semiconductor Transducer Devices

Various transduction principles based for example on piezoelectric (QCM) or optical (SPR) devices have been mentioned in the previous section in relation to the detection of different biological recognition events. The further discussion of transducer devices for biosensors is constricted to electrochemical transduction elements based on semiconducting transducers. Modern semiconductor technology allows the microfabrication of sensor devices and the integration with electronic circuits for on-chip signal amplification and processing. The ongoing miniaturization of such devices enables the cost-effective fabrication of compact bioanalytical systems, as portable lab-on-chip systems for clinical diagnosis, environmental monitoring or patient self-monitoring. Even applications in the human body ("in-vivo") for a continuous blood analysis combined with an instant drug delivery system are discussed. Therefore, the development of sensor devices based on chemically inert and biocompatible semiconductor materials are a basic requirement.

Semiconductor based electrochemical transducers operate by either amperometric or potentiometric signal transduction:

**Amperometric transducers** measure the current resulting from the electrochemical oxidation or reduction of an electroactive species, for example a redox couple or a redox active enzyme or compound. As transducer devices for amperometric sensors, generally inert metal or carbon electrodes are utilized. Only highly conductive semiconductors inert against electrochemical decomposition, as for example nanocrystalline diamond [Yang, 2002], [Härtl, 2004], are suitable for amperometric semiconductor transducers.

In **potentiometric semiconductor transducers**, no charge transfer across the sensor surface but changes in the surface potential of a field-effect device are measured. They detect either (i) ionic concentration changes altering the surface potential, (ii) the intrinsic charge of the analyte molecule, or (iii) changes in the electrolyte potential. Semiconductor electrodes, and in particular solution-gate field-effect transistors (SGFETs) are promising devices for a sensitive detection of biological recognition events. SGFET devices are FETs without gate metallization. The gate region is in direct contact with an electrolyte solution, forming a liquid Schottky contact. The gate-source voltage  $V_{GS}$  is controlled via the electrolyte by additional electrodes. Utilization of SGFETs as transducer devices further benefits from the direct amplification and conversion of the potential signal into a current signal.

An SGFET suitable as transducer for biosensors has to meet specific requirements:

## 1. Introduction

---

- Biological processes proceed in liquid environment, often under physiological conditions. Thus, the sensor surface is in direct contact with an electrolyte solution. A reliable, sensitive and reproducible sensor operation requires a transistor surface which is chemically stable in the electrolytic environment under operating conditions.
- In order to resolve even small signal amplitudes excited by biological events, a high signal-to-noise ratio of the transducer device must be ensured.
- Depending on the biological recognition reactions, a surface layer sensitive to pH or other ions is needed.
- To enable a direct connection of the biological sensing element to the transducer, a functional immobilization of the bioreceptor to the device surface must be feasible.

Field-effect transducers used for biosensor applications are usually realized in silicon technology with a silicon dioxide gate dielectric, either as light-addressable potentiometric sensors [Parce, 1989], [McConnell, 1992], [Owicki & Parce, 1992] or as SGFETs [Bergveld, 1976], [Fromherz, 1991], [Offenhäusser, 1997], [Ingebrandt, 2001]. A main drawback of these devices is their long-term drift in electrolytes due to the electrochemical instability of the SiO<sub>2</sub>-surface during exposure to electrolyte solutions [Abe, 1979]. Furthermore, Si-based transducers with SiO<sub>2</sub>-surface layers exhibit a high noise level due to mobility fluctuations caused by trapping and detrapping of carriers to and from trap states at the interface to the surface oxide layer [Jakobson, 1998], hindering the detection of small signal amplitudes like action potentials of mammalian cells.

Despite of the deficiencies of silicon-based devices described above, most SGFETs are realized in silicon due to the advanced silicon technology. Whereas the device drift and stability can be significantly improved by the deposition of additional metal-oxide (Al<sub>2</sub>O<sub>3</sub>, Ta<sub>2</sub>O<sub>5</sub>) or silicon nitride (Si<sub>3</sub>N<sub>4</sub>) layers on the exposed sensor surface, the reduction of device noise requires complex device concepts like buried-channel FETs [Völker & Fromherz, 2005] or floating-gate devices [Cohen, 2004], [Meyburg, 2006].

An alternative approach to meet the specific requirements for biosensor transducers is the realization of SGFET devices based on wide bandgap materials such as silicon carbide, diamond, or group III-nitrides. Apart from their capabilities in high temperature, high power and high frequency electronics, these materials exhibit excellent properties for sensor applications in harsh environments [Lloyd Spetz, 1997], [Krötz, 1999], [Kohn, 1999], [Schalwig, 2002b], [Eickhoff, 2003], and diamond based biosensor transducers have already been realized [Yang, 2002], [Tachiki, 2003], [Härtl, 2004], [Song, 2006].

Due to their inherent material properties, group III-nitrides are a promising material system for the realization of sensitive and stable transducers for biosensor devices. InN, GaN, and AlN form a continuous alloy system with a direct optical bandgap, ranging from 0.7 eV for InN and 3.4 eV for GaN to 6.2 eV for AlN in the thermodynamically stable hexagonal wurtzite phase ( $\alpha$ -phase) [Ambacher, 1998]. Thus, group III-nitrides are mainly utilized for optoelectronic applications, as blue and UV-light emitting diodes (LEDs) [Nakamura, 1997] or solar-blind UV

detectors [Razeghi & Rogalski, 1996]. Due to the thermal stability and chemical inertness of the material system [Ambacher, 1998], chemical sensors for the detection of hydrogen and hydrogen containing gases based on Pt:GaN Schottky diodes have been realized, and were operated at elevated temperatures up to 600 °C [Luther, 1999], [Schalwig, 2002b], [Schalwig, 2002c]. Hexagonal group III-nitrides exhibit a spontaneous and piezoelectric polarization. At the interface of AlGaN/GaN heterostructures, a two-dimensional electron gas (2DEG) is formed due to the difference in the spontaneous polarization of the adjacent GaN and AlGaN layers. Based on this effect, high electron mobility transistors (HEMTs) with a surface-near 2DEG can be realized [Ambacher, 1999]. These devices are mainly utilized for high power and high frequency applications, and have recently been employed for chemical sensing in gases [Schalwig, 2002a]. SGFET devices based on AlGaN/GaN heterostructures benefit from the high stability of III-nitrides in liquids, and their potential for fluid monitoring applications or the detection of protein binding has been demonstrated [Neuberger, 2001], [Neuberger, 2003], [Eickhoff, 2003], [Kang, 2005]. Further, a utilization of AlGaN/GaN based transistors for the detection of the extracellular action potential of cells was proposed [Eickhoff, 2000].

### 1.2 Scope of this Work

The main focus of this work is a fundamental investigation of the AlGa<sub>N</sub> material system with regard to the realization of biochemical sensors operating in aqueous liquids. The development of a new device for the recording of extracellular cell signals based on AlGa<sub>N</sub>/Ga<sub>N</sub> heterostructures - and hence eluding the familiar problems of the generally used silicon based devices - was a further objective. The potential of AlGa<sub>N</sub>/Ga<sub>N</sub> SGFETs as biosensor transducers was evaluated and first biosensing applications were implemented.

Several key issues for the application of the AlGa<sub>N</sub> alloy system and in particular AlGa<sub>N</sub>/Ga<sub>N</sub> transistors in biosensors are discussed in detail:

- (i) Electrical performance of AlGa<sub>N</sub>/Ga<sub>N</sub> based transistors operating in aqueous electrolytes.
- (ii) Electrochemical properties of the Ga<sub>N</sub>/electrolyte interface.
- (iii) Biological functionalization of AlGa<sub>N</sub> surfaces.

The different required surface characterization techniques, such as X-ray photoelectron spectroscopy (XPS) or electrochemical impedance spectroscopy, as well as optical methods based on fluorescence microscopy are described in Chapter 2.

AlGa<sub>N</sub>/Ga<sub>N</sub> transistors and transistor arrays for operation in liquid environment were designed, processed, and investigated. A description of their layer structure and the device layout is given in Chapter 3. As all metallic wiring has to be carefully protected from the electrolytic environment, the device packaging is of particular importance.

Major electrical device properties, such as transistor characteristics and low-frequency noise performance were investigated and compared to the data of standard SGFET devices implemented in silicon technology (Chapter 4).

Chapter 5 deals with the chemical nature of the Ga<sub>N</sub> surface and the physical chemistry of the Ga<sub>N</sub>/electrolyte interface. The surface of native and thermally oxidized Ga<sub>N</sub> was analyzed by XPS, revealing the formation of a native oxide in atmosphere (Section 5.2). Basic principles of the semiconductor/electrolyte junction are introduced, and the fundamental difference to metal/electrolyte interfaces is pointed out (Section 5.1). Electrochemical analysis of the Ga<sub>N</sub>/electrolyte interface was performed by impedance spectroscopy and cyclic voltammetry measurements on planar Ga<sub>N</sub> electrodes (Section 5.3). Important interface properties such as flatband voltage and interface resistance were extracted from the impedance spectroscopy data by equivalent circuit models and compared to results from photoelectrochemical methods. Measurement errors due to deviations from an ideal interface are discussed in detail. The extracted data allow for determination of the energetic position of the band edges at the interface relative to the redox levels in the electrolyte. Results for n- and p-type doping, various doping levels, growth methods, as well as different Al-concentrations in AlGa<sub>N</sub> electrodes are compared. Measurements of charge transfer over the Ga<sub>N</sub>/electrolyte interface with and without



redox couples present in the solution are shown in Section 5.3.7. The response of native and oxidized GaN surfaces to pH and other ions, which is an important issue regarding ISFET or EnFET applications of AlGaN/GaN SGFETs, was investigated, and interpreted by means of the site-binding theory in Section 5.4.

Chapter 6 is dedicated to different strategies for the organic functionalization of III-nitride based transducers: (i) supported lipid bilayer membranes, (ii) organic silane monolayers, and (iii) cell-transistor hybrid systems. Artificial cell membranes were deposited by vesicle fusion on AlGaN electrodes. The lateral mobility of the lipids was investigated by an optical technique (continuous bleaching), taking advantage of the optical transparency of the sapphire substrate and the AlGaN film (Section 6.1.2). The dependence of the lateral diffusion on the lipid headgroup charge was investigated and compared to results obtained on sapphire and glass substrates. The membrane formation process and the electrical membrane properties were analyzed by impedance spectroscopy (Section 6.1.3). Various equivalent circuits for an electrical modelling of the membrane are compared. Functionalization of GaN surfaces by a monolayer of organic silanes enables various possibilities for a covalent attachment of receptor molecules. The electrical properties of octadecyltrimethoxysilane (ODTMS) monolayers on GaN were characterized and the surface coverage was estimated (Section 6.2). The suitability of AlGaN/GaN SGFETs for the measurement of extracellular cell signals was demonstrated by cultivating rat heart muscle cells directly on the surface of the transistor array. The spontaneous electrical activity of the cardiac myocyte syncytium was reflected by changes in the transistor channel current and successfully recorded. These measurements present the first extracellular recording of cell action potentials by a transistor device not implemented in silicon technology (Section 6.3).

## 2. Experimental Methods

### 2.1. Surface Analytical Methods

#### 2.1.1. X-Ray Photoelectron Spectroscopy

X-ray photoelectron spectroscopy is a highly surface sensitive analysis method, providing information on the material composition of the topmost 10 – 100 Å of a solid state surface as well as on the chemical bonding configuration of the elements. The measurement principle, the setup and the data acquisition and evaluation techniques are described in the following.

#### Measurement Principles and Setup

In XPS surface analysis, the sample is irradiated in ultra high vacuum with monochromatic soft X-rays ( $150 \text{ eV} < h\nu < 3000 \text{ eV}$ ) and the energy spectrum of the emitted photoelectrons is recorded. The impinging photons interact with an atom in the solid surface region by the photoelectric effect, causing the emission of a core or valence electron. Photons in this energy range have a penetration depth in solids of the order of 1 – 10  $\mu\text{m}$ . A kinetic energy distribution of the emitted photoelectrons is recorded by an electron energy analyzer. The binding energy  $E_B$  of the core level from which the photoelectron was emitted is determined from the kinetic energy of the photoelectron  $E_{kin}$  by

$$E_B = h\nu - E_{kin} - e\Phi_S, \quad (2.1)$$

where  $h\nu$  is the energy of the photon and  $\Phi_S$  the spectrometer work function. Energy relaxation of the ions after the photoemission process mainly occurs via emission of an Auger electron. The competing relaxation by emission of a fluorescent X-ray photon is a minor process in this energy range.

Since electrons have a very short inelastic mean free path  $\lambda_m$  in solids up to some tens of Angstroms, mainly photoelectrons originating from the few top atomic layers reach the detector without energy loss. The electrons that suffer an energy loss before reaching the surface by inelastic scattering processes contribute to the background of the photoelectron spectrum.

In this work, a system consisting of a X-ray source with Mg and Al anode (RQ-20/38C, SPECS, Berlin, Germany) and a hemispherical electron energy spectrometer (EA 10 MCD, SPECS, Berlin, Germany) was used for XPS analysis. The system was mounted in a UHV analytic chamber with a background pressure of  $2 \times 10^{-10}$  mbar.

In the X-ray source, electrons emitted by a hot cathode are accelerated by a high voltage and hit the Mg or Al anode, resulting in emission of Bremsstrahlung and the characteristic X-rays, with a main contribution from the  $K_\alpha$ -lines. As no monochromator is used, a narrow line width of the anode  $K_\alpha$ -line is essential, as it limits the energy resolution of the system. The  $K_\alpha$  photon energy of the utilized Mg and Al anode as well as their natural linewidth are given in the following Table 2.1.

X-ray	photon energy [eV]	natural linewidth [eV]
Mg $K_\alpha$	1253.6	0.70
Al $K_\alpha$	1486.6	0.85

**Table 2.1:** Photon energy and natural line width of the X-ray  $K_\alpha$  lines of a Mg and Al anode used for excitation.

The energy resolution of the spectrometer  $\Delta E$  results from a convolution of the natural linewidth of the non-monochromatic X-ray source  $\Delta E_{photo}$ , the Lorentzian broadening of the photoemission line  $\Delta E_{emission}$ , and the spectrometer-induced broadening  $\Delta E_{an} = k \cdot E_{pass}$ . A first approximation for the energy resolution is

$$\Delta E = \left( \Delta E_{emission}^2 + \Delta E_{photo}^2 + \Delta E_{an}^2 \right)^{1/2}, \quad (2.2)$$

assuming that all broadenings are of Gaussian form [Briggs & Grant, 2003]. With the natural Mg  $K_\alpha$  -line width of 0.7 eV, the live time of the emitted photoelectrons ( $10^{-14} - 10^{-13}$  s) and an analyzer constant of  $k = 1.3 \times 10^{-2}$  given by the manufacturer, the detector yields an ideal theoretical resolution of 0.9 eV. The pass energy  $E_{pass}$  of the detector was set to 29.6 eV for all measurements. From measurements of the silver  $Ag3d_{5/2}$  photoemission line, an experimental energy resolution of 1.01 eV was obtained.

## Data Acquisition and Evaluation

In this section, the acquisition and evaluation of X-ray photoelectron spectra is discussed. As no commercial software package was used for the data analysis, the employed evaluation steps and algorithms are briefly described.

X-ray photoemission spectra were recorded with a step width of 0.0305 eV and an integration time of 2 s. Particularly for peaks of low intensity, several sweeps over the energy range were performed to obtain a good signal-to-noise ratio.

To obtain information on the chemical bonding from an XPS spectrum, the spectrum is fitted by ideally shaped peaks by a non-linear least square fit algorithm. Proper treatment of the spectral background and utilization of adequate lineshapes are main requirements for a correct extraction of the measurement results from the spectrum.

Analysis of the measured spectral data was conducted in several consecutive steps:

## 2. Experimental Methods

---

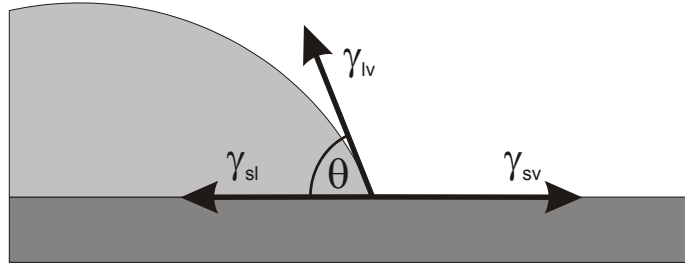
- During recording of the XPS spectra, the count rate of individual channels was significantly distorted by electromagnetic noise caused by a magnetic valve. The corresponding data points were traced with a filter algorithm and replaced by linear interpolation.
- Photoelectrons that are ejected by high-energy Bremsstrahlung of the anode or undergo inelastic scattering processes form a sizable background, that has to be removed in order to recover the significant spectra. Here, the background correction introduced by Shirley is followed [Shirley, 1972], which is usually sufficient for core level spectra. The more precise procedure of Tougaard requires spectra recorded over a large energy range accompanied by comparably long measurement times [Tougaard, 1997].

For the Shirley background correction, the spectrum is smoothed several times and a constant background is subtracted. The asymmetric background step associated with most core-level peaks is taken into account by an inelastic scattering correction, assuming a background at a kinetic energy  $E_{kin}$  that is proportional to the integrated intensity for all kinetic energies  $E_{kin}^* > E_{kin}$ , and divided by the intensity integral over the whole energy range. For the considered section of a spectrum from  $E_{kin}^{\min}$  to  $E_{kin}^{\max}$ ,  $I'(E_{kin})$  and  $I''(E_{kin})$  denote the intensity of the channel corresponding to the kinetic energy  $E_{kin}$  before and after the correction, respectively, and the corrected intensity  $I''(E_{kin})$  is calculated by

$$I''(E_{kin}) = I'(E_{kin}) - I'(E_{kin}^{\min}) \frac{\int_{E_{kin}}^{E_{kin}^{\max}} I'(E_{kin}^*) dE_{kin}^*}{\int_{E_{kin}^{\min}}^{E_{kin}^{\max}} I'(E_{kin}^*) dE_{kin}^*}. \quad (2.3)$$

- For resistive samples, the electrostatic charging can shift the peak position to higher binding energies. Therefore, accurate identification of the chemical state of an element requires the calibration of the energy scale by the characteristic emission lines of a reference material. In the ideal case, the calibration allows the comparison of results obtained from different experiments among each other and with binding energies given in literature. Here, a thin layer of Au was deposited on parts of the sample surface by sputtering in most experiments. All energies were referred to the Au 4f<sub>7/2</sub> peak position of the Au 4f doublet, for which an energy of 84.0 eV is given in the literature [Moulder & Chastain, 1992].
- For deconvolution of energy spectra in XPS analysis, Voigt type lineshapes are generally employed. The Voigt function is defined as a convolution between a Gaussian and a Lorentzian function. Instead of the real Voigt function, the more practical linear combination of a Gaussian and Lorentzian function in terms of a mixing parameter  $m$  is used in this work:

$$\frac{I(E)}{I(E_0)} = (1 - m) \cdot \exp \left[ -4 \ln 2 \frac{(E - E_0)^2}{\Delta E^2} \right] + m \cdot \left[ 1 + 4 \frac{(E - E_0)^2}{\Delta E^2} \right]^{-1} \quad (2.4)$$



**Figure 2.1:** Force balance between the liquid/vapor, solid/vapor and the solid/liquid surface tension at the three-phase contact line. The mechanical equilibrium is described by the Young-equation.

In Eq. 2.4,  $E_0$  denotes the peak center and  $\Delta E$  the full width at half maximum (FWHM). To restrict the number of fit parameters during data analysis, particularly when two or more lines are necessary for an appropriate deconvolution of the spectra, a constant mixing parameter of  $m = 0.3$  was assumed. Thus, the peak amplitude  $I(E_0)$ , the position  $E_0$ , and the FWHM  $\Delta E$  of each line remain as free parameters. The fit to the spectral data was performed by a non-linear Levenberg-Marquardt algorithm.

### 2.1.2 Contact Angle Measurements

Contact angles are established in a system with three distinct phases (solid/liquid/vapor) and express the wettability of a surface by a liquid. Contact angle phenomena at solid surfaces are studied mainly for two reasons: (i) The wetting behavior is important for a number of technological and biological phenomena and processes, such as the spreading of paints or lubricants on surfaces, or the deposition of lipid monolayers, bilayers, and the adsorption of proteins on solid supports for biophysical studies [de Gennes, 1985], [Nissen, 1999], [Sigal, 1998]. (ii) As the contact angle is related to the surface free energy (surface tension), chemical properties of the surface as well as the effect of surface modification, passivation, or aging can be investigated. Furthermore, chemical and structural surface inhomogeneities can be studied by determining the hysteresis between advancing and receding contact angles in dynamic contact angle measurements [de Gennes, 1985], [Kroll, 1994].

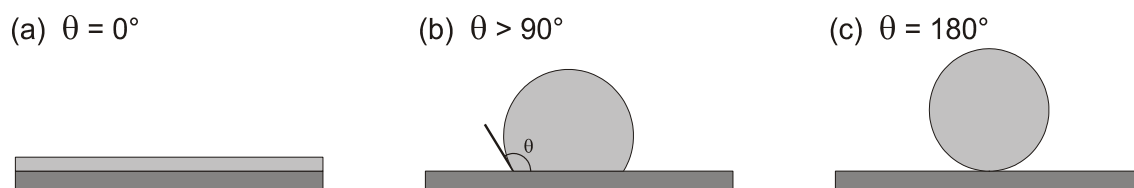
Assuming a liquid droplet on an ideal surface as illustrated in Figure 2.1, three interface free energies per unit area need to be considered:  $\gamma_{sl}$  denotes the surface tension at the solid-liquid interface,  $\gamma_{lv}$  at the liquid-vapor interface, and  $\gamma_{sv}$  at the solid-vapor interface, respectively. Three surface tension forces act at the three-phase contact line, each force along the interface between the corresponding phases. Under mechanical equilibrium conditions (force balance), the relation between the contact angle  $\theta$  and the surface tensions is given by the Young equation:

$$\gamma_{sv} = \gamma_{sl} + \gamma_{lv} \cdot \cos(\theta) \quad (2.5)$$

Four states for the wetting of a surface are distinguished by the contact angle [Dörfler, 1994]:

## 2. Experimental Methods

---



**Figure 2.2:** Wetting of a liquid on a solid substrate. (a) complete wetting, (b) partial wetting state: poor wetting of the surface, (c) complete drying.

- $\theta = 0^\circ$  The surface is completely wetted by the liquid. A uniform liquid film covers the whole solid surface and no droplets are formed on the surface. In Figure 2.2 (a), the *complete wetting state* is illustrated.
- $\theta < 90^\circ$  The liquid partially wets the surface. The *partial wetting state* is depicted in Figure 2.1.
- $\theta > 90^\circ$  The solid surface is not or just incompletely wetted by the liquid (Figure 2.2 (b)).
- $\theta = 180^\circ$  The liquid does not wet the surface at all. The *complete drying state* is shown in Figure 2.2 (c).

The contact angle  $\theta$  depends on the chemical constitution of both, the solid and the liquid. A qualitative description of wetting phenomena is given in a review by Zisman et al. [Zisman, 1964]. Assuming no chemical bonding between the adsorbate and the substrate, the liquid/solid energy and the surface tension are controlled by van der Waals interactions. Hence, the surface will be wetted by the liquid if the solid has a dielectric polarizability which is greater than that of the liquid or a high polarization. Because of its high surface tension of 72 mN/m, water does not spread or wet most surfaces. Table 2.2 summarizes the contact angle of water on various surfaces.

substrate	contact angle $\theta$
long-chain fatty acid	104°
long-chain alcohol	90°
polytetrafluorethylene (Teflon®)	110°
polyvinyl chloride (PVC)	69°
glass	0°

**Table 2.2:** Contact angle of water on different surfaces according to [Fujimoto, 1993], [Dörfler, 1994], [Yasuda, 1994].

Sigal et al. have investigated contact angles of water on self-assembled monolayers (SAMs) of alkane thiols on gold with various functional groups [Sigal, 1998]. In this case, the wetting

angle depends on the polarizability of the functional group exposed to the liquid. Their results for some important functional groups are summarized in Table 2.3.

functional group	contact angle $\theta$
-CH <sub>3</sub>	112 °
-CF <sub>3</sub>	118 °
-OH	< 15 °

**Table 2.3:** Contact angle of water on SAMs of alkane thiols with various functional groups on gold [Sigal, 1998].

**Static contact angle measurements** For the determination of static contact angles, a droplet of 2 – 5  $\mu\text{l}$  liquid was applied to the investigated surface by an adjustable micropipette. A cross-section of the droplet was recorded by a CCD-camera and the wetting angle was then evaluated by a digital image processing software. Wetting angles given in this work have been determined by an averaging over at least 3 measurements.

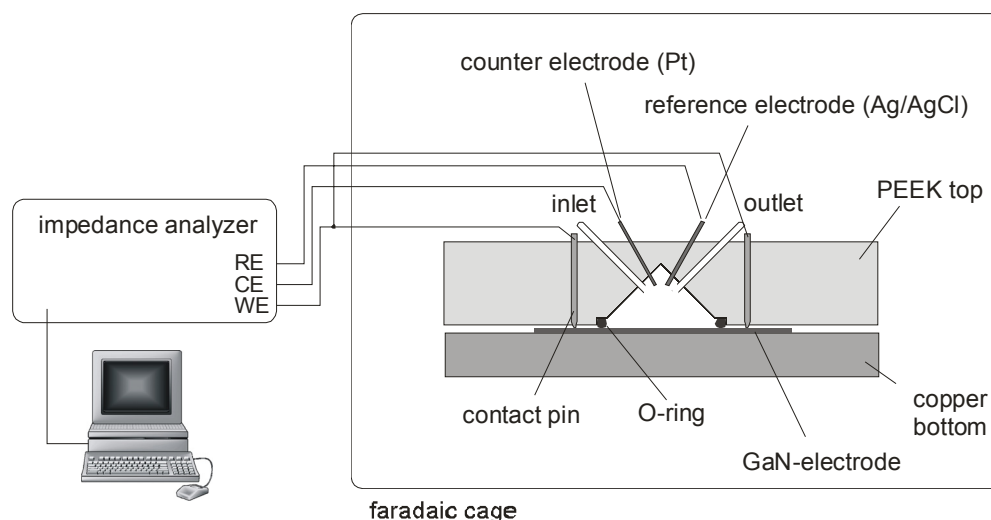
**Dynamic contact angle measurements** In the dynamic contact angle measurements a droplet was applied to the surface by a syringe. The syringe tip remained immersed into the droplet, allowing a variation of the droplet volume by a step motor attached to the syringe. The droplet volume was linearly increased by 15  $\mu\text{l/s}$  to a maximum volume of 15  $\mu\text{l}$ . By a CCD-camera, a cross-section of the droplet was continuously recorded and the contact angle and edge of the droplet were evaluated by a digital image processing software. Volume variation and picture recording was coordinated and controlled by a LabView program via a serial interface.

## 2.2 Electrochemical Techniques

### 2.2.1 Electrochemical Measurement Setup

Electrochemical experiments were performed in a flow chamber fabricated of PEEK with a three electrode setup. A schematic view of the flow chamber and the measurement setup is given in Figure 2.3. In a three electrode setup, the voltage between the *working electrode* (WE) and a *reference electrode* (RE) is regulated by a potentiostat. However, a current flow through the reference electrode must be avoided, as it would change the concentration of the reference redox species at the reference electrode and hence the reference redox potential (see Eq. (5.15)). This would impede the accurate determination of the absolute working electrode potential. Therefore, a third electrode, the so-called *counter electrode* (CE) is added to the setup and the current passes solely between the working electrode and the counter electrode. The three electrode setup consisted of an Ag/AgCl reference electrode filled with 3 M KCl

## 2. Experimental Methods



**Figure 2.3:** Schematic view of the electrochemical setup with flow cell and impedance analyzer.

(Metrohm, Filderstadt, Germany), a platinum counter electrode, and the GaN electrode operated as the working electrode. A VoltaLab 40 potentiostat (PGZ 301, Radiometer Analytical) was used for voltage control, signal generation, and data acquisition during cyclic voltammetry and impedance spectroscopy experiments. The flow chamber was sealed by an O-ring, which resulted in a circular active sample area of  $0.128 \text{ cm}^2$ . The flow chamber volume was approximately  $15 \mu\text{l}$ . The GaN electrode was contacted by four spring loaded gold contact pins in the corners. Buffer was continuously pumped through the flow chamber with a peristaltic pump (ISMATEC, Glattburg, Österreich), at a typical flow rate of  $1.2 \text{ ml/min}$ . The electrochemical cell was placed in an opaque Faradaic cage and shielded connections were used. The sample was in complete darkness during the experiments.

### 2.2.2 Buffer Solutions

Phosphate buffered saline (PBS) at pH 7, containing  $10 \text{ mM}$  sodium phosphate ( $\text{NaH}_2\text{PO}_4 / \text{Na}_2\text{HPO}_4$ ) was used as a standard buffer for the electrochemical experiments. The buffer was adjusted with sodium chloride to a total ionic strength of  $50 \text{ mM}$ , and degassed in an exsiccator directly before the experiments. This buffer is referred to as **standard PBS buffer** in the following. In some experiments **redox buffer**, consisting of standard buffer with  $1 \text{ mM}$  each of potassium hexacyanoferrate(III) and hexacyanoferrate(II) trihydrate was used, which resulted in an iron-cyanide redox couple in solution.

The **standard TRIS buffer** contained  $10 \text{ mM}$  of Tris(2-carboxyethyl)phosphine hydrochloride (TRIS) and was adjusted to a total ionic strength of  $50 \text{ mM}$  by NaCl.

The **standard HEPES buffer** contained  $10 \text{ mM}$  of N-2-Hydroxyethylpiperazine-N'-2-ethanesulfonic acid (HEPES). The total ionic strength was adjusted by NaCl to  $50 \text{ mM}$ . The



HEPES buffer was used in various concentrations in different applications. The buffer and salt concentration is given within the description of the respective experiment.

### 2.2.3. Impedance Spectroscopy

Impedance spectroscopy is a prominent electrochemical technique to study the electrical properties of materials and their interfaces to electrolytes. This method is particularly suitable for the analysis of complex systems whose electrical properties are determined by various processes with different time constants [Macdonald, 1987], [Barsoukov & Macdonald, 2005]. In biophysics, this noninvasive and label-free technique allows the study of biological systems and materials in their natural environment [Sackmann, 1996]. Several impedance spectroscopy studies of organic self-assembled monolayers on planar electrodes or organic molecules attached to solid supports have been reported [Sabatani, 1993], [Janek, 1998]. Lipid bilayer membranes containing functional proteins have been characterized by several groups with regard to ionic transport and dielectric properties [Gritsch, 1998], [Raguse, 1998], [Naumann, 2002], [Terrettaz, 2003], [Römer & Steinem, 2004]. Of special interest for biosensor applications are the transduction and analysis of biorecognition events at the surface of electrodes [Stelzle, 1993], [Cornell, 1997], [Katz & Willner, 2003].

#### Impedance Spectroscopy in the Time and Frequency Domain

In impedance spectroscopy, the current response of a system to an externally applied voltage is measured. For measurements in the time domain, the probe ac voltage signal is a voltage step or white noise composed of a multitude of frequencies [Barsoukov & Macdonald, 2005]. As all frequencies of the spectrum are applied simultaneously, this so-called spectral analysis has a high time resolution and is suitable for the dynamical analysis of fast processes [Wiegand, 2000]. The impedance of the system is obtained by Fourier-transformation of the transient voltage and current signals and Eq. (2.6).

For the so-called harmonic measurements in the frequency-domain, a monochromatic sinusoidal voltage signal  $U(t) = U_0 \cdot \sin(\omega t)$  is applied, causing a current response of  $I(t) = I_0 \cdot \sin(\omega t + \varphi(\omega))$  phase shifted with respect to the applied potential by  $\varphi(\omega)$ . In order to maintain a linear current response of the system, the amplitude of the applied ac voltage signal should be small, usually in the order of the thermodynamic fluctuations of 25 mV at room temperature. The complex impedance  $Z(\omega)$  of the system is defined as the Fourier-transform of the applied ac voltage  $\hat{U}(\omega)$  divided by the Fourier-transform of the current response  $\hat{I}(\omega)$ .

$$Z(\omega) = \frac{\hat{U}(\omega)}{\hat{I}(\omega)} \quad (2.6)$$

## 2. Experimental Methods

---

The impedance can be represented either in the complex notation as the sum of its real part  $Z'(\omega)$  and imaginary part  $Z''(\omega)$  or by applying Euler's law in polar coordinates by the absolute value of the impedance  $Z_0(\omega)$  and the phase shift  $\varphi(\omega)$ :

$$Z(\omega) = Z'(\omega) + Z''(\omega) = Z_0(\omega) [\cos(\varphi(\omega)) + i \cdot \sin(\varphi(\omega))] = Z_0(\omega)e^{i\varphi(\omega)} \quad (2.7)$$

Frequency domain spectra are obtained by sequential measurement of the impedance over a certain amount of periods for different frequencies  $\omega$ . By this technique, a high signal-to-noise ratio in the frequency range of interest can be achieved [Macdonald, 1987].

### Recording and Analysis of Impedance Data

**Recording of impedance spectra** The impedance measurements presented in this work were performed in the frequency domain with the setup and impedance analyzer described in Section 2.2.1. A  $750 \Omega$  resistor was connected in series with the GaN working electrode in order to obtain a well-defined impedance at high frequencies. The ac excitation signal amplitude was 20 mV. The impedance spectra were generally recorded in the frequency range between 50 kHz and 50 mHz with 5 - 20 frequencies per decade. Bode plots were used to visualize the impedance spectra, where the absolute impedance  $Z_0(\omega)$  and the phase shift  $\varphi(\omega)$  are plotted versus the frequency  $f = \omega/2\pi$ .

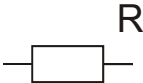

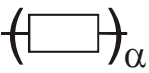

**Analysis of impedance spectra and equivalent circuits** Impedance data is analyzed in terms of equivalent circuit models to quantify the electrical properties of the investigated system. The equivalent circuit is constructed of discrete electrical components and corresponds to an appropriate physical description of the system [Macdonald, 1987]. However, any model circuit includes only a finite number of elements and is just an approximation of the real system. Structural inhomogeneities or dynamic processes can hardly be resolved, and just average values for the electrical parameters are obtained. Complications arise from ambiguities in the data interpretation, as complex circuits are not unique in their impedance vs. frequency dependence and rearrangement of circuit elements can reproduce the same behavior, but with different values obtained for the electrical components. In such cases, the choice of an adequate equivalent circuit model must be based on additional physical information about the system under investigation. The theoretical impedance spectra obtained from the equivalent circuit models were adapted to the experimental impedance spectra using a Levenberg-Marquardt algorithm for complex non-linear curve fitting.

Table 2.4 summarizes the discrete elements used in the equivalent circuits in this study. **Resistances** and **capacitances** represent lump-constant properties with ideal behavior and are therefore denoted as *ideal elements*. Real systems are often not described adequately just by ideal circuit elements. Geometry effects like structural inhomogeneities and surface roughness lead to a distribution of conductivity and the measured current response averages over all microscopic current pathways. In such cases, the introduction of *distributed elements* often

allow a more accurate modeling of the real system. **Constant phase elements (CPE)** can be included into the model circuit to account for a distribution of time constants at inhomogeneous interfaces. The CPE is an empirical impedance function expressed by

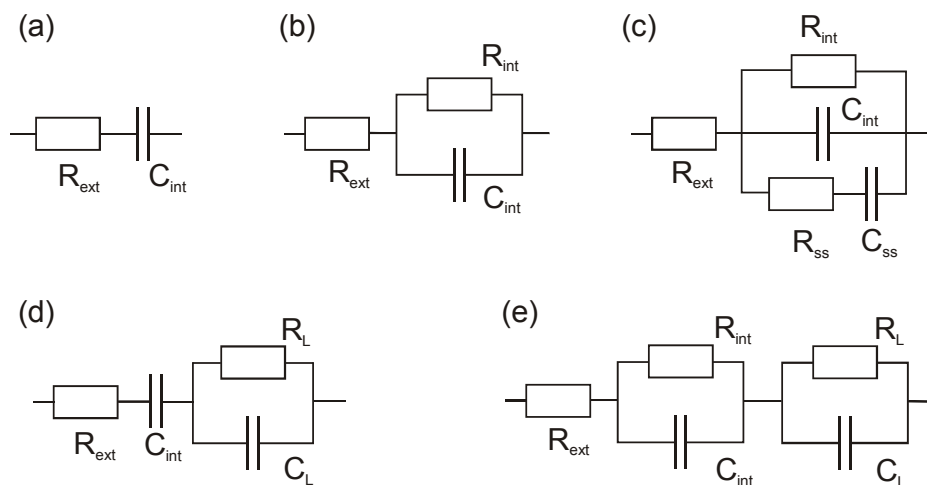
$$Z_{CPE}(\omega) = K \cdot (i\omega)^{-\alpha} \quad (2.8)$$

The extreme cases of  $\alpha = 0$  and  $\alpha = 1$  describe the ideal behavior of a resistance ( $K = R$ ) and a capacitance ( $K = 1/C$ ), respectively [Barsoukov & Macdonald, 2005]. The deviation of the exponent  $\alpha$  from these ideal values is assigned to inhomogeneities and represents a measure for the ideality of the system. The impedance behavior of polycrystalline electrodes and the influence of surface roughness have been described successfully by the consideration of CPEs [Fleig & Maier, 1996] [Delevie, 1989]. For rough surfaces, the exponent  $\alpha$  of the CPE could be related to the fractal dimension of the surface [Liu, 1985]. In general, the utilization of CPEs in the equivalent models can significantly improve the accuracy of the spectral fit to most experimental data. However, a physical interpretation of the derived quantities is rarely possible, and only qualitative information can be obtained. Hence, CPEs are solely used to estimate the ideality of the applied circuit model consisting of ideal elements throughout this work.

symbol	element	impedance $Z_i(\omega)$
 R	resistance R	$Z_R(\omega) = R$
 C	capacitance C	$Z_C(\omega) = (i\omega C)^{-1}$
 $\alpha$  $\alpha$	constant phase elements (CPE)	$Z_{CPE}(\omega) = K \cdot (i\omega)^{-\alpha}$

**Table 2.4:** Summary of the discrete elements used in the equivalent circuit models throughout this work.

## 2. Experimental Methods

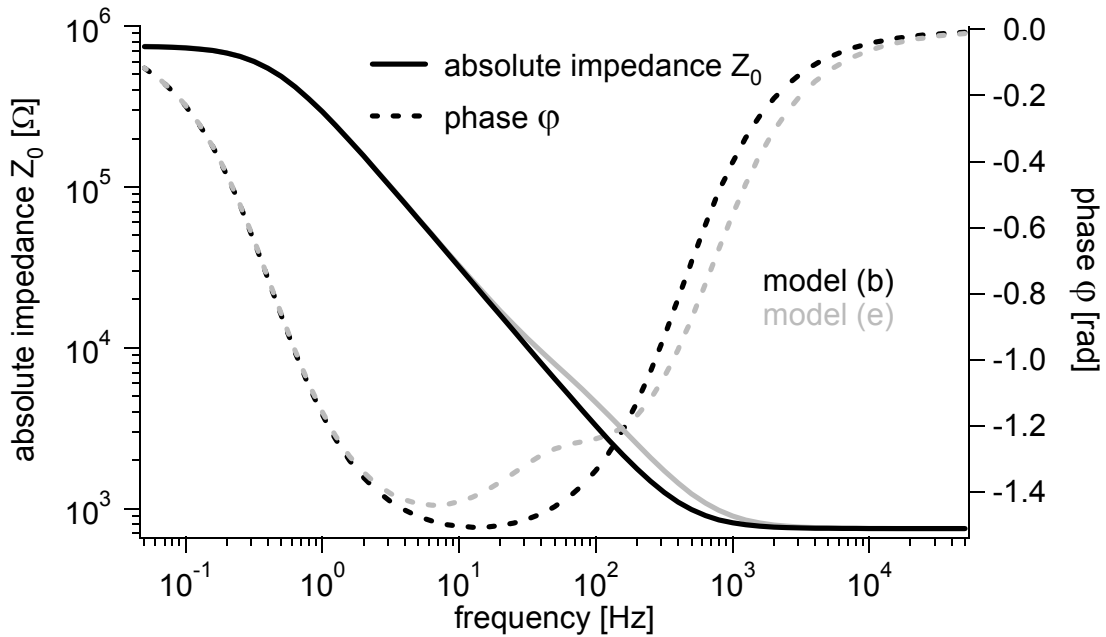


**Figure 2.4:** Equivalent circuit models used for the evaluation of impedance data in this work.

The equivalent circuits mainly used for data interpretation in this work are summarized in Figure 2.4. The fit models reflect different physical situations. In all models, a single ohmic resistance  $R_{ext}$  is used to summarize the external impedance contributions that are not related to the interface, as the resistance of the bulk semiconductor, the electrolyte, the cables, etc. In the experiments, this resistance is dominated by the  $750\ \Omega$  resistor in series with the working electrode.

- Model (a): The resistance  $R_{ext}$  in series with the capacitance  $C_{int}$ , is used to describe an ideal polarizable interface without any faradaic processes.
- Model (b): The so-called *Randles circuit* [Macdonald, 1987] includes a capacitance  $C_{int}$  in parallel with a polarization or interface resistance  $R_{int}$  and the external resistance  $R_{ext}$ .
- Model (c): This model describes an interface capacitance  $C_{int}$  and resistance  $R_{int}$ , with surface states ( $C_{ss}$ ,  $R_{ss}$ ) providing a parallel current pathway.
- Model (d) is used to describe an ideal polarizable interface with an additional - often organic - surface layer ( $C_L$ ,  $R_L$ ) that shows ideal behavior.
- Model (e): Two Randles circuits in series are used to describe an interface capacitance  $C_{int}$  with a parallel resistance  $R_{int}$ , and an additional ideal surface layer ( $C_L$ ,  $R_L$ ).

As discussed above, for estimation of the ideality of an applied equivalent circuit model, a capacitance of the respective circuit is replaced by a CPE. Modifications of model (e) used for the interpretation of the impedance data of solid supported bilayer membranes are given in Section 6.1.3. In Figure 2.5, simulated impedance spectra are shown in the Bode representation. The black curves represent the absolute impedance and phase versus frequency behavior of



**Figure 2.5:** Simulated impedance spectra of a Randles circuit (model (b), black curves), and with an additional serial RC-element (model (e), grey curves). The spectra are calculated for  $R_{ext} = 750 \Omega$ ,  $C_{int} = 0.5 \mu\text{F cm}^{-2}$ ,  $R_{int} = 750 \text{k}\Omega \text{cm}^2$ ,  $R_L = 2.5 \text{k}\Omega \text{cm}^2$ , and  $C_L = 1 \mu\text{F cm}^{-2}$ .

a Randles circuit ( $R_{ext} = 750 \Omega$ ,  $C_{int} = 0.5 \mu\text{F cm}^{-2}$ ,  $R_{int} = 750 \text{k}\Omega \text{cm}^2$ ). For high frequencies, the impedance of the interface capacitance  $C_{int}$  is negligible, and the serial external resistance  $R_{ext}$  determines the total circuit impedance ( $Z_0 \sim R_{ext}$ ) and the phase shift ( $\varphi(\omega) = 0$ ). At intermediate frequencies, the interface capacitance  $C_{int}$  is dominating the impedance behavior ( $Z_0 \sim 1/C_{int}$ ,  $\varphi(\omega) = -\pi/2$ ). In this frequency range, the circuit could be described just as well by the simple model (a). In the low frequency range, the impedance of the interface capacitance  $C_{int}$  becomes larger than the interface resistance  $R_{int}$ , and the capacitance is short cut. The total impedance and the phase is determined by the interface resistance ( $Z_0 \sim R_{int}$ ,  $\varphi(\omega) = 0$ ). The grey curves in Figure 2.5 illustrate the Bode plot of the discussed Randles circuit with an additional RC-element in series (model (e)), representing a surface add-layer, as for example a lipid bilayer membrane on the electrode. The resistance and capacitance for the additional layer was  $R_L = 2.5 \text{k}\Omega \text{cm}^2$  and  $C_L = 1 \mu\text{F cm}^{-2}$ , respectively. In this example of model (e), the time constants of the two RC-elements are sufficiently different to distinguish their contributions. A clear signature for the additive  $R_L C_L$ -element is seen at intermediate frequencies, and the electrical quantities of the circuit elements can be extracted individually. However, model (e) is no unique description for the impedance spectrum shown in Figure 2.5. Based on model (c), an identical spectrum but with different quantities for the extracted electrical properties can be obtained ( $R_{ext} = 750 \Omega$ ,  $C_{int} = 0.33 \mu\text{F cm}^{-2}$ ,  $R_{int} = 750 \text{k}\Omega \text{cm}^2$ ,  $C_{ss} = 0.16 \mu\text{F cm}^{-2}$ ,  $R_{ss} = 23 \text{k}\Omega \text{cm}^2$ ). Thus, additional physical

information is essential for the choice of the adequate model in the data evaluation process. In many cases, the analysis of a set of impedance spectra recorded under different measurement conditions (e.g. external dc bias voltage) facilitates the choice of the proper circuit model. Data recording and evaluation by circuit models must be an iterative process in impedance spectroscopy.

### 2.2.4. Cyclic Voltammetry

Cyclic voltammetry is a standard technique in electrochemistry with metallic electrodes: the current response of a system is recorded during a cyclic change of the external dc voltage between the *upper* and *lower switching potentials* at a constant sweep velocity ( $dV_{bias}/dt = const$ ). The method is mostly used with metal and degenerated semiconductor electrodes, and capable of assaying trace concentrations of an electroactive analyte and obtaining quantities such as redox potentials, electron transfer rates and numbers, or diffusion coefficients. Electrochemical reactions at the electrode surface like adsorption or electrode corrosion can be characterized and a verification of the stability of the electrode material is possible [Macdonald, 1987], [Finklea, 1988].

The cyclic voltammetry techniques developed for metal electrodes can be transferred to non-degenerated semiconductor electrodes only partially and by consideration of the major differences: (i) For metal electrodes, the redox levels of the species in solution are shifted with the applied external potential with respect to the metal Fermi level. At a semiconductor electrode the electrolyte redox levels remain fixed with respect to conduction and valence band edge at the semiconductor surface for a variation of the external voltage (q.v. Section 5.1.3). (ii) For semiconductor electrodes, the number of free charge carriers available for charge transfer to redox species in the solution changes exponentially with the external potential, whereas it remains unchanged for metals (q.v. Section 5.1.4).

Nevertheless, cyclic voltammetry provides a supplemental method for the characterization of semiconductor electrodes and the corresponding electrochemical processes. Reproducible cyclic voltammograms over time verify the stability of the investigated electrodes in the ambient electrolyte and specified potential window. Determination of the semiconductor band edges is possible by studying the current flow for a series of redox couples as a function of their redox level  $E_{redox}^0$  [Morrison, 1969]. The properties of charge transfer reactions to redox species can be investigated, e.g. diffusion limited redox reactions are detected as peaks in the voltammogram. The peak shape depends strongly on the sweep velocity [Finklea, 1988].

### 2.2.5. Photoelectrochemical Measurement Setup

For the photoelectrochemical measurements, a three electrode setup was used as described in Section 2.2.1. The voltage between the GaN working electrode and the Ag/AgCl reference electrode was controlled by a Wenking POS2 potentiostat (Bank Elektronik - Intelligent Controls).

The GaN electrodes were mounted in a PEEK sample holder and contacted in two opposite corners by spring loaded gold contact pins. The sample contacts and the wiring were protected from the electrolyte by an O-ring, defining the active electrode area to around 0.25 cm<sup>2</sup>. The teflon electrolyte container was equipped with a special mounting for the sample holder and a sapphire window to allow UV illumination of the sample. As a light source, a high-pressure xenon lamp was employed. The spectral power density for the spectral range over the GaN bandgap energy was around 10 mW/cm<sup>2</sup> at the sample surface [Zaus, 2004].

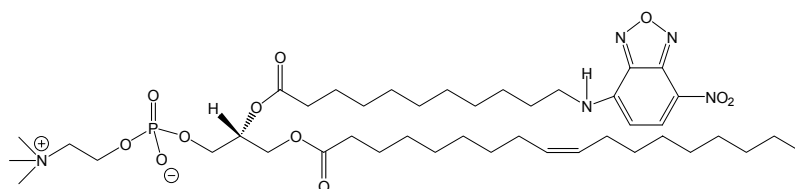
## 2.3. Optical Techniques

Parts of this work deal with the establishment and investigation of artificial lipid cell membranes on the surface of planar group-III nitride electrodes. As both the sapphire substrate and the semiconducting film of these electrodes are optically transparent, the biological system on the electrode surface could be studied by fluorescence techniques from the substrate backside. For this purpose, group-III nitride films deposited on double side polished sapphire substrates have been used. Fluorescence microscopy was used to visualize the homogeneity of the deposited lipid bilayer membranes. As the lateral mobility of lipids and proteins is of major importance for the functionality of membrane components [Hoppe, 1983], diffusivity and mobility of lipids in the prepared lipid bilayers have been measured by the continuous bleaching technique, which is based on fluorescence microscopy imaging.

### 2.3.1. Fluorescence Microscopy

The technique of fluorescence microscopy has become an essential tool in cell-biology and biomedical science. For visualization, the investigated system is stained with fluorescent dyes. After optical excitation, these molecules emit red-shifted light.

For optical investigation of lipid bilayer membranes, a nitrobenzoxadiazol (NBD) fluorescence dye attached to the fatty acid of a phospholipid was used. In Figure 2.6, the chemical structure of the chain-labeled fluorescence lipid NBD-phosphatidylcholine (NBD-PC) is shown. Excitation and emission wavelengths of NBD are 460 nm and 534 nm, respectively.



**Figure 2.6:** Chemical structure of the chain labeled fluorescence lipid 1-Oleoyl-2-[12-[(7-nitro-2-1,3-benzoxadiazol-4-yl)amino]dodecanoyl]-sn-Glycero-3-Phosphocholine (NBD-PC).

## 2. Experimental Methods

---

As fluorescence dyes are known to interact with biological systems, the molecular fraction of labeled lipids was kept as small as possible to preserve undisturbed membranes. A proportion of 1 mol% of fluorescence-labeled lipids was used throughout this work.

**Fluorescence microscopy setup** For fluorescence studies of lipid membranes an inverted microscope (Axiovert 200, Carl Zeiss, Göttingen, Germany) was used. The system is equipped with a high-pressure mercury lamp (HBO 100, Osram, Munich, Germany) and Achromplan long distance objectives (63x (N.A. 0.75) or 20x (N.A. 0.4)), purchased from Carl Zeiss. The fluorescence filter sets of the microscope can be adapted to the used fluorescence dyes. A combination of exciter (440/21 nm), dichroic (455 nm), and emitter (510/23 nm) was used (Omega Filters, USA) for NBD-PC. The fluorescence images and films were recorded using a cooled CCD camera (Orca ER, Hamamatsu Photonics, Herrsching, Germany), digitized by a frame-grabber card (Stemmer Imaging, Puchheim, Germany), and processed by the imaging software Open Box [Keller, 2001].

### 2.3.2 Continuous Bleaching

Whereas for *fluorescence recovery after photobleaching* (FRAP) experiments a special measurement setup is necessary to evaluate the lateral diffusion coefficient of lipid membranes [Axelrod, 1976], *continuous bleaching* is a convenient method to measure diffusion constants using a standard fluorescence microscope setup, as introduced in Section 2.3.1 [Dietrich & Tampé, 1995], [Dietrich, 1997]. In this technique, a defined area of the lipid membrane is continuously illuminated by the excitation wavelength of the incorporated fluorescence dye, resulting in a partial photochemical decomposition of the dye molecules and a continuous decrease in brightness. In-diffusion of unbleached labeled lipids from the unilluminated region leads to a spatial fluorescence intensity profile at the edges of the illuminated area. The concentration profile can be described by extending Fick's second law of diffusion by an additional term which describes the photobleaching:

$$\frac{dc(x, y)}{dt} = D \cdot \nabla^2 c(x, y) - B(x, y) \cdot c(x, y). \quad (2.9)$$

Here,  $c(x, y)$  denotes the concentration of unbleached dye molecules,  $D$  is the diffusion coefficient, and  $B(x, y)$  is the rate of photobleaching, which depends on the chemical nature of the dye, its environment, and the light intensity [Dietrich, 1997].

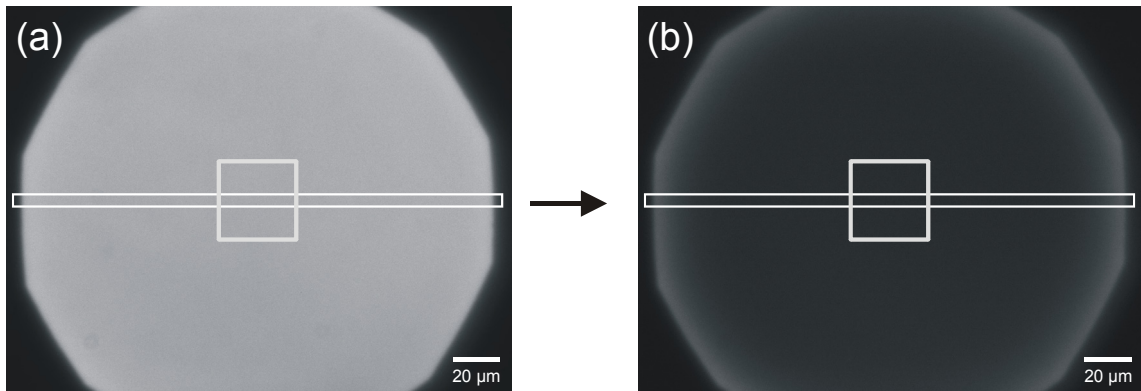
Assuming an illuminated half-plane for  $x \geq 0$  and a constant photobleaching rate  $B_0$ , the concentration profile for longer times within the illuminated area can be approximated by

$$c(x, t) = c(x = 0, t) \cdot e^{-\frac{x}{\lambda}} + e^{-B_0 t} \quad (2.10)$$

with

$$\lambda = \sqrt{\frac{D}{B_0}} \quad (2.11)$$





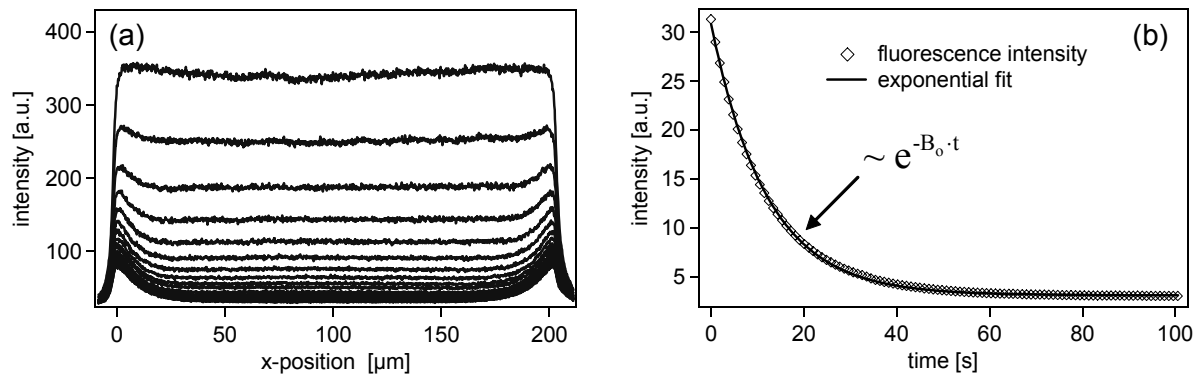
**Figure 2.7.:** Fluorescence image of a lipid membrane at  $t = 0$  s (a) and after prolonged illumination (b). The oblong white box denotes the area of the extracted intensity line profiles. The average brightness was taken from the center area (square).

Note that the shape of the profile, a monoexponential decay with a decay length of  $\lambda$ , is stationary after longer times, whereas the prefactor  $c(x = 0, t)$  never approaches a stationary value [Dietrich, 1997]. The diffusion constant  $D$  can be calculated from the decay length  $\lambda$  for a known bleaching rate  $B_0$ .

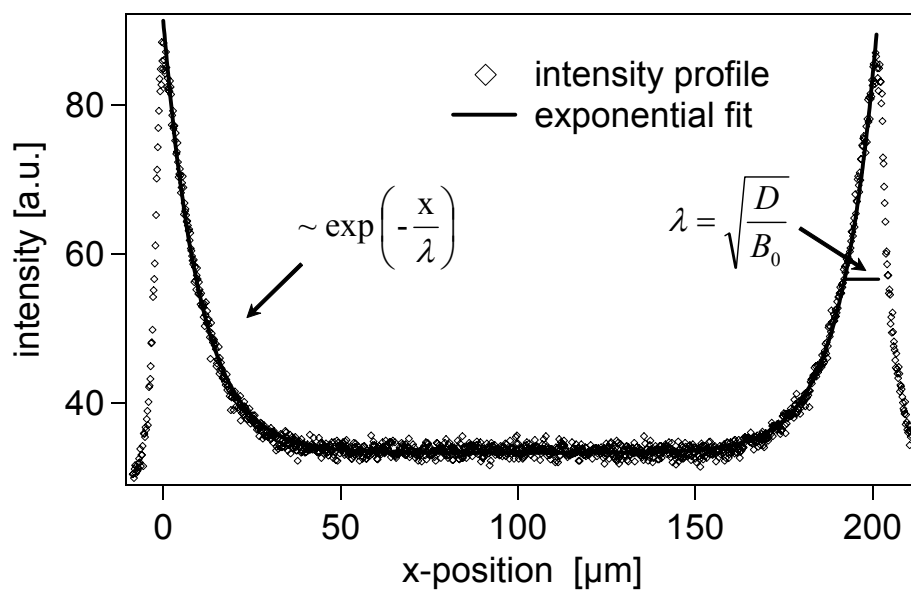
In the used setup, the illuminated area of the lipid membrane was defined by the circular aperture of the microscope (diameter  $\approx 200 \mu\text{m}$ ). Figure 2.7 shows the fluorescence image of a lipid membrane (a) at the beginning and (b), after prolonged illumination. For the evaluation of the decay length  $\lambda$ , intensity line profiles averaged for 10 parallel pixels were extracted from the fluorescence image across the illuminated area (white box in Figure 2.7 (a) and (b)). In Figure 2.8 (a) line profiles for increasing illumination times are depicted. The decay length,  $\lambda$ , was calculated from the exponential decay of the fluorescence intensity at the left and right edge (Figure 2.9). The bleaching rate  $B_0$  was determined from the decrease in average brightness of a square area ( $\approx 1000 \mu\text{m}^2$ ) at the center of the aperture (square in Figure 2.7 (a) and (b)) by an exponential fit (Figure 2.8 (b)).

Continuous bleaching is a suitable method for the measurement of relatively fast diffusion processes, as it monitors long range diffusion of lipids. With the described setup, diffusion processes with constants higher than  $0.1 \mu\text{m}^2 \text{s}^{-1}$  can be studied. The more precise FRAP-method allows the investigation of diffusion processes of membranes with slow molecular motion and limited lateral diffusion, as for example phospholipid membranes in the gel phase. Most of the experimental error in continuous bleaching experiments arises from the inhomogeneous illumination of the sample, leading to a difference in the diffusion constants extracted for the left and the right rim. Furthermore, the approximation of a mobile fraction of 100% of the lipids is not probable in most cases. In total, the experimental relative error of the determined diffusion constants is around 25%.

## 2. Experimental Methods



**Figure 28:** (a) Intensity line profiles across the illuminated area, illustrating the decrease in fluorescence intensity with continuous bleaching. (b) Average fluorescence intensity in the center of the illuminated region. The bleaching rate  $B_0$  was obtained by an exponential fit.



**Figure 29:** Intensity line profile across the illuminated area after prolonged illumination. The decay length  $\lambda$  was extracted from the exponential decay at the rim.

## 3. Structure and Processing of the III-Nitride based Transducer Devices

In this work, SGFET devices based on AlGaIn/GaN heterostructures or GaN:Si/GaN:Mg double layers as well as bare GaN electrodes deposited on sapphire substrates have been utilized as transducers for biochemical sensors. In this chapter the different layer structures, surface treatments as well as the device processing and packaging are described.

### 3.1. Layer Structure of the Transducer Devices

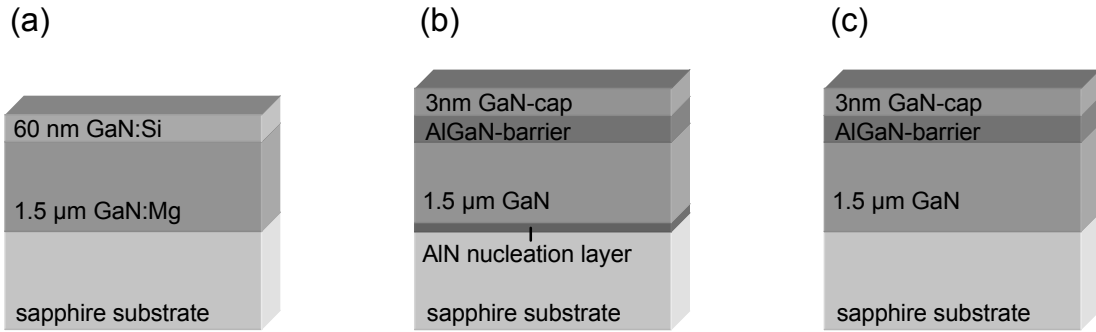
The III-nitride epilayers were deposited either by plasma assisted molecular beam epitaxy (PAMBE) or metal organic chemical vapor deposition (MOCVD) on c-plane sapphire substrates, resulting in a wurtzite crystal lattice structure. Details of the growth methods can be found for example in [Murphy, 1999] or [Ponce, 1996]. During PAMBE growth, the deposition of a thin AlN nucleation layer at the initial growth stage results in Ga-face (0001) polarity, whereas direct deposition on the sapphire substrate leads to N-face (000 $\bar{1}$ ) polarity. MOCVD growth on sapphire substrates always results in GaN layers with Ga-face polarity. Layer structures with N-face and Ga-face polarity are characterized by slightly different surface morphologies and stabilities, as well as by a reversal of internal polarization fields, which determine the polarity of piezoelectric and pyroelectric surface and interface charges [Ambacher, 1998].

#### 3.1.1. Transistor Structures

Two fundamentally different types of III-nitride based SGFETs have been used in this work: GaN:Si channel devices and AlGaIn/GaN high electron mobility transistors (HEMT) with GaN cap layers. The schematic layout of these structures is shown in Figure 3.1.

The GaN:Si channel device (Figure 3.1 (a)) consisted of a 60 nm-thick Si-doped GaN channel on a 1.5  $\mu\text{m}$ -thick GaN buffer layer with N-face polarity. The latter was partially compensated with Mg to achieve a high resistivity compared to the thin Si-doped channel close to the surface. The carrier densities at room temperature were determined by C-V measurements to  $3 \times 10^{18} \text{ cm}^{-3}$  in the Si-doped top layer, and  $5 \times 10^{15} \text{ cm}^{-3}$  in the Mg-compensated buffer layer. The GaN:Si/GaN:Mg double layer structures were grown by PAMBE at the Walter Schottky Institute.

### 3. Structure and Processing of the III-Nitride based Transducer Devices



**Figure 3.1:** III-nitride layer structures for SGFET devices: (a) PAMBE grown GaN:Si/GaN:Mg double layer structures and Ga-face AlGaN/GaN HEMT structures with a GaN cap-layer grown either by PAMBE (b) or MOCVD (c).

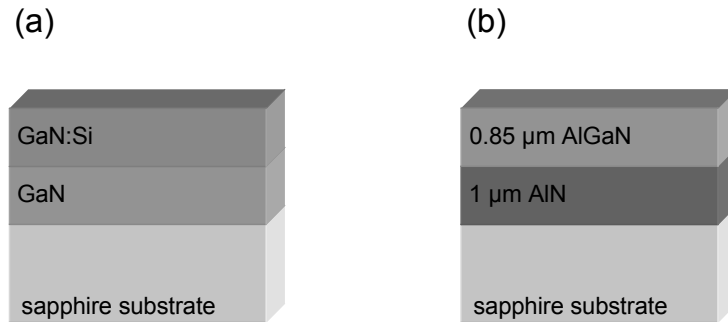
The AlGaN/GaN HEMT structures were either deposited by PAMBE at the Cornell University (Ithaca, New York), by MOCVD at the University of Magdeburg (Germany), or TopGaN (Warsaw, Poland). The PAMBE-grown heterostructures consisted of a 35 nm AlGaN barrier on a 1.5  $\mu\text{m}$  GaN buffer (Figure 3.1 (b)). The Al content in the AlGaN barrier was determined by high-resolution X-ray diffraction measurements to  $x = 0.28$ . On top of the AlGaN barrier, a 3 nm GaN cap layer was deposited. The Ga-face polarity of the whole structure was induced by a thin AlN nucleation layer on the sapphire substrate. In C-V measurements, the 2DEG carrier density was determined to  $6.1 \times 10^{12} \text{ cm}^{-2}$ .

The barriers of the MOCVD-grown AlGaN/GaN transistors (Figure 3.1 (c)) had a thickness of 20 – 30 nm and an Al content ranging from  $x = 0.2$  to  $x = 0.3$ . The 1.5  $\mu\text{m}$ -thick GaN buffer layer was compensated by Fe-doping in some devices. Room temperature sheet carrier concentrations and mobilities obtained from Hall measurements were between  $1 \times 10^{13}$  and  $1.2 \times 10^{13} \text{ cm}^{-2}$  and from 1100 to 1240  $\text{cm}^2/(\text{V s})$ , respectively.

#### 3.1.2 Electrode Structures

The schematic layout of the electrode sensor structures is shown in Figure 3.2. All electrodes used in this work exhibited Ga-face polarity. MOCVD grown n-type GaN layers of different doping levels were supplied by TopGaN (Figure 3.2 (a)). The GaN electrodes with higher doping levels consisted of a 2.9  $\mu\text{m}$  GaN buffer and a 0.25  $\mu\text{m}$  GaN:Si top layer with Si-concentrations of around  $10^{19} \text{ cm}^{-3}$ . The lower doped samples ( $N_D = 2 - 4 \times 10^{18} \text{ cm}^{-3}$ ) had a 1.7  $\mu\text{m}$  GaN buffer layer and a 2.9  $\mu\text{m}$  GaN:Si film.

III-nitride electrodes grown by PAMBE were provided by CEA Grenoble (France) and had a 1  $\mu\text{m}$  thick undoped AlN buffer layer on the sapphire substrates. As a surface layer, AlGaN films of different Si or Mg doping concentrations with a thickness of 0.85  $\mu\text{m}$  and Al concentrations ranging from  $x = 0$  to 0.5 were deposited (Figure 3.2 (b)). The doping concentration of the GaN films was determined in the electrochemical characterization from Mott-Schottky plots.



**Figure 3.2:** Layer structure of GaN and AlGaN electrodes: (a) MOCVD grown GaN electrodes and (b) PAMBE grown AlGaN electrodes ( $x = 0 - 0.5$ ).

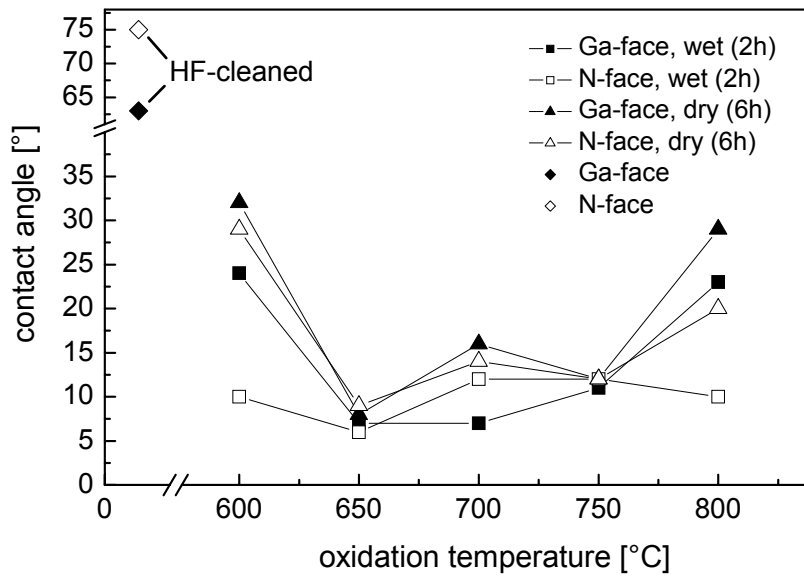
## 3.2 Surface Treatments

For various application of III-nitrides in biosensors, the chemical surface properties have to be controlled. A chemical modification of the surface should provide either (i) a hydrophilic surface for the deposition of highly mobile lipid membranes, or (ii) an oxidic surface, as metal oxide surfaces are known to be chemically stable in electrolyte solutions and show a high sensitivity towards pH. The oxidic GaN surface is compared with native GaN layers concerning this aspect. Or, (iii) the presence of hydroxyl bonds for a subsequent chemical functionalization with silane molecules.

Apart from the standard cleaning processes with organic solvents, basically two surface treatments have been applied throughout this work: (i) thermal oxidation at elevated temperatures between 600 °C and 800 °C, and (ii) a chemical surface treatment in a 3:1 mixture of  $\text{H}_2\text{SO}_4/\text{H}_2\text{O}_2$  (piranha etch), which, apart from removal of organic contaminants, leads to the activation of surface hydroxyl groups. Both processes as well as their influence on the wetting properties and the surface roughness of the investigated samples are described in the following. The chemical surface composition of native, piranha treated, and thermally oxidized GaN layers has been analyzed by XPS and is given in Section 5.2.

### 3.2.1 Thermal Oxidation

Thermal oxidation was carried out in a horizontal quartz tube furnace in dry or wet oxygen atmosphere. The cleaned samples were introduced into the heated furnace under nitrogen flux and subsequently oxidized under oxygen flux at a flow rate of 10 sccm and process temperatures ranging from 600 °C to 800 °C. The wet oxidation atmosphere was generated by adding water vapor to the oxygen. For this purpose, the  $\text{O}_2$  was passed through a deionized water bubbler.

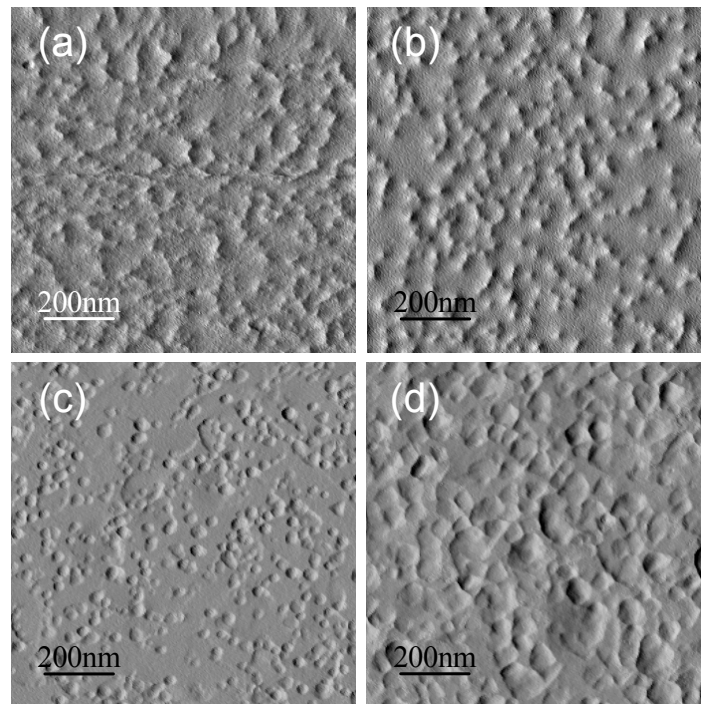


**Figure 3.3.:** Contact angle of a water droplet on thermally oxidized GaN surfaces with Ga- and N-face polarity after wet and dry oxidation as a function of oxidation temperature. For comparison, the contact angles of non-oxidized HF-cleaned GaN films are given.

The influence of the oxidation atmosphere and temperature on the wetting properties of the surface was investigated. In Figure 3.3 the static contact angle of a water droplet is shown as a function of the oxidation temperature for wet and dry oxidation. For comparison, the contact angle of a HF-cleaned GaN surface is also shown. Thermal oxidation led to a significant reduction of the contact angle, independent from the other process parameters. In addition, wet oxidation for 2 h resulted in more hydrophilic surfaces than a similar dry oxidation, which can be attributed to the lower oxidation rate in the latter case [Readinger, 1999]. Dry oxidation for 6 h lead to a comparable hydrophilicity.

Oxidation at temperatures below 600 °C resulted in rather poor hydrophilicity, indicating that in this case the oxide layer is not continuous. At oxidation temperatures between 650 °C and 750 °C, very small contact angles ( $< 10^\circ$ ) were observed for both wet and dry oxidation. For higher oxidation temperatures, the contact angle increases again, up to more than 20°. The same behavior is observed for both, N-face and Ga-face polarity. However, due to a higher oxidation rate, N-face samples show a better wetting behavior, even at lower oxidation temperatures.

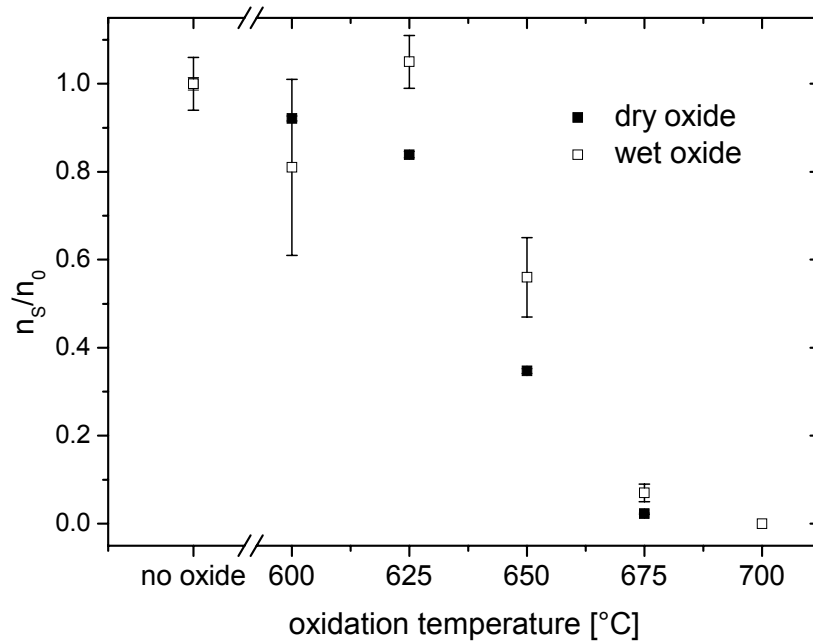
As shown by Wolter et al. [Wolter, 2000], the formation process of  $\text{Ga}_x\text{O}_y$  on the GaN surface is characterized by island growth and subsequent coalescence. At 650 °C, the surface coverage of the oxide layer is high enough to minimize the wetting angle. Hence, a closed oxide layer is assumed on the surface. When the oxidation temperature exceeds 750 °C, a strong increase in surface roughness was revealed by atomic force microscopy (AFM) measurements for the oxidized surface ( $\sim 10$  nm rms) in comparison to the untreated surface ( $\sim 1$  nm rms), resulting from the three-dimensional growth of the oxide layer. AFM amplitude images of GaN layers



**Figure 3.4:** AFM amplitude images of a MBE-grown GaN surface (a) before oxidation, and after dry oxidation at (b) 600 °C, (c) 700 °C, and (d) 800 °C.

that have been dry thermally oxidized at temperatures ranging from 600 °C to 800 °C are shown in Figure 3.4. As pinning can disturb wetting on a solid surface [Robbins & Joanny, 1987], an increase in surface roughness can provide an explanation for the increased contact angles at high oxidation temperatures. For the deposition of defect-free lipid bilayers with high lateral mobility, hydrophilic as well as smooth surfaces are required. For this reason, the oxidation temperature during the device preparation must not exceed 700 °C.

For a later application of transistor devices with thermal oxide surfaces in biochemical sensors, it must be ensured that the electronic device properties do not deteriorate under the process conditions. On that account, the sheet carrier density,  $n_S$ , of the polarization induced 2DEG of AlGaN/GaN heterostructure transistors was investigated as a function of the oxidation temperature. The results for an oxidation time of 2 h in both wet and dry atmospheres are shown in Figure 3.5. For both oxidation processes a similar decrease of  $n_S$  with increasing oxidation temperature was observed, starting at process temperatures over 600 °C. The fact that the decrease in carrier concentration is not affected by the oxidation atmosphere suggests that the dominating mechanism is not the oxidation itself but rather a thermal device degradation. Therefore, surface hydrophilization by thermal oxidation does not provide a viable route for the hydrophilization of AlGaN/GaN transistor structures.



**Figure 3.5:** Decrease of the relative sheet carrier density  $n_s/n_0$  in a  $\text{Al}_{0.22}\text{Ga}_{0.78}\text{N}/\text{GaN}$  transistor structure after wet and dry thermal oxidation as a function of temperature. The oxidation time was 2 h.

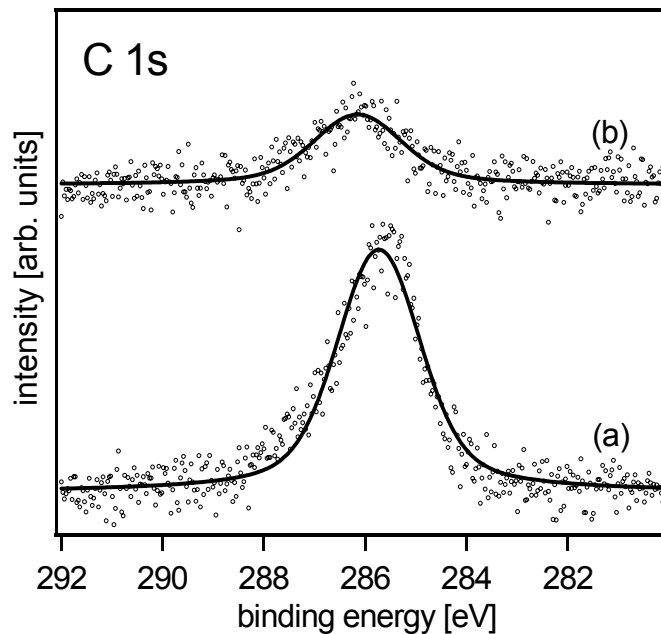
However, up to process temperatures of 700 °C, no significant degradation of the conductivity was observed for thermally oxidized GaN:Si channel devices. Hence, these transistors can be successfully hydrophilized by a thermal oxidation and the ion sensitivity of thermal  $\text{Ga}_x\text{O}_y$  oxides layers and native GaN surfaces can be compared by employing these devices.

#### 3.2.2 Chemical Surface Treatment

For some applications, the GaN surface was treated in piranha etch, which is a hot mixture of sulfuric acid ( $\text{H}_2\text{SO}_4$ ) and hydrogen peroxide ( $\text{H}_2\text{O}_2$ ). Due to its strong oxidizing properties, piranha etch is used to remove organic contaminants from the substrate surface. As most surfaces are as well hydroxylated, piranha treatment creates hydrophilic surfaces. In this work, a  $\text{H}_2\text{SO}_4/\text{H}_2\text{O}_2$  mixture of 3:1 was used. The substrates were immersed for around 20 min, thoroughly rinsed with deionized water and dried under nitrogen flux.

XPS analysis of piranha treated GaN samples revealed a strong reduction of the organic surface contaminants (Figure 3.6). In contrast to thermally oxidized surfaces (q.v. Section 5.2), no change in the O1s peak intensity or relative peak contributions was observed, indicating no further increase of the native oxide. The thickness of the native oxide layer was determined in [Baur, 2005] by X-ray reflectivity measurements to  $10 \pm 2 \text{ \AA}$ . Piranha treatment of GaN induces

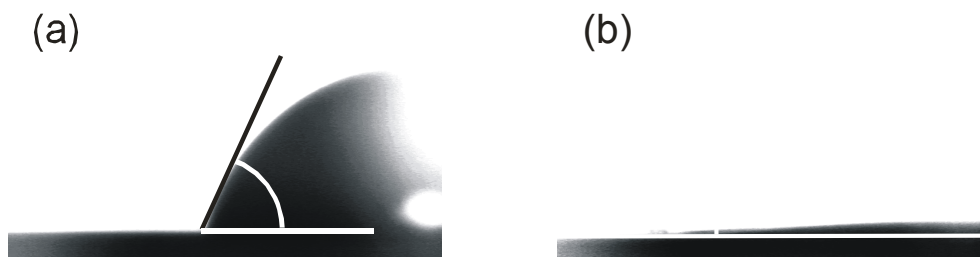




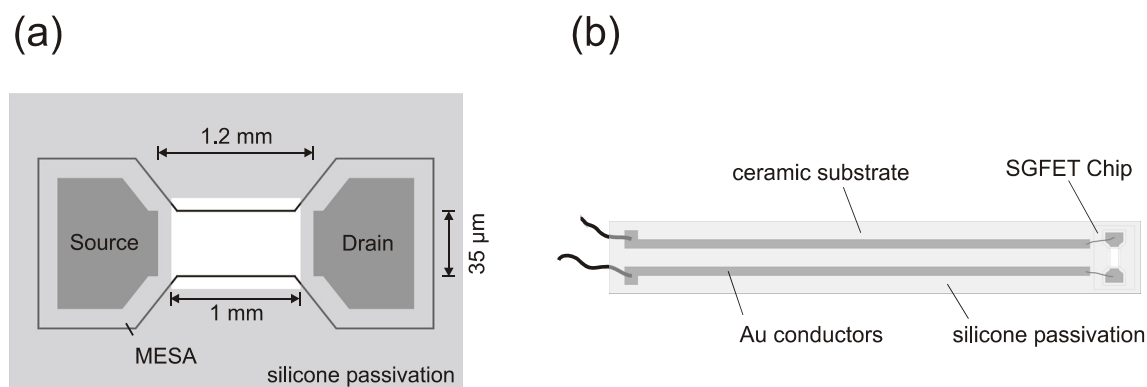
**Figure 3.6.:** C1s spectra of a native MOCVD-grown GaN surface (a) and after wet chemical surface treatment by piranha (b).

hydrophilic surface properties, reflected by small water wetting angles  $< 10^\circ$ . In Figure 3.7 the water contact angle on GaN films before and after the wet chemical oxidation is shown. The contact angle is reduced from  $74^\circ$  to less than  $5^\circ$  by the process.

In contrast to thermal oxidation, no increase in surface roughness after the treatment was observed. Apart from the hydroxylation of the GaN surface required for subsequent covalent biochemical functionalization with silane molecules, the method is a promising surface preparation for the deposition of defect-free lipid bilayer membranes.



**Figure 3.7.:** Wetting of a GaN surface by a water droplet (a) before, and (b) after wet chemical oxidation in piranha etch. The water contact angle was decreased from  $74^\circ$  to less than  $5^\circ$ .



**Figure 3.8:** (a) Geometrical layout of the single SGFET transistor. The total chip size is  $3.2 \times 2.3 \text{ mm}^2$ . (b) Schematic illustration of the packaging of single SGFET devices on ceramic holders.

### 3.3. Processing and Packaging of the Transducer Devices

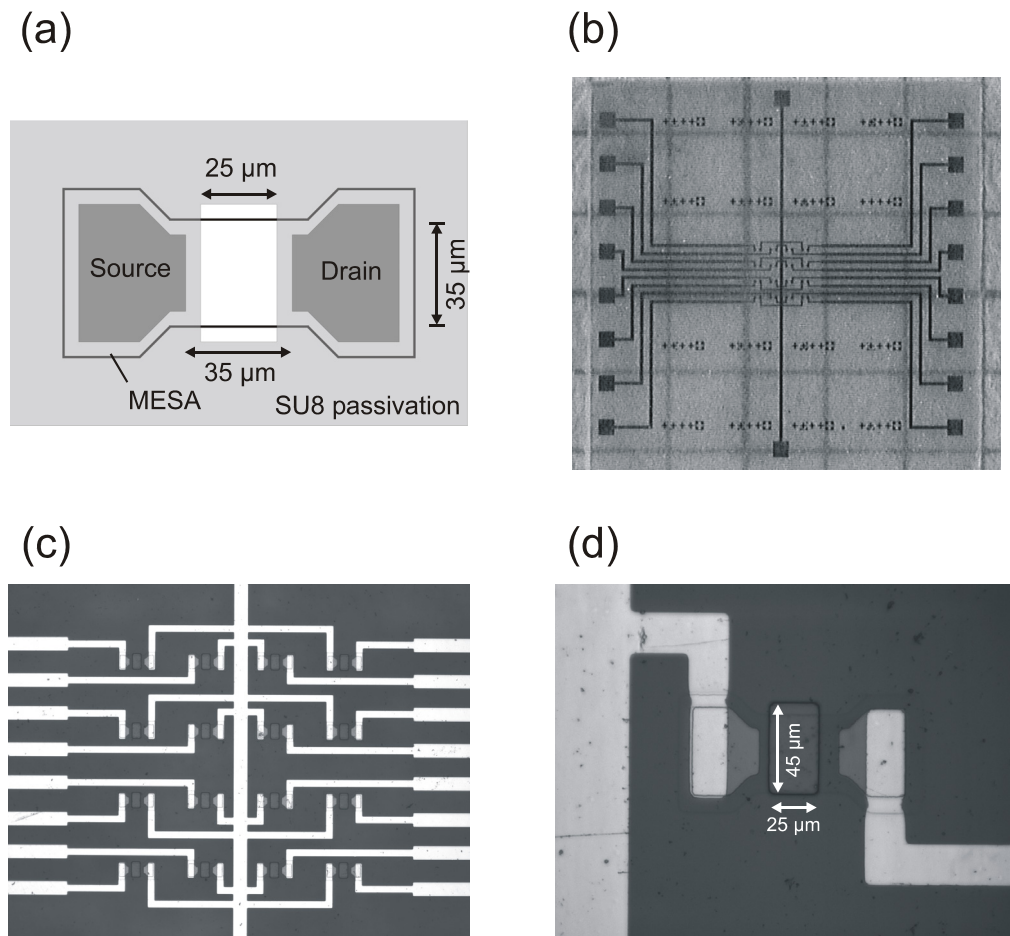
The results presented in this work have been basically obtained by three different types of transducer devices: single transistor devices with a large gate area, transistor arrays with small gate dimensions and GaN or AlGaN electrodes. The processing and packaging of these devices is described in the following.

#### 3.3.1. Single SGFET Devices

Due to the large dimensions, the single transistor devices allowed facile packaging and were employed for (i) basic characterization of the behavior of III-nitride based transistor devices in electrolyte solutions, (ii) analyzation of the ion sensitivity of native and thermally oxidized GaN layers, and (iii) EnFET applications of the device. The geometrical layout of the single SGFET is given in Figure 3.8 (a). Single transistors were processed on AlGaN/GaN heterostructures as well as on GaN:Si/GaN:Mg double layers.

The source-drain spacing was 1.2 mm and defined by the Ti (30 nm)/Au (300 nm) contacts, which have been annealed at  $700^\circ\text{C}$  for 2 min in vacuum to ensure ohmic behavior. Laterally, the conducting channel was defined by etching of a 100 nm deep MESA structure.

For SGFET applications, a protection of the source and drain contact and the electrical connections from the electrolyte solution is essential. The single transistors were fixed on  $40 \times 4 \text{ mm}^2$  ceramic substrates. The source and drain contact were connected by wire bonding to two Au conductors on the substrate. At the other end of the ceramic substrate, the two Au conductors were connected to insulated cables. A schematic picture of the packing is shown in Figure 3.8 (b). Except for a small opening defining the exposed gate area to  $1 \times 0.5 \text{ mm}^2$ , the whole transistor and periphery was then covered by a layer of silicon rubber. The robust packing allowed an easy handling of the sensor device during the experiments and straightforward

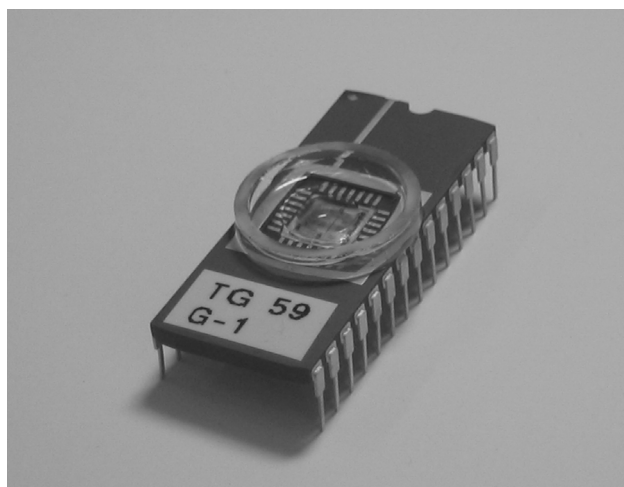


**Figure 3.9.:** (a) Layout of an individual SGFET element. Pictures of (b) the whole  $4 \times 4$  SGFET chip , (c) the transistor array in the middle of the chip, and (d) a single transistor element. The total chip size was  $5 \times 5 \text{ mm}^2$ .

measurement setups for basic experiments, as exposure of the whole sensor to the electrolyte solution was possible, and was also adopted for the investigation of other materials [Härtl, 2004], [Garrido, 2005].

### 3.3.2 SGFET Arrays

Transistor arrays were processed exclusively on MOCVD grown AlGaIn/GaN heterostructures. They were mainly applied for recording of cell action potentials and the investigation of the low-frequency noise of the SGFETs. The arrays consisted of 16 individual devices, arranged in a  $4 \times 4$  matrix centered on a  $5 \times 5 \text{ mm}^2$  chip. Single transistor elements with a channel width of 35 μm and a source-drain spacing of 35 μm were patterned by Ar ion beam etching. A layout of the single transistor elements is given in Figure 3.9 (a). The Ti/Au source and drain



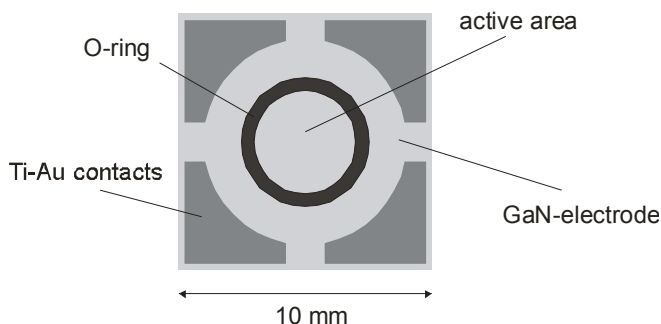
**Figure 3.10.:** Encapsulated 16-channel SGFET chip based on an AlGa<sub>N</sub>/Ga<sub>N</sub> heterostructure. The chip was mounted on a 28pin DIL-ceramic socket.

contacts were prepared as described above for single SGFETs. The transistors were connected in a common source configuration, with individual control of the drain voltages. The source and drain contacts were connected by Au conductors to bondpads in the outer region of the chip. The exposed gate length was defined by photolithographic opening of the epoxy-based passivation layer, which covered the whole inner region of the chip. Figure 3.9 (b) - (d) show the whole 16-channel SGFET chip, the 4 × 4 transistor array in the middle of the chip and a single transistor element prior to packaging.

For packaging, the SGFET arrays were mounted on a standard 28DIL ceramic chip carrier and contacted by wire bonding. As an electrolyte reservoir and culture dish for the cells, a glass ring was glued onto the DIL socket. To insulate the wiring from the electrolyte, a small silicone funnel with an opening for the active chip area was glued onto the chip and encapsulated by a silicone glue. The total electrolyte reservoir was about 400 μl. In Figure 3.10, the fully encapsulated SGFET chip is shown.

#### 3.3.3. Electrode Transducers

Single Ga<sub>N</sub> or AlGa<sub>N</sub> electrode transducers were processed on the Ga<sub>N</sub> and AlGa<sub>N</sub>/Al<sub>N</sub> layer structures shown in Figure 3.2. Due to the insulating sapphire substrate, the samples were contacted by four Ti (30 nm)/Au (100 nm) contact pads from the top. A schematic layout of the electrodes is given in Figure 3.11. Because of the large contact area, ohmic contacts could be realized without an additional annealing step. In some cases, the sample was thermally oxidized prior to the deposition of the Ti/Au contacts. If so, the oxide was opened at the contact pads by a HF-dip, taking advantage of the lift-off mask later used for the structuring of the contacts. Directly before the measurements, most electrodes were wet chemically treated in a



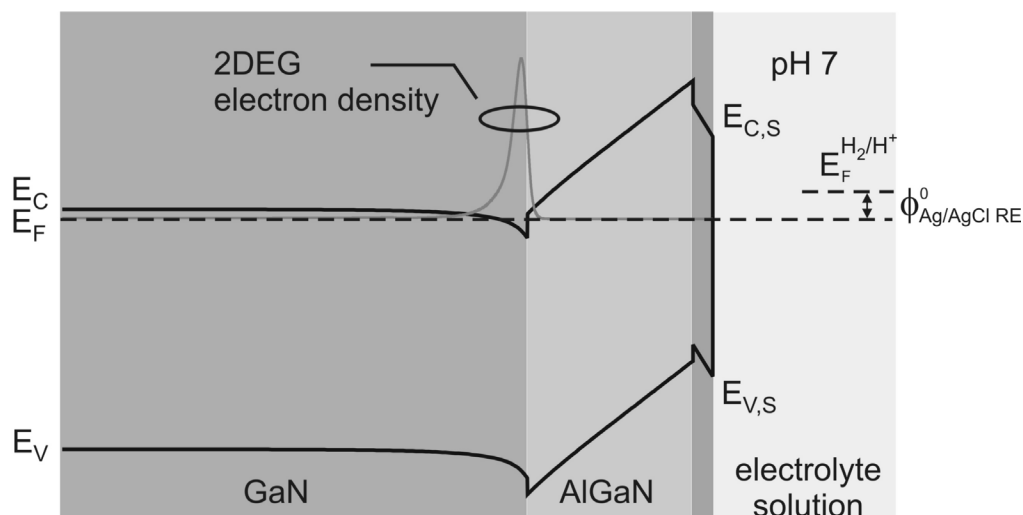
**Figure 3.11.:** Schematic layout of the GaN or AlGaIn electrodes. The active sample area is defined by the O-ring of the flow chamber to  $0.128 \text{ cm}^2$ .

3:1 mixture of  $\text{H}_2\text{SO}_4/\text{H}_2\text{O}_2$  as described in Section 3.2.2. Due to the Au top layer, the contacts could endure the treatment by the strongly oxidizing solution.

For most electrode devices, no packaging was necessary, as the electrodes were operated in the electrochemical flow chamber described in Section 2.2.1. The contacts were protected from the analyte solution by the O-ring sealing off the flow chamber, which furthermore defined the active sample area to  $0.128 \text{ cm}^2$ . Some smaller samples were individually packaged, as described for single transistor devices in Section 3.3.1. In that case, their contacts and wiring were protected by a layer of silicone rubber.

## 4. Electronic Characteristics of AlGaN /GaN SGFETs

In this chapter, the electronic properties of SGFET devices based on AlGaN/GaN high-electron-mobility transistor structures are discussed. In contrast to a regular FET, in a SGFET the metal gate is replaced by a solution gate. As extensively discussed in Chapter 5, the contact of the GaN transistor surface to the electrolyte solution behaves as a Schottky contact and the gate voltage can be controlled via the solution potential by means of appropriate electrochemical electrodes. In Figure 4.1 the band structure and electron density of an AlGaN/GaN SGFET with a 3 nm GaN cap-layer in contact with an electrolyte solution at pH 7 is shown. The band structure was calculated by nextnano<sup>3</sup> [Birner, 2006] for a gate-source voltage of  $V_{GS} = 0$  V, applied between the Ag/AgCl reference electrode of the solution and the source contact. The Schottky barrier of 1.12 V corresponds to the determined energy difference between the conduction band edge at the GaN surface and the Ag/AgCl reference redox level in solution (q. v. Section 5.3.3). The AlGaN barrier used in the calculation had a thickness of 25 nm and an Al content of 25%. The unintentional doping of the AlGaN barrier and the underlying GaN buffer were assumed to be n-type in a concentration of  $10^{15} \text{ cm}^{-3}$  and  $10^{17} \text{ cm}^{-3}$ , respectively. The ionization energy of the corresponding donor impurity level was assumed to be 20 mV. AlGaN/GaN single SGFETs



**Figure 4.1.:** Band structure and electron density profile of an AlGaN/GaN SGFET with a 3 nm GaN-cap layer in contact with an electrolyte solution at pH 7, calculated by nextnano<sup>3</sup>. A thickness of 25 nm and Al content of 25% was assumed for the AlGaN barrier.

and device arrays were characterized with regard to a possible application as transducers in biochemical sensors or the recording of electrophysiological signals. Basic device properties such as transistor characteristics and low-frequency noise have been analyzed under physiological conditions and are discussed in the following sections.

## 4.1. Transistor Characteristics

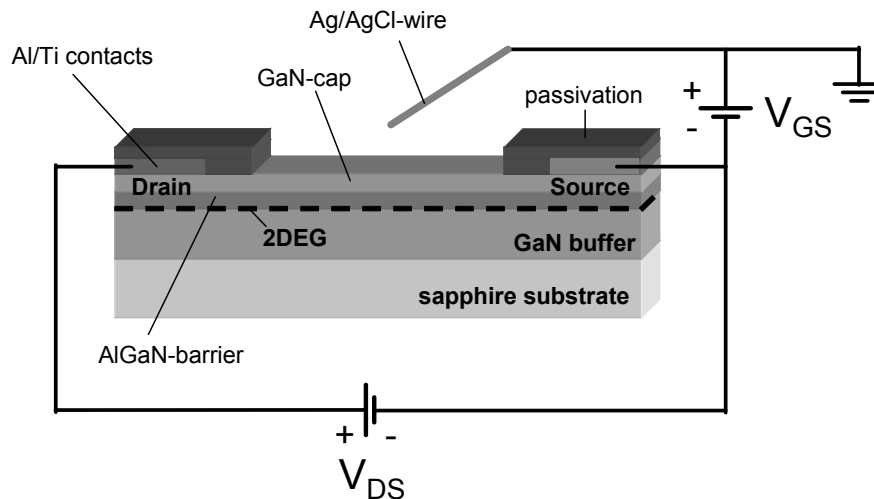
For the electrical characterization of the AlGaIn/GaN SGFETs two types of transistor characteristics have been measured: the output characteristics, where the drain-source channel current,  $I_{DS}$ , is recorded versus the drain-source voltage,  $V_{DS}$ , at a constant gate-source voltage,  $V_{GS}$ , and the transfer characteristics  $I_{DS}$  vs.  $V_{GS}$  at constant  $V_{DS}$ . By taking the derivative of the latter, the transconductance,  $g_m$ , of the device can be obtained.

The current-voltage (IV) characteristics were recorded either by

- (a) two interconnected sourcemeters (model 2400, Keithley Instruments Inc, Cleveland, Ohio) for voltage control ( $V_{DS}$ ,  $V_{GS}$ ) and current readout ( $I_{DS}$ ). Instrument control and data readout was performed by LabView routines via GPIB bus.
- (b) a measurement system at the Forschungszentrum Jülich, consisting of a digital IO board for voltage control, a preamplifier stage for current to voltage conversion, a second amplifier stage for offset compensation and signal amplification, and a A/D-conversion board for data recording. The system is described in detail in [Sprössler, 1998], and was used as well for the recording of noise spectra or extracellular cell signals. In the latter cases, a battery based power supply was used for the amplifier system to avoid noise pickup from the electricity network.

A schematic view of the electrical setup and wiring is given in Figure 4.2. To reduce the noise, the electrolyte was kept at ground potential for most applications. For the control of the electrolyte voltage, a simple Ag/AgCl-wire electrode was used in most cases. These kind of electrodes are not suitable for ISFET applications due to their large drift and low precision ( $< 5$  mV), but can substitute the bulky three electrode setup for the recording of simple transistor characteristics or short signal pulses.

Figure 4.3 (a) and (b) show the output and transfer characteristics of an individual element of a SGFET array, recorded with deionized water as an electrolyte solution. The transistors are operated in the linear regime with a maximum  $V_{DS}$  of 0.5 V to avoid excessive heat development at the gate surface during sensor operation ( $P(0.5 \text{ V})/A_{Gate} \approx 15 \text{ W cm}^{-2}$ ), which could influence or even damage the organic system or passivation layer on top. In the  $V_{DS}$  region of drain-source current saturation, a higher transconductance would be expected [Neuberger, 2003]. As observable for  $V_{GS} < -2.5 \text{ V}$ , the conductive channel is not fully depleted by the applied gate voltage. The remaining current is attributed to the leakage due to the conductive GaN

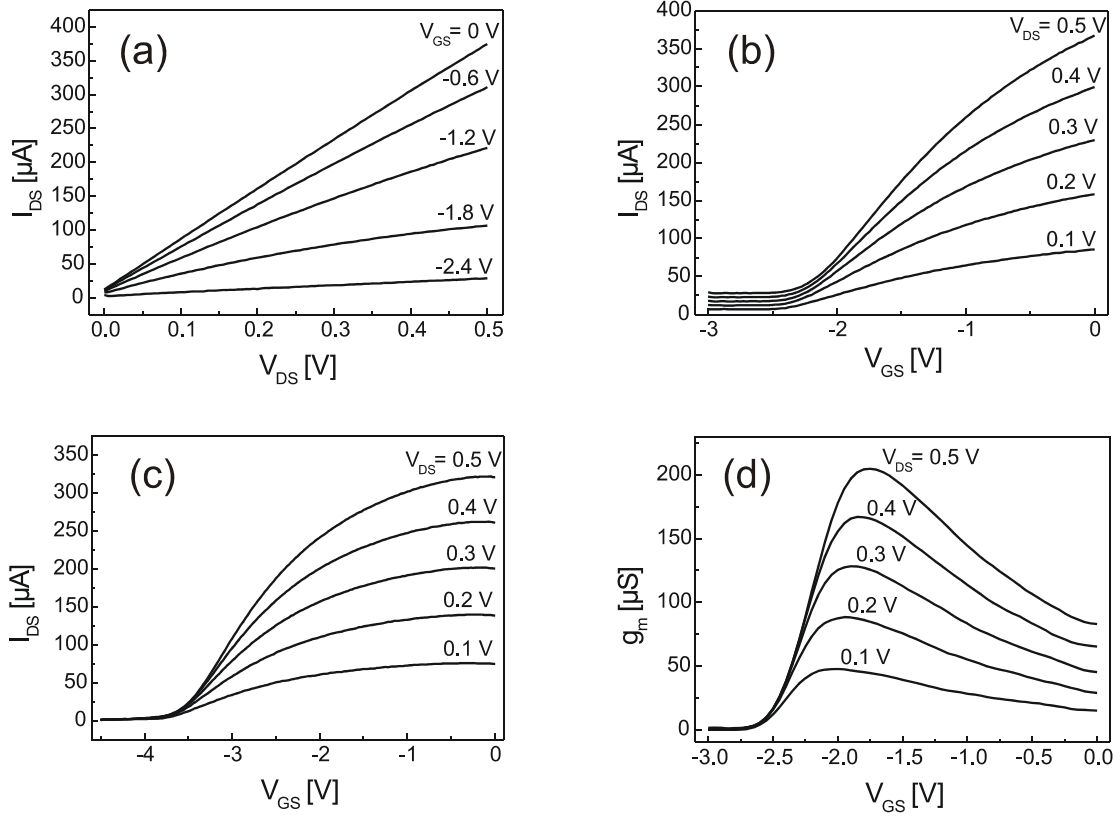


**Figure 4.2:** Setup and wiring of the SGFET devices.  $V_{GS}$  is applied to the electrolyte solution via a Ag/AgCl-wire electrode. In most applications, the electrolyte was held at ground potential for noise reduction.

buffer. For transistor structures on Fe-compensated GaN buffers, the parasitic current was considerably smaller (Figure 4.3 (c)). The transconductance of the transistor is obtained by taking the derivative of the transfer curves and is shown in Figure 4.3 (d). Under the usual operation conditions ( $V_{DS} = 0.5$  V), the devices exhibited a maximum transconductance  $g_m$  of 0.2 mS. The leakage current,  $I_{GS}$ , through the electrolytic gate was negligible ( $< 2$  nA) under these biasing conditions. Note that the maximum transconductance could be easily enhanced by increasing the gate width to length ratio of the transistor. As the main application of the presented AlGaN/GaN SGFET arrays was the recording of action potentials from cardiac myocyte cells, the gate geometry was adapted to the cell size and not optimized for maximum transconductance.

The output, transfer, and transconductance characteristics of a single large area SGFET device operated with standard PBS buffer as an electrolyte solution are presented in Figure 4.4 (a) - (c). Due to the smaller width to length ratio of the gate, the obtained transconductance for equal drain-source voltages was smaller compared to the characteristics of an individual device of the SGFET array. A maximum transconductance  $g_m$  of 0.14 mS was achieved at  $V_{DS} = 0.5$  V.





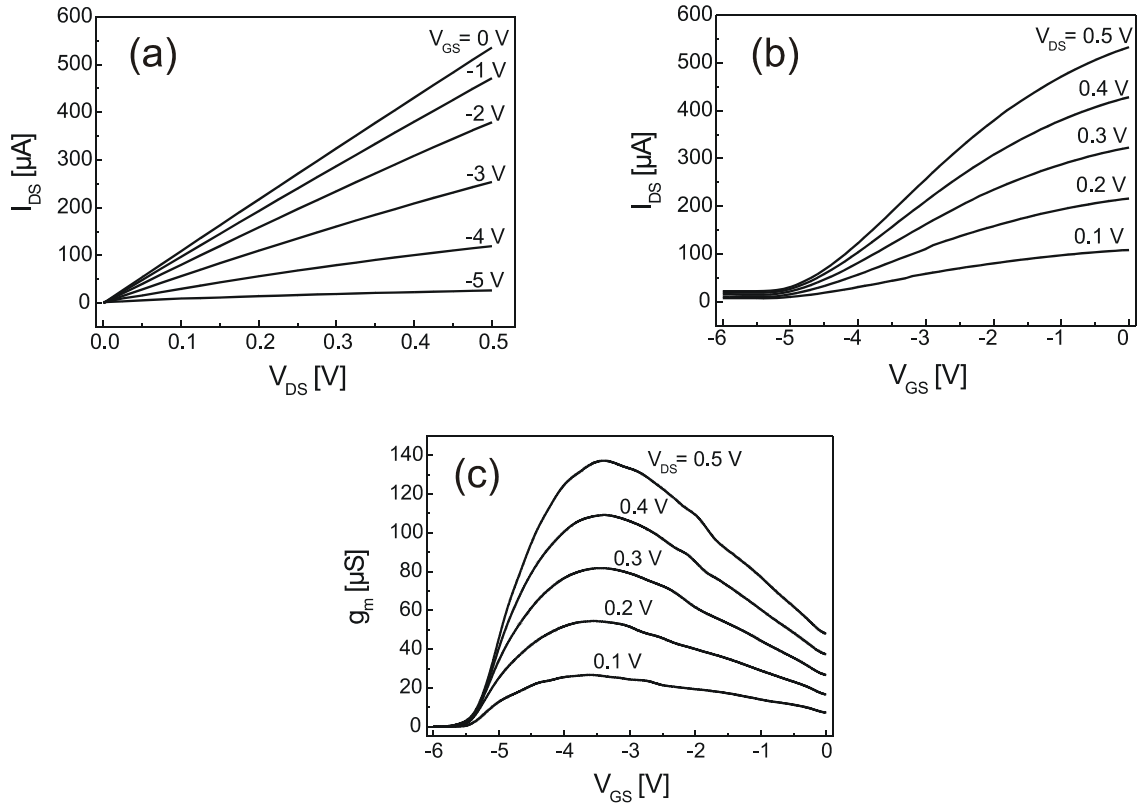
**Figure 4.3:** (a) Output, and (b) transfer characteristics of the individual device of an AlGaIn/GaN SGFET array. By differentiation, the transconductance  $g_m$  (d) is obtained. In (c), the transfer characteristics of a device with a Fe-compensated GaN buffer is shown.

## 4.2 Low Frequency Noise

The sensitivity of a bioelectronic transducer device is limited by its signal-to-noise ratio and determines the resolution of the whole biosensor. A low background noise level is of particular importance for the recording of electrophysiological signals, which can lead to low voltage transients to be resolved by the transducer in the range  $< 100 \mu\text{V}$  for the action potentials of mammalian neurons [Vassanelli & Fromherz, 1998]. As cell action potentials and other biological signals occur at low frequencies, the low frequency noise ( $1 \text{ Hz} < f < 1 \text{ kHz}$ ) of the transistor arrays was analyzed for different gate-source voltages at room temperature.

The presented low frequency noise measurements provide a basis to estimate the capability of AlGaIn/GaN SGFETs for cell signal recording applications in comparison to the Si-based FET devices usually used in this field. For a precise identification of the responsible noise mechanisms, a more detailed and comprehensive analysis would be necessary.

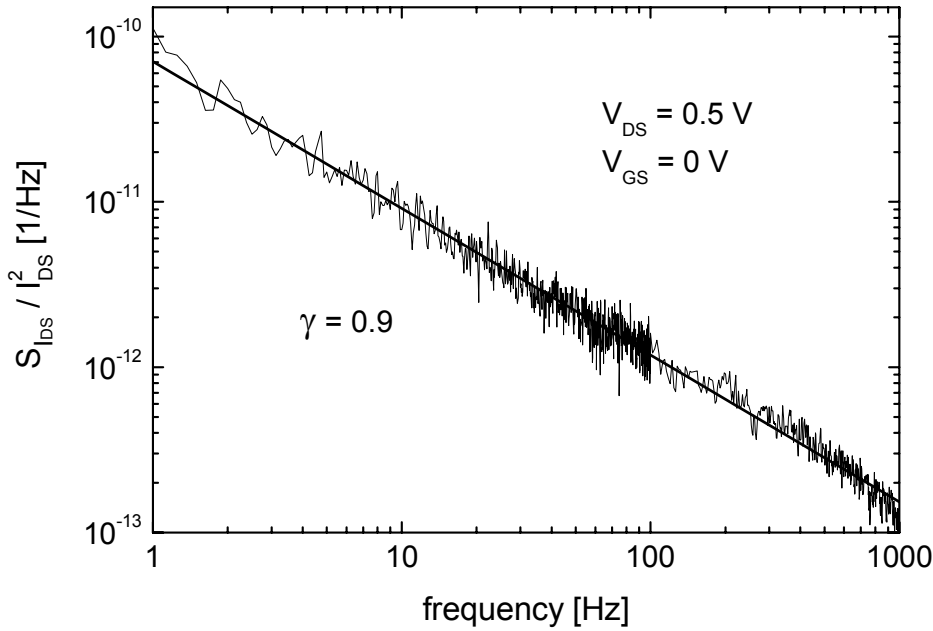
#### 4. Electronic Characteristics of AlGaN/GaN SGFETs



**Figure 4.4:** (a) Output, (b) transfer, and (c) transconductance characteristics of a large area single AlGaN/GaN SGFET.

For recording of the noise spectra, a FFT spectrum analyzer (35670A Dynamic Signal Analyzer, Hewlett Packard, Palo Alto, California) was used in combination with the measurement setup (b) described in Section 4.1. The voltage signal equivalent to the drain-source current  $I_{DS}$  of the transistor was feed into the spectrum analyzer after the second amplifier stage of the measurement system. Spectra were taken in two frequency ranges: (a) from 0 to 100 Hz with a resolution of 800 channels averaging 25 times, and (b) from 0 to 3.2 kHz with a resolution of 1600 channels averaging 50 times. As a lowpass filter at 3 kHz is included in the measurement system to reduce the noise level during action potential recording, the spectra were truncated at a maximum frequency of 1 kHz.

All presented noise measurements have been recorded with deionized water as an electrolyte solution from the same individual transistor device of an AlGaN/GaN SGFET array. The corresponding transistor characteristics are given in Figure 4.3. Figure 4.5 shows the noise power density spectrum of the drain source current noise  $S_{I_{DS}}$ , normalized by  $I_{DS}^2$ . The frequency behavior follows the typical  $1/f^\gamma$  dependence of low frequency flicker noise, with an exponent  $\gamma$  close to unity. The  $1/f$  or flicker noise is generated by random fluctuations of the electrical conductivity [Hooge, 1981], either by fluctuation of the number of contributing charge carriers



**Figure 4.5.:** Frequency dependence of the relative spectral noise density  $S_{I_{DS}}/I_{DS}^2$  of an AlGaIn/GaN SGFET at  $V_{DS} = 0.5V$  and  $V_{GS} = 0V$ . A  $1/f^\gamma$  behavior with  $\gamma = 0.9$  is observed.

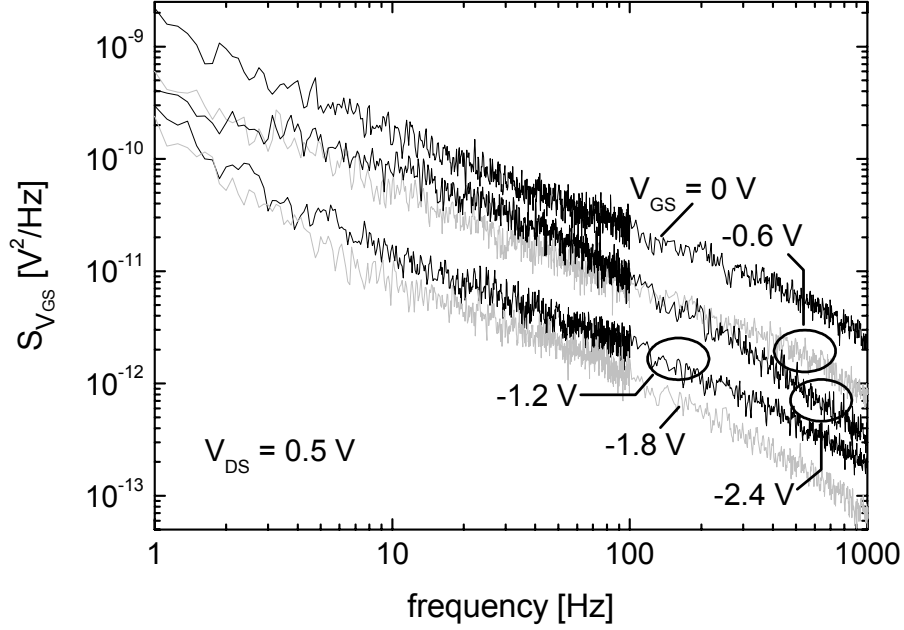
or their mobility. McWhorter proposed a theory to explain the  $1/f$  noise by fluctuations in the number of charge carriers by generation and recombination (G-R noise), mostly via centers with energy levels in the bandgap [McWhorter, 1957]. The model can be generalized to capture and emission processes with distributed time constants. In silicon based FETs, the low frequency noise is mainly caused by trapping and detrapping of single inversion carriers to and from trap states at the Si/SiO<sub>2</sub> interface [Jakobson, 1998].

A second model for the origin of low frequency noise relates the conductivity fluctuations to fluctuations in the charge carrier mobility. Even so the existence of mobility fluctuations has been proved experimentally, a clear theory for the noise mechanism is still missing [Hooge, 1981].

Independent of the model assumed for the origin of the noise, the  $1/f$  noise can be characterized by an empirical equation introduced by Hooge [Hooge, 1972]. In the Hooge equation, the relative noise spectral density of the current,  $S_I$ , the voltage,  $S_V$ , or the resistance,  $S_R$ , is inversely proportional to the total number of conduction carriers  $N$  by a dimensionless proportionality factor  $\alpha$ , the so called Hooge parameter:

$$\frac{S_I}{I^2} = \frac{S_V}{V^2} = \frac{S_R}{R^2} = \frac{\alpha}{N} \cdot \frac{1}{f} \quad (4.1)$$

The Hooge parameter  $\alpha$  depends on the material, the crystal quality and the noise mechanism. It allows the comparison of the  $1/f$  noise level in different semiconductor materials, structures

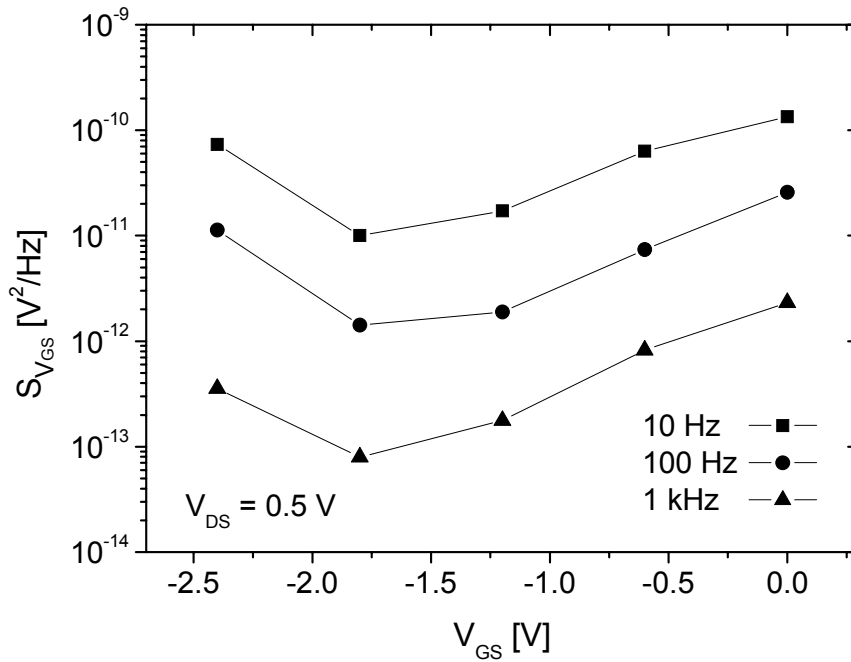


**Figure 4.6.:** Equivalent gate-voltage noise power density spectra for different  $V_{GS}$  at  $V_{DS} = 0.5$  V.

and geometries [Hooge, 1994]. The Hooge parameters of some important materials and devices will be given later in this section.

From the  $S_{I_{DS}}/I_{DS}^2$  spectra and the corresponding  $1/f^\gamma$ -fit shown in Figure 4.5, a Hooge parameter of  $5 \times 10^{-3}$  can be calculated for the AlGaN/GaN SGFET with an assumed number of contributing charge carriers of  $N = 7.5 \times 10^7$  under the gate, as deduced from the 2DEG density measured by Hall. For usual AlGaN/GaN heterostructure FETs with Pt-gates or AlGaN/GaN metal-oxide-semiconductor heterostructure FETs, grown either on sapphire or SiC substrates, Hooge parameters of the order of  $10^{-5} - 10^{-4}$ , up to  $10^{-2}$  have been reported [Balandin, 1998], [Garrido, 1998], [Rumyantsev, 2000a]. Different possible sources for the  $1/f$  noise in AlGaN/GaN devices were discussed in these publications. The lowest Hooge parameters for HEMTs based on AlGaN/GaN are comparable to values of  $10^{-5} - 10^{-4}$  measured for AlGaAs/GaAs MODFETs [Duh & Van der Ziel, 1985], which are of the same order as in GaAs layers [Hooge & Tacano, 1993]. For Si MOSFETs  $\alpha$  values even lower than  $10^{-6}$  at room temperature have been reported [Duh & Van der Ziel, 1985].

For the measurement of electrophysiological cell signals, low potential changes have to be resolved at the gate surface of the SGFET device. Hence, not the drain-source current noise but the equivalent gate input noise is decisive, and was calculated from  $S_{I_{DS}}$  by  $S_{V_{GS}} = S_{I_{DS}}/g_m^2$ . The equivalent gate input noise was analyzed for different operation conditions by variation of  $V_{GS}$  to find an ideal operation point with minimum background noise. Figure 4.6 shows the  $V_{GS}$  noise power density spectra for different gate voltages  $V_{GS}$  between 0 and  $-2.4$  V. The

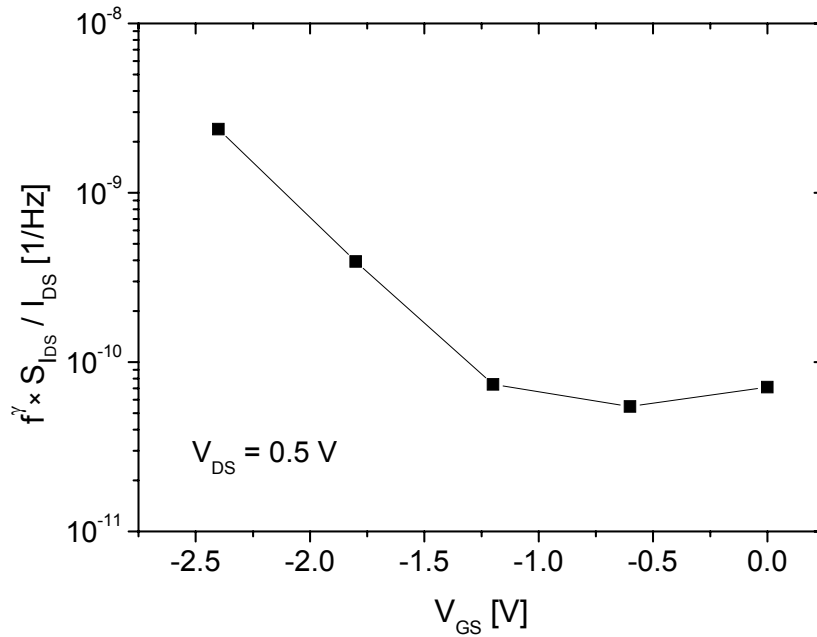


**Figure 4.7.:** Variations of the equivalent gate-voltage noise power spectral density as a function of  $V_{GS}$  for different frequencies.

exponent  $\gamma$  varies with  $V_{GS}$  between  $\gamma = 0.9 - 1.3$ . The noise power spectral density exhibits a minimum for  $V_{GS} = -1.8$  V, as also shown in Figure 4.7 for different frequencies. The ideal  $V_{GS}$  operation point for the recording of signals with low amplitudes coincides to the  $V_{GS}$  of maximum transconductance of the transistor. On this account, fluctuations of the potential at the interface to the electrolyte can be excluded as the dominating noise mechanism, in that  $S_{V_{GS}}$  would be independent of  $V_{GS}$  for that case.

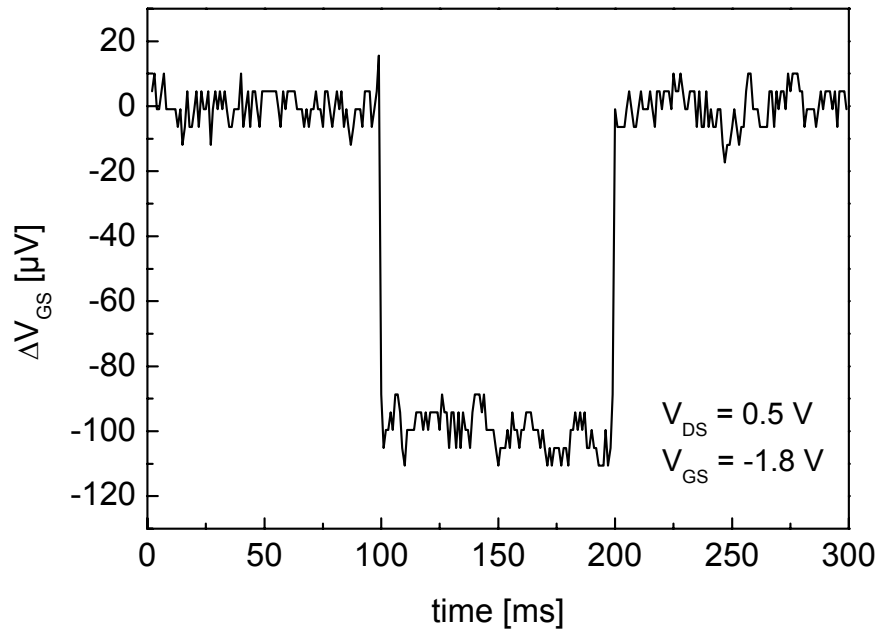
Not only  $S_{V_{GS}}$  but also the normalized spectral density of the drain-source current noise  $S_{I_{DS}}/I_{DS}^2$  exhibits a strong dependence on  $V_{GS}$ . Figure 4.8 shows the relative spectral density  $S_{I_{DS}}/I_{DS}^2$  obtained between 1 Hz and 1 kHz, multiplied by the frequency  $f^\gamma$ . A strong increase for bias voltages  $< -1.2$  V is observed. A similar trend for the  $V_{GS}$  dependence was reported by Garrido et al. [Garrido, 2000a] for AlGaIn/GaN HEMTs with Pt-gates and Ti/Al ohmic contacts. The authors distinguish between the noise sources in two different  $V_{GS}$  regimes: for negative  $V_{GS}$  close to zero, the device noise is dominated by the ohmic contacts. Even for contacts with low resistivity compared to the channel resistance, the noise contribution from the contacts cannot be neglected. Non-homogeneous contacts with pitted morphology as observed for GaN, can lead to current constrictions enhancing the contact noise [Garrido, 2000a]. The authors further reported that improvement of the contact technology reduced the noise power density by one order of magnitude.

For more negative  $V_{GS}$ , the contribution of the channel dominates, and fluctuations in the carrier mobility are proposed as a possible mechanism. As limiting process for the electron mobility at



**Figure 4.8:** Dependence of the normalized spectral density of the drain-source current noise  $S_{I_{DS}}/I_{DS}^2$ , multiplied by the frequency  $f^\gamma$ , on the gate-source voltage  $V_{GS}$ .

low temperatures ( $< 50$  K), scattering at charged dislocations was identified for these samples, dominating over other low-temperature scattering mechanisms like alloy or interface scattering [Garrido, 2000b]. A theoretical study by Jena et al. confirms dislocation scattering as the mobility-limiting mechanism for AlGaN/GaN structures with high dislocation densities of the order of  $10^9 - 10^{10} \text{ cm}^{-2}$  [Jena, 2000]. Even at room temperature, where scattering at optical phonons is the predominant process, a significant contribution of the scattering at charged dislocations was reported [Garrido, 2000b]. Very effective screening of the dislocations by the 2DEG could explain the suppression of  $1/f$  noise in AlGaN/GaN HEMT devices compared to GaN layers [Py & Buehlmann, 1996], and the increase in relative noise power density with reduced electron density in the channel [Levinshtein, 1998], [Garrido, 1998]. However, transport measurements by Link et al. could not confirm scattering at charged dislocations as the limiting scattering mechanism at low temperatures. Depending on the carrier density in the 2DEG, either scattering at remote ionized impurities ( $n_{2DEG} < 7.5 \cdot 10^{12} \text{ cm}^{-2}$ ), or alloy scattering was identified as the most important factor ( $n_{2DEG} > 7.5 \cdot 10^{12} \text{ cm}^{-2}$ ) [Link, 2004]. For room temperature, no significant contribution of low-temperature scattering mechanisms was reported, and the mobility is only determined by optical phonon scattering. No influence of the carrier concentration on the 2DEG mobility was observed at room temperature [Link, 2004]. Thus, a mobility limiting contribution of dislocation scattering in AlGaN/GaN 2DEGs at room temperature, and the consequential contribution to the low-frequency noise, is strongly dependent on the dislocation density.



**Figure 4.9.:** Transient response of an AlGaIn/GaN SGFET to a 100  $\mu\text{V}$  pulse applied for 100 ms via the electrolyte gate. Deionized water was used as an electrolyte solution.

A different explanation for the increasing noise densities with lower  $V_{GS}$  was given by Rummyantsev et al., relating the device noise to the leakage current over the gate [Rummyantsev, 2000b]. However, it was found that the contribution of the leakage current to the transistor noise is only significant for transistors with a small Hooge parameter ( $\alpha \approx 10^{-5} - 10^{-4}$ ). For devices exhibiting relatively high Hooge parameters  $\alpha \approx 10^{-3}$ , even a high gate leakage current in the order of  $10^{-3} - 10^{-2}$  compared to the channel current does not significantly influence the device output noise [Rummyantsev, 2000b]. As a Hooge parameter of  $\alpha = 5 \times 10^{-3}$  was determined for the device corresponding to data presented in Figure 4.8, a considerable noise contribution from the gate leakage current can be excluded.

A contribution of noise sources located at the surface of the ungated region between the source and drain contact can also be excluded, as a decrease of  $S_{I_{DS}}/I_{DS}$  would be expected with decreasing  $I_{DS}$  [Rummyantsev, 2001].

From the  $1/f$  noise figure of the device, a peak-to-peak noise amplitude of around 100  $\mu\text{V}$  can be estimated for the equivalent gate input noise at the operation point ( $V_{DS} = 0.5 \text{ V}$ ,  $V_{GS} = -1.8 \text{ V}$ ), which is of the same order of magnitude as reported for comparable silicon-based devices usually employed for the recording of cell action potentials [Offenhusser, 1997], [Vassanelli & Fromherz, 1999], [Ingebrandt, 2003].

The signal-to-noise ratio of various devices processed from different heterostructures and in separate runs was analyzed by recording the source-drain current change upon application of a test pulse to the electrolytic gate for a time interval of 100 ms. From the source-drain current

variation, the change in equivalent gate-source voltage was calculated. Strong variations in the signal-to-noise ratio were obtained for the different characterized transistors. For the best devices a 100  $\mu\text{V}$  pulse was clearly resolved on the background noise with a signal-to-noise ratio of 5 : 1, as demonstrated in Figure 4.9. Hence, the tested devices exhibited a strong variation in the low frequency noise, probably caused by the non-optimized ohmic contacts.

For the reduction of the device noise in silicon based transistors, complex device concepts like floating-gate devices [Cohen, 2004], [Meyburg, 2006] and buried-channel FETs were applied [Völker & Fromherz, 2005]. The most effective noise reduction was achieved by the buried channel concept as recently reported by Völker et al. [Völker & Fromherz, 2005]. The low peak-to-peak equivalent gate voltage noise of around 25  $\mu\text{V}$  of these optimized devices was sufficient for recording of signals from individual mammalian nerve cells.

In conclusion, the noise properties of the presented AlGaN/GaN SGFETs allow the recording of electrophysiological cell signals with an accuracy at least comparable to standard silicon devices. However, strong variations in the low frequency noise have been obtained, which is assumed to be caused by the non-optimized ohmic contacts. The best tested devices exhibited a noise level of 25  $\mu\text{V}$  peak-to-peak, comparable to buried-channel silicon SGFETs suitable for the recording of mammalian neuron activity.



## 5. Physical Chemistry of the GaN /Electrolyte Interface

In biochemical sensors based on III-nitride transducer devices, the chemical and electrochemical properties of the nitride surface and its interface to the electrolyte are of major importance. The nitride surface either serves as an interfacing layer between the inorganic transducer and the organic sensor functionalization, or as the sensitive element of the sensor. The III-nitride transducers fabricated and characterized in this work all exhibited a GaN surface, which was modified by thermal oxidation or chemical surface treatment in piranha etch for some applications.

In this chapter, the physical chemistry of the GaN surface and the GaN/electrolyte interface is discussed. In the first part (5.1) a general outline of the semiconductor/electrolyte junction is given, discussing the charge and potential distribution, the charge transfer over the interface and the electrochemical reactions occurring at a GaN surface in contact with electrolytic solutions. Further, the physics of a semiconductor/electrolyte junction under illumination is addressed. The second part (5.2) is devoted to the analysis of the chemical composition of native and thermally oxidized GaN surfaces by XPS. Section 5.3 describes the electrochemical and photo-electrochemical analysis of the GaN/electrolyte interface. Extracted material properties like the flatband voltage and the energetic position of the band edges with respect to the hydrogen redox level are presented. In the concluding part (5.4), the sensitivity of the GaN surfaces towards various ions in solution is discussed.

### 5.1. The Semiconductor /Electrolyte Interface

Semiconductor/electrolyte interfaces are investigated for fundamental as well as for practical reasons. Semiconductor electrodes play a major role in fundamental studies of charge transfer processes between solid-state electrodes and redox ions in electrolytes, or the contribution of electrons of the solid to catalytic reactions occurring at the surface. As a main advantage in contrast to metal electrodes, the surface density of electrons or holes available for charge transfer can be carefully controlled by the applied potential or by illumination. Furthermore, charge transfer can only occur at discrete energy levels via the conduction or valence band or via surface states, as the redox levels in solution are usually pinned with respect to the semiconductor valence and conduction band levels at the surface. On the other hand, semiconductor/electrolyte junctions are important for many practical applications as for example solar energy conversion, electrochemical semiconductor device processing (e.g. anodic oxidation or etching), and biochemical semiconductor sensor technology.

The pioneering work in electrochemistry and photoelectrochemistry of semiconductors was performed by Brattain and Garrett at Bell Labs in 1954. They investigated how chemical reactions occurring at a germanium electrode immersed into electrolytic solutions were influenced by the semiconducting properties of the germanium and by illumination [Brattain & Garrett, 1954]. In the following years, other semiconductors such as ZnO, CdS, GaP, or TiO<sub>2</sub> were studied [Dewald, 1960], [Morrison, 1969],[Williams & Bube, 1960], [Memming & Schwandt, 1968], [Boddy, 1968] and first models for the charge distribution at semiconductor/electrolyte junctions and the kinetics of the electron transfer between electrolyte and semiconductor were established [Gerischer, 1960], [Gerischer, 1961], [Boddy, 1965]. Beginning from the early 70s, there was an increasing interest in semiconductor/electrolyte junctions for solar energy conversion, after Fujishima and Honda had pointed out the possibility of the photoelectrolysis of water at semiconductor electrodes using sunlight [Fujishima & Honda, 1972]. They discussed a photoelectrochemical cell where the irradiation of an n-type TiO<sub>2</sub> semiconductor electrode leads to the decomposition of water accompanied by oxygen evolution at the TiO<sub>2</sub> electrode and hydrogen evolution at the platinum counter electrode. Alternatively to the conversion of optical energy into chemical energy in photoelectrolysis or photocatalysis, optical energy can be converted into electrical energy in so-called liquid junction solar cells or electrochemical photovoltaic cells. In these regenerative cells the electrolyte remains effectively unchanged. They are mostly based on n-type II/VI or III/V semiconductors with matched redox couples as for example n-InP/V<sup>2+</sup>,V<sup>3+</sup>, n-CdSe/S<sub>2</sub><sup>2-</sup>,S<sub>n</sub><sup>2-</sup> or n-WSe/I<sup>-</sup>,I<sub>3</sub><sup>-</sup> [Ennaoui, 1993]. For the n-CdSe/ [Fe(CN)<sub>6</sub>]<sup>3-</sup>,[Fe(CN)<sub>6</sub>]<sup>4-</sup>, conversion coefficients of 16.4% have been reported [Licht & Peramunage, 1990]. In dye-sensitized electrochemical photovoltaic cells, also known as Grätzel cells, the light is not absorbed by the semiconductor but a layer of photosensitive dye molecules adsorbed on its surface. The excited dyes then inject electrons into the semiconductor conduction band. Thereafter, the oxidized dye molecules are reduced by a matched redox species in the solution which is regenerated at the counter electrode. Conversion coefficients of 8% have been reported by Grätzel and co-workers for their original design, utilizing a porous TiO<sub>2</sub> film as the semiconductor electrode and I<sup>-</sup>/I<sub>3</sub><sup>-</sup> as a redox couple [O'Regan & Grätzel, 1991].

In the following sections, basic principles for the semiconductor/liquid interface regarding electronic energy levels, charge and potential distribution, electron transfer kinetics, as well as the influence of electronic surface states are discussed.

### 5.1.1. Electronic Energy Levels in Semiconductors

A detailed description of the electronic energy levels in semiconductors is given by the band theory of solids, as for example in [Yu & Cardona, 1996]. In the following, some basic concepts and relations are presented. The main characteristic of a semiconductor is the energy separation of the conduction and valence band by a forbidden bandgap  $E_G$ . The valence and conduction band states correspond to the empty and filled electronic energy levels at  $T = 0$  K, respectively. The Fermi Level,  $E_F$ , which represents the electrochemical potential of electrons in solids is

located in the bandgap,  $E_G$ , leading to a relatively low density of free carriers. For energies close to the band edge, the density of electronic states  $N(E)$  in the conduction and valence band increases with the square root of the energy difference to the band edge,

$$N_C(E) \propto (E - E_C)^{\frac{1}{2}} \quad (5.1)$$

and

$$N_V(E) \propto (E_V - E)^{\frac{1}{2}} \quad (5.2)$$

with  $E_C$  and  $E_V$  denoting the energies of the conduction band minima and the valence band maxima, respectively [Sze, 1981].

Under equilibrium conditions, the electron density  $n$  and hole density  $p$  in a non-degenerate semiconductor can be described by

$$n = N_C \cdot \exp\left(-\frac{E_C - E_F}{kT}\right) \quad (5.3)$$

and

$$p = N_V \cdot \exp\left(-\frac{E_F - E_V}{kT}\right) \quad (5.4)$$

where  $N_C$  and  $N_V$  represent the effective densities of states in the conduction and valence band, respectively. They are given by

$$N_C = 2 \left(\frac{2\pi m_e kT}{h^2}\right)^{3/2} M_c \quad (5.5)$$

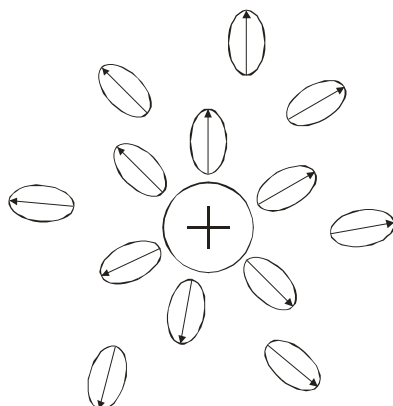
and

$$N_V = 2 \left(\frac{2\pi m_h kT}{h^2}\right)^{3/2}, \quad (5.6)$$

with the number of equivalent minima in the conduction band,  $M_c$ , and the density-of state effective mass of electrons  $m_e$  and holes  $m_h$ . From a combination of Eqs. (5.3) and (5.4), the intrinsic carrier density can be obtained:

$$np = n_i^2 = N_C N_V \cdot \exp\left(-\frac{E_G}{kT}\right) \quad (5.7)$$

For intrinsic semiconductors, the Fermi level  $E_F$  is located close to the middle of the bandgap. Doping of a semiconductor with donor or acceptor impurities leads to the formation of impurity levels with energies in the semiconductor bandgap. An n-type semiconductor is doped with donor atoms that exhibit energy levels close to the conduction band. In that case, the Fermi level  $E_F$  lies also close to the conduction band edge. On the other hand, p-type conductivity is obtained when acceptor atoms with corresponding energy levels close to the valence band are introduced. In this case, the Fermi level  $E_F$  is close to the valence band edge [Sze, 1981].



**Figure 5.1.:** Solvated cation surrounded by the inner sphere dipoles of the solvent and the outer sphere dipoles.

### 5.1.2 Electronic Energy Levels in Liquids

Ions in solution are surrounded by a solvation shell of polar solvent molecules and other ions or molecules of the solution. The strong interaction between the ion and the nearest solvent dipoles leads to the formation of an inner sphere complex which can be considered almost as a compound. The outer sphere consists of loosely bound solvent molecules and counter ions (Figure 5.1). The structure of the solvation shell depends strongly on the charge of the ion and, therefore, differs between the reduced and oxidized ionic state. Electron transfer to or from the ion leads to a rearrangement of the solvent molecules around the ion and a change in the related electronic energy levels [Gerischer, 1960], [Morrison, 1977], [Memming, 2001]. Solvated ions that can be oxidized and reduced by pure electron transfer are referred to as redox couples. To describe the electronic energy levels related to an ionic redox couple in solution first the electrochemical potential of electrons in the redox system has to be defined.

### The Electrochemical Potential of Redox Couples in Solution

The chemical potential of an ion  $i$  in solution is

$$\mu_i = \mu_i^0 + RT \ln a_i = \mu_i^0 + RT \ln \gamma_i c_i \quad (5.8)$$

with the standard chemical potential,  $\mu_i^0$ , the ion activity,  $a_i$ , the activity coefficient,  $\gamma_i$ , and the concentration of the ion,  $c_i$ . The expression can be simplified to

$$\mu_i = \mu_i^0 + RT \ln c_i \quad (5.9)$$

for diluted solutions where ion-ion interactions can be neglected ( $\gamma = 1$ ). The electrochemical potential of a species  $i$  with charge  $Z_i$  is

$$\tilde{\mu}_i = \mu_i + Z_i F \phi \quad (5.10)$$

where  $F$  is the Faraday constant and  $\phi$  the electrical potential at the position of the species. At equilibrium, the electrochemical potential of a species,  $\tilde{\mu}_i$ , is constant over all contacting phases

$$\tilde{\mu}_i = \text{const.} \quad (5.11)$$

Gradients in  $\tilde{\mu}_i$  lead to a net flux of the species.

For chemical reactions, the gradient in free energy between the product and educt side determines the reaction rate. At equilibrium, the reaction rate must be equal in both directions and the electrochemical potentials of the educts and products are related by

$$\sum_i v_i \tilde{\mu}_i = 0 = \Delta G_{\text{equil}} \quad (5.12)$$

with the stoichiometric coefficients  $v_i$  taken negative for the educts and positive for the products.

Applying Eq. (5.12) to the redox reaction



for the exchange of an electron between the redox couple Red/Ox and an inert metal electrode results in

$$\tilde{\mu}_{e,\text{redox}} = \tilde{\mu}_{\text{red}} - \tilde{\mu}_{\text{ox}} \quad (5.14)$$

for the electrochemical potential  $\tilde{\mu}_{e,\text{redox}}$  of the electrons, and application of Eqs. (5.9) and (5.10) yields

$$\tilde{\mu}_{e,\text{redox}} = \mu_{\text{redox}}^0 + kT \ln \left( \frac{c_{\text{ox}}}{c_{\text{red}}} \right) \quad (5.15)$$

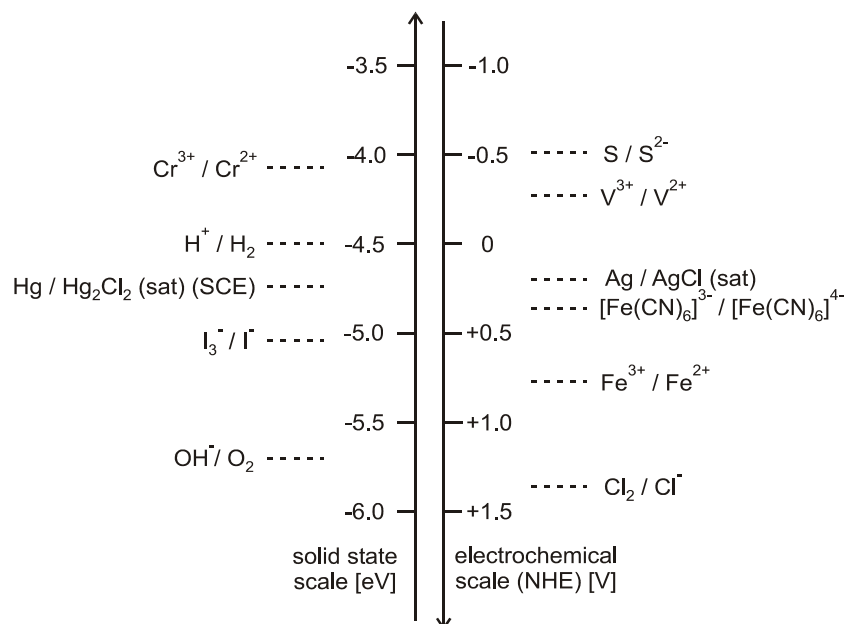
with the concentrations,  $c_{\text{ox}}$  and  $c_{\text{red}}$ , for the oxidized and reduced species of the redox system, respectively.

The electrochemical potential of the redox system is equivalent to the electron Fermi level in solution.

$$E_{F,\text{redox}} = \tilde{\mu}_{e,\text{redox}} \quad (5.16)$$

Fermi energies are generally given on an absolute scale versus the vacuum level. In contrast, the redox potential  $\phi_{\text{redox}}$  corresponding to a redox system is measured and tabulated versus a standard reference electrode, for instance the **Standard Hydrogen Electrode (SHE)** or the **Standard Calomel Electrode (SCE)**. The standard redox potential  $\phi_{\text{redox}}^0$  of a redox couple<sup>1</sup> is negative if it tends to give up electrons more easily to an inert platinum electrode than the hydrogen redox couple  $\text{H}^+/\text{H}_2$  at standard ambient conditions ( $T = 298 \text{ K}$ , solutes at a concentration of  $1 \text{ M}$ , and gases at  $1 \text{ bar}$ ). The standard redox potential of the  $\text{H}^+/\text{H}_2$  redox system at standard

<sup>1</sup> In most electrochemical textbooks the standard redox potential of a redox couple or electrode is denoted by  $E^0$ . Throughout this work  $\phi_{\text{redox}}^0$  is used to avoid confusion with electronic energy levels.



**Figure 5.2:** Electrochemical potential of different redox systems given on an absolute scale versus the vacuum level and on the electrochemical scale with respect to the NHE.

conditions,  $\phi_{\text{H}^+/\text{H}_2}^0$ , was chosen as an arbitrary zero for redox potentials in electrochemistry (SHE). The energy of the  $\text{H}^+/\text{H}_2$  redox system versus the vacuum level was determined by various authors to values between 4.3 eV [Trasatti, 1977] and 4.7 eV [Gomer & Tryson, 1977]. Here, an average value of 4.5 eV [Lohmann, 1967] is used.

On an absolute scale the Fermi level of the redox system is then given by

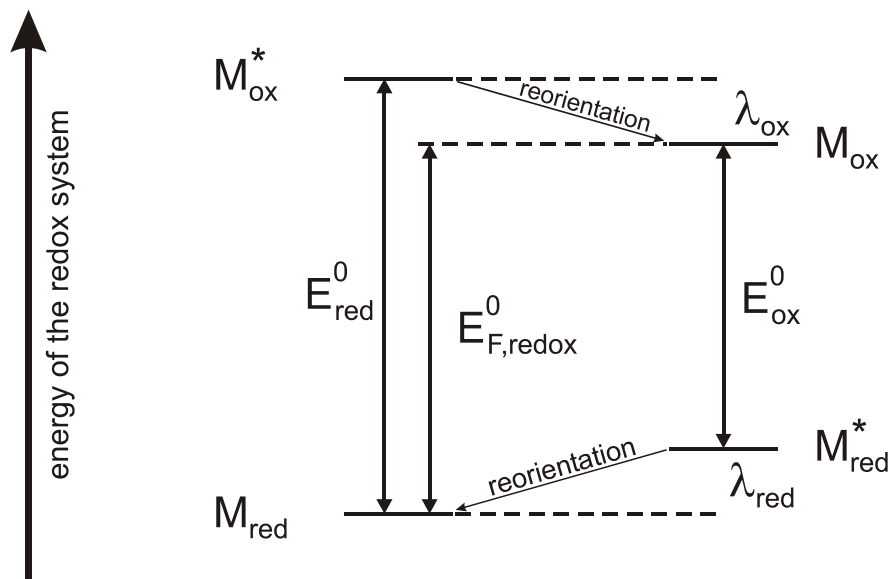
$$E_{F,\text{redox}} = -4.5 \text{ eV} - e\phi_{\text{redox}}, \quad (5.17)$$

using the SHE as a reference.

Energy levels of important redox systems are shown in Figure 5.2 on an absolute scale versus the vacuum level and on the conventional electrochemistry scale versus the SHE.

The energy level,  $E_{F,\text{redox}}$ , of a redox system is not an electronic but a thermodynamic energy level and used to describe equilibrium conditions. It reflects differences in not only the electronic energy but in the total energy involved in an electron transfer reaction, including for instance the reorganization energy of the hydration shell after an electron transfer.

The electronic energy states in solution are described in the following section in terms of the Gerischer model [Gerischer, 1960], [Gerischer, 1961], [Memming, 2001].

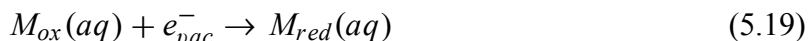


**Figure 5.3:** Total energy of a redox system in its reduced or oxidized state. The fast occurring electron transfer processes lead to excited redox states ( $M_{ox}^*$  and  $M_{red}^*$ ), still surrounded by the solvation shell of the initial form. The energy differences are electronic energies.

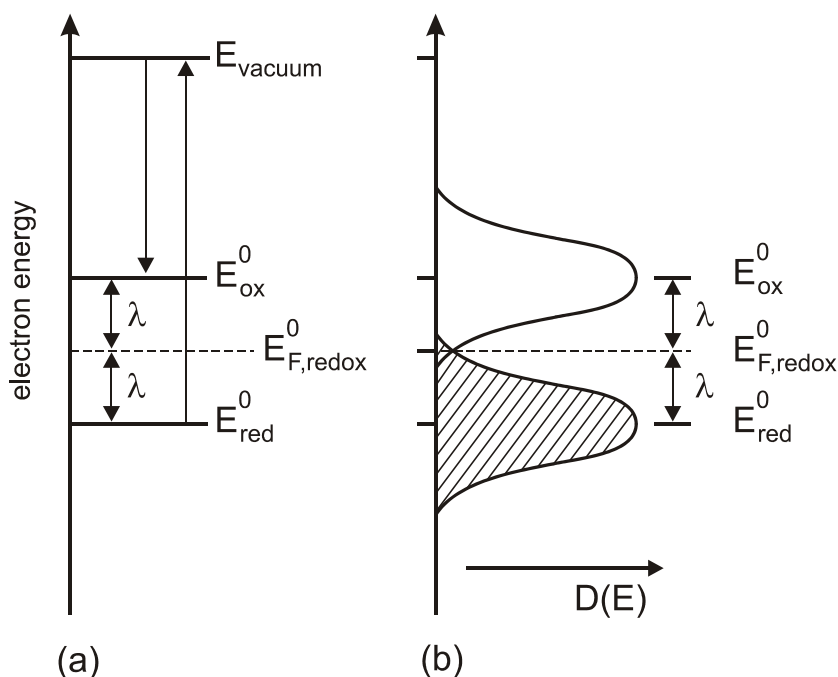
### The Gerischer Model of Electronic States in Solution

In an electrolyte containing the univalent redox system  $M_{ox}(aq)/M_{red}(aq)$ ,  $M_{red}(aq)$  represents the occupied and  $M_{ox}(aq)$  the unoccupied electronic state. The interaction of the ions with the surrounding solvation shell differs for the reduced and oxidized ionic species and, therefore, the energy levels involved in electron transfer are different from the thermodynamic level  $E_{F,redox}$ . The energy level of the occupied electronic state is the required work  $E_{red}^0$  to transfer an electron from the  $M_{red}(aq)$  ion to the vacuum level. The energy level of an unoccupied electronic state is the work  $E_{ox}^0$  gained if an electron from the vacuum is captured by the  $M_{ox}(aq)$  ion.

A quantitative estimation of the difference between the electronic energy levels involved in electron transfer and the thermodynamic level  $E_{F,redox}$  can be made by considering the following reaction cycle, starting from the  $M_{red}(aq)$  redox ion in its reduced form:



The schematic diagram of the energetic states involved in the reaction cycle is given in Figure 5.3. Initially, the redox system is in its reduced form, and surrounded by the solvation shell of its reduced form, specified as  $M_{red}$ . During an electron transfer, this solvation shell is regarded as unchanged, as the transfer of electrons is fast compared to the thermal movement



**Figure 5.4:** Electron energies (a) and energy distributions (b) of a redox system in the occupied and unoccupied state. The electronic energy levels are the differences of the total energies (see Figure 5.3).

and reorganization of the molecules in the solvation shell (Franck-Condon principle). Reorganization of the solvation shell occurs when the electron transfer is completed.

Transferring an electron from the  $M_{red}$  state into the vacuum requires the energy  $E_{red}^0$  and leads to the oxidized excited form  $M_{ox}^*$  of the ion, still surrounded by the typical solvation shell of the reduced form. After the electron transfer, the solvent shell reorganizes until the equilibrium conditions for the shell of the oxidized species  $M_{ox}$  are reached. The free energy change during this relaxation process is the reorganization energy  $\lambda_{ox}$ . In the reverse process, an electron is captured by the oxidized species  $M_{ox}$ , resulting in the reduced excited form  $M_{red}^*$ , still surrounded by the solvation shell of the oxidized form. Thereby, the energy  $E_{ox}^0$  is gained. The free energy change during the relaxation to the initial state  $M_{red}$  is  $\lambda_{red}$ . Summation of the energies around the redox-cycle yields

$$E_{red}^0 - \lambda_{ox} = E_{ox}^0 + \lambda_{red} = E_{F,redox}^0 \quad (5.20)$$

which can also be deduced from Figure 5.4, in which the electronic energies of the cycle are plotted versus the vacuum level. Within the experimental accuracy, the reorganization energies for reduced and oxidized species  $\lambda_{red}$  and  $\lambda_{ox}$  can be regarded as equal ( $\lambda = \lambda_{red} = \lambda_{ox}$ ), simplifying Eq. (5.20) to

$$E_{red}^0 - E_{ox}^0 = 2\lambda \quad (5.21)$$



and yielding

$$E_{F,redox}^0 = \frac{1}{2}(E_{red}^0 + E_{ox}^0). \quad (5.22)$$

However, the derived values  $E_{red}^0$  and  $E_{ox}^0$  are only the mean values for the electronic energy states in solvents. Thermal fluctuations of the solvation shell lead to a broadening of the electronic energy levels and result in a Gaussian distribution of the solvation states [Gerischer, 1960]. Considering that the density of electronic states is proportional to the concentration  $c_{red}$  and  $c_{ox}$  of the reduced or oxidized species of the redox system, the total density of states is given by

$$D_{red}(E) = \frac{c_{red}}{\sqrt{4\pi\lambda kT}} \cdot \exp\left(-\frac{(E - E_{red}^0)^2}{4kT\lambda}\right) \quad (5.23)$$

and

$$D_{ox}(E) = \frac{c_{ox}}{\sqrt{4\pi\lambda kT}} \cdot \exp\left(-\frac{(E - E_{ox}^0)^2}{4kT\lambda}\right) \quad (5.24)$$

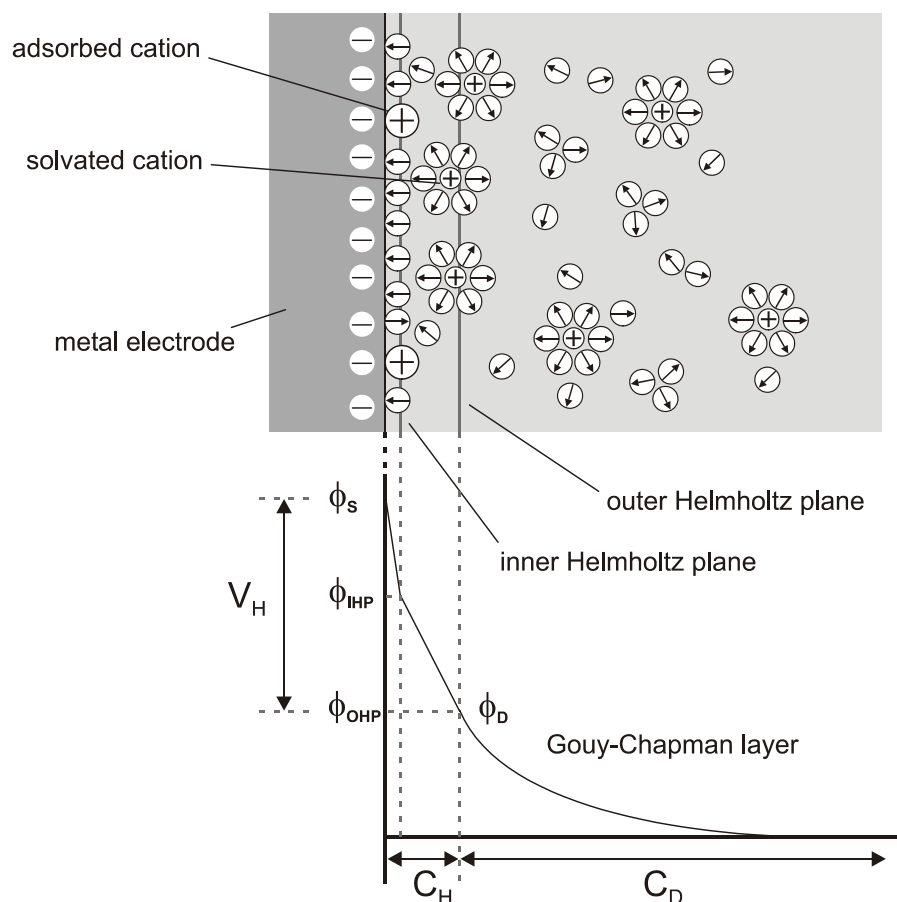
for the occupied and unoccupied energy levels in solution, respectively. The density distributions of the solvation states are illustrated in Figure 5.4 for equal concentrations. For typical reorganization energies  $\lambda$  of about 1 eV, the half-width of the density distributions is of the order of 0.5 eV [Morrison, 1977].

### 5.1.3. Potential and Charge Distribution at the Semiconductor /Electrolyte Interface

After immersion of a solid into an aqueous solution, charge is exchanged between the solid surface and the electrolyte and charged layers are built up in both, the solid and the adjacent liquid. The resulting space charge region in the solid is discussed in detail for the case of semiconductors in Appendix A.3.

In the Gouy-Chapman-Stern model [Stern, 1924], [Bard & Faulkner, 2001], the solution side of the solid/liquid interface is divided into two regions. First, the Helmholtz layer is formed by ions which are adsorbed electrostatically or chemically to the solid surface. Next to the Helmholtz layer, solvated ions form a diffuse space charge region in which an excess of positive or negative ions exists. This region is called the Gouy-Chapman layer.

In the following sections, the electrical properties of the Helmholtz layer, the Gouy-Chapman layer, the semiconductor space charge layer, as well as the potential distribution at the semiconductor/electrolyte interface will be discussed.



**Figure 5.5:** Charge distribution and potential decay at a metal electrode surface, described in the extended Stern model.

### The Helmholtz Double Layer

The Helmholtz double layer plays a major role in most electrochemical processes at solid state electrodes. Most models for the Helmholtz layer at all kinds of solid surfaces are modifications or extensions of the basic model which Stern proposed in 1924 for the description of mercury/electrolyte interfaces [Stern, 1924]. In Figure 5.5, a schematic picture of the extended Stern model is presented. The surface has a charge of  $\sigma_0$  and an electrical potential of  $\phi_s$ . At the **inner Helmholtz plane** (IHP), only unsolvated ions are specifically bound to the surface. Due to their solvation shell, solvated ions cannot approach the surface closer than a certain distance  $d$ . The plane of closest approach for solvated ions is called the **outer Helmholtz plane** (OHP). Electrically, the regions between the surface and the inner Helmholtz plane and the region between the inner and the outer Helmholtz plane can be approximated as capacitors, with the capacitances  $C_1$  and  $C_2$ , respectively. In most electrical experiments it is impossible to separate the contributions of the capacitances  $C_1$  and  $C_2$ , thus they are mostly described as a single Helmholtz capacitance,  $C_H$ .

The potential difference between the potential,  $\phi_S$ , at the solid surface and the potential,  $\phi_{OHP}$ , at the OHP defines the Helmholtz double layer voltage  $V_H$ ,

$$V_H = \phi_S - \phi_{OHP}. \quad (5.25)$$

The mercury and silver iodide surfaces, for which the Helmholtz double layers have been extensively studied in experiment and theory, are examples for the two classes of surface/electrolyte interfaces: polarizable interfaces and reversible interfaces [Stumm, 1970]. For **polarizable interfaces**, the potential drop  $V_H$  across the double layer is determined by an externally applied voltage or the redox level in the electrolyte. At a **reversible interface**, adsorption and desorption of the potential determining ionic species from the solution at the surface determine the double layer potential  $V_H$ . The double layer characteristics for the two classes of interfaces are very similar, differing mainly in the reason for the potential difference over the double layer. In some text books and throughout this work, the expression "polarizable interface" is used to describe interfaces where the application of an external potential does not lead to an electron transfer over the interface. Conversely, at ideal nonpolarizable interfaces electron transfer is easily possible (see e.g. [Bockris & Reddy, 1970]).

Graham has given a detailed review on the mercury/solution interface and the dependence of the double layer capacitance on the applied potential and the chemical composition of the electrolyte [Grahame, 1947]. For **mercury/solution** interfaces, the surface charge is given by the electronic charge on the mercury. For negatively polarized electrodes, cations are predominant at the IHP and  $C_H$  is of the order of  $20 \mu\text{F cm}^{-2}$ . For positive polarizations, the IHP is populated mainly by anions and  $C_H$  is of the order of  $40 \mu\text{F cm}^{-2}$  [Stumm, 1970]. At the reversible **silver iodide/solution** interface, the surface charge  $\sigma_S$  is exclusively determined by the adsorbed potential-determining  $\text{Ag}^+$  and  $\text{I}^-$  ions [Lyklema & Overbeek, 1961]. In the case of zero surface charge and an ionic strength of 0.1 M, the double layer capacitance  $C_H$  is about  $30 \mu\text{F cm}^{-2}$  for most electrolyte compositions, sharply increasing for positive polarizations and slightly decreasing for negative polarizations. In most models, the interface between an **oxide surface** and an electrolyte is considered as a reversible interface, similar to the AgI surface [Yates, 1974], [Davis, 1978]. The surface charge is formed by the potential determining ions  $\text{H}^+$  and  $\text{OH}^-$ . Additionally, specific adsorption of electrolyte ions is considered in the formation of ion pairs or surface complexes at charged surface sites with counterions [Yates, 1974], [Davis, 1978]. A more detailed description of the specific adsorption reaction and the charge and potential distribution at oxide/electrolyte interfaces is given in Section 5.4.2, where the site-binding model of Yates et al. is described. The double layer capacitance and surface charge density of many oxide/solution interfaces is much larger than for the mercury and silver iodide surfaces described above. Typical values reported for  $C_H$  are of the order of  $40 \mu\text{F cm}^{-2}$  for  $\delta\text{-MnO}_2$ ,  $90 \mu\text{F cm}^{-2}$  for  $\gamma\text{-Al}_2\text{O}_3$ ,  $250 \mu\text{F cm}^{-2}$  for  $\beta\text{-MnO}_2$  [Stumm, 1970], and  $70 \mu\text{F cm}^{-2}$  for  $\text{TiO}_2$  [Stumm, 1970], [Westall & Hohl, 1980]. However, the differential double layer capacitances obtained from experiments depend significantly on the electrostatic model applied for the oxide/solution interface. A comparison of different models is given by Westall et al. [Westall & Hohl, 1980]. They have determined the free parameters for different models like dissociation constants, reaction constants for the formation of ion pairs,

and double layer capacitances by fitting the experimental acid-base titration data for  $\text{Al}_2\text{O}_3$  and  $\text{TiO}_2$  surfaces. They concluded that no model is preferable for the accurate physical description of the interface, as all models could represent the experimental data equally well, resulting in different values for the corresponding free parameters in the different models. However, minimum Helmholtz capacitances of  $57 \mu\text{F cm}^{-2}$  for  $\gamma\text{-Al}_2\text{O}_3$  and  $53 \mu\text{F cm}^{-2}$  for  $\text{TiO}_2$  were obtained for the different models.

The spatial extension of the Helmholtz double layer can be estimated assuming the double layer capacitance  $C_H$  to be independent of the applied potential

$$C_H = \frac{\varepsilon_H \varepsilon_0}{d}. \quad (5.26)$$

The dielectric constant  $\varepsilon_H$  of the medium, consisting of strongly polarized water molecules is not clear and assumed to have values between 5 and 20 in the literature [Morrison, 1980], [Memming, 2001]. Considering the dielectric constant  $\varepsilon_H \approx 5.9$  for fully oriented water and measured values for the Helmholtz capacitance on mercury of around  $20 \mu\text{F cm}^{-2}$ , this leads to an approximated thickness  $d$  of a few Angstroms for the Helmholtz double layer.

In the following, the origin of the Helmholtz double layer voltage  $V_H$  under open circuit conditions is discussed for different electrode materials.

**Metals** In the case of metals, the Helmholtz double layer voltage  $V_H$  is defined mainly by electron exchange between the metal and redox ions in solution. An initial difference in the Fermi levels  $E_F$  of the metal and  $E_{F,redox}$  of the electrolyte leads to electron transfer and the formation of a double layer. At equilibrium, the double layer potential is adjusted to equalize the Fermi levels  $E_F$  of the metal and  $E_{F,redox}$  of the solution. Surface adsorption of ions plays only a minor role in the built-up of the Helmholtz potential, as most of the surface charge arises in the metal.

**Insulators** For insulators, the charge on the surface results only from ions or dipoles adsorbed from the liquid, as there is no exchange of free carriers. The Helmholtz potential is, therefore, controlled by adsorption and desorption processes (reversible interface) and not by adjustment of the electrochemical potential for electrons of the two contacting phases. In most cases, a few sorts of ions dominate the surface charge, and  $V_H$  adjusts itself to equalize the adsorption and desorption rate for these so-called potential-determining ions (PDI). As a consequence, the Helmholtz potential is strongly dependent on the concentration of the potential-determining ions in the bulk solution. The Helmholtz potential of oxidic surfaces is defined mainly by adsorption and desorption of protons and hydroxide ions and depends on the pH of the solution, as described in detail by the site-binding model in Section 5.4.2.

**Semiconductors** The Helmholtz double layer potential at a semiconductor/liquid interface can be either determined by adsorption/desorption processes or by electron or hole transfer

reactions to appropriate redox levels in electrolyte. For non-degenerate semiconductors,  $V_H$  is found to be controlled mainly by adsorption/desorption processes, as the charge in the space charge region of the semiconductor due to electron exchange with redox ions is much smaller than the ionic charge involved in adsorption at the surface of the semiconductor [Madou & Morrison, 1989]. Furthermore, the ionic surface coverage changes only slightly with the externally applied voltage, as most of the potential drop occurs in the semiconductor space charge region, as discussed in Section 5.1.3. An intermediate case between metals and insulators exists for degenerate semiconductors, for which redox processes as well as adsorption/desorption reactions influence  $V_H$ .

For the description of the semiconductor/electrolyte junction, many authors follow the early interpretations by Gerischer [Gerischer, 1961], where equilibration of the Fermi level in the semiconductor and of an electrolyte containing a redox couple is achieved by electron exchange at the interface. Adsorption of ions still dominates the Helmholtz potential in this model, and the potential drop in the space charge region of the semiconductor is adjusted so that the total potential difference equalizes the initial difference in Fermi energies. However, as redox levels can be located in the bandgap region, the exchange current rates at semiconductor/electrolyte interfaces can be extremely low. Particularly for wide bandgap semiconductors, a thermodynamic equilibrium with respect to charge transfer can seldom be assumed [Morrison, 1977].

### The Gouy-Chapman Layer

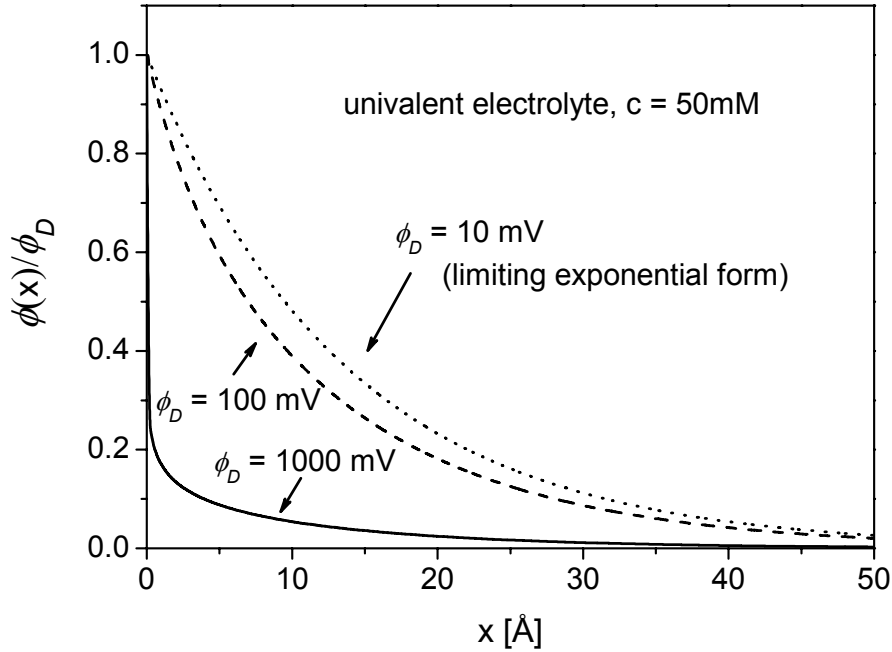
Particularly for solutions with low ionic concentrations, the charge of the solid surface is not completely counterbalanced by the ionic charge accumulated at the outer Helmholtz plane. Therefore, a diffuse layer of charge extending from the OHP into the solution is introduced in the Gouy-Chapman model, in which an excess of ions of one charge exists. The electrostatic attraction of the ions in this layer to the charged surface is counterbalanced by the random thermal motion. Thus, the local ion density at a distance  $x$  from the surface can be described by the Boltzmann equation:

$$n_i(x) = n_i^0 \cdot \exp\left(\frac{-z_i e \phi(x)}{kT}\right), \quad (5.27)$$

where  $n_i^0$  and  $n_i(x)$  are the densities of the ionic species  $i$  in the bulk solution and at a distance  $x$ , respectively,  $z_i$  is the charge of the ions  $i$ , and  $\phi(x)$  is the potential at a distance  $x$  with respect to the bulk solution potential. The potential  $\phi(x)$  is related to the charge density  $\rho(x)$  by the one-dimensional Poisson equation:

$$\rho(x) = -\epsilon\epsilon_0 \frac{d^2\phi(x)}{dx^2}. \quad (5.28)$$

Combination of Eqs. (5.27) and (5.28) yields the Poisson-Boltzmann equation, describing the potential and charge distribution in the diffuse layer. In the Gouy-Chapman layer, the dielectric constant of "free" water ( $\epsilon = 80$ ) can be assumed for the electrolyte [Bockris & Reddy, 1970].



**Figure 5.6:** Potential distribution through the diffuse layer according to the Gouy-Chapman model, calculated for a 50 mM univalent electrolyte and different values of the potential  $\phi_D$  at the OHP.

For a symmetric electrolyte (equal concentrations of cations and anions) the potential profile in the Gouy-Chapman layer is given by

$$\frac{\tanh(ze\phi/4kT)}{\tanh(ze\phi_D/4kT)} = \exp(-\kappa x) \quad (5.29)$$

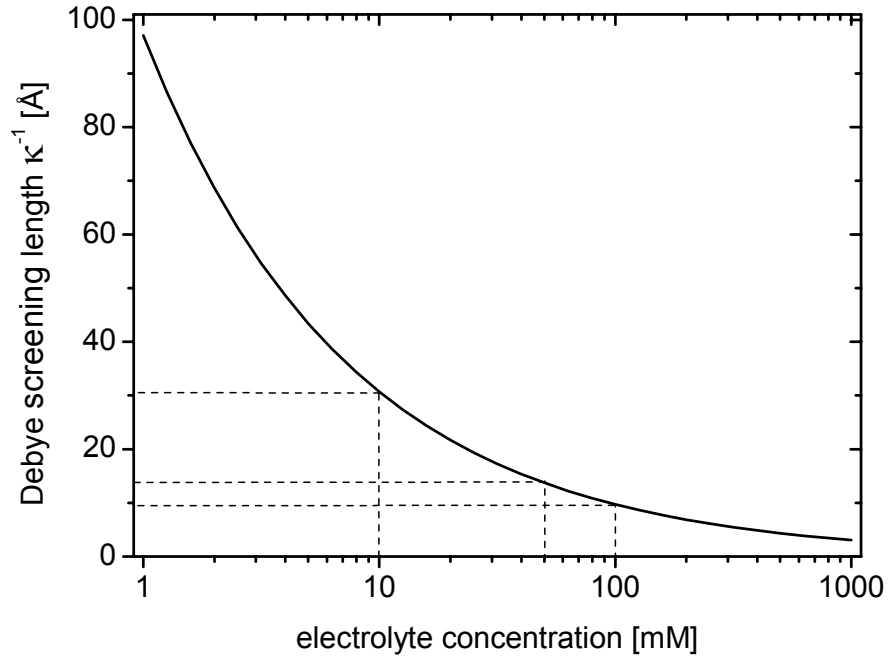
with

$$\kappa = \sqrt{\frac{2n^0 z^2 e^2}{\epsilon \epsilon_0 kT}} \quad (5.30)$$

where  $\phi_D$  is the potential at the OHP,  $n^0$  the bulk density of each ion and  $ze$  the ionic charge. In Figure 5.6, potential profiles calculated for a 50 mM univalent electrolyte ( $z = 1$ ) and different values of  $\phi_D$  are presented. For small  $\phi_D$ , an asymptotic exponential form

$$\phi = \phi_D \exp(-\kappa x) \quad (5.31)$$

for the potential decay is approached. The extension of the diffuse layer,  $\kappa^{-1}$ , is the Debye screening length in the electrolyte. In the Debye-Hückel theory, this value describes a characteristic length for the spatial decay of potentials in diluted electrolyte solutions [Bockris & Reddy, 1970]. It is an important parameter for potentiometric biochemical sensors, as it allows an estimation of the maximum distance from the transducer surface where a change



**Figure 5.7.:** Debye screening length for an univalent electrolyte with ionic concentrations ranging from 1 mM to 1 M.

in charge is still detectable and not completely screened by a surrounding ionic cloud. Figure 5.7 illustrates the decrease of the Debye screening length with increasing ionic concentration for a univalent electrolyte.

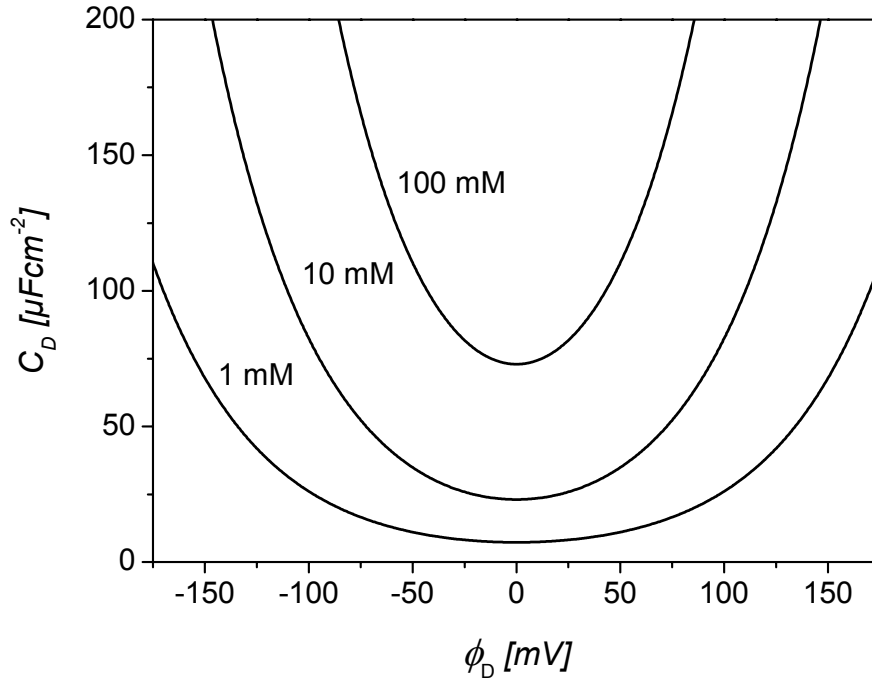
According to the Gouy-Chapman theory, the diffuse layer charge per unit area in the diffuse layer is given by the modified Graham equation:

$$\sigma_D = - \left( 8kT \varepsilon \varepsilon_0 n^0 \right)^{1/2} \sinh \left( \frac{ze\phi_D}{2kT} \right). \quad (5.32)$$

By taking the derivative of Eq. (5.32) with respect to  $\phi_D$ , the differential capacitance of the Gouy-Chapman layer can be obtained:

$$C_D = \left( \frac{2z^2 e^2 \varepsilon \varepsilon_0 n^0}{kT} \right)^{1/2} \cosh \left( \frac{ze\phi_D}{2kT} \right). \quad (5.33)$$

In Figure 5.8, the capacitance of the diffuse layer is illustrated for different ion concentrations versus the potential  $\phi_D$  at the OHP. High potentials  $\phi_D$  or high ion concentrations  $n^0$  lead to a strong accumulation of ions in the diffuse layer and cause an increase in the capacitance  $C_D$ .



**Figure 5.8:** Differential capacitance of the diffuse layer calculated according to the Gouy-Chapman model for different ionic concentrations of a monovalent electrolyte.

### The Gouy-Chapman-Stern Model of the Solid /Electrolyte Interface

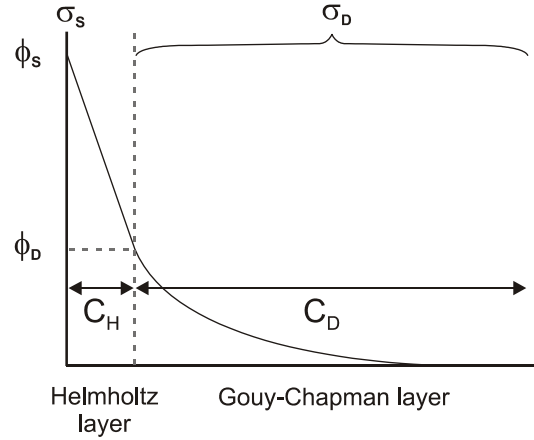
In the previous sections, a physical description of the Helmholtz and the Gouy-Chapman layer was given. According to the Gouy-Chapman-Stern model, they form the electrical double layer at the solid/solution interface, the so-called Gouy-Chapman-Stern (GCS) layer. In Figure 5.9, an illustration of the Gouy-Chapman-Stern model is presented. The charge of the surface  $\sigma_S$  is formed by the potential determining ions, which are  $H^+$  and  $OH^-$  for oxidic surfaces. The counter charge  $\sigma_D$  is located at the OHP and the adjacent diffuse space charge region. Regarding Eq. (5.32), the potential of the solid surface  $\phi_S$  relative to the bulk electrolyte is given by

$$\phi_S = -\frac{\sigma_D}{C_H} \mp \frac{2kT}{ze} \sinh^{-1} \left( \frac{|\sigma_D|}{(8kT\epsilon\epsilon_0 n^0)^{1/2}} \right). \quad (5.34)$$

The total capacitance  $C_{GCS}$  of the electrical double layer can be described as a serial capacitance of the Helmholtz capacitance  $C_H$  and the capacitance of the diffuse layer  $C_D$ :

$$\frac{1}{C_{GCS}} = \frac{1}{C_H} + \frac{1}{C_D}. \quad (5.35)$$





**Figure 5.9.:** Illustration of the electrical double layer at the solid/electrolyte interface as described by the Gouy-Chapman-Stern model.

For small values of  $\sigma_D$  or high ionic concentrations of the electrolyte, the capacitance  $C_D$  (Eq. 5.33) can be linearized and the total double layer capacitance  $C_{GCS}$  is given by

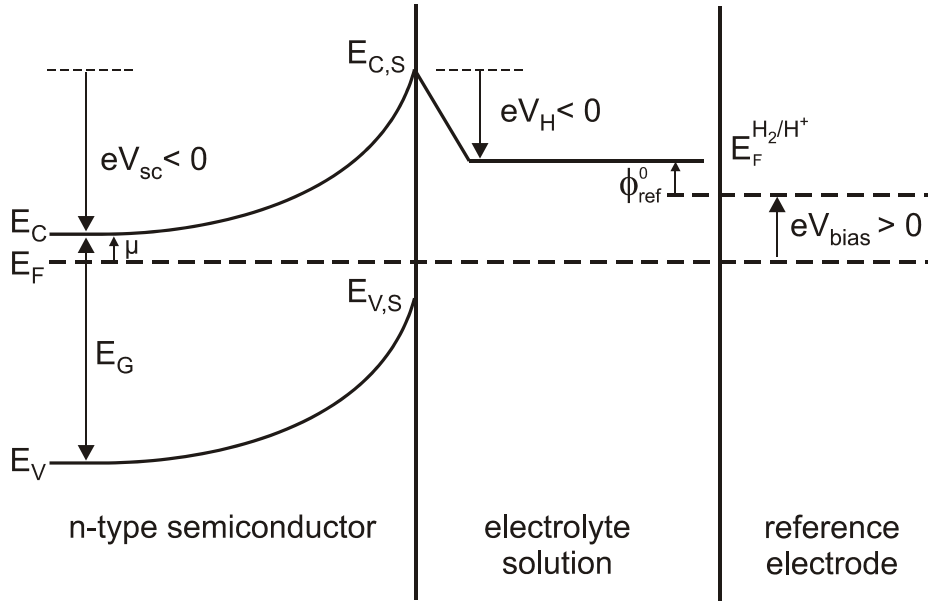
$$\frac{1}{C_{GCS}} = \frac{1}{C_H} + \left( \frac{kT}{2z^2 e^2 \epsilon \epsilon_0 n^0} \right)^{1/2}. \quad (5.36)$$

In case of concentrated solutions, the thickness of the Gouy-Chapman layer becomes negligibly small and almost all charge of the diffuse layer is located at the OHP. Under such conditions, the Gouy-Chapman layer is indistinguishable from the Helmholtz double layer and the total capacitance,  $C_{GCS}$ , is given by the Helmholtz capacitance,  $C_H$ . For the experiments described in this work, electrolytes with high ionic concentrations  $\geq 50$  mM have been used. Even for zero potential ( $\phi_D = 0$ ), the diffuse capacitance  $C_D$  is of the order of  $50 \mu\text{F cm}^{-2}$  for these concentrations, and increases strongly for small positive or negative potentials. Hence, a contribution of the Gouy-Chapman layer can be neglected, and the whole potential drop and capacitance of the solution side are attributed to the potential  $V_H$  and capacitance  $C_H$  of the dominating Helmholtz layer, respectively. For low ionic concentrations, the diffuse capacitance  $C_D$  is of the order of or even smaller than the Helmholtz capacitance  $C_H$  and cannot be neglected.

### Potential Distribution at the Semiconductor /Electrolyte Interface

The electrical properties of an ideal semiconductor/electrolyte interface can be approximated as a serial connection of the semiconductor space charge capacitance,  $C_{sc}$ , on the solid side, and the capacitances of the Helmholtz layer,  $C_H$ , and the Gouy-Chapman layer,  $C_D$ , on the solution side.

$$\frac{1}{C_t} = \frac{1}{C_{sc}} + \frac{1}{C_H} + \frac{1}{C_D} \quad (5.37)$$



**Figure 5.10:** Schematic view of the potential distribution at a semiconductor/electrolyte interface for the approximation of high ion concentrations and with an external bias voltage  $V_{bias}$  applied between the semiconductor electrode and a reference electrode in the solution.

Here, the electrical contribution of semiconductor surface states and Faradaic processes at the semiconductor surface, which are accompanied by charge transfer over the interface, are neglected. The total capacitive contributions of the electrical double layer at the solution side have already been discussed in Section 5.1.3 and can be summarized in  $C_{GCS}$ . A detailed discussion of the semiconductor space charge layer and its capacitance  $C_{sc}$  can be found in Appendix A.3.

Figure 5.10 gives a schematic view of the potential distribution at the n-type semiconductor/electrolyte interface for the approximation of high ion concentrations and with an external bias voltage  $V_{bias}$  applied between the semiconductor electrode and a reference electrode in the solution. As a reference potential, the redox level  $\phi_{H^+/H_2}^0$  of the  $H^+/H_2$  redox couple at standard conditions (SHE) is used. From the figure, a relation between the applied external voltage and the internal potentials of the junction can be derived

$$\mu - eV_{sc} + eV_H - e\phi_{ref}^0 = eV_{bias} \quad (5.38)$$

with:

$$V_{sc} = \phi_S - \phi_{bulk}^{sc}, \text{ the band bending in the semiconductor}$$

$$V_H = \phi_S - \phi_{OHP}, \text{ the potential drop over the Helmholtz layer}$$

$$\phi_{ref}^0 \text{ electrochemical potential of the reference electrode}$$

$V_{bias} = \phi_{bulk}^{sc} - \phi_{ref} = -(E_F - E_{F,ref})/e$ , the external bias potential applied to the semiconductor electrode versus the reference electrode

$\mu = E_C - E_F$ , the energy difference between the conduction band and Fermi level of the semiconductor in the bulk.

As  $\mu$  and  $\phi_{ref}$  are constants and independent of the external bias, Eq. (5.38) can be rewritten as

$$const - eV_{sc} + eV_H = eV_{bias} \quad (5.39)$$

A change in the external potential is distributed among a change in the potential differences over the semiconductor space charge layer and the Helmholtz layer, respectively.

$$-\delta V_{sc} + \delta V_H = \delta V_{bias} \quad (5.40)$$

Under the approximation that the density of adsorbed ions at the semiconductor surface does not depend on the external potential, a change of the electrode potential results in a change of the charge densities in the semiconductor space charge layer and at the OHP according to

$$\delta\sigma_{sc} = -\delta V_{sc} \cdot C_{sc} \quad (5.41)$$

$$\delta\sigma_{OHP} = -\delta V_H \cdot C_H \quad (5.42)$$

and  $\delta\sigma_{sc} = -\delta\sigma_{OHP}$ . Thus, the potential changes  $\delta V_s$  and  $\delta V_H$  can be related to the capacitances  $C_{sc}$  and  $C_H$  by

$$\frac{\delta V_{sc}}{-\delta V_H} = \frac{C_H}{C_{sc}}, \quad (5.43)$$

i.e. the distribution of the potential change is given by the inverse ratio of the capacitances.

For a moderately doped semiconductor ( $N_{D,A} \approx 10^{15} - 10^{19} \text{ cm}^{-3}$ ) in depletion, because of  $C_{sc} \ll C_H$  changes in the external potential mainly appear across the space charge layer of the semiconductor rather than across the Helmholtz layer, and the space charge layer capacitance  $C_{sc}$  dominates the measurable electrode capacitance  $C_t$  [Pleskov, 1980], [Nozik & Memming, 1996]. As a consequence, the band edges at the surface of the semiconductor,  $E_{C,S}$  and  $E_{V,S}$ , can be regarded as fixed relative to the redox levels in the electrolyte. The surface band edges do not shift with a change in the semiconductor Fermi level relative to the electrolyte redox levels, whereas the band edges in the bulk and the band bending do. However, changes in the ionic composition of the electrolyte can alter  $V_H$ , and the surface band edges are shifted with  $V_H$  [Nozik, 1978], [Bard & Faulkner, 2001]. **This is an important difference to the properties of metal/electrolyte interfaces.** In the metal, no space charge layer is developed due to the high density of free carriers and the charge on the solid side is localized at the surface. Hence, the potential drop appears exclusively over the Helmholtz layer on the solution side and the measured capacitance corresponds to the Helmholtz capacitance  $C_H$ . At a metal electrode, the redox levels in solution are shifted with applied external potential relative to the metal Fermi level [Morrison, 1977]. Under accumulation or inversion conditions, the capacitance of a semiconductor space charge layer strongly increases and the assumption that a potential change develops only across the space charge layer must be abandoned.

## 5. Physical Chemistry of the GaN/Electrolyte Interface

---

The semiconductor electrodes used in this work were exclusively operated in depletion, and space charge layer capacitances  $C_{sc}$  of up to  $1 \mu\text{F cm}^{-2}$  have been obtained for the electrodes with highest carrier concentration. Assuming a Helmholtz capacitance not less than  $20 \mu\text{F cm}^{-2}$ , the externally applied voltage appears mainly across the semiconductor depletion layer.

A particularly important reference potential for semiconductor electrodes is the value of the external potential  $V_{bias}$  under flatband conditions,  $V_{fb}$ , when there is no band bending and hence no space charge region or potential drop in the semiconductor. Under flatband conditions, Eq. (5.38) can be simplified to:

$$\mu + eV_H - e\phi_{ref} = eV_{fb}. \quad (5.44)$$

By means of Eq. 5.44, the relation between the external potential  $V_{bias}$  and the potential drop  $V_{sc}$  in the semiconductor electrode is generally given by

$$V_{sc} = -(V_{bias} - V_{fb}). \quad (5.45)$$

Note that the Helmholtz voltage  $V_H$ , and therefore just as well the flatband voltage  $V_{fb}$  are dependent on the ionic composition of the electrolyte. In electrochemistry, the external bias voltage is defined as the potential of the electrode versus a reference electrode ( $V_{bias} = \phi_{bulk}^{sc} - \phi_{ref}$ ). As a consequence, the external bias and the potential decay in the semiconductor ( $V_{sc} = \phi_S - \phi_{bulk}^{sc}$ ), which is defined as the potential of the surface with respect to the bulk semiconductor, have different signs. For the unique specification of a semiconductor flatband potential, the electrolyte composition and reference electrode used during the experiment must be given.

Under the assumption that any potential variation occurs across the semiconductor space charge layer, the Mott-Schottky Eq. (A.8) for an n-type semiconductor capacitor in depletion can be rewritten to Eq. (5.46):

$$\frac{1}{C_{sc}^2} = \left( \frac{2}{eN_D\epsilon_{sc}\epsilon_0} \right) \left[ (V_{bias} - V_{fb}) - \frac{kT}{e} \right]. \quad (5.46)$$

From the slope of the  $1/C_{sc}^2$  vs.  $V_{bias}$  plot, the donor concentration in a depth  $W(V_{bias})$  (see Eq. A.9) can be calculated. For uniform doping, a straight line is observed. An extrapolation of the Mott-Schottky plot to  $1/C_{sc}^2 = 0$ , yields  $V_{fb} = V_{bias} - \frac{kT}{e}$ , and the flatband voltage  $V_{fb}$  can be obtained from the intercept with the potential axis by accounting for  $\frac{kT}{e}$ .

The measurement of the flatband voltage  $V_{fb}$  allows the determination of the semiconductor conduction and valence band edge in dependence of the electrolyte composition with respect to the hydrogen redox level. Combining Eq. (5.38) and Eq. (5.44), the semiconductor conduction and valence band edge at the surface are given by

$$E_{C,S} = -eV_{fb} + \mu - e\phi_{ref} \quad (5.47)$$

and

$$E_{V,S} = -eV_{fb} + \mu^* - e\phi_{ref} \quad (5.48)$$

respectively, with  $\mu^* = E_F - E_V$ , the energy difference between the Fermi level and the valence band edge of the semiconductor in the bulk.

#### 5.1.4. Charge Transfer Processes

According to the Gerischer model [Gerischer, 1960], [Gerischer, 1961], [Memming, 2001], charge transfer between a semiconductor electrode and a redox system in solution occurs isoenergetically (Franck-Condon principle, see Section 5.1.2) between occupied and unoccupied energy levels at both sides of the interface. The charge transfer rate is proportional to the density of occupied and unoccupied isoenergetic energy levels. At an ideal interface without surface states, a charge transfer must occur via the conduction or valence band of the semiconductor. The charge transfer processes via the conduction band are illustrated for an n-type semiconductor in Figure 5.11.

Considering the reduction of an oxidizing agent in solution by electron capture from the conduction band, the transfer rate and the **cathodic current** density  $j_c^-$  depend on the electron density,  $n_s$ , at the semiconductor surface and the density of oxidized redox states in solution with energy levels corresponding to the conduction band (see Figure 5.11 (a)):

$$j_c^- \propto \int_{E_C}^{\infty} n_s D_{ox}(E) dE. \quad (5.49)$$

Under the assumption that electron transfer occurs mainly within  $kT$  of the conduction band edge, Eq. 5.49 can be simplified to

$$j_c^- \propto n_s D_{ox}(E_{C,S}). \quad (5.50)$$

According to Eq. (A.2), the electron density,  $n_s$ , at the semiconductor surface depends exponentially on the band bending. The relative position of the conduction band at the surface,  $E_{C,S}$ , and the oxidizing level in solution,  $E_{ox}^0$ , on the other hand, are fixed under external bias, and the density of available oxidizing states at an energy level  $E_{C,S}$  remains constant (see Figure 5.11 (a) and (d)). Providing that an external potential change appears exclusively over the semiconductor, and inserting Eqs. (A.2) and (5.45) in Eq. (5.50), one obtains

$$j_c^- \propto D_{ox}(E_{C,S}) n_0 \exp\left(\frac{-e(V_{bias} - V_{fb})}{kT}\right) \quad (5.51)$$

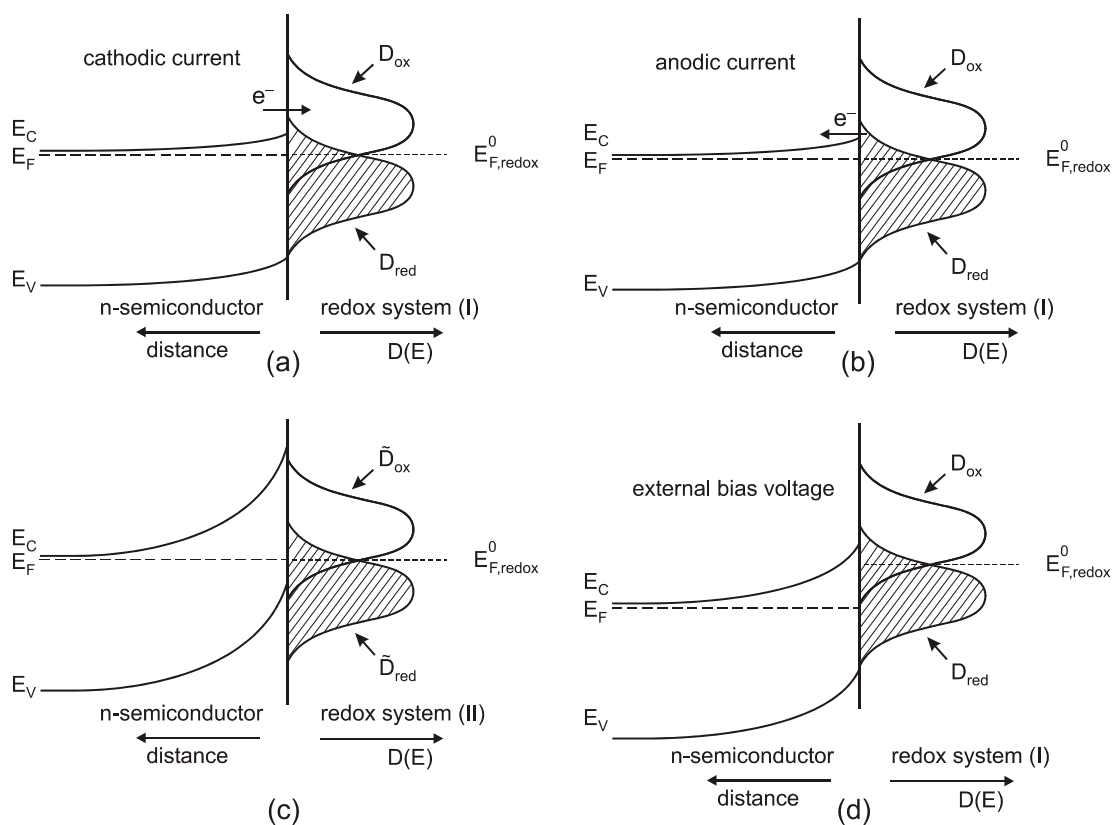
for the dependence of the cathodic current on the externally applied bias voltage. Thus, the cathodic current density at an n-type semiconductor electrode at room temperature should change by one order of magnitude for every 60 mV variation of the electrode potential  $V_{bias}$ .

For the oxidation of a reduced species by an electron transfer from a reduced redox ion to the conduction band of the semiconductor (see Figure 5.11 (b)), the **anodic current**  $j_c^+$  density, using the same approximations as above, is given by

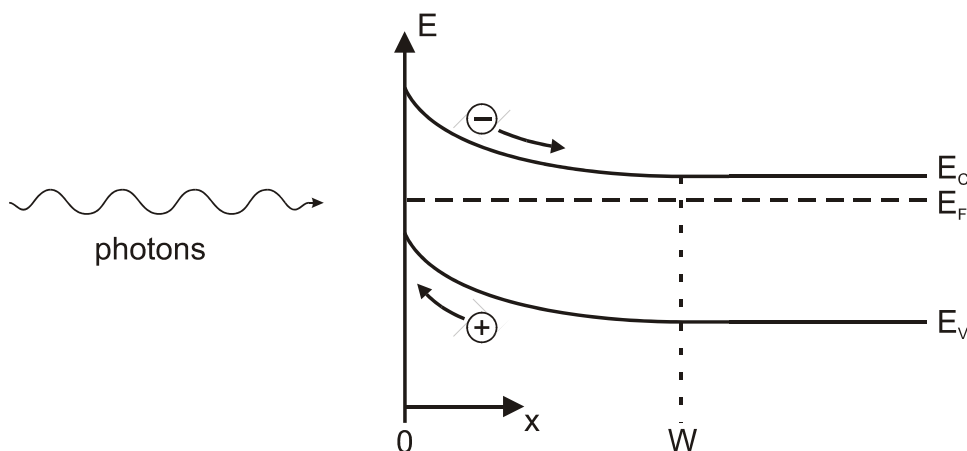
$$j_c^+ \propto N_C D_{red}(E_{C,S}). \quad (5.52)$$

The anodic current is therefore independent of the electrode potential and the band bending in the semiconductor.

Similar expressions are obtained for the valence band of a semiconductor and a hole transfer into (anodic current  $j_V^+$ ) or from (cathodic current  $j_V^-$ ) a redox level in solution.



**Figure 5.11:** Energy-band diagram and density of occupied and unoccupied redox states for an n-type semiconductor in contact with a redox electrolyte. (a) and (b) illustrate the cathodic and anodic charge transfer processes via the conduction band. Equilibrium between the semiconductor Fermi level and the redox level in the solution is assumed. (c) The densities of occupied and empty redox states available for isoenergetic charge transfer depend on the electrochemical potential of the redox system. (d) External bias changes only the band bending in the semiconductor, but not the energetic position of the band energies  $E_{C,S}$ ,  $E_{V,S}$  at the surface relative to the redox levels  $E_{ox}^0$ ,  $E_{red}^0$  in solution.



**Figure 5.12:** Illumination of an n-type Schottky barrier results in the generation of electron hole pairs. Free charge carriers generated in the depletion layer ( $x \leq W$ ) are separated and contribute to the photocurrent. The contribution of carriers generated outside of the depletion region ( $x > W$ ) is neglected.

For n-type semiconductors, the conduction band processes described above are majority carrier processes and dominate charge transfer and electrode reactions in the dark. Under illumination, minority carriers may be generated and the rate of electrode reactions and charge transfer involving minority carriers may change significantly, as described to some extent in the following section.

### 5.1.5. Illumination of the Semiconductor /Electrolyte Junction

In the following, the basic principles of a semiconductor/electrolyte junction under illumination are discussed as far as they are essential for the determination of the flatband voltage by the photocurrent method (Section 5.3.2). The semiconductor/electrolyte junction can be treated as a Schottky barrier in that case. A more general and detailed discussion of the semiconductor photoelectrochemistry can be found for example in [Gerischer, 1966] or [Gurevich & Pleskov, 1986].

Illumination of a semiconductor electrode with light of a photon energy larger than the bandgap results in the generation of electron-hole pairs in the region close to the surface corresponding to the absorption length  $\alpha^{-1}$ . In the case of an illuminated Schottky-barrier, the electrons and holes that are generated in the depletion region are separated by the present electric field, and a photocurrent which depends on the width  $W$  of the depletion layer is observed (Figure 5.12). If the photo-generation rate is constant throughout the space charge layer, which is the case for  $\alpha W \ll 1$ , a linear relation between the photocurrent  $j_{ph}$  and the depletion width  $W$  is obtained.

According to Gärtner, the photoinduced generation rate of electron-hole pairs is given by

$$g(x) = (1 - R)\eta\varphi_0\alpha \cdot \exp(-\alpha x), \quad (5.53)$$

where  $R$  is the reflection,  $\eta$  the quantum efficiency,  $\varphi_0$  the photon flux rate and  $x$  the distance from the semiconductor surface. For the following considerations, a quantum efficiency of  $\eta = 1$  is assumed and reflection is neglected ( $R = 0$ ) [Gärtner, 1959]. Both parameters have no influence on the determination of the flatband voltage from photocurrent measurements.

Under the further assumptions that (i) all photogenerated electrons and holes contribute to the photocurrent, and (ii) that contributions from carriers generated outside of the space charge region that reach the depletion layer by diffusion can be neglected [Butler, 1977], the photocurrent density is described by:

$$j_{ph} = e \int_0^W g(x) dx = -e\varphi_0 [\exp(-\alpha W) - 1]. \quad (5.54)$$

The dependence of the depletion layer width  $W$  of the semiconductor on the applied bias voltage  $V_{bias}$  is obtained by combining the Eq. (A.9) from Appendix A.3 and Eq. (5.45):

$$W = \sqrt{\frac{2\varepsilon_{sc}\varepsilon_0}{eN_D} |V_{bias} - V_{fb}|} \quad (5.55)$$

If the space charge layer width  $W$  is small compared to the absorption length  $\alpha^{-1}$ , expression (5.54) for the photocurrent density  $j_{ph}$  can be approximated by a Taylor expansion around  $W = 0$ , yielding

$$j_{ph} = e\varphi_0\alpha W = \varphi_0\alpha \sqrt{\frac{2\varepsilon_{sc}\varepsilon_0 e}{N_D} |V_{bias} - V_{fb}|}. \quad (5.56)$$

In a plot of  $j_{ph}^2$  versus  $V_{bias}$  the flatband voltage  $V_{fb}$  can be extracted from the intersection of an extrapolation of the linear photocurrent region to the V-axis.

### 5.1.6. Surface States

In the previous sections, the influence of surface states on the electrical properties of semiconductor/electrolyte interfaces has been neglected. However, for some semiconductor electrodes surface states may have a major influence. They originate either from the discontinuity of the crystal lattice (Tamm states) or from adsorbed atoms at the surface (Shockley states) [Mjamlin & Pleskov, 1967]. Of special interest are surface states with corresponding energy levels  $E_{ss}$  within the band gap. Their occupation probability can be described by the Fermi function. The relaxation time constant  $\tau$  for the equilibration of a surface state with the bands of the semiconductor is an important parameter for the electrical contribution of surface states in experiments with sweeping potentials.



A high density  $N_{ss}$  of surface states with an energy  $E_{ss}$  can lead to a pinning of the surface Fermi level at the energy  $E_{ss}$ , as described by the Bardeen model [Cowley & Sze, 1965] for the dependence of the Schottky-barrier height at a metal/semiconductor junction on the work function of the metal. Generally, more ionic semiconductors show less tendency to Fermi level pinning than more covalent semiconductors [Bard & Faulkner, 2001]. In the Bardeen limit, the variation of an external potential only varies the occupation of the surface states but not the charge and band bending in the semiconductor space charge layer.

The interfaces of n-GaAs, p-GaAs, and n-Si to aqueous electrolytes exhibit a strong Fermi level pinning [Bard & Faulkner, 2001]. The surface states contribute considerably to the potential drop in the Helmholtz layer and the control of the band bending is limited. However, for many semiconductors (e.g. Ge) the density of surface states observed in aqueous solutions is much smaller than expected and an interaction with water molecules is proposed to rationalize these almost perfect surfaces [Nozik & Memming, 1996].

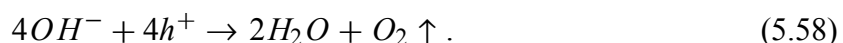
### 5.1.7. Electrochemical Reactions at the GaN/Electrolyte Interface

At the interface between a semiconductor and an electrolyte, there is a change in the conduction mechanism. Whereas electrons and holes are responsible for the charge transport in the semiconductor, ionic conduction is predominant in the electrolyte. Thus, a charge transfer over the interface is always accompanied by an electrochemical reaction in which an electron or hole is accepted or emitted by the semiconducting electrode.

In aqueous electrolytes, the generation of hydrogen and oxygen are major reactions occurring at the semiconductor electrode. They proceed according to the basic equations for water electrolysis:



and



The redox potentials of these halfcell reactions versus the SHE at 25 °C are given by

$$\phi_{H^+/H_2} = -0.059 \text{ V} \times pH \text{ (vs. SHE)} \quad (5.59)$$

and

$$\phi_{OH^-/O_2} = +1.229 \text{ V} - 0.059 \text{ V} \times pH \text{ (vs. SHE)} \quad (5.60)$$

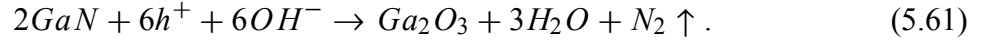
[Beach, 2003]. The halfcell reaction (5.57) at pH 0 defines the redox potential of the SHE and shows a Nernstian dependence on the pH of the solution,  $pH_{sol}$ .

Whereas in the electrolysis reactions the electrode is not part of the reaction and stays unchanged, the electrode surface is chemically modified in other processes, accompanying charge transfer over the interface. For GaN electrodes, oxidation of the surface is of major importance.

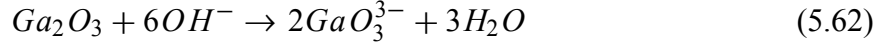
## 5. Physical Chemistry of the GaN/Electrolyte Interface

---

A proposed mechanism for the electrochemical oxidation of GaN, described for example in [Rotter, 2000], [Nowak, 2001], is



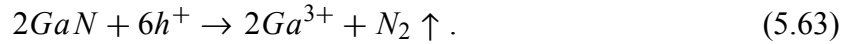
If the reaction takes place in basic aqueous solutions, the generated  $Ga_2O_3$  can be chemically dissolved by hydroxide ions



and the GaN surface is etched. The given equations are the overall reactions of several subsequent reaction steps involving the interplay between the aqueous solvent and the hydroxide [Peng, 1998a], [Peng, 1998b]. Both processes consume high amounts of  $OH^-$  and strongly depend on the solution pH, being limited by the diffusion of  $OH^-$  to the surface [Rotter, 2000].

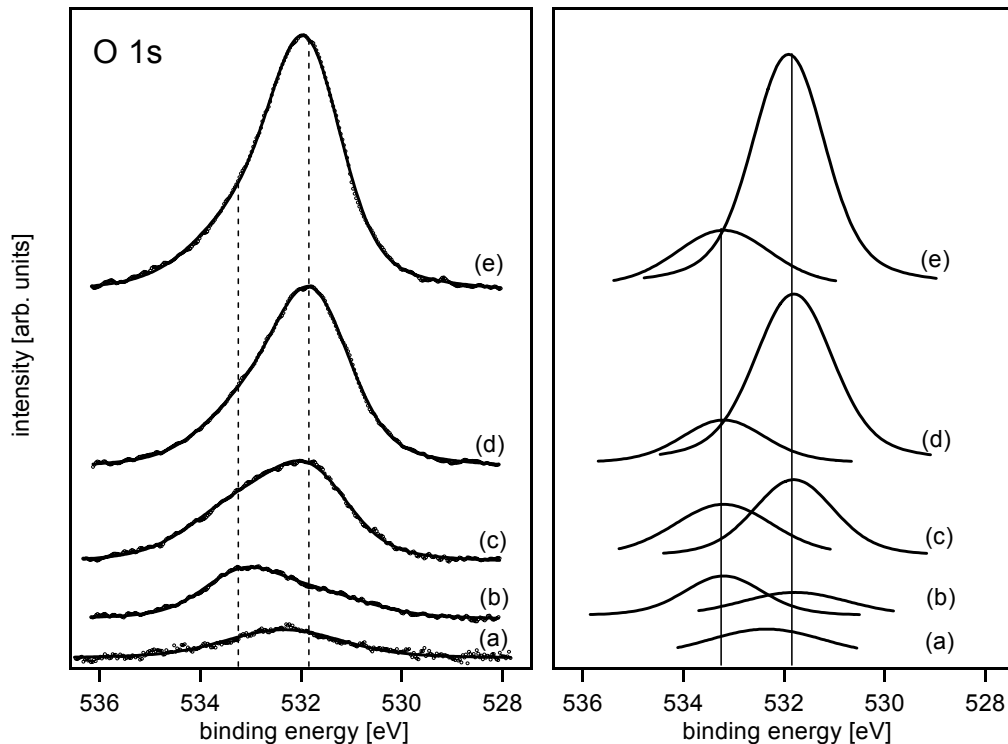
The presence of holes at the interface is crucial for the progress of the GaN surface oxidation. As in n-type GaN holes are minority carriers, this material is usually oxidized photoanodically by UV-irradiation. The generated holes are accumulated at the interface by a suitable band bending that is adjusted by the external bias voltage  $V_{bias}$  [Rotter, 2000], [Nowak, 2001]. In strong basic solutions, the built oxide is dissolved by  $OH^-$  and the GaN is photoanodically etched [Peng, 1998a], [Nowak, 2001].

In acidic solutions (1M  $H_2SO_4$ ), the following photoelectrochemical etching reaction was proposed by Huygens and co-workers [Huygens, 2000]:



### 5.2 Chemical Characterization of the GaN Surface

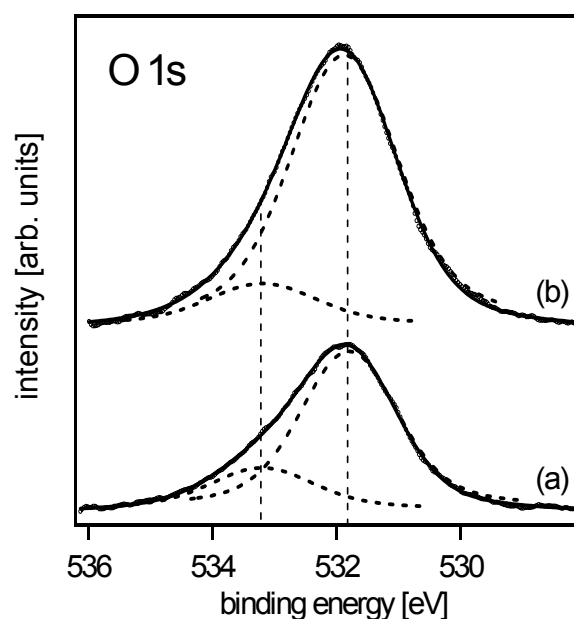
The chemical composition of native as well as thermally oxidized GaN surfaces was discussed in theory and experiment by various groups. Even at room temperature, GaN was found to form a native oxide layer when exposed to atmosphere [Prabhakaran, 1996], [Lin, 2000], [Hashizume, 2001], [Shalish, 2001]. Various reports address the interaction of oxygen with GaN at room temperature, studied by selective exposition of clean and ordered GaN (0001) surfaces to oxygen atmosphere [Bermudez, 1996], [Janzen, 1999], [Watkins, 1999]. However, somewhat different results have been reported. Watkins et al. have observed an increase in the oxygen surface coverage with increasing oxygen exposure, which saturated at an oxygen coverage of  $\Theta_{ox} = 0.9$  ML at an  $O_2$ -exposure of  $10^8$  L [Watkins, 1999]. Bermudez has found a saturation of the oxygen coverage already at an exposure of 200 L and  $\Theta_{ox} = 0.4$  ML [Bermudez, 1996]. A plateau in the oxygen coverage at  $\Theta_{ox} = 0.4$  ML was observed by Janzen and co-workers starting at around  $10^3$  L. The surface coverage further increased for exposures exceeding  $10^3$  L [Janzen, 1999]. According to density-functional theory calculations by Zywiets et al., adsorption of oxygen on (0001) GaN is exothermic for coverages up to  $\Theta_{ox} = 0.8$  ML [Zywiets, 1999]. Both, experiments and theoretical calculations have indicated a



**Figure 5.13:** O1s XPS spectral data and fit (left), and deconvolution (right) for MBE grown (0001) GaN after growth and exposure to laboratory air for (a) 30 s and (b) several days and after dry thermal oxidation for 2 h at (c) 600 °C, (d) 700 °C and (e) 800 °C. Data analysis by nonlinear least square optimization motivated the deconvolution into two peaks centred around 531.8 eV and 533.2 eV (dashed lines). For (a), a deconvolution was not reasonable due to the low O1s signal intensity.

binding of the oxygen to the Ga atoms. No binding of oxygen to the N atom could be observed. Reports in the literature about the thermal oxidation of GaN compare wet and dry oxidation atmosphere as well as oxidation temperatures ranging from 450 °C up to 900 °C [Wolter, 1997], [Readinger, 1999], [Wolter, 2000]. Wet as well as dry thermal oxidation at 900 °C lead to the formation of monoclinic  $\beta$ -Ga<sub>2</sub>O<sub>3</sub>, as identified by XRD. According to Readinger et al., wet oxidation leads to higher oxidation rates, but results in more irregular oxide formation and poor electrical oxide quality [Readinger, 1999].

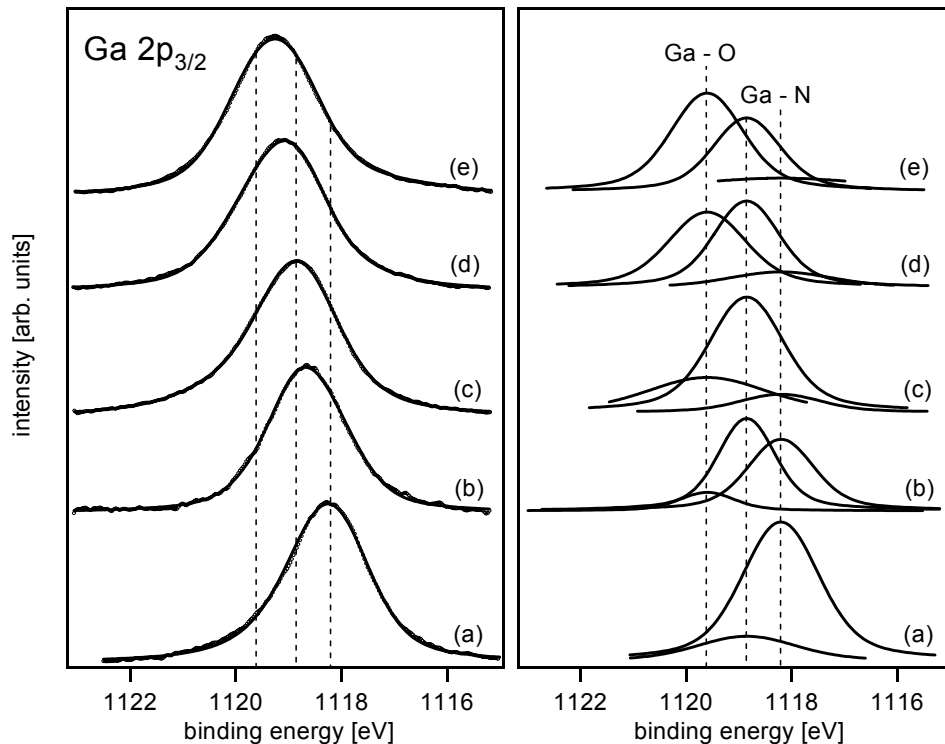
The chemical composition of as-grown GaN (0001) surfaces exposed to atmosphere was analyzed by XPS measurements and compared to GaN that was dry thermally oxidized at different temperatures between 600 °C and 800 °C. Due to their different kinetic energies, electrons emitted from different core levels vary in their inelastic mean free paths  $\lambda_m$  in solids, which determine the surface sensitivity. The analyzed Ga2p<sub>3/2</sub>, O1s, and N1s core level spectra recorded with the Mg K $\alpha$  line exhibit a  $\lambda_m$  of 4, 9 and 10 ML, respectively.



**Figure 5.14:** O1s spectral data for MBE-grown (0001) GaN after dry thermal oxidation at 700 °C, for (a) 2 h, and (b) 6 h. Deconvolution of the spectra revealed two peaks centred around 531.8 eV and 533.2 eV (dashed lines).

In Figure 5.13 the O1s spectra of MBE-grown GaN, after growth and exposure to atmosphere and after dry thermal oxidation are presented. Figure 5.15 shows the Ga2p<sub>3/2</sub> spectra for the same set of samples. Already after an exposure of the as-grown surface to laboratory air for only 30 s, a clear O1s peak is observable. Because of the comparably low signal intensity, a deconvolution in various contributions is not reasonable. After several days at atmosphere, two distinct peaks can be found in the O1s spectra, centered around binding energies of 531.8 eV and 533.2 eV. Whereas the peak intensity at higher binding energies remains more or less constant after dry thermal oxidation between 600 °C and 800 °C, the contribution at lower binding energies significantly increases with oxidation temperature. The binding energy scale was referred to the Au 4f<sub>7/2</sub> peak position at 84.0 eV, as described in Section 2.1.1.

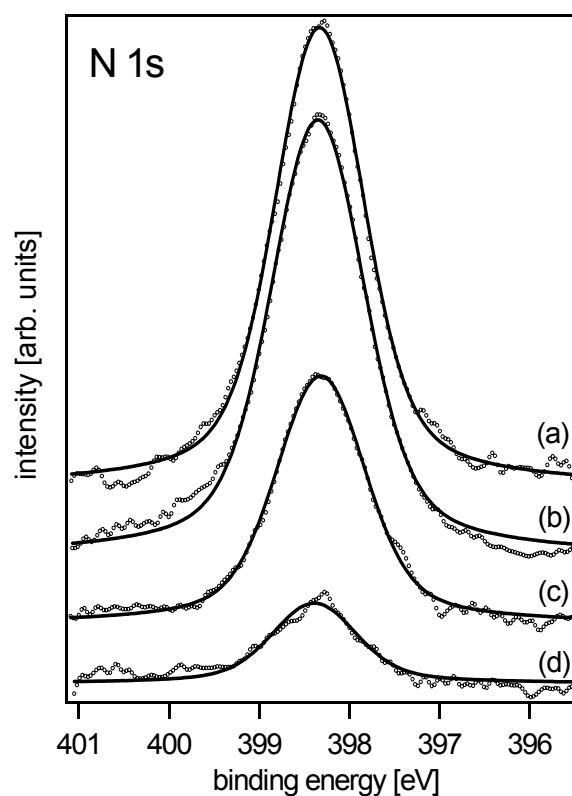
The observation of two contributing peaks to the O1s spectra is in accordance with various reports in the literature. For untreated GaN surfaces, Shalish and co-workers have observed two peaks at 531.6 eV and 532.8 eV [Shalish, 2001]. The low energy peak was completely removed by etching in HCl. Prabhakaran et al. have found two contributions at binding energies of 531.3 eV and 532.7 eV. The high energy contribution was significantly reduced by an overnight annealing in vacuum at 230 °C [Prabhakaran, 1996]. King et al. have observed a single broad O1s peak centered at 532.4 – 532.7 eV for native GaN surfaces, and the development of a pronounced peak at 531.5 eV by UV/ozone treatment, which was attributed to the possible formation of stoichiometric Ga<sub>2</sub>O<sub>3</sub> [King, 1998]. In conclusion, the low O1s energy peak observed in Figure 5.13 around 531.8 eV can be assigned to the Ga-O bond of a gallium oxide



**Figure 5.15:** Ga $2p_{3/2}$  spectra of MBE-grown (0001) GaN after growth and exposure to laboratory air for (a) 30 s and (b) several days, and after dry thermal oxidation for 2 h at (c) 600 °C, (d) 700 °C and (e) 800 °C. The peaks obtained by deconvolution are attributed to GaN (1118.2 eV), gallium oxide (1119.6 eV), and an intermediate phase (1118.85 eV).

or oxynitride formed at the surface. For the thermodynamically most stable monoclinic  $\beta$ -Ga $_2$ O $_3$  phase, Ga-O binding energies ranging from 531.1 eV to 531.85 eV are reported in the literature [Mizokawa, 1988], [Carin, 1990], [Hollinger, 1994]. This assumption is supported by the Ga $2p_{3/2}$  spectral data shown in Figure 5.15 and a comparison of the O1s core level spectra of GaN surfaces dry oxidized at 700 °C for 2 h and 6 h presented in Figure 5.14. Whereas the low energy contribution at 531.8 eV nearly doubled in intensity, the intensity of the peak around 533.2 eV remained unchanged. Thus, the O1s peak at higher energies is not influenced by the oxide growth but originates from an oxide containing adsorbate. The high binding energy component around 533.2 eV is most probably caused by the adsorption of a thin water film on the GaN surface and the formation of O-H bonds, explaining the independence of the peak intensity on the oxidation temperature and the intensity reduction by overnight annealing in vacuum. The O1s spectral energies for H $_2$ O and O-H bonds are given as 533.3 eV and 533.1 eV, respectively [Moulder & Chastain, 1992], [Lin, 2000].

For a consistent interpretation of the more surface sensitive Ga $2p_{3/2}$  spectra, a deconvolution in three peaks centred around 1118.2 eV, 1118.85 eV and 1119.6 eV is necessary. After the



**Figure 5.16:** The N1s spectra for MBE grown (0001) GaN (a) before oxidation, and after dry thermal oxidation for 2 h at (b) 600 °C, (c) 700 °C, and (d) 800 °C.

exposure of an as grown GaN surface to laboratory air for 30 s, the signal is dominated by the low energy peak, which can be attributed to the Ga-N bond of GaN in accordance with Ref. [Wolter, 1997]. A second peak at higher binding energies is already observable. After an exposure of several days to atmosphere, the peak at 1118.85 eV is significantly increased. At the same time the contribution of the Ga-N bond is reduced and a third peak at 1119.6 eV becomes visible. Dry thermal oxidation resulted in a shift of the spectral intensity to the peaks at higher binding energies. With increasing oxidation temperature, the peak at 1119.6 eV becomes more and more pronounced, and is therefore ascribed to the Ga-O bond. This is in close agreement to observations of Wolter et al., who reported a shift in the Ga2p core level binding energy from Ga-N to Ga-O type bonding of 1.3 eV [Wolter, 1997]. The contribution of the Ga-N bond vanished almost completely at higher oxidation temperatures. However, after oxidation at 800 °C, still a significant peak at the intermediate energy of 1118.85 eV was present, and attributed to an intermediate chemical bonding state between Ga-N and Ga-O. The formation of an intermediate chemical bonding state between Ga-N and Ga-O was also observed by means of the Ga3d spectra for GaN dry thermally oxidized at 800 °C and 900 °C, as described in Ref. [Wolter, 2000]. As all core levels of an atom experience the same binding energy shift [Briggs & Grant, 2003], the results can be adopted for the Ga2p core level spectra.

The intermediate chemical bonding state was explained by the formation of an intermediate phase between GaN and gallium oxide. The authors speculated about the initial formation of a continuous gallium oxynitride layer on the GaN surface after 1 h of dry oxidation at 800 °C, followed by an island growth of gallium oxide, preferentially above threading dislocations [Wolter, 2000]. For oxidation at 850 °C, the formation of an intermediate oxynitride layer at the GaN/oxide interface was confirmed by Auger depth profiles [Kim, 2001]. Even for the 2 h thermal oxidation at 800 °C, no closed oxide layer was formed, as (i) a significant N1s peak was observable (Figure 5.16), and (ii) the highly surface sensitive Ga2p spectra still showed the significant contribution of an intermediate phase.

For GaN surfaces treated wet chemically by a H<sub>2</sub>SO<sub>4</sub>/H<sub>2</sub>O<sub>2</sub> 3:1 mixture as described in Section 3.2.2, no change in the contributions to the Ga2p<sub>3/2</sub> or O1s core levels was observed (data not shown), leading to the conclusion of a chemically unchanged surface. However, as described in Section 3.2.2, a significant reduction of the C1s peak intensity was found, indicating the removal of organic surface adsorbates.

In conclusion, as grown GaN surfaces show the immediate formation of a native oxide or oxynitride layer after exposure to atmosphere. For dry thermal oxidation, the formation of a gallium oxide was observed, concluded from characteristic peaks increasing with the oxidation temperature in the O1s and Ga2p<sub>3/2</sub> spectra around 531.8 eV and 1119.6 eV, respectively. Island growth of gallium oxide, preferentially at threading dislocations was assumed and confirmed by cross sectional transmission electron microscopy micrographs for a 2 h dry oxidation at 700 °C in Ref. [Weidemann, 2005].

### 5.3. Electrochemical and Photoelectrochemical Characterization

A basic electrochemical investigation of GaN electrodes and the GaN/electrolyte interface was performed by cyclic voltammetry and impedance spectroscopy. Of special interest was the determination of the flatband voltage  $V_{fb}$ , as it allows the calculation of the energetic position of the conduction and valance band edges  $E_{C,S}$  and  $E_{V,S}$  at the interface relative to the redox level of the reference electrode. The band levels at the interface are fixed with respect to the electrolyte redox levels (q.v. Section 5.1.3) for most semiconductors, and charge transfer does only occur isoenergetically. Thus, knowledge of the relative energetic levels is essential for a comprehension of the electrochemical processes at the interface and a possible utilization of the semiconductor electrode in photoelectrochemical cells for solar energy conversion or photocatalysis. Furthermore, knowledge of  $V_{fb}$  allows the determination of the concentration of charge carriers available for charge transfer at the semiconductor surface from the bulk concentration, as  $V_{bias} - V_{fb}$  represents the band bending in the semiconductor under the assumption that any potential change occurs exclusively in the depletion region (Eq. (5.45)).

Flatband potentials are usually obtained by measurement of the photocurrent or the interfacial capacitance of the semiconducting electrode. In both methods, a physical property depending

on the space charge layer width is observed over a range of applied potentials and extrapolated to flatband conditions. In this work, the flatband voltage was mainly estimated from the capacitance-voltage relation of the GaN electrodes. For that, the capacitance of the semiconductor depletion region,  $C_{sc}$ , was extracted from impedance spectroscopy data by equivalent circuit models. For comparison, flatband voltages of GaN-electrodes were determined from photocurrent measurements. The obtained results and the limitations of the measurement methods are discussed with respect to the results reported by other groups.

Charge transfer processes over the GaN/electrolyte interface have been investigated for electrolytes with and without redox couples by cyclic voltammetry.

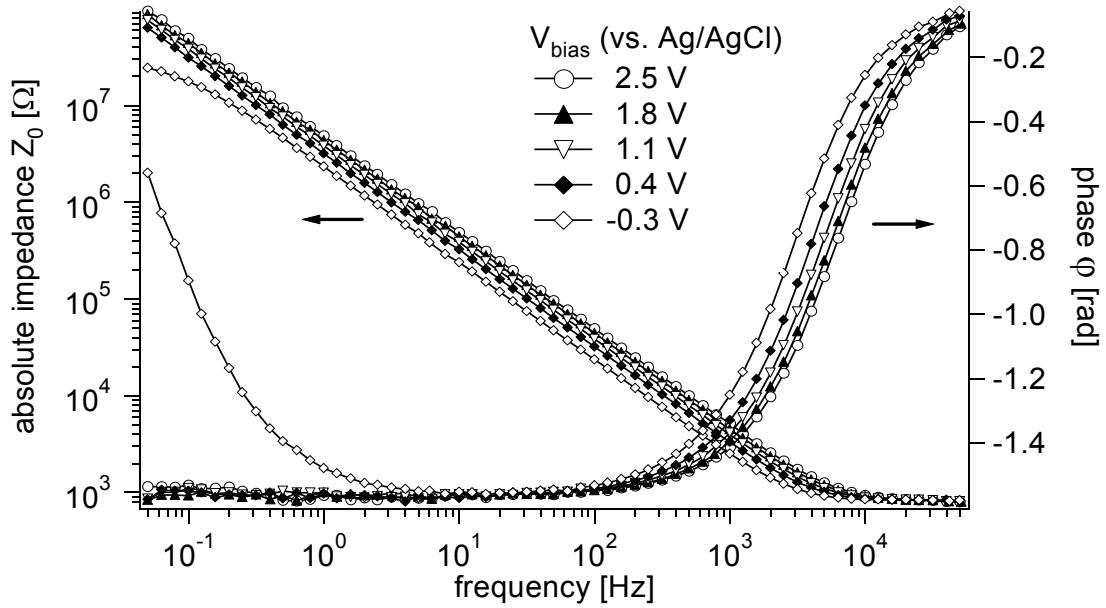
The pH response of native and thermally oxidized GaN surfaces was measured with different transistor devices, and the cross sensitivity towards  $\text{Na}^+$ ,  $\text{K}^+$ , and  $\text{Ca}^{2+}$  was analyzed.

### 5.3.1. Impedance Spectroscopy Analysis of GaN Electrodes and Determination of the Flatband Voltage

The electrochemical characterization of GaN electrodes was performed by the setup described in Section 2.2.1. The bias voltage was applied versus an Ag/AgCl (3 M KCl) reference electrode. If not particularly stated, all electrochemical measurements were performed in standard PBS buffer at pH 7. Reproducible cyclic voltammograms between  $-0.5$  V and  $2.5$  V over time verify the stability of the investigated GaN electrodes in the ambient electrolyte and the specified potential window. The onset of an exponential increase of the cathodic current was observed at  $-0.5$  V, which is discussed in detail in Section 5.3.7. During the impedance analysis, no spectra were taken at voltages below  $-0.5$  V, in order to avoid large cathodic currents over the GaN/electrolyte interface. In Figure 5.17, the impedance spectra of a MOCVD grown n-type GaN electrode recorded sequentially at different bias voltages in a frequency range between 50 mHz and 50 kHz are presented. For bias voltages above  $-0.2$  V the spectra can be interpreted by the serial connection of a resistance  $R_{ext}$  dominating at high frequencies ( $> 1$  kHz) and the interface capacitance  $C_i$ , dominating the medium and low frequency range. This corresponds to the equivalent circuit model (a) discussed in Section 2.2.3, describing an ideal polarizable interface without any Faradaic processes present. Figure 5.18 shows the impedance spectrum taken at  $V_{bias} = 1.8$  V and fitted by the circuit model (a). The serial resistance  $R_{ext}$  includes the resistance of the electrolyte, the bulk semiconductor, the contacts and connections, and is dominated by the  $750 \Omega$  resistor connected in series with the working electrode. Spectra recorded at  $V_{bias} < -0.2$  V show the indication of an additional resistance  $R_i$  in parallel to the capacitance  $C_i$  of the interface in the low frequency range ( $< 1$  Hz). Circuit model (b) exhibits a good approximation of the impedance data at low bias voltages, as shown in Figure 5.19 for  $V_{bias} = -0.3$  V.

As discussed in Section 5.1.3, the extracted interface capacitance  $C_i$  is a serial connection of the capacitances  $C_D$  and  $C_H$  of the Gouy-Chapman and the Helmholtz layer, and the capacitance  $C_{sc}$  of the semiconductor space charge region. Under the existing measurement conditions





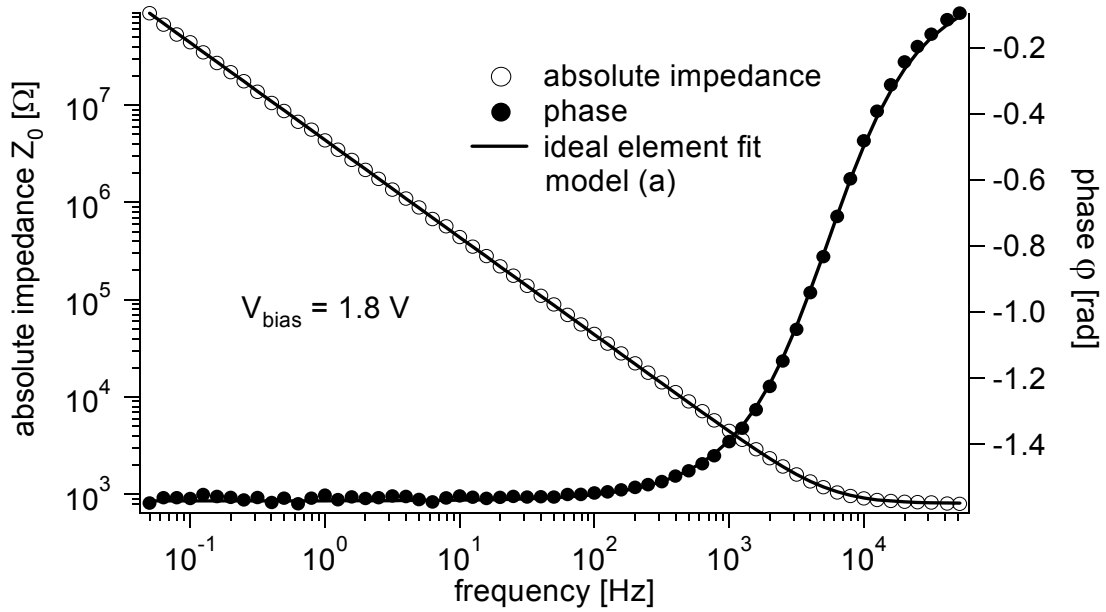
**Figure 5.17:** Impedance spectra of an n-type GaN electrode recorded at different bias voltages between 2.5 V and  $-0.5$  V applied versus an Ag/AgCl reference electrode. The electrode was immersed into the standard PBS buffer at pH 7.

of concentrated electrolytes (50 mM) and a moderately doped semiconductor in depletion, the capacitive contribution of the electrochemical double layer is negligible in the serial connection ( $C_D > 50 \mu\text{F cm}^{-2}$ ,  $C_H > 20 \mu\text{F cm}^{-2}$ ,  $C_{sc} < 1 \mu\text{F cm}^{-2}$ ), and the interface capacitance  $C_i$  can be interpreted as the capacitance of the semiconductor space charge region  $C_{sc}$ . The dependence of the extracted capacitance  $C_{sc}$  and the interface resistance  $R_i$  on the bias potential is presented in Figure 5.20 in the potential range between  $-0.5$  V and 2.5 V. The corresponding impedance spectra have been taken in steps of 100 mV.

As for bias voltages  $V_{bias} > -0.2$  V no indication of a parallel resistance is visible in the impedance spectra, the interface resistance exceeds  $50 \text{ M}\Omega \text{ cm}^2$  in this potential range. For more negative voltages, an interface resistance decreasing rapidly with more negative potential can be extracted from the impedance data. The onset of this decrease of the interface resistance  $R_i$  varied between  $-0.1$  V and  $-0.4$  V for the different GaN electrodes investigated.

The extracted capacitance  $C_{sc}$  exhibits the voltage dependence of the depletion layer capacitance of an n-type semiconductor with homogeneous distribution of donors and can be approximated by the Mott-Schottky equation (A.8) discussed in Section A.3.

The flatband potential can be estimated from the Mott-Schottky plot shown in Figure 5.21, where  $1/C_{sc}^2$  is plotted versus the external bias voltage  $V_{bias}$ . For a semiconductor in depletion



**Figure 5.18:** Impedance spectrum recorded at  $V_{bias} = +1.8$  V (vs. Ag/AgCl). The interface capacitance can be extracted to  $C_i = 0.28 \mu\text{F cm}^{-2}$  by approximation with the equivalent circuit model (a) (solid line).

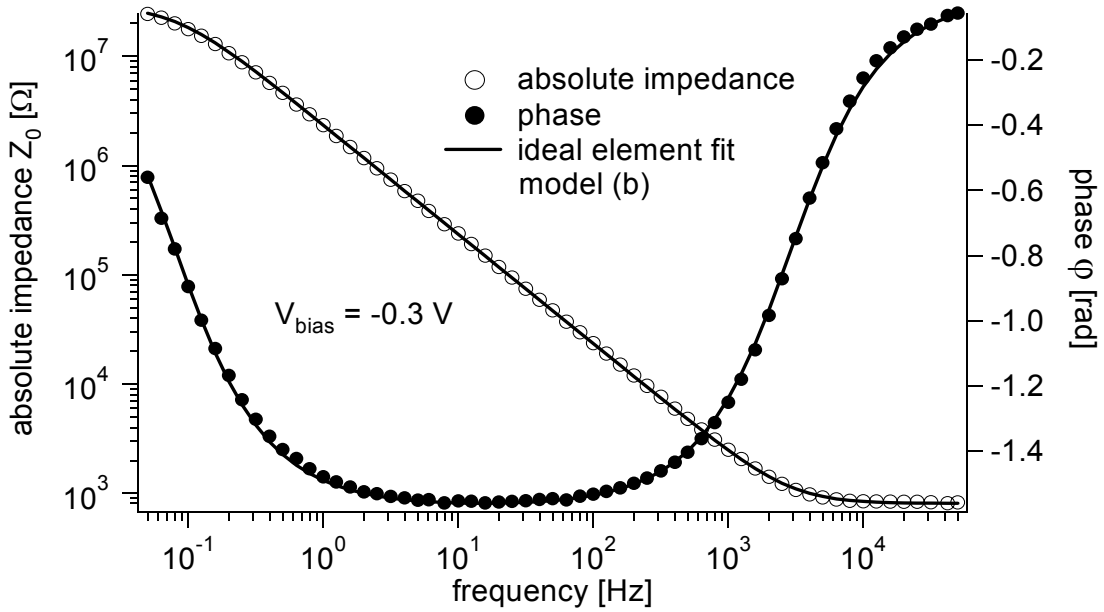
with uniform n-type doping, a straight line is expected according to equation

$$\frac{1}{C_{sc}^2} = \left( \frac{2}{eN_D\epsilon_{sc}\epsilon_0} \right) \left[ (V_{bias} - V_{fb}) - \frac{kT}{e} \right], \quad (5.64)$$

as derived in Appendix A.3. The flatband voltage  $V_{fb}$  can be obtained from the intersection of the linear extrapolation with the x-axis ( $1/C_{sc}^2 = 0$ ). From the slope of the Mott-Schottky plot, the concentration of ionized donors  $N_D$  can be calculated.

According to a detailed discussion by Gomes and Cardon [Cardon & Gomes, 1978], [Gomes & Cardon, 1982], the flatband voltage  $V_{fb}$  and the ionized donor density  $N_D$  can only be correctly extracted from the Mott-Schottky relationship under the following assumptions of an ideal Schottky barrier:

- (i) The bulk semiconductor and the electrolyte have zero resistance.
- (ii) The barrier has perfectly blocking properties.
- (iii) The capacitance of the Helmholtz layer and of other possible surface layers is sufficiently large to be neglected.
- (iv) No surface states are present.



**Figure 5.19:** Impedance spectrum recorded at  $V_{bias} = -0.3$  V (vs. Ag/AgCl). At low frequencies, the contribution of an additional resistance  $R_i$  parallel to  $C_i$  is visible. The solid line corresponds to a fit by circuit model (b) ( $C_i = 0.53 \mu\text{F cm}^{-2}$ ,  $R_i \approx 4 \text{ M}\Omega \text{ cm}^2$ ).

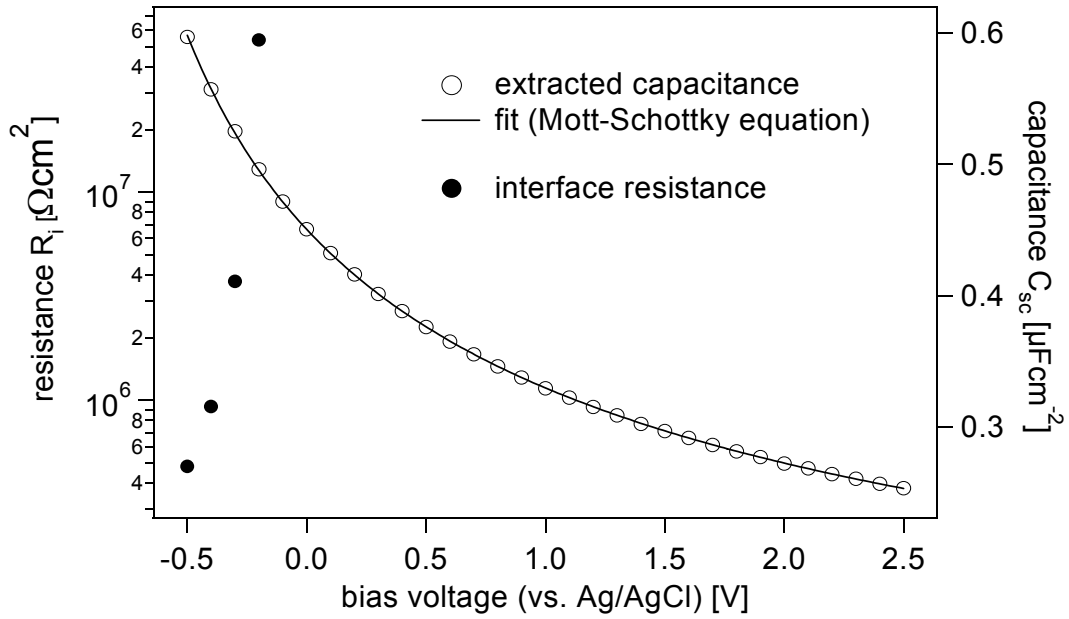
(v) The spatial distribution of donors is homogeneous.

In the following sections, the results obtained by the described method for GaN electrodes are discussed with respect to the requirements of an ideal Schottky barrier of Gomes & Cardon. All considerations and equations are given for an n-type semiconductor.

**(i) Non-negligible series resistance** The series resistance arising from the bulk semiconductor, the contacts, or the electrolyte are considered in the external serial resistance  $R_{ext}$  of the circuit model for data extraction.

**(ii) Imperfectly blocking barrier** Faradaic currents flowing over the GaN/electrolyte interface are accounted for in the equivalent circuit model by an interface resistance  $R_i$  in parallel to the capacitance of the interface  $C_i$  (circuit (b)). This is particularly important for voltages near the flatband potential.

**(iii) Additional surface layers** In Section 5.1.3, the Mott-Schottky relationship has been derived under the assumption that the capacitance of any additional surface layer (e.g. the Helmholtz-layer) is sufficiently large to be neglected ( $C_L \gg C_{sc}$ ), and any potential drop



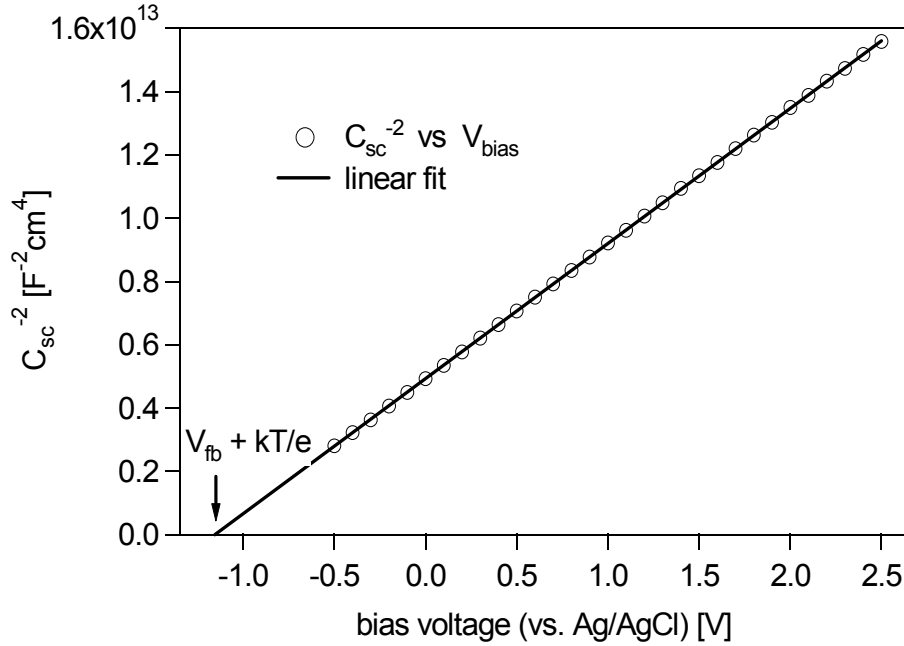
**Figure 5.20:** Interface capacitance,  $C_i$ , and resistance,  $R_i$ , extracted by the circuit models (a) ( $V_{bias} > -0.2V$ ) and (b) ( $V_{bias} \leq 0.2V$ ) as a function of the applied bias voltage,  $V_{bias}$ . The solid line represents the fit of the capacitance  $C_i$  by the Mott-Schottky equation for ideal Schottky barriers using Eq. (5.64).

occurs mainly in the depletion region of the semiconductor ( $|\phi_{sc}| \gg |\phi_L|$ ). Especially for highly doped semiconductors and dielectric layers like oxides or organic functionalizations, these requirements are not met and there is a notable potential drop over the surface layer. De Gryse et al. have calculated the relationship between the observable  $C_i^{-2}$  and the external bias  $V_{bias}$  for the general case of an additional surface layer with a voltage-independant capacitance,  $C_L$  [De Gryse, 1975]. The linear dependence of  $C_i^{-2}$  on  $V_{bias}$  is still maintained, but the intersection  $V_0$  with the voltage axis is shifted according to

$$V_0 = V_{fb} + \frac{kT}{e} - \frac{eN_D\epsilon_{sc}\epsilon_0}{2C_L^2}. \quad (5.65)$$

However, the slope of the Mott-Schottky plot is not affected by the additional capacitance  $C_L$ , and the density of ionized donors  $N_D$  can still be extracted correctly. Thus, the following conclusions can be drawn:

- It cannot be concluded from a linear Mott-Schottky dependence that the potential drop over additional surface layers is negligible, as often assumed in the literature.
- A non-linearity in the Mott-Schottky relation cannot be caused by additional layers with voltage-independant capacitances covering the surface .



**Figure 5.21.:** Mott-Schottky plot of the space charge capacitance,  $C_{sc}$ . The intersection of the linear extrapolation with the x-axis ( $1/C_{sc}^2 = 0$ ) yields the flatband voltage of  $V_{fb} = -1.18V$ . From the slope,  $N_D$  can be calculated to  $N_D = 3.2 \cdot 10^{18} cm^{-3}$ .

- The Mott-Schottky plot does not allow the correct determination of  $V_{fb}$  unless  $C_L$  is known. However, the shift or error in  $V_{fb}$  depends linearly on the doping ratio corresponding to  $-\frac{eN_D \epsilon_{sc} \epsilon_0}{2C_L^2}$  and becomes marginal for weakly doped semiconductors.

**(iv) Capacitive contribution of surface states and Fermi level pinning** The physical nature of surface states has been already discussed in Section 5.1.6. According to Nicollian and Goetzberger, their capacitive contribution can be considered by a series connection of the surface state capacitance,  $C_{ss}$ , and resistance,  $R_{ss}$ , in parallel to the space charge layer capacitance [Nicollian & Goetzberger, 1967]. Both,  $C_{ss}$  and  $R_{ss}$ , are frequency independent but depend strongly on the relative position of the electronic level of the surface state  $E_{ss}$  to the Fermi level  $E_F$ . As  $C_{ss}$  results from a change in charge of the surface states, it is only significant under the condition that the Fermi level at the surface is near the surface state level  $E_{ss}$ .

The contribution of the surface states to the system impedance can also be considered by a frequency dependent parallel capacitance and conductance, and the total capacitance of the interface is then described by

$$C_i = C_{sc} + \frac{C_{ss}}{1 + \omega^2 \tau^2}, \quad (5.66)$$

## 5. Physical Chemistry of the GaN/Electrolyte Interface

---

where  $\tau$  is the characteristic time constant of the surface state defined by the product of  $C_{ss}$  and  $R_{ss}$  [Nicollian & Goetzberger, 1965]. Thus, the capacitive contribution of the surface states is only relevant at (i) low frequencies ( $\omega \lesssim 1/\tau$ ), and (ii) for a small range of applied bias voltage when  $E_F$  is close to  $E_{ss}$ .

For high surface state densities,  $N_{ss}$ , the surface states further contribute considerably to the potential drop in the Helmholtz layer. A pinning of the surface Fermi level is observed for  $E_F$  being close to  $E_{ss}$  and the control of the band bending in the semiconductor by an external potential is limited (q.v. Section 5.1.6).

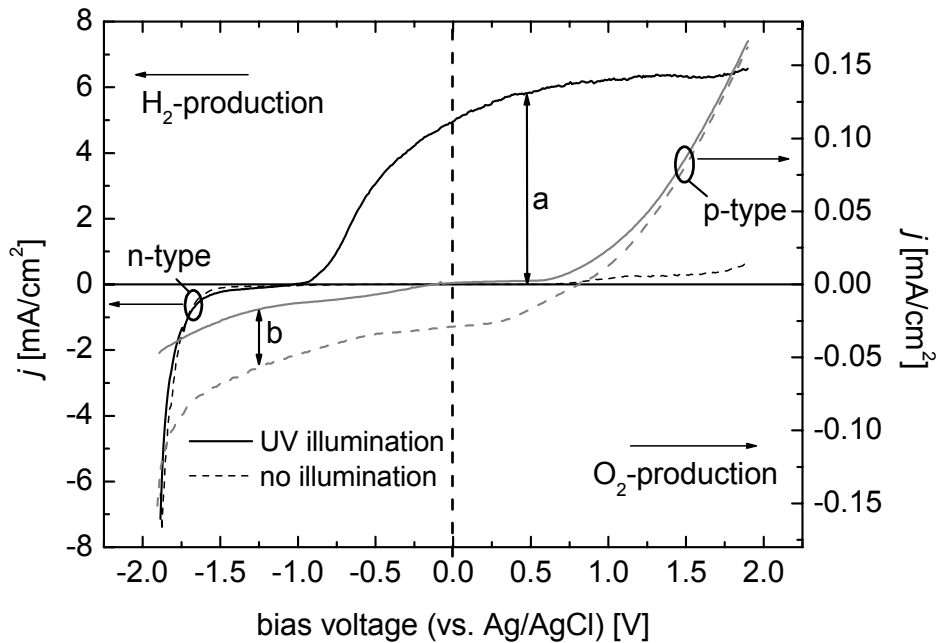
The capacitive contribution of surface states can often be separated from  $C_{sc}$  by their influence on the impedance spectra at low frequencies. If no separation is possible, a deviation in the otherwise linear  $C_i^{-2}$  versus  $V_{bias}$  plot is observed over the small voltage range corresponding to  $E_F$  being close to  $E_{ss}$ . Surface states showing a distribution in energy may contribute over a wider potential region to the interface capacitance and no linear dependence of  $C_i^{-2}$  on  $V_{bias}$  is expected.

For GaN and AlGaIn surfaces, surface donor states have been proposed by various groups to explain the 2DEG formation in GaN/AlGaIn/GaN and AlGaIn/GaN heterostructures [Ibbetson, 2000], [Jogai, 2003], [Koley & Spencer, 2005]. Either a single surface donor with discrete ionization energy ( $E_C - E_{ss} = 1.65$  eV) or a distribution of states ( $E_C - E_{ss} = 1.0 - 1.8$  eV) was suggested to explain the 2DEG carrier densities obtained for AlGaIn barriers of different thickness [Ibbetson, 2000], [Koley & Spencer, 2005]. However, according to Ref. [Shockley & Read, 1952], the characteristic time constants  $\tau$  for the exchange of electrons with the conduction band are very large for such deep surface states. Hence, a capacitive contribution is not expected.

No indication of an electrical contribution of the surface states is noticed in the impedance spectra and the Mott-Schottky plots are perfectly linear. Hence, a contribution of the surface states to the interface capacitance is excluded for the investigated GaN and AlGaIn/electrolyte interfaces.

**(v) Non-uniform distribution of donors** A considerable variation of the donor density perpendicular to the surface results in a non-linear Mott-Schottky relation, as the slope  $d(1/C_{sc}^2)/dV_{bias}$  for a certain potential is depending on the donor concentration in a depth corresponding to the width of the depletion layer  $W(V_{bias})$  [Sze, 1981]. Furthermore, no flatband conditions can be established near the surface. For a non-uniform distribution of donors parallel to the surface, a simple linear Mott-Schottky relation is not expected either [Gomes & Cardon, 1982]. As the Mott-Schottky plot 5.21 shows a perfect linear relation, a uniform distribution of donors can be assumed.

In conclusion, most deviations from the ideal Schottky barrier approximation required for a correct extraction of  $V_{fb}$  and  $N_D$  from Mott-Schottky plots can be ruled out or easily accounted for by adequate equivalent circuits for the conducted experiments with GaN electrodes. However,

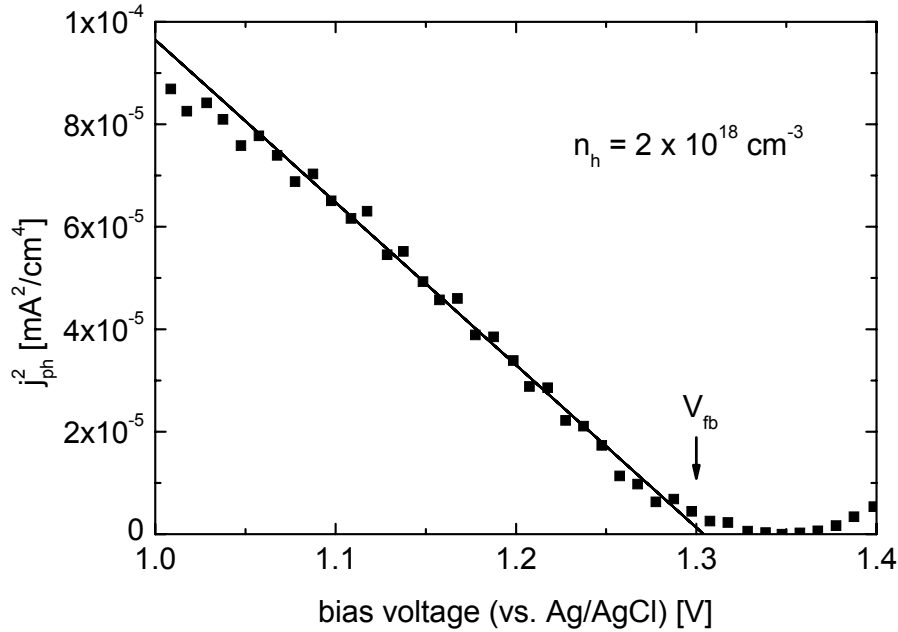


**Figure 5.22:** Current density,  $j$ , over the interface to the electrolyte for an n-type and a p-type MBE grown GaN electrode versus the applied bias voltage  $V_{bias}$  [Zaus, 2004]. The arrows a and b denote the photo-activated contribution for the n-type and p-type electrode, respectively.

the influence of additional surface layers for the determination of the flatband voltage  $V_{fb}$  from capacitance measurements can never be excluded.

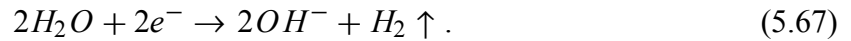
### 5.3.2 Photoelectrochemical Characterization of GaN Electrodes

In this section, the electrochemical characterization of GaN electrodes under UV illumination is described. The main objective was the determination of the flatband voltage of n- and p-type GaN surfaces by the photocurrent method. A 0.5 M KOH solution at pH 13.6 was used as an electrolyte. A high-pressure xenon lamp was utilized for UV illumination. In Figure 5.22, the current over the interface of an n-type and p-type GaN electrode to the electrolyte is shown for different external bias voltages,  $V_{bias}$ , and current densities with and without UV illumination are compared. For the n-type GaN electrode, an anodic photocurrent is observed. At anodic bias potentials the semiconductor is in depletion. Holes that are photo-generated in the depletion region are driven to the GaN/electrolyte interface by the band bending and consumed at the interface to the electrolyte by one of two possible reactions: production of oxygen or oxidation of the GaN to  $\text{Ga}_2\text{O}_3$ , as described by Eqs. (5.58) and (5.61), respectively. At cathodic bias voltages close to flatband conditions, the electron density at the interface increases and the



**Figure 5.23:** Photocurrent of a Mg-doped p-type GaN-electrode ( $n_h = 2 \times 10^{18} \text{ cm}^{-3}$ ). A flatband-voltage of  $V_{fb} = 1.31 \text{ V} \pm 0.02 \text{ V}$  is extracted from the extrapolation of the linear region of the  $j_{ph}^2$  vs  $V_{bias}$  plot.

production of hydrogen is observed. In alkaline solutions, the hydrogen production is better described by

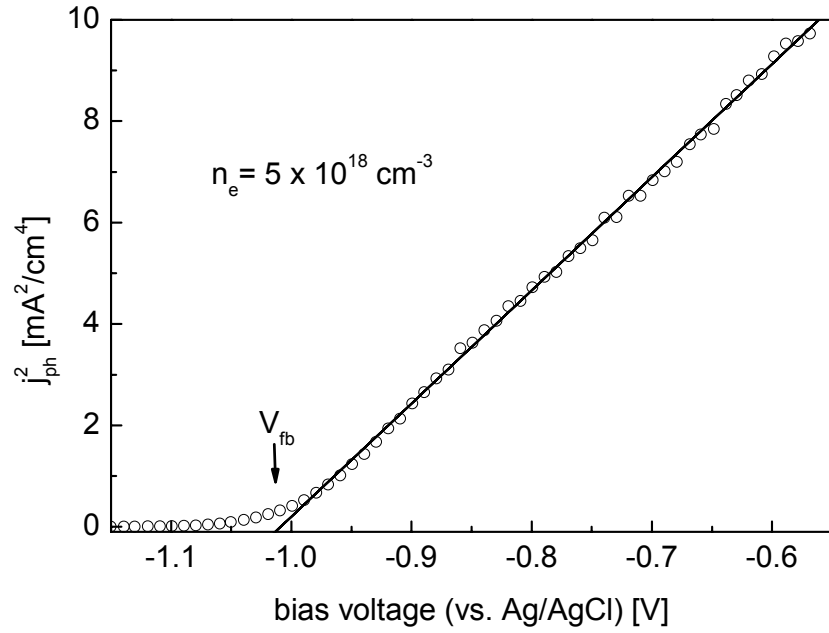


As electrons are the majority carriers in n-type semiconductors, this process is more or less independent of the density of photogenerated electron-hole pairs and can be observed with and without UV illumination. For p-type GaN, holes are the majority carriers and the dependence on UV illumination is inverted. Whereas the cathodic production of hydrogen is strongly depending on the amount of photo-generated electrons, the anodic surface reactions are independent of the UV illumination.

As discussed in Section 5.1.5, a linear dependence of  $j_{ph}^2$  on  $V_{bias}$  exists for conditions close to the flatband situation. From this linear region, the flatband voltage  $V_{fb}$  can be extracted by linear extrapolation from the intersection with the V-axis. Figure 5.23 shows the photocurrent data for a Mg-doped p-type GaN electrode. The hole density was determined by Hall-measurements to  $n_h = 2 \times 10^{18} \text{ cm}^{-3}$  at room temperature. A flatband voltage of  $V_{fb} = 1.31 \text{ V} \pm 0.02 \text{ V}$  relative to the Ag/AgCl reference electrode was extracted from the data.

The relation of the photocurrent and the applied bias voltage for an n-type GaN electrode ( $n_e \approx 5 \times 10^{18} \text{ cm}^{-3}$ ) is shown in Figure 5.24. A flatband voltage of  $V_{fb} = -1.02 \text{ V} \pm 0.02 \text{ V}$  is obtained from the plot.



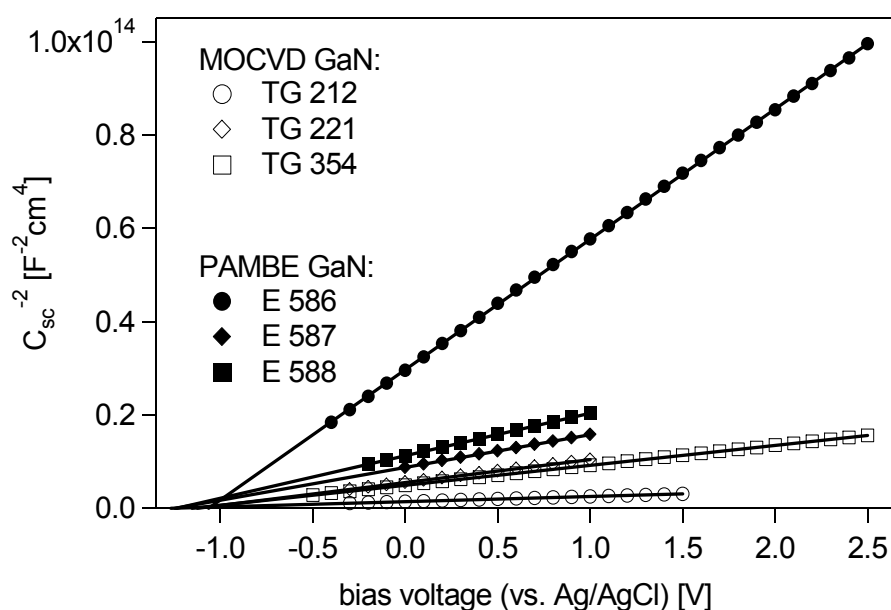


**Figure 5.24:** Photocurrent of a Si-doped n-type GaN-electrode ( $n_e = 5 \times 10^{18} \text{ cm}^{-3}$ ). The determined flatband voltage is  $V_{fb} = -1.02 \text{ V} \pm 0.02 \text{ V}$ .

It should be noted that the given values for  $V_{fb}$  have been measured in an alkaline solution at pH 13.6. A direct comparison with the  $V_{fb}$  obtained from the impedance spectroscopy experiments at pH 7 is not possible, as  $V_{fb}$  is strongly depending on the pH of the solution.

In the following, the main requirements for a correct determination of the flatband voltage from photocurrent measurements are summarized:

- (i) The photo-generation rate must be constant throughout the depletion layer to ensure the linear relation between the photocurrent and the depletion layer width. This requirement can be assumed as met if the depletion width  $W$  is much smaller than the absorption length  $\alpha^{-1}$  ( $\alpha W \ll 1$ ) for the irradiated spectrum. For  $|V_{bias} - V_{fb}| < 0.4 \text{ V}$ , which corresponds to the linear region of the  $j_{ph}^2$  vs.  $V_{bias}$  plots in Figures 5.23 and 5.24, the width of the depletion layer for a doping of  $2 \times 10^{18} \text{ cm}^{-3}$  is smaller than 15 nm. As the absorption length  $\alpha^{-1}$  in GaN for photons with an energy larger than the bandgap is around 100 nm and slowly decreasing for smaller wavelengths [Muth, 1997], the condition  $\alpha W \ll 1$  holds.
- (ii) All electrons and holes that are photo-generated in the depletion layer contribute to the photocurrent. The photo-generation of the electron-hole pairs is the current-limiting process. All contributions from carriers generated outside of the depletion layer can be neglected.



**Figure 5.25:** Mott-Schottky plots of MOCVD and PAMBE grown n-type GaN-electrodes with different donor concentrations.

- (iii) The applied external bias voltage drops mainly over the semiconductor depletion layer. If this is not the case, the depletion width  $W$  does not follow the square root dependence on  $V_{bias}$  as given in Eq. (5.55).

In Section 5.3.4, the results for the flatband voltage of n- and p-type GaN electrodes obtained from photocurrent measurements are discussed together with the values extracted from impedance measurements and results reported in the literature.

### 5.3.3. Comparison of MOCVD and PAMBE Grown GaN Electrodes with Different Doping Densities

GaN electrodes with different densities of Si-donors were grown either by MOCVD or by PAMBE and were characterized electrochemically according to Section 5.3.1. Prior to the measurements, the GaN surfaces were wet chemically treated in a 3:1 mixture of  $H_2SO_4/H_2O_2$  to remove organic contaminants, as described in Section 3.2.2. An exemplary Mott-Schottky plot for the n-type GaN electrodes prepared from different samples is presented in Figure 5.25. All Mott-Schottky plots allowed excellent linear fits and the extracted flatband voltages and doping densities are given in Table 5.1. All examined GaN-surfaces exhibit comparable flatband voltages. However, some small discrepancies depending on the growth method and doping densities are obtained. Regarding the MOCVD grown GaN electrodes, a more negative flatband voltage is extracted for higher Si-concentrations, as can be seen in Figure 5.26, where  $V_{fb}$  is

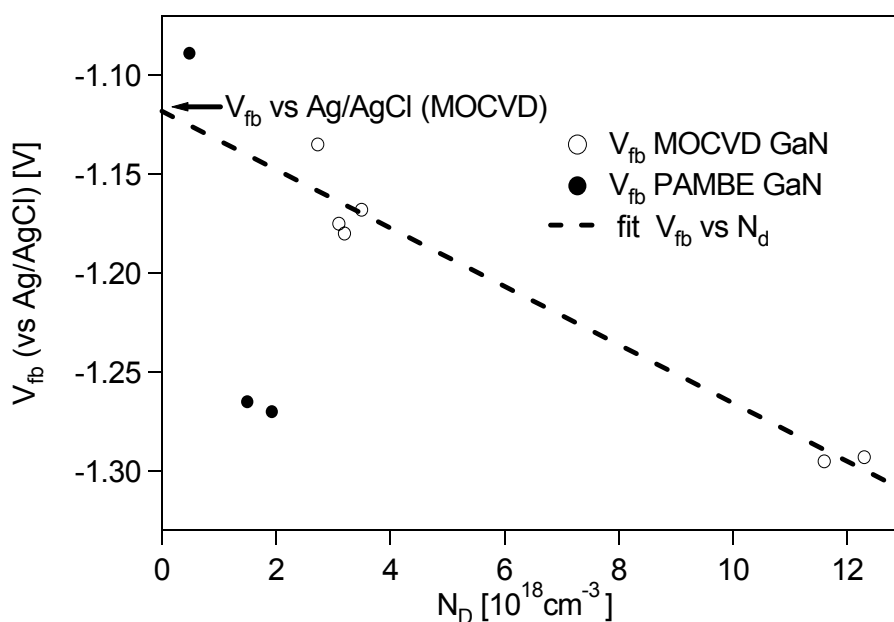
sample	growth method	donor density $N_D$ [ $\text{cm}^{-3}$ ]	flatband voltage $V_{fb}$ [V]
TG 212 G	MOCVD	$(1.16 \pm 0.1) \times 10^{19}$	$-1.30 \pm 0.01$
TG 212 K	MOCVD	$(1.23 \pm 0.1) \times 10^{19}$	$-1.29 \pm 0.01$
TG 221 E	MOCVD	$(2.7 \pm 0.1) \times 10^{18}$	$-1.14 \pm 0.01$
TG 221 L	MOCVD	$(3.1 \pm 0.1) \times 10^{18}$	$-1.18 \pm 0.01$
TG 354 B	MOCVD	$(3.5 \pm 0.1) \times 10^{18}$	$-1.17 \pm 0.01$
TG 354 E	MOCVD	$(3.2 \pm 0.1) \times 10^{18}$	$-1.18 \pm 0.01$
E 586	PAMBE	$(4.8 \pm 0.1) \times 10^{17}$	$-1.09 \pm 0.01$
E 587	PAMBE	$(1.9 \pm 0.1) \times 10^{18}$	$-1.27 \pm 0.01$
E 588	PAMBE	$(1.5 \pm 0.1) \times 10^{18}$	$-1.27 \pm 0.01$

**Table 5.1:** Flatband voltage  $V_{fb}$  and donor density  $N_D$  for MOCVD and PAMBE grown n-type GaN electrodes extracted from Mott-Schottky plots. The given errors are only corresponding to the accuracy of serial measurements. No systematic errors of the measurement technique or setup are included.

plotted versus  $N_D$ . This trend could be caused by either (i) a different surface chemistry - but it is very unlikely that Si concentrations even as high as  $10^{19} \text{ cm}^{-3}$  have an influence on the surface reactions, or (ii) additional surface layers. From XPS analysis of GaN it is known, that a thin native oxide layer is present on the surface (q.v. Section 5.2). As mentioned in Section 5.3.1, the influence of an additional surface layer on the extracted flatband voltage cannot be prevented and a shift between the real  $V_{fb}^{\text{real}}$  and the extracted  $V_{fb}^{\text{ext}}$  towards more negative  $V_{fb}$  is obtained. This shift depends on the doping density according to

$$V_{fb}^{\text{ext}} = V_{fb}^{\text{real}} - \frac{eN_D \epsilon_{sc} \epsilon_0}{2C_L^2}, \quad (5.68)$$

were  $C_L$  is the serial capacitance of the surface oxide layer. Under the assumption of identical surface chemistry and an equal oxide layer for the examined MOCVD GaN electrodes, the real flatband voltage  $V_{fb}$  and the capacitance of the oxide  $C_L$  can be obtained by a linear fit of  $V_{fb}^{\text{ext}}$  vs.  $N_D$ . From the data presented in Figure 5.26, a corrected flatband voltage of  $V_{fb} = -1.12 \pm 0.02 \text{ V}$  can be calculated. The corrected  $V_{fb}$  is utilized for n-type GaN in all further discussions. The capacitance,  $C_L$ , of the surface oxide is derived to  $C_L = 2.2 \mu\text{F cm}^{-2}$ . The thickness of the native surface oxide layer on MOCVD-grown GaN was determined in Ref. [Baur, 2005] by X-ray reflectivity measurements to  $10 \pm 2 \text{ \AA}$ . Assuming the dielectric constant of  $\beta\text{-Ga}_2\text{O}_3$  ( $\epsilon_{\text{Ga}_2\text{O}_3} = 3.57$  [Rebien, 2002]), a comparable capacitance of  $3.1 \mu\text{F cm}^{-2}$  is obtained. As only three different PAMBE samples have been analyzed, similar estimations of  $C_L$  and a corrected  $V_{fb}$  are not really meaningful for PAMBE GaN. Assuming an equal  $V_{fb}$  for MOCVD and PAMBE GaN, a thicker native surface oxide is obtained on PAMBE grown GaN-surfaces.

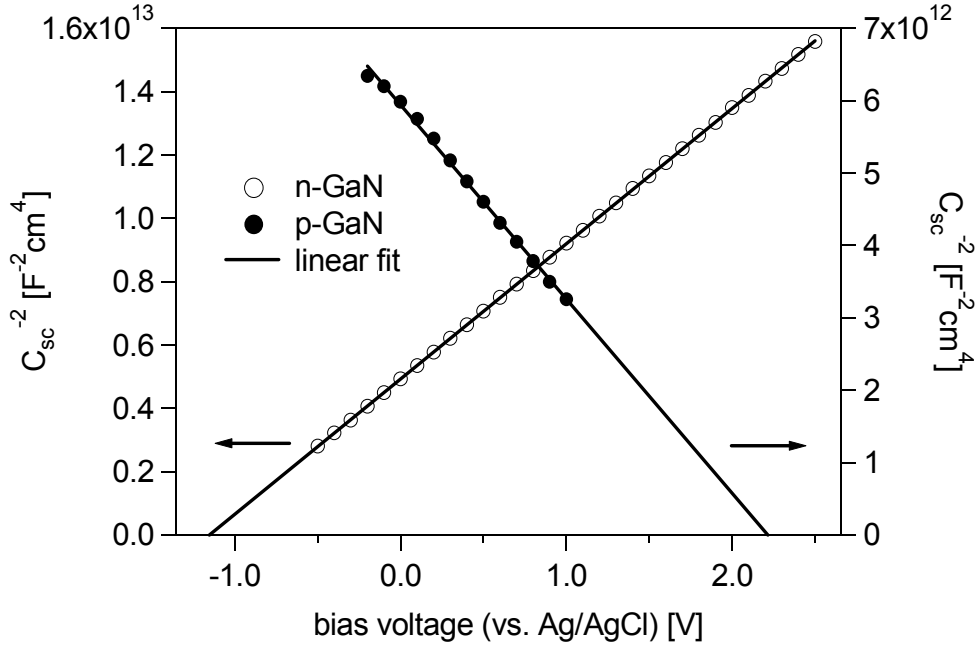


**Figure 5.26:** Flatband voltages  $V_{fb}$  for n-GaN extracted from Mott-Schottky plots versus the doping ratio  $N_D$ . From the linear fit, a real  $V_{fb}$  of  $-1.12 \pm 0.02$  V can be obtained for MOCVD GaN.

### 5.3.4. Determination of the Energetic Levels of the Band Edges at the GaN/Electrolyte Interface

As described in Section 5.1.3, the conduction band and valence band edges of a semiconductor at the interface to an electrolyte,  $E_{C,S}$  and  $E_{V,S}$ , can be obtained from measurement of the flatband potential in relation to the energetic level of a reference electrode, according to Eq. (5.47) and Eq. (5.48), respectively. For that, the assumption of fixed energetic positions at the interface relative to the electrolyte redox levels has to be fulfilled. If  $E_{C,S}$  and  $E_{V,S}$  are determined independently for an n- and p-type electrode, the bandgap,  $E_G$ , of the semiconductor can be determined under the assumption that both samples exhibit similar chemical surface behavior. In Figure 5.27 Mott-Schottky plots for an n- and p-type GaN electrode immersed into standard PBS buffer at pH 7 are shown. The capacitance  $C_{sc}$  of the Mg-doped p-type GaN was extracted from impedance spectroscopy data.

In the previous section, a flatband voltage of  $V_{fb} = -1.12 \pm 0.02$  V versus an Ag/AgCl reference electrode has been derived for n-type GaN. The used Ag/AgCl reference electrode is filled with 3 M KCl and has an electrochemical potential of  $U_{ref} = 210$  mV versus the SHE. For a Si-doping level between  $10^{18} \text{ cm}^{-3}$  and  $10^{19} \text{ cm}^{-3}$ , the Fermi level is close to the conduction band and  $\mu = E_C - E_F$  can be neglected within the accuracy of the experiment. With Eq. (5.47), the energetic position of the conduction band edge,  $E_{C,S}$ , at the interface to the

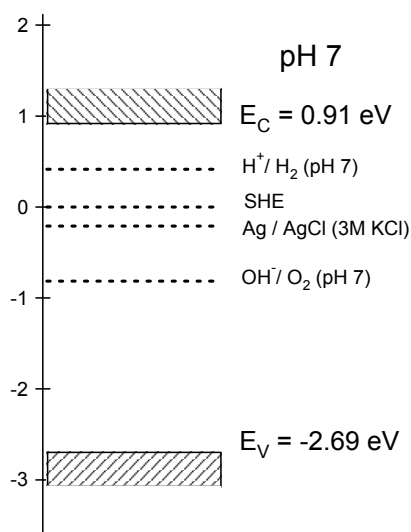


**Figure 5.27.:** Mott-Schottky plot for the space charge capacitance  $C_{sc}$  of n-type and p-type GaN. For p-type GaN, a flatband voltage of  $V_{fb} \approx -2.27 \pm 0.2$  V and a density of ionized acceptor atoms of  $N_A \approx 5 \cdot 10^{18} \text{ cm}^{-3}$  is determined.

electrolyte is calculated to  $E_{C,S} = 0.91 \pm 0.02$  eV (vs. SHE) at pH 7 in standard PBS buffer. Note that  $E_{C,S}$  is strongly influenced by the ionic composition of the electrolyte.

From the Mott-Schottky plot of p-type GaN, a density of ionized acceptors of  $N_A \approx 5 \times 10^{18} \text{ cm}^{-3}$  was derived and the flatband voltage was determined to  $V_{fb} = 2.27 \pm 0.2$  V. However, the capacitive contribution of an oxide layer that may be present on the surface cannot be excluded and the corresponding shift in  $V_{fb}$  is considered in the given experimental error. The energy difference between the Fermi level and the valence band  $\mu^* = E_F - E_V$  is estimated to  $\mu^* = 210$  mV from the ionization energy of the Mg-acceptors [Götz, 1999]. By means of these results, the energetic position of the valence band edge  $E_{V,S}$  can be derived with Eq. (5.48) to  $E_{V,S} = -2.69 \pm 0.2$  eV (vs. SHE) at pH 7. In Figure 5.28 the determined conduction and valence band edges at the interface are shown versus the SHE. From the obtained relative energetic positions of band edges, the bandgap of GaN can be calculated to  $E_G = 3.60 \pm 0.2$  eV. This result is in good agreement with the bandgap of  $E_G = 3.39$  eV measured by optical absorption [Maruska & Tietjen, 1969].

The results for the flatband voltage  $V_{fb}$  and the energetic position of the electronic levels of GaN,  $E_{C,S}$  and  $E_{V,S}$ , that have been obtained by the impedance measurements are in good agreement with the findings published by other groups for GaN and acquired by an equivalent method. For the energetic position of the conduction band  $E_{C,S}$  at pH 7, Kocha et al. have found a value of  $E_{C,S} = 0.89$  eV [Kocha, 1995], Huygens and co-workers reported  $E_{C,S} = 0.96$  eV



**Figure 5.28:** Energetic position of the conduction band edge  $E_{C,S}$  and valence band edge  $E_{V,S}$  at the interface to the electrolyte relative to the redox level of the SHE.

[Huygens, 2000], and Beach et al. determined a value of  $E_{C,S} = 0.94$  eV [Beach, 2003]. The energies are given relative to the redox level of the SHE. The quoted literature results have all been obtained from n-type GaN electrodes by impedance measurements, and the published valence band position were calculated from  $E_{C,S}$  and  $E_G$ . No results obtained by impedance spectroscopy from p-type GaN electrodes have been published so far. Furthermore, the possible influence of a surface oxide layer on the determined  $V_{fb}$  is not discussed in the literature for GaN electrodes.

However, a strong influence of the measurement method on the obtained flatband voltage was found. In Section 5.3.2, the flatband voltage of an n-type and p-type GaN electrode at pH 13.6 was determined by photocurrent based measurements to  $-1.02$  V and  $1.31$  V versus the Ag/AgCl reference electrode, respectively. With a dependence of the surface potential on the pH concentration of  $56$  mV/pH, which is anticipated from Section 5.4, the band edges obtained from photocurrent experiments can be calculated to  $E_{C,S} = 0.44$  eV and  $E_{V,S} = -2.12$  eV vs. SHE at pH 7 by the procedure described above. Thus, a large discrepancy to the results obtained from impedance spectroscopy exists. Whereas the  $E_{C,S}$  obtained from n-type GaN electrodes is around half an electron volt lower in energy if determined from photocurrent measurements, the valence band edge  $E_{V,S}$ , which is determined from p-type electrodes, is around half an eV higher compared to impedance results. The bandgap calculated from the band edges is  $E_G = 2.57$  eV and around 1 eV smaller than the value obtained from impedance measurements. A similar trend has been observed by Beach et al., who reported energetic positions of  $E_{C,S} = 0.62$  eV and  $E_{V,S} = -2.12$  eV (vs. SHE at pH 7) determined from n- and p-GaN electrodes by the photocurrent method.

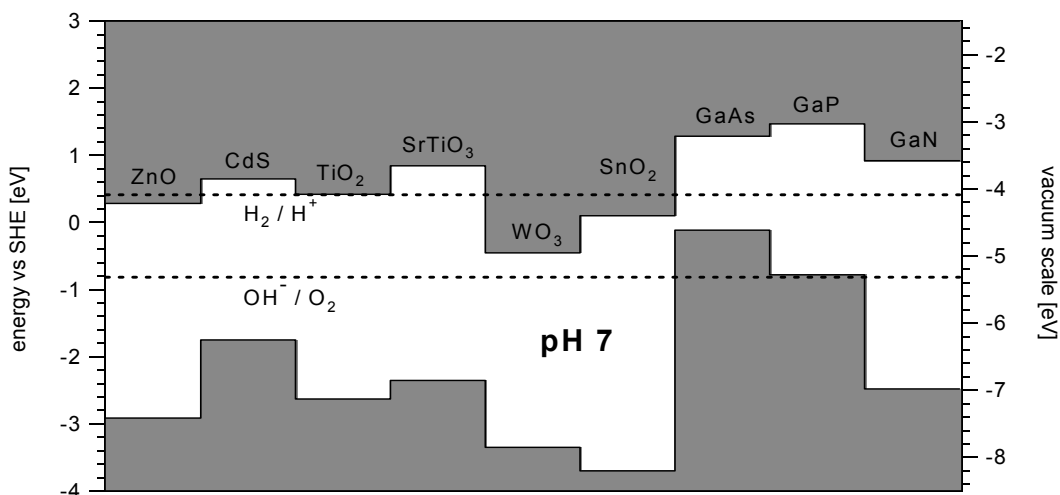
The observed discrepancy can originate from slow charge transfer kinetics at the interface between the semiconducting electrode and the electrolyte. If more minority carriers reach the interface as are consumed in the surface reactions, minority carriers are accumulated at the interface and the flatband potential is shifted. In case of an n-type semiconductor, the bias voltages  $V_{bias}$  are shifted to more positive values, in case of a p-type semiconductor to more negative values. Similar observations have been reported by Bansal and Turner for p-GaInP<sub>2</sub> electrodes [Bansal & Turner, 2000]. Furthermore, the photocurrent for the n-GaN electrode is related either to the production of oxygen or the oxidation of the GaN surface. The surface oxidation is in some equilibrium with the solvation of the built oxide by the hydroxide ions of the strong basic environment.  $V_{fb}$  can only be determined correctly if the thickness of the surface oxide remains small and the surface composition and chemistry remain constant during the experiment.

In conclusion, the determination of the energetic position of the conduction band edge  $E_{C,S}$  from impedance measurements at n-type GaN was possible and the observed results are comparable to values reported in the literature. In addition, the surface level of the valence band edge,  $E_{V,S}$ , was successfully extracted for Mg-doped p-type GaN electrodes, and the calculated bandgap  $E_G$  is close to reported values from optical absorption spectroscopy. Thus, the Mg-doped p-type and Si-doped n-type GaN electrodes exhibit similar chemical surface behavior under the measurement conditions applied. Care must be taken when band edge levels are obtained from photocurrent measurements, as slow charge transfer kinetics can cause interface charging, resulting in a significant shift of the obtained energy levels. Hence, band edge levels at the interface of GaN to an electrolyte determined by impedance spectroscopy and Mott-Schottky evaluation show a much higher accuracy. Still a shift is observed in the evaluated  $V_{fb}$  due to the influence of additional surface layers, but their contribution is negligible for weakly doped electrodes.

At pH 7, the redox levels for the reduction of H<sup>+</sup> to H<sub>2</sub> ( $\phi_{H^+/H_2} = -0.413$  V) and the oxidation of OH<sup>-</sup> to O<sub>2</sub> ( $\phi_{OH^-/O_2} = 0.816$  V) are located between the obtained energetic positions of the band edges  $E_{C,S}$  and  $E_{V,S}$  at the interface (see Figure 5.28). Thus, GaN electrodes are suitable for the electrolysis of water in electrochemical cells, and photoelectrolysis with n-type GaN electrodes should be possible without an external bias voltage. The anodic overpotential for the oxygen evolution reaction  $\eta_a = -eE_{V,S} - \phi_{OH^-/O_2}$  was determined to  $\eta_a = 1.87$  V at pH 7.

Like most other semiconductors that meet the requirements for an application in photoelectrolysis or electrochemical photovoltaics, which are mainly oxide semiconductors with bandgaps larger than 3 eV [Nozik & Memming, 1996], GaN shows only a poor absorption of the solar spectrum, and GaInN might be a more suitable candidate for solar energy conversion [Beach, 2003].

In Figure 5.29, the energetic band edge positions at the interface to an aqueous electrolyte are shown for various semiconductors in comparison to the investigated GaN electrodes and the redox levels for photoelectrolysis at pH 7.



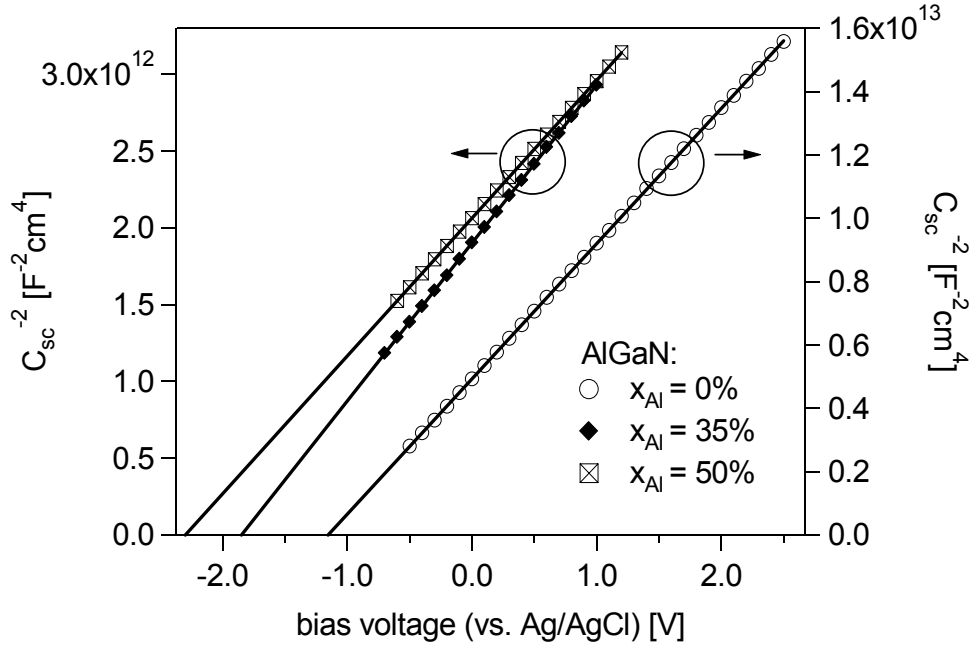
**Figure 5.29.:** Energetic position of the conduction band and valence band edge of different semiconductors in contact with an electrolytic solution at pH 7. The electronic positions are given versus the vacuum scale (right axis) and on the electrochemical scale versus the SHE (left axis).

### 5.3.5. Energetic Position of the Band Edges at the AlGaN/Electrolyte Interface

In addition to the discussed GaN electrodes, MBE-grown n-type  $\text{Al}_x\text{Ga}_{1-x}\text{N}$ -electrodes with Al concentrations of  $x_{\text{Al}} = 0.35$  and  $0.5$  have been analyzed by electrochemical impedance spectroscopy in standard PBS buffer at pH 7. Fitting with the equivalent circuit model (b) produced excellent approximations of the measured data. The interface capacitance  $C_i$  extracted from this model is interpreted as the capacitance of the semiconductor space charge layer  $C_{sc}$ . Any contribution of additional surface layers is neglected, as it cannot be separated from the dominant space charge layer contribution. The extracted data for  $1/C_{sc}^2$  of the AlGaN electrodes versus  $V_{bias}$  is presented in Figure 5.30 along with the data for GaN, and good agreement with the behavior of an ideal semiconductor space charge region is found. Ionized donor densities of  $N_D = 1.3 \times 10^{19} \text{ cm}^{-3}$  and  $N_D = 1.5 \times 10^{19} \text{ cm}^{-3}$  were extracted for Al-contents of  $x_{\text{Al}} = 0.35$  and  $0.5$ , respectively.

A linear extrapolation of the Mott-Schottky plots yield a flatband voltage of  $V_{fb}^{x=0.35} = -1.87 \text{ V}$  for an Al-concentration of  $x = 0.35$  and  $V_{fb}^{x=0.5} = -2.32 \text{ V}$  for  $x = 0.5$ . For GaN, the value of  $V_{fb} = -1.12 \text{ V}$  established in Section 5.3.3 is used in the following discussion. By means of Eq. (5.47), the energetic position of the conduction band at the AlGaN/electrolyte interface  $E_{C,S}$  is obtained from  $V_{fb}$  relative to the redox potential of the SHE. Again,  $\mu = E_C - E_F$  can be assumed to be negligible within the experimental accuracy. The results for  $E_{C,S}$  are summarized in Table 5.2. The position of the valence band edge  $E_{V,S}$  is then calculated





**Figure 5.30:** Mott-Schottky plots for AlGaIn-electrodes with different Al content  $x$ . By linear extrapolation, flatband voltages of  $V_{fb}^{x=0.35} = -1.87$  V for  $x = 0.35$  and  $V_{fb}^{x=0.5} = -2.32$  V for  $x = 0.5$  are obtained.

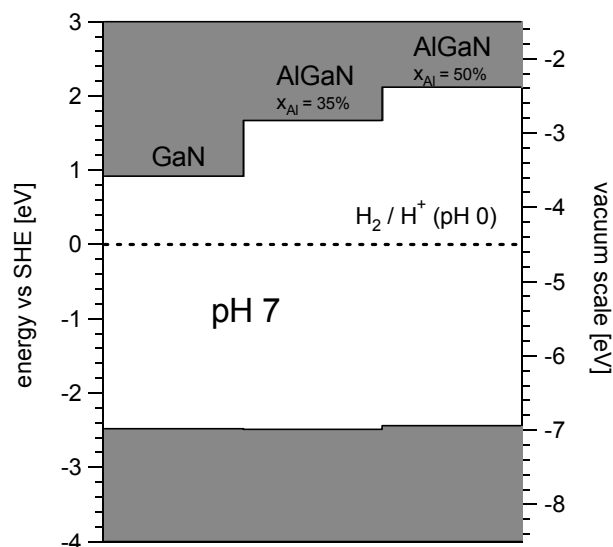
from  $E_{C,S}$  with knowledge of the bandgap  $E_G$  of the semiconductor. The required bandgap  $E_{G,AlGaIn}$  of the ternary  $Al_xGa_{1-x}N$  alloy in wurtzite structure has been experimentally shown to obey a quadratic dependence on the Al molar fraction  $x$  given by

$$E_{G,AlGaIn}(x) = x \cdot E_{G,AlN} + (1 - x) \cdot E_{G,GaN} - b \cdot x \quad (5.69)$$

with a bowing parameter  $b$  [Koide, 1987], [Brunner, 1997]. For the evaluation of the  $E_{G,AlGaIn}$ , values of  $E_{G,AlN} = 6.2$  eV [Yim, 1973] and  $E_{G,GaN} = 3.39$  eV [Maruska & Tietjen, 1969] have been used for the bandgap of AlN and GaN, respectively, and a bowing parameter of  $b = 1.0$  eV was assumed [Koide, 1987]. The calculated  $E_{G,AlGaIn}$  and  $E_{V,S}$  for the different Al concentrations can be found in Table 5.2. An illustration of the energetic position of

$x_{Al}$	flatband voltage $V_{fb}$ [V]	$E_G$ [eV]	$E_{C,S}$ vs. SHE [V]	$E_{V,S}$ vs. SHE [V]
0	$-1.12 \pm 0.02$	3.39	0.91	-2.48
0.35	$-1.87 \pm 0.05$	4.15	1.66	-2.49
0.5	$-2.32 \pm 0.05$	4.55	2.11	-2.44

**Table 5.2:** Flatband voltage,  $V_{fb}$ , and energetic positions  $E_{C,S}$  and  $E_{V,S}$  of AlGaIn electrodes with different Al molar fraction,  $x$ . The position of  $E_{V,S}$  is calculated directly from  $E_{C,S}$  by subtracting the bandgap energy,  $E_G$ .



**Figure 5.31.:** Illustration of the conduction and valence band edge for  $\text{Al}_x\text{Ga}_{1-x}\text{N}$  alloys with different Al-content. The electronic positions are given versus the vacuum scale (right axis) and on the electrochemical scale versus the SHE (left axis).

the band edges is given in Figure 5.31 with respect to the SHE potential and the vacuum level. The observed locations of the valence band maxima agree fairly well and seem to be independent of the Al molar fraction  $x$  of the examined electrode. Similar observations have been reported in the literature, for example for the Schottky barrier height of Au on III-V and II-VI semiconductors. McCaldin and co-workers have reported that the energy difference between the valence band edge and the Fermi level of Au is independent of the cation and depends primarily on the particular anion for a large number of cubic and hexagonal III-V and II-VI semiconductors. Furthermore, a clear relation between the position of the valence band edge and the Pauling electronegativity of the semiconductor anion is observed [McCaldin, 1976a], [McCaldin, 1976b]. An analogous observation was reported by Swank for the solid-vacuum interface of different II-VI semiconductors, where the photoelectric threshold voltage is defined mainly by the chalcogen, and a linear dependence of the photoelectric threshold voltage on the chalcogen electronegativity was found [Swank, 1967].

The valence band offset between GaN and AlN has been experimentally determined by different methods like XPS and photoluminescence, and widely varying values ranging from 0.15 eV to 1.4 eV have been reported [Rizzi, 1999], [Waldrop & Grant, 1996], [Westmeyer, 2006]. Vurgaftam and co-workers recently reviewed the experimental results of various groups for the conduction band offset between GaN and AlN. The large differences among the reported values were ascribed to differences in strain, defect density, and film stoichiometry among the investigated samples [Vurgaftman & Meyer, 2003]. Satpathy et al. have derived the Al-content

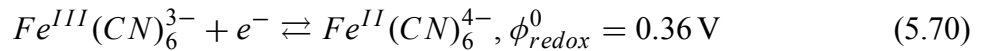
dependence of the valence band offset between GaN and  $\text{Al}_x\text{Ga}_{1-x}\text{N}$  by ab initio density-functional calculations, and magnitudes of 0.60 eV and 0.77 eV were given for  $x_{\text{Al}} = 0.35$  and 0.5, respectively [Satpathy, 2004]. The reported relation between the valence band offset and Al-concentration is not confirmed by the measurements presented here. However, it should be noted that the results reported here present the first data obtained by impedance spectroscopy measurements.

In contrast to the valence band edge position, no clear relation can be obtained between the electronegativity of the anion and the position of the valence band edge at the semiconductor/electrolyte interface for the series GaN, GaP, GaAs. The relative position of the band edges for these semiconductors at pH 7 are shown in Figure 5.29. The Pauling electronegativities of the anions N, P and As are 3.04, 2.19 and 2.18, respectively. However, the measured flatband voltage and thereby the position of the band edges is strongly dependent on the chemical equilibrium reactions at the semiconductor surface that affect the Helmholtz-voltage  $V_H$ , but the surface chemistry of GaN, GaP and GaAs is not expected to be similar.

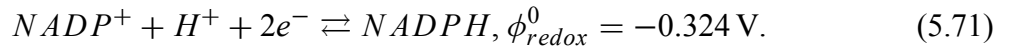
### 5.3.6. Influence of Different Buffer Solutions and Redox Ions on the Flatband Voltage

The influence of the buffer solution on the energetic band position at the solid/electrolyte interface was analyzed by means of impedance experiments and extraction of the corresponding flatband voltage. The utilized buffers are described as PBS, HEPES, and TRIS standard buffer solutions in Section 2.2.2. Each had a buffer concentration of 10 mM and was adjusted to a total ionic strength of 50 mM with sodium chloride. No influence of the buffer solution on the extracted  $V_{fb}$  was notable within the accuracy of the experiment, hence it is assumed that the various buffers do not react chemically with the GaN surface.

In addition, the influence of different redox couples on  $V_{fb}$  and the open circuit potential (ocp) were examined. For that purpose, 2 mM of iron-cyanide or of nicotinamide adenine dinucleotide phosphate ( $\text{NADP}^+$ ) were added to the standard PBS buffer at pH 7. Therewith, the redox level of the electrolyte was determined either by

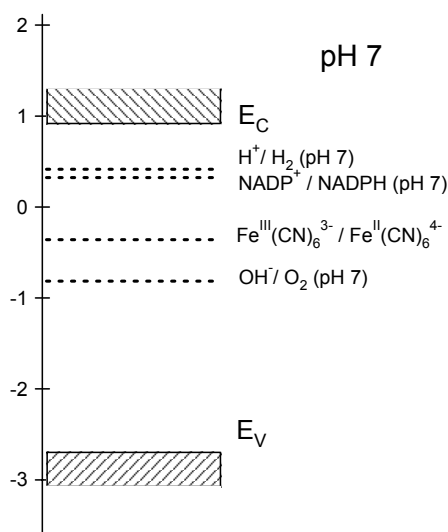


or



The energetic position of the redox levels relative to the GaN band edges is given in Figure 5.32.

Only a slight difference in  $V_{fb}$  was observed between the pure PBS buffer ( $V_{fb} = -1.18 \text{ V}$ ) and the buffers containing iron cyanide ( $V_{fb} = -1.19 \text{ V}$ ) or  $\text{NADP}^+/\text{NADPH}$  ( $V_{fb} = -1.20 \text{ V}$ ). Thus, no influence of the electrolyte redox level on the  $V_{fb}$  was obtained within the accuracy of the measurement. This is an important issue for the application of GaN gate layers in the ISFET devices discussed in Section 5.4.1, as the surface potential should only be determined by the concentration of the ion of interest and not by the redox potential of the electrolyte

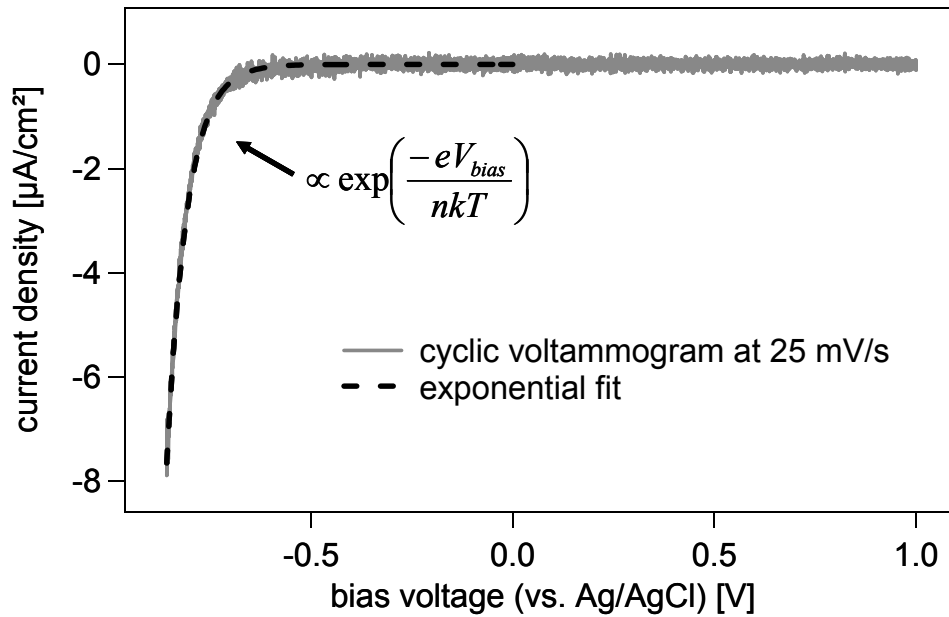


**Figure 5.32:** Redox levels of the iron cyanide and the  $\text{NADP}^+/\text{NADPH}$  redox couple versus the GaN band edges at the interface to the electrolyte.

in ion-sensitive applications. Analogous results have been reported by Huygens et al., who observed no change in  $V_{fb}$  upon the addition of the iron cyanide redox couple to the electrolyte [Huygens, 2000]. However, the Gerischer model assumes an equilibration of the semiconductor and the electrolyte Fermi levels by charge transfer over the interface and, therefore, a dependence of the ocp on the electrolyte redox level. Hence, the potential difference between the electrolyte Fermi level defined by the redox couple and the level of the reference electrode should be measured as the ocp of a semiconductor electrode. This assumption could not be confirmed for the measurements of the ocp at GaN electrodes. Comparable ocp were determined for iron cyanide ( $ocp = -0.17$  vs. Ag/AgCl) and  $\text{NADP}^+/\text{NADPH}$  ( $ocp = -0.18$  vs. Ag/AgCl) redox ions. As remarked by Morrison and discussed in Section 5.1.3, equilibrium due to charge transfer cannot always be assumed at the semiconductor/electrolyte interfaces, since the charge exchange rates can be extremely low, especially for wide bandgap semiconductors [Morrison, 1977]. It should be noted that this result of a non-equilibrium at the GaN/electrolyte interface regarding charge transfer has no consequence for measurements where an external voltage is applied.

### 5.3.7. Charge Transfer over the GaN/Electrolyte Interface

In Section 5.3.2, photocurrent measurements of GaN electrodes in basic solution (0.5 M KOH, pH 13.6) have already been discussed. Under UV illumination, current contributions from minority carriers are of major importance. Here, cyclic voltammetry was employed to study the charge transfer without illumination, which, for a wide-bandgap semiconductor at room



**Figure 5.33.:** Cyclic voltammogram of a MOCVD-grown GaN-electrode that has been chemically oxidized. The data were recorded with a scan speed of 25 mV/s. The cathodic current density showed the exponential behavior of a Schottky diode with an ideality factor of  $n = 1.7$ .

temperature, is restricted to majority carrier processes only. The experiments were performed in pure standard PBS buffer (pH 7) and with 2 mM of the iron-cyanide redox couple ( $\text{Fe}^{\text{III}}(\text{CN})_6^{3-} / \text{Fe}^{\text{II}}(\text{CN})_6^{4-}$ ) added (redox buffer).

### Cyclic Voltammetry in Standard PBS Buffer

In Figure 5.33, the cyclic voltammogram for a piranha-treated MOCVD-grown n-type GaN electrode is shown. For potentials larger than  $-0.6$  V no current flow is observed, and the electrode can be considered as ideally polarizable. It should be noted that the current density for the charging and discharging of the semiconductor/electrolyte interface is of the order of  $25 \text{ nA cm}^{-2}$  for the maximum capacitance of  $1 \text{ } \mu\text{F cm}^{-2}$  and cannot be resolved in the cyclic voltammetry experiment, as the peak-to-peak background noise is of the order of  $200 \text{ nA cm}^{-2}$ . At a bias potential below  $-0.6$  V, the cathodic current increases exponentially, as predicted by the Gerischer model, and  $\text{H}^+$  is reduced to  $\text{H}_2$  by the electrons transferred into the electrolyte according to Eq. (5.57) and forms hydrogen gas. The experimental values of the cathodic current density do not follow exactly the ideal behavior given by Eq. (5.51) of the Gerischer

model, but can be expressed as for the thermionic-emission current of a real Schottky-contact by

$$j_c^- \propto \exp\left(\frac{-eV_{bias}}{nkT}\right), \quad (5.72)$$

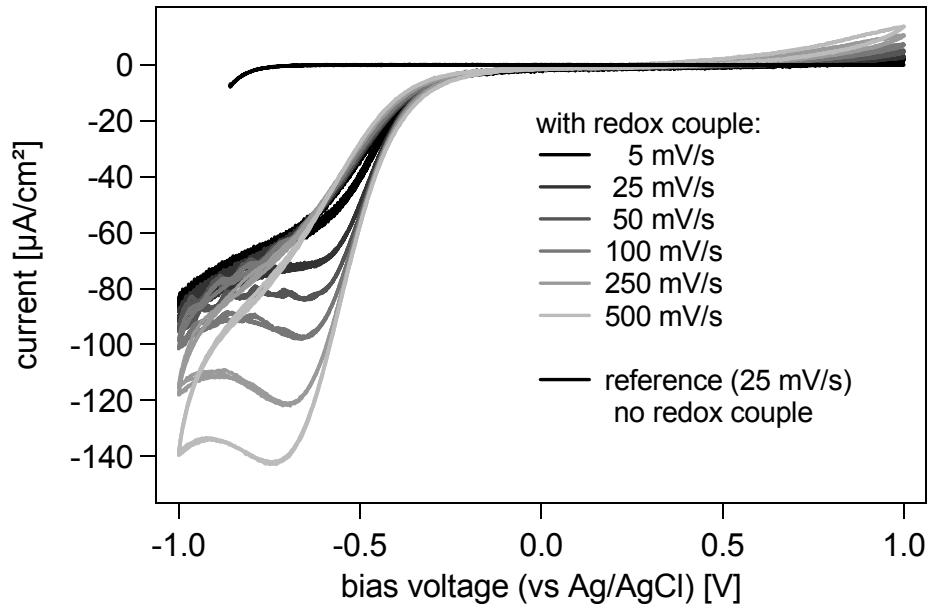
where  $n$  is the ideality factor [Sze, 1981]. A fit of the data presented in Figure 5.33 between 0 V and the lower switching potential of  $-0.85$  V reveals an ideality factor of  $n = 1.7$ . The analysis of a set of MOCVD and PAMBE grown n-type GaN electrodes mostly revealed ideality factors around  $n = 2$ , but exceptions with values up to  $n = 4$  have been found. No influence of the growth method was notable. For comparison, ideality factors ranging from  $n = 1.04$  to 2.6 have been reported for metal Schottky contacts on n-type GaN surfaces [Schmitz, 1996], [Kampen & Mönch, 1997], [Weidemann, 2005].

From the Gerischer model,  $n = 1$  is expected and the cathodic current density should change by one order of magnitude for a bias voltage variation of 60 mV. For a variety of semiconductor/electrolyte junctions the cathodic current increases exponentially with the electrode potential  $V_{bias}$ , but ideality factors much larger than  $n = 1$  are frequently found. This deviation from theory is mostly explained by electron transfer via surface states, but a clear understanding of the processes is still missing [Nozik & Memming, 1996]. Only a few systems obtaining  $n = 1$  have been reported in the literature, for example the junction of ZnO to a 10 mM solution of  $\text{KMnO}_4$  at pH 8.7 [Morrison, 1969].

A detailed discussion of effects beyond the thermionic-emission model that, hence, lead to ideality factors  $n > 1$ , can be found for example in Refs. [Rhoderick & Williams, 1988] or [Tung, 2001]. **Recombination** of electrons and holes in the semiconductor depletion region causes an additional recombination current, provided that enough minority carriers are available. For n-type GaN/electrolyte contacts, holes have to be injected from the electrolyte into the GaN valance band. As no appropriate redox ions were present for the discussed measurements, recombination can be excluded as a reason for the increased ideality factors. **Additional surface layers** lead to an increased ideality factor if a notable part of the applied bias potential drops across that layer (e.g. Section 5.3.1). For an interface without surface states, a simplified expression from Ref. [Rhoderick & Williams, 1988] yields

$$n(V_{bias}) = 1 + \frac{C_{sc}(V_{bias})}{C_L}. \quad (5.73)$$

As known from previous discussions in Sections 5.2 and 5.3.3, a native oxide layer is present on the investigated MOCVD-grown GaN electrodes, which exhibits a capacitance  $C_L$  of about  $2 \mu\text{F cm}^{-2}$ . For bias voltages between  $-0.4$  V and  $-0.8$  V, ideality factors between  $n = 1.3$  and 1.4 are calculated by means of Eq. (5.73). **Nonuniform barrier heights** along the GaN/electrolyte interface might be a further reason for the high ideality factors obtained [Tung, 2001], especially for a contact area as large as  $0.128 \text{ cm}^2$ . For metal Schottky contacts on n-type GaN, nonuniform barrier heights at the metal/GaN interface were suggested as the main reason for the high ideality factors in Refs. [Kampen & Mönch, 1997] and [Weidemann, 2005].

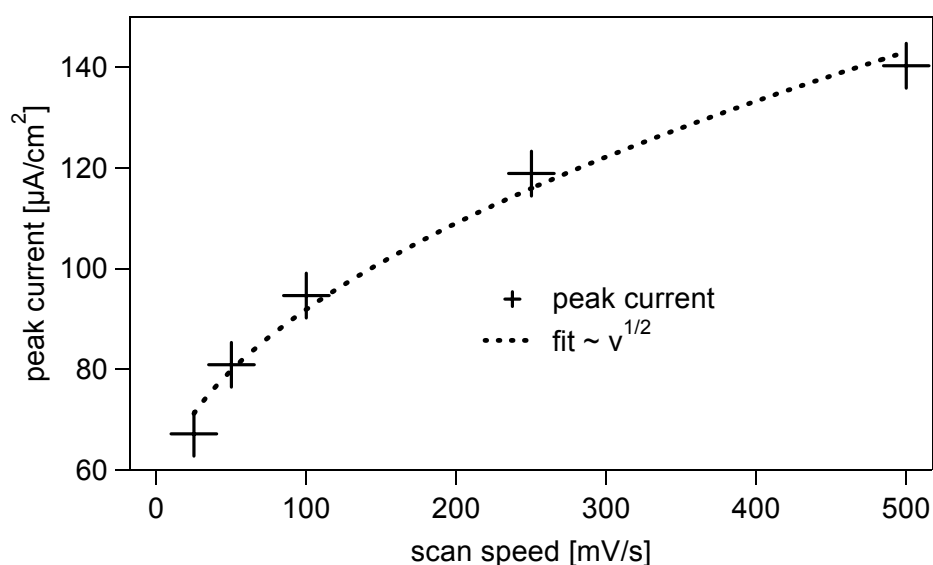


**Figure 5.34:** Cyclic voltammogram of an n-type GaN-electrode in redox buffer. The data were recorded at different scan speeds  $v$ . For comparison, a reference curve measured in standard buffer is given ( $v = 25$  mV/s).

### Cyclic Voltammetry in Redox Buffer

As described in Section 5.1.7, the current over the solid/liquid interface is always related to an oxidation or reduction reaction in which an electron or hole is accepted or emitted by the solid electrode. With the selective addition of a redox couple to the electrolyte, a reaction partner is present in the solution, which accepts or donates electrons at a distinct redox level. Here, the iron-cyanide redox couple with a redox level of  $\phi_{redox}^0 = 0.36$  V was used in a concentration of 2 mM. In Figure 5.34, cyclic voltammograms of an n-type GaN electrode recorded at different scan speeds,  $v$ , in redox buffer are presented. Four consecutive cycles are shown for each scan speed. A cyclic voltammogram taken in standard buffer at  $v = 25$  mV (q.v. Figure 5.33) is given as a reference.

For a potential sweep from 0 V to  $-1$  V, an exponential increase in the cathodic current is observed starting from  $-0.3$  V, which peaks at around  $-0.6$  V to  $-0.7$  V. This increase results from the increased number of electrons available at the electrode surface for the reduction of  $\text{Fe}^{III}(\text{CN})_6^{3-}$  to  $\text{Fe}^{II}(\text{CN})_6^{4-}$ . The reduction of  $\text{Fe}^{III}(\text{CN})_6^{3-}$  reduces its concentration at the surface if the reaction rate exceeds the diffusive exchange with the bulk solution, and the current during a potential sweep is reduced again after a peak. In the reverse scan direction, no peak is visible, as no holes are available at the surface of the wide-bandgap semiconductor for the oxidation of the redox species. The area under the reduction peak as well as the peak height showed a clear dependence on the sweep rate,  $v$ , of the experiment. In Figure 5.35, the peak



**Figure 5.35:** Peak current of the measurements presented in Figure 5.34 versus the scan speed,  $v$ . The square root dependence typical for diffusion-limited processes is observed.

height is plotted versus the scan speed  $v$ . The peak height increases with the square root of the scan speed  $v$ , which is typical for a diffusion limited reaction [Finklea, 1988].

### 5.3.8. Summary

In conclusion, n-GaN electrodes have been found to exhibit an ideally polarizable interface for  $V_{bias} - V_{fb} > 1$  V and can be described electrically by the equivalent circuit model (a) for such external voltages. Closer to the flatband condition, Faradaic contributions have been observed and model (b) gave a fair approximation of the electrical properties. The extracted interface capacitance,  $C_i$ , followed the behavior of an ideal semiconductor depletion capacitance and no influence of surface states was noted. The band edges at the interface are almost "pinned" with respect to the solution redox levels and have been determined to  $E_{C,S} = 0.91$  eV and  $E_{V,S} = -2.69$  eV versus the  $\text{H}^+/\text{H}_2$  redox level from the flatband voltages of  $V_{fb} = -1.12$  V for an n-type and of  $V_{fb} = 2.27$  V for a p-type GaN electrode. The flatband voltage was evaluated from the Mott-Schottky plots of the depletion layer capacitance extracted from impedance spectroscopy measurements. The doping dependence of the determined  $V_{fb}$  was attributed to the capacitive contribution of an additional surface layer ( $C_L \approx 2 \mu\text{F cm}^{-2}$ ). A correct determination of  $V_{fb}$  from photocurrent measurements was not possible, presumably due to a slow charge transfer kinetics across the interface. For AlGaN electrodes, the valence band edge at the interface to the solution,  $E_{V,S}$ , was found to be independent of the Al-concentration for Al molar ratios,  $x$ , ranging from 0 to 0.5.



The cathodic current of electrons reducing  $H^+$  to  $H_2$  at n-type GaN electrodes showed an exponential dependence on the applied external potential with an ideality factor of  $n \approx 2$ . A considerable contribution of surface states to the charge transfer process is assumed. No anodic current is observed due to the absence of holes at the semiconductor surface. Charge transfer to an iron cyanide redox couple in solution showed a clear diffusion limited process. Again, just the reduction peak of the redox reaction was observed, as no holes are available at the semiconductor surface for the oxidation reaction.

## 5.4. Ion-Sensitivity of GaN Surfaces

One important result of the discussion in Section 5.1.3 was that at the interface between a moderately doped semiconductor and an electrolyte the energetic positions of the semiconductor band edges are fixed relative to the redox levels in the electrolyte as far as variations in the externally applied bias potential are concerned, but can shift for changes in the electrolyte composition. The charge,  $\sigma_S$ , at the semiconductor surface is mainly determined by the adsorbed potential-determining ions (PDIs), and the potential,  $\phi_S$ , between the semiconductor surface and the bulk electrolyte adjusts to equilibrate the adsorption and desorption reactions for the respective bulk concentration of the PDIs. Thus, a finite dependence of  $\phi_S$  on the PDI concentration in the solution is expected, which directly influences the relative energetic levels at the interface. For this reason, the electrolyte composition is always specified along with results for  $V_{fb}$ ,  $E_{C,S}$ , and  $E_{V,S}$ .

As a native oxide layer is present on the surface of GaN (q.v. Section 5.2),  $H^+$  and  $OH^-$  are expected to be the PDI at the GaN/electrolyte interface, and the surface potential,  $\phi_S$ , should be influenced by the pH of the aqueous solution. Hence, determination of the pH sensitivity of native GaN surfaces is of major interest in this context and will be compared to the response of thermally oxidized GaN.

Determination of the GaN surface sensitivity towards  $H^+$  and other ions involved in biomolecular processes is essential for the application of III-nitride based transducers in biosensors or physiological research [Berman & Hébert, 1974], [Alberts, 2002]. The pH change in the direct environment of a cell is a main observable in whole cell biosensors monitoring the cell metabolism in response to an analyte [Parce, 1989], [McConnell, 1992], [Owicki & Parce, 1992], [Baumann, 1999]. In enzyme-based biosensors, the analyte is catalytically converted by enzymes, and the concentration of a reaction product, often  $H^+$ , is measured by the transducer [Caras & Janata, 1980], [Poghossian, 2001], [Pijanowska, 2003]. Moreover,  $Na^+$ ,  $K^+$ , and  $Ca^{2+}$  are the main ions forming the action potentials of cells.

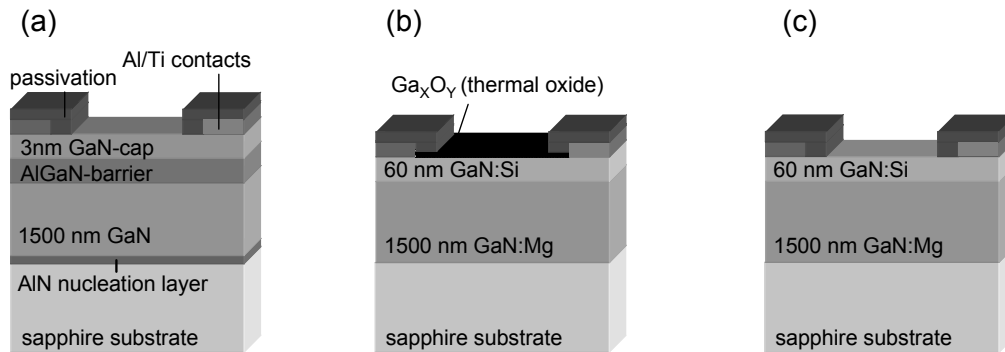
The dependence of the GaN surface potential,  $\phi_S$ , on the pH of the electrolyte can be determined for example by employing GaN electrodes, where changes in the surface potential  $\phi_S$  are directly related to  $V_{fb}$  via Eq. (5.44) [Kocha, 1995], [Huygens, 2000], [Beach, 2003]. However, determination of  $V_{fb}$  is time consuming and therefore not an adequate method for

transient pH measurements. In addition, deviations from the ideal Schottky barrier assumption, like for example dielectric surface layers, can influence both, the observed interfacial capacitance  $C_i$ , and the assumed potential drop in the semiconductor depletion region,  $V_{sc}$  (q.v. Section 5.3.1). Under ideal conditions, an accuracy of around 10 mV can be reached [Madou & Morrison, 1989].

A faster technique for the determination of the pH response is the constant capacitance method. In this case, the electrode is operated in depletion and the capacitance is measured. Upon changes of the ionic composition of the electrolyte, for instance the pH, the measured capacitance is kept constant by an external electronic control circuit that adjusts the bias potential by  $\Delta V_{bias}$  via the Ag/AgCl reference electrode and a potentiostat. Hence, the pH dependent change in the surface potential,  $\Delta\phi_S$ , is compensated by the bias potential variation,  $\Delta V_{bias}$ , yielding a direct measure for the potentiometric response of the surface. During the measurement, the electronic conditions in the semiconductor electrode regarding the band bending,  $V_{sc}$ , or the charge in the semiconductor depletion layer,  $\sigma_{sc}$ , are constant. Consequently, the observed pH response is decoupled from the electronic conditions in the capacitive transducer. Deviations from the ideal semiconductor/electrolyte junction that affect the assumption of potential variations occurring exclusively over the semiconductor depletion layer have no influence on the measured response, but of course on the background noise and the drift of the transducer.

If the investigated surface layer can be prepared as the gate layer of a SGFET device, the internal signal transduction and amplification of the transistor can be utilized for the measurement of the ionic surface response. Here, the channel current,  $I_{DS}$ , of the transistor is kept constant by an external circuit that adjusts the gate potential,  $V_{GS}$ . Bergveld was the first to report in the early 70s about an ion-sensitive FET based on a Si p-channel transistor with a SiO<sub>2</sub> gate layer, which responded to H<sup>+</sup> and Na<sup>+</sup> [Bergveld, 1970], [Bergveld, 1972]. However, the response mechanism of these devices was not clear at the beginning. Some authors proposed that the response was caused by a diffusion of H<sup>+</sup> ions and alkali metals through the oxide to the Si-SiO<sub>2</sub> interface, changing the interface charge [Revesz, 1977], [Bergveld, 1978]. Further investigations and comparison with layers that obtain a comparably low ionic diffusion like Si<sub>3</sub>N<sub>4</sub> or Al<sub>2</sub>O<sub>3</sub>, revealed that ionic diffusion is not the primary response mechanism, but most probably responsible for the drift and aging of the device [Siu & Cobbold, 1979], [Madou & Morrison, 1989]. The main response arises from surface reactions in the Helmholtz-layer at the oxide/electrolyte interface, as described in Section 5.1.3. As a simple combination of the ideal Nernst characteristics and the general MOSFET equations could not explain the pH response of ISFETs with a SiO<sub>2</sub> gate layer, and only give a first-order approximation for most other oxides, the more detailed site-binding model was developed to describe the chemical surface processes and the ionic response of the devices [Yates, 1974], [Siu & Cobbold, 1979], [Bousse, 1983]. The site-binding model will be introduced in Section 5.4.2.

ISFETs based on SiO<sub>2</sub> gate layers show rather low response and poor stability. The application of other inorganic gate materials such as Si<sub>3</sub>N<sub>4</sub>, Al<sub>2</sub>O<sub>3</sub>, or Ta<sub>2</sub>O<sub>5</sub> resulted in a substantial improvement of both stability and sensitivity and lead to the development of commercially available ISFETs [Matsuo & Wise, 1974], [Esashi & Matsuo, 1978], [Abe, 1979], [Bousse, 1994].

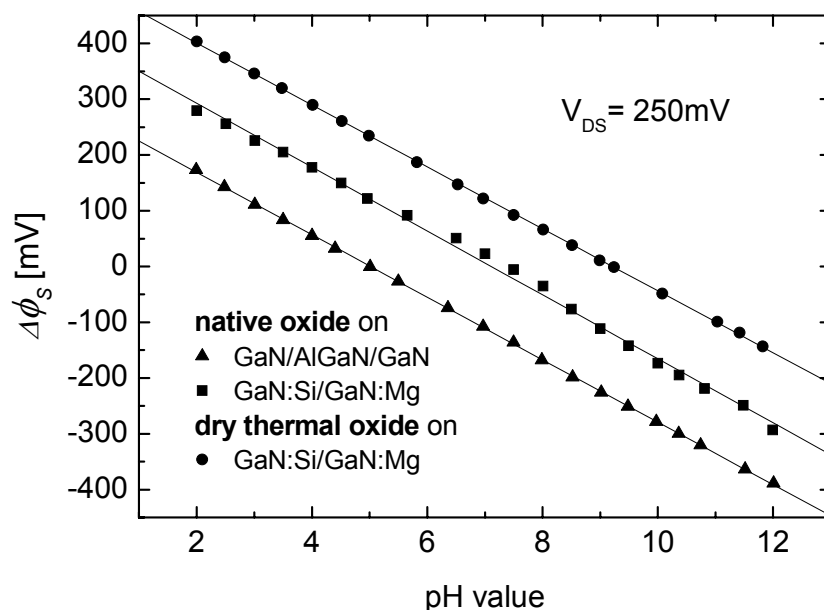


**Figure 5.36:** Schematic layout of pH-sensitive SGFET devices based on (a) GaN/AlGaIn/GaN and (b), (c) GaN:Si/GaN:Mg heterostructures. The surface of sample (b) was thermally oxidized at 700 °C for 2 h.

#### 5.4.1. Ion-Sensitivity of GaN Surfaces Measured by III-Nitride Based Field Effect Transistors

In the course of this thesis, transistor structures based on GaN:Si/GaN:Mg double layers and GaN/AlGaIn/GaN heterostructures have been used to investigate the ion sensitivity of GaN surfaces. The layout and processing of the devices has been discussed in Chapter 3. A schematic layout of the different employed transistor structures is given in Figure 5.36. As-deposited GaN surfaces with a native oxide were tested for GaN/AlGaIn/GaN transistors. Comparative measurements were made on the dry thermally oxidized GaN surface of a GaN:Si/GaN:Mg transistor. The oxide was formed during a 2 h process in dry oxygen atmosphere at 700 °C. These transistors exhibit a much smaller transconductance than the AlGaIn/GaN HEMTs, but can be thermally oxidized without a degradation of the device. Additional investigation of the same device with an as-grown GaN surface allowed the comparison of similar surfaces on different readout devices (structures (a) and (c) in Figure 5.36). In addition, the sensitivity of native and thermally oxidized GaN surfaces could be compared on equal device structures (structures (b) and (c)).

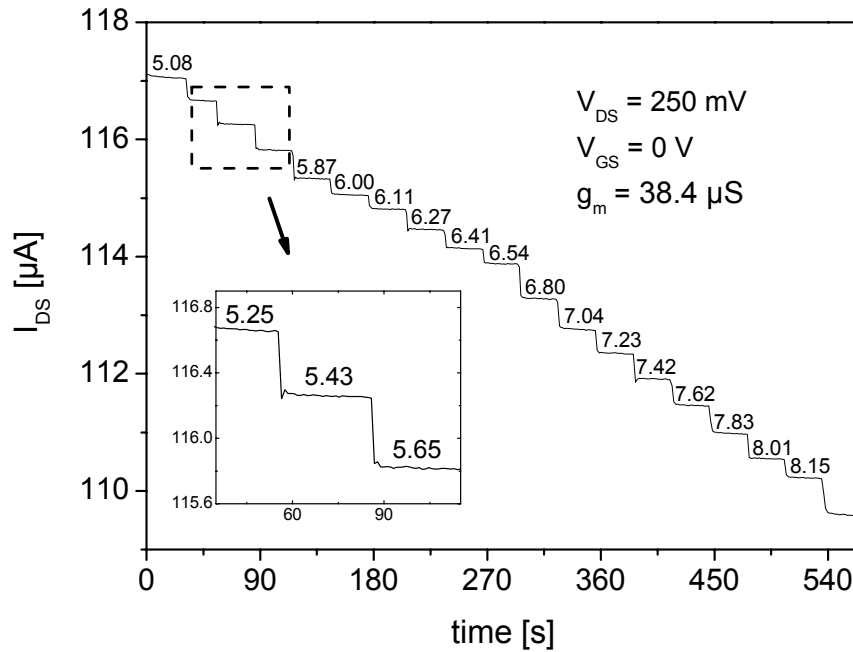
All pH-sensitive measurements were performed at a constant temperature of 23 °C in the dark with a three electrode setup. A potentiostat was employed to control the gate voltage  $V_{GS}$  relative to the reference electrode (q.v. Chapter 4). The pH of the solution was determined by a pH glass electrode (WTW pH90) and adjusted by titration with dilute NaOH or HCl with a background of 100 mM NaCl / 10 mM HEPES to define the overall ionic strength. The solution was mechanically stirred to ensure homogeneous ion concentration and a constant flow to the gate surface.



**Figure 5.37.:** Variation of the surface potential,  $\Delta\phi_S$ , for as grown and dry thermally oxidized GaN surfaces as a function of pH. As transducer devices, GaN/AlGaN/GaN and GaN:Mg/GaN:Si SGFETS have been used. For clarity the datasets are shifted by a constant potential offset.

In Figure 5.37 the change in the surface potential,  $\Delta\phi_S$ , as a function of the electrolyte pH is shown for the different investigated surfaces and transducer devices. During the measurement, all transistor devices were operated at  $V_{DS} = 250$  mV at a constant channel current  $I_{DS}$ , which was controlled by adjustment of the gate voltage,  $V_{GS}$ , as described above. The change in the surface potential,  $\Delta\phi_S$ , corresponds to the negative gate voltage change,  $\Delta V_{GS}$ . An almost linear dependence was obtained for all three sample structures over the entire pH range between pH 2 and pH 12. Identical native oxide surface layers on different device structures - the GaN/AlGaN/GaN and the GaN:Si/GaN:Mg transistor - showed almost identical sensitivities of  $56.0$  mV/pH and  $57.3$  mV/pH, respectively. The similar results of identical surfaces on different transducers demonstrate that the pH sensitivity is primarily a surface effect. In comparison to the native oxide on the as-grown GaN surfaces, the thermally oxidized GaN surface showed an almost equal sensitivity of  $56.6$  mV/pH. Hence, the observed  $\phi_S$  vs. pH behavior, which was close to the linear Nernstian response of  $58.7$  mV/pH at  $23^\circ\text{C}$  is attributed to the oxidic  $\text{Ga}_x\text{O}_y$  surface according to the site-binding model as developed by Yates et al. and described in Section 5.4.2.

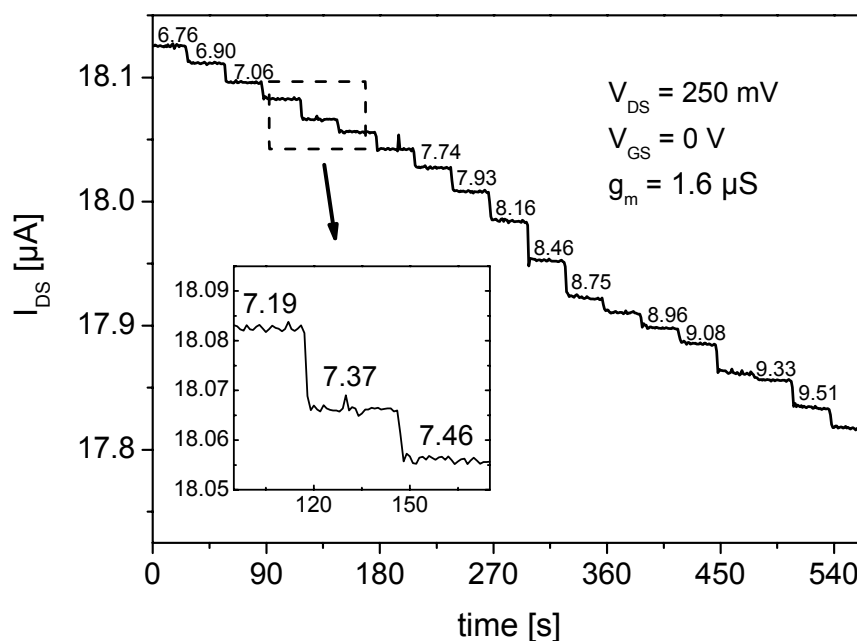
Other groups have measured the pH sensitivity of GaN surfaces by determination of the flatband-voltage,  $V_{fb}$ , of GaN electrodes at different pH values. The dependence of  $V_{fb}$  on the electrolyte pH directly corresponds to the  $\phi_S$  vs. pH behavior. Kocha et al. have obtained a linear dependence of  $55$  mV/pH from the Mott-Schottky plots of impedance spectra recorded for n-type GaN electrodes at pH 2, 5, 10, and 14 [Kocha, 1995]. In another publication, the



**Figure 5.38:** Transient behavior of the channel current,  $I_{DS}$ , of an AlGaIn/GaN SGFET with an as-grown GaN cap-layer during changes of the electrolyte pH. Numbers correspond to the pH values measured with a calibrated pH meter.

pH sensitivity was determined by the same method and at comparable n-GaN electrodes to  $60 \text{ mV}/\text{pH}$  [Huygens, 2000]. However, only a few measurements in concentrated HCl,  $\text{H}_2\text{SO}_4$ , and KOH solutions were performed. Beach and co-workers reported a  $V_{fb}$  vs. pH dependence of  $46 \text{ mV}/\text{pH}$  from impedance measurements and of  $47 \text{ mV}/\text{pH}$  from photocurrent measurements at n-GaN electrodes between pH 2 and 12. In contrast, they obtained a value of  $63 \text{ mV}/\text{pH}$  from photocurrent measurements at p-GaN electrodes [Beach, 2003].

These different groups have reported a linear and high sensitivity over the entire pH range, in agreement with the results of this work. However, as discussed earlier in this section, the determination of the pH sensitivity from measurements of  $V_{fb}$  is an imprecise method which is subject to various sources of error. Furthermore, the sensitivities given in most publications are based on only a few data points. Special care must be taken in the interpretation of results gained by photocurrent measurements, as the observed  $V_{fb}$  are shifted for GaN-electrodes (Section 5.3.4). The size of the error is determined by the charge transfer kinetics and therefore strongly influenced by the pH of the solution. Consequently, a large deviation is reported for the sensitivities obtained for n-type and p-type GaN by the photocurrent method [Beach, 2003]. To investigate the transient response of the GaN-based ISFET devices, time resolved measurements of the drain-source current,  $I_{DS}$ , were performed at  $V_{DS} = 250 \text{ mV}$  and  $V_G = 0 \text{ V}$ . The pH of the electrolyte was changed in steps between 0.1 and 0.3 pH by titration with diluted NaOH every 30 s. Records of the transient measurements performed with two different GaN-based ISFET devices, the GaN/AlGaIn/GaN transistor with an as-grown



**Figure 5.39.:** Transient behavior of the source-drain current,  $I_{DS}$ , of an GaN:Si-channel SGFET with a dry thermally oxidized GaN surface during changes of the electrolyte pH. Numbers correspond to the pH values measured with a calibrated pH meter.

GaN cap-layer and the GaN:Si/GaN:Mg FET with a dry thermal surface oxide, are presented in Figures 5.38 and 5.39, respectively. Both devices showed an immediate response to changes in the pH. Right after titration, small oscillations due to the mixing of the solution and a slight drift are observable. In contrast, delay times of some seconds have been reported for SiO<sub>2</sub> gate ISFETs [Fung, 1986]. As expected from the transconductance of the two devices at the operation conditions, the change of channel current,  $\Delta I_{DS}$ , is larger for the GaN/AlGaIn/GaN HEMT structure ( $g_m = 38.4$  μS) than for the GaN:Si channel device ( $g_m = 1.6$  μS). A resolution better than 0.02 pH for the HEMT structure and of 0.1 pH for the other device is estimated. However, the investigated transistor structures have not yet been optimized for ISFET applications and were also not operated at their point of maximal transconductance. An enhanced transconductance due to a larger channel width to length ratio or optimization of other important device parameters such as barrier thickness, doping concentration, and layer thicknesses, is likely to further improve the device resolution.

In addition to the pH response, the surface sensitivity towards Na<sup>+</sup>, K<sup>+</sup>, Ca<sup>2+</sup>, and Cl<sup>-</sup> which are involved in the metabolism of cells and the formation of cell action potentials, was investigated in the range between  $10^{-5}$  M and  $2 \times 10^{-3}$  M under physiological conditions at pH 7. For this purpose, the Ag/AgCl reference electrode was replaced by a double chamber reference electrode with a 1 M TRIS solution as an outer electrolyte. The electrolyte solution was a 50 mM HEPES buffer. Ion concentrations were measured by ion-selective electrodes

(ISE) with glass (Metrohm Na<sup>+</sup>-ISE 6.0501.100), crystal (Metrohm Cl<sup>-</sup>-ISE 6.0502.120,) or polymer membranes (Metrohm K<sup>+</sup>-ISE 6.0504.110, Ca<sup>2+</sup>-ISE 6.0504.110) and an ion meter (Metrohm 781 pH/Ion Meter). Compared to the pH sensitivity, significantly lower responses were measured for the other investigated ions. The results are summarized in Table 5.3.

ion	$\Delta\phi_S / \text{dec.}$
H <sup>+</sup>	56 – 57 mV
K <sup>+</sup>	< 2 mV
Na <sup>+</sup>	< 5 mV
Ca <sup>2+</sup>	< 2 mV
Cl <sup>-</sup>	< 2 mV

**Table 5.3:** Ion-induced change of the GaN surface potential,  $\Delta\phi_S$ , per decade change in ion concentration in a range between  $10^{-5}$  M and  $2 \times 10^{-3}$  M.

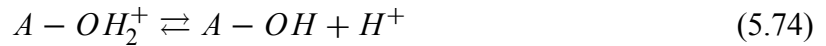
The present results demonstrate that III-nitride based ISFET devices with a GaN surface layer are promising transducer devices for biochemical sensors where a transient in pH is monitored, as they feature a high linear sensitivity, a fast response, and a low cross sensitivity to other ions. The ISFET devices based on AlGaIn/GaN heterostructures exhibit a superior resolution compared to the GaN:Si channel devices, as they exhibit a much higher transconductance.

In some publications by Chaniotakis and co-workers, an anion sensitivity and selectivity has been reported for GaN surfaces [Chaniotakis, 2004], [Alifragis, 2005], [Chaniotakis, 2005]. Their results are based on potentiometric measurements of the ocp, meaning that the bulk potential of the GaN electrode was measured relative to an Ag/AgCl reference electrode by a high impedance voltmeter. Potentiometric measurements are usually applied for metal electrodes, which are often modified with ionselective membranes [Janata, 1989]. However, this measurement method is not applicable to semiconductor electrodes. In contrast to metal electrodes, the surface potential cannot be directly measured, as, except for the flatband situation, the potential in the bulk semiconductor is not equal to the surface potential. For moderate doping, potential variations mainly appear in the semiconductor space charge layer rather than across the electrolytic double layer. It is evident from Figure 5.10 that under equilibrium conditions, the obtained ocp is the difference between the Fermi level and the redox level of the reference electrode and does not correspond to the surface potential  $\phi_S$ . Any change in the surface potential  $\phi_S$  is compensated by a change in the semiconductor band bending. Only for highly doped semiconductors, the change in ocp might reflect the change in the surface potential. As it is explicitly stated in [Chaniotakis, 2004], [Alifragis, 2005] that undoped GaN electrodes have been used, this possibility can be excluded. In the interpretation of the impedance measurements supporting the arguments of the authors, a flatband situation was assumed for the GaN electrodes under different ionic conditions and potential variations of several hundred mV. This is certainly not the case [Chaniotakis, 2005] for the described type of electrodes.

### 5.4.2 Site-Binding Model of the Oxide/Electrolyte Interface

The site-binding or site-dissociation model was formulated by Yates et al. in 1974 for the description of the electrical double layer at the interface between an oxide and an aqueous electrolyte [Yates, 1974]. As  $H^+$  and  $OH^-$  are the potential determining ions at oxidic surfaces, the model considers the dependence of the surface charge and surface potential on the  $H^+$  and  $OH^-$  concentration, hence, the pH of the solution. The model has been thoroughly discussed and extended to other surfaces in subsequent publications [Healy, 1977], [Davis, 1978] and [Healy & White, 1978]. Siu and Cobbold first have applied the site-binding model to explain the pH sensitive performance of silicon-based ISFETs with a  $SiO_2$  gate surface layer [Siu & Cobbold, 1979]. Their approach was further developed and used to describe the pH response of ISFETs with  $Al_2O_3$  or  $Ta_2O_5$  gate layers by Bousse et al. [Bousse, 1983], Fung et al. [Fung, 1986] and van Hal et al. [van Hal, 1995].

In the site-binding model, the formation of ionizable hydroxyl surface sites ( $A - OH$ ) is assumed at an oxide surface exposed to an aqueous electrolyte. The hydroxyl sites exhibit amphoteric character - they can become positively charged by protonation or negatively charged by deprotonation, according to the following surface dissociation reactions:



Furthermore, the site-binding model assumes an ideally polarizable interface between the solid and the liquid. In Figure 5.40 (a) schematic illustration of the surface sites at an oxide/water interface and their protonation is given for different pH values. The equilibrium between the relative concentration of positive [ $A - OH_2^+$ ], neutral [ $A - OH$ ], and negative [ $A - O^-$ ] surface sites and the proton concentration at the interface [ $H^+$ ]<sub>S</sub> is described by two effective surface dissociation constants:

$$K_+ = \frac{[A - OH] \cdot [H^+]_S}{[A - OH_2^+]}, \text{ and} \quad (5.76)$$

$$K_- = \frac{[A - O^-] \cdot [H^+]_S}{[A - OH]}. \quad (5.77)$$

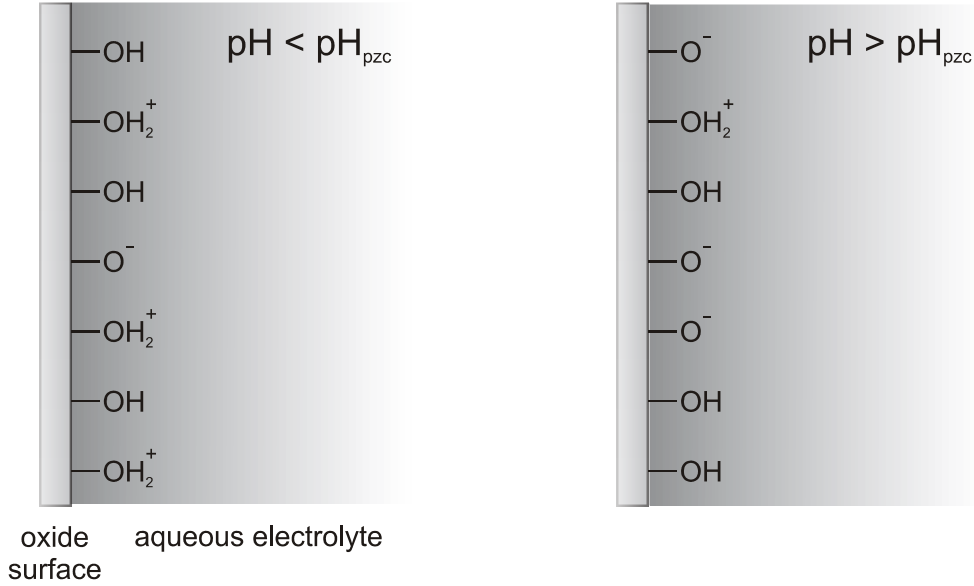
If no binding of other ions than the potential determining  $H^+$  to the surface sites is considered, the surface charge per unit is given by

$$\sigma_S = e \cdot ([A - OH_2^+] - [A - O^-]), \quad (5.78)$$

and the total density of sites at the interface  $N_S$  is

$$N_S = [A - OH] + [A - OH_2^+] + [A - O^-]. \quad (5.79)$$





**Figure 5.40:** Amphoteric hydroxyl surface sites at an oxide/electrolyte interface. At the  $pH$  of the point of zero charge,  $pH_{pzc}$ , the surface is electrically neutral. The surface obtains a positive net charge for  $pH < pH_{pzc}$  (left) and a negative net charge for  $pH > pH_{pzc}$  (right).

For the relation of the surface concentration of protons  $[H^+]_S$  to the bulk value  $[H^+]$  the Boltzmann statistics is applied:

$$[H^+]_S = [H^+] \exp\left(\frac{-e\phi_S}{kT}\right) \quad (5.80)$$

By means of Eqs. (5.74) to (5.80), a relation between the surface potential,  $\phi_S$ , the surface charge,  $\sigma_S$ , and the pH of the bulk electrolyte can be established. The corresponding derivation is described in Appendix A.4 and yields

$$\ln [H^+] = \ln \sqrt{K_- K_+} + \frac{e\phi_S}{kT} + \sinh^{-1}(\alpha_S/\delta) - \ln(1 - \alpha_S), \quad (5.81)$$

with the definitions of  $\alpha_S = \frac{\sigma_S}{eN_S}$  and  $\delta = 2\sqrt{K_-/K_+}$ . The parameter  $\delta$  was introduced in Ref. [Healy & White, 1978] and characterizes the tendency of a surface site to diprotonate. For most oxide surfaces, the  $\delta$  parameter is small [Healy & White, 1978], and the approximation  $\delta^2 \ll 1$  was made in the derivation of Eq. (5.81).

At the point of zero charge the number of positively charged surface sites  $[A - OH_2^+]$  equals the number of negatively charged surface sites  $[A - O^-]$ . The surface is electrically neutral ( $\alpha_S = 0$ ) and  $\phi_S = 0$ . From Eq. (5.81) the pH at the point of zero charge,  $pH_{pzc}$ , is deduced as

$$pH_{pzc} = -\log \sqrt{K_- K_+}. \quad (5.82)$$

## 5. Physical Chemistry of the GaN/Electrolyte Interface

---

Introduction of  $\text{pH}_{pzc}$  into Eq. (5.81) yields a relation between  $\phi_S$ ,  $\sigma_S$ , and the difference of the solution pH and the  $\text{pH}_{pzc}$ :

$$2.303(\text{pH}_{pzc} - \text{pH}) = \frac{e\phi_S}{kT} + \sinh^{-1}(\alpha_S/\delta) - \ln(1 - \alpha_S) \quad (5.83)$$

To obtain a direct dependence of the surface potential  $\phi_S$  on the pH, the Gouy-Chapman-Stern model described in Section 5.1.3 is adopted for the relation between the surface charge,  $\sigma_S$ , and the surface potential,  $\phi_S$ , at a solid/electrolyte interface.

The charge at the surface of the semiconductor,  $\sigma_S$ , and the charge in the semiconductor space charge region  $\sigma_{sc}$  must be balanced by the counter charge  $\sigma_D$  in the electrolyte:

$$\sigma_{sc} + \sigma_S = -\sigma_D \quad (5.84)$$

Under the assumption of high ionic concentrations - which was surely met under the experimental conditions - the surface potential  $\phi_S$  is related to counter charge,  $\sigma_D$ , by  $\phi_S = -\sigma_D/C_H$ , where  $C_H$  is the Helmholtz double layer capacitance. With Eq. (5.84) follows

$$\phi_S = \frac{\sigma_{sc} + \sigma_S}{C_H}. \quad (5.85)$$

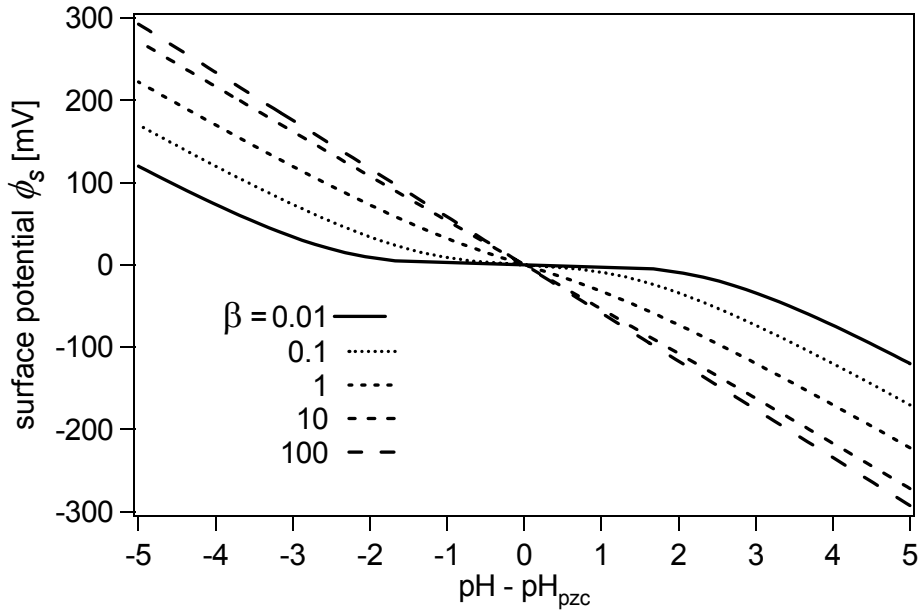
As thoroughly discussed by Madou and Morrison [Madou & Morrison, 1989], the charge  $\sigma_{sc}$  in the space charge region of a nondegenerated semiconductor is usually by far smaller than the ionic surface charge,  $\sigma_S$ , and can therefore be ignored in Eq. (5.85).

In general, the ionic charge at the oxide surface of a semiconductor or insulator is only dependent on the surface chemistry represented by the dissociation constants. The comparably small charge in the semiconductor or an externally applied potential only have a marginal influence on the surface reactions (q.v. Section 5.1.3) and therewith the surface charge and potential. In consequence, the surface chemistry that determines  $\sigma_S$  and  $\phi_S$  is decoupled from the semiconductor device beneath, and in particular is not influenced by the measurement or the electronic conditions of the device.

Equation (5.83) describes a Nernstian variation of the surface potential,  $\phi_S$ , with the pH including two correction terms. The second term describes the saturation of the pH response for a high fraction of charged surface sites. The total number of surface sites is around  $5 \times 10^{14} \text{ cm}^{-2}$  to  $10^{15} \text{ cm}^{-2}$  for oxidic surfaces [Healy & White, 1978]. Under the assumption of a capacitance  $C_H = 20 \mu\text{F cm}^{-2}$  for the dominant Helmholtz-layer and a Nernstian dependence of  $59 \text{ mV/pH}$  for the surface potential, around  $10^{13} \text{ cm}^{-2}$  surface sites are charged for every pH of divergence from  $\text{pH}_{pzc}$ . Hence, even under extreme pH conditions only a small fraction of the surface sites is charged and the second correction term in Eq. 5.83 can be neglected.

In total, the dependence of the surface potential,  $\phi_S$ , on pH under the assumptions discussed is given by

$$2.303(\text{pH}_{pzc} - \text{pH}) = \frac{e\phi_S}{kT} + \sinh^{-1}\left(\frac{e\phi_S}{kT} \frac{1}{\beta}\right), \quad (5.86)$$



**Figure 5.41.:** Relation between the surface potential,  $\phi_S$ , and the pH of an aqueous electrolyte for different sensitivity factors,  $\beta$ . With increasing  $\beta$ , the relation approaches a linear Nernstian pH-dependence.

where the sensitivity factor,  $\beta$ , is defined as

$$\beta = \frac{e^2 N_S \delta}{C_H k T}. \quad (5.87)$$

The relevance of the remaining  $\sinh^{-1}$ -correction term for a linear Nernstian pH response is mainly determined by the sensitivity factor,  $\beta$ . In Figure 5.41,  $\phi_S$  is plotted versus the pH of the electrolyte for oxide surfaces with different  $\beta$ . For a large sensitivity factor  $\beta$ , the correction term can be ignored and a linear Nernstian pH dependence is observed. In case of small  $\beta$ , the correction term has a severe influence and a S-shaped response curve with the point of zero charge (pzc) as an inflection point is found. Around the pzc, when  $\phi_S \ll \frac{kT}{e}$ , the correction term can be linearized and the  $\phi_S$  vs. pH relation is linear according to

$$\phi_S = 2.303(pH_{pzc} - pH) \frac{kT}{e} \left( \frac{\beta}{1 + \beta} \right). \quad (5.88)$$

The sensitivity factor,  $\beta$ , mainly depends on the density of surface sites,  $N_S$ , which is more or less equal for most oxide surfaces, and the introduced variable  $\delta$ , which is a measure for the surface reactivity. The variable  $\delta$  as well as the  $pH_{pzc}$  at which the surface is electrically neutral, are determined by the two equilibrium constants,  $K_-$  and  $K_+$ , of the dissociation reactions, and can be conveniently expressed by using their logarithms ( $pK_{\pm} = -\log K_{\pm}$ ). The  $pH_{pzc}$  is given by the average of their logarithms:  $pH_{pzc} = \frac{1}{2}(pK_- + pK_+)$ . Their difference,

## 5. Physical Chemistry of the GaN/Electrolyte Interface

---

$\Delta pK = pK_- - pK_+$ , expresses the relative strength of the two surface acids  $A - OH_2^+$  and  $A - OH$  for proton dissociation leads to  $\delta = 2 \times 10^{-\Delta pK/2}$ . Surfaces which obtain a large difference,  $\Delta pK$ , in the acidic strength of their surface sites have a low tendency to associate or dissociate protons around  $pH_{pzc}$ .  $\delta$  and accordingly the sensitivity factor,  $\beta$ , for such surfaces is low and a sub-Nernstian behavior is observed. For oxide surfaces with smaller  $\Delta pK$ , the sensitivity factor increases and the  $\phi_S$  vs. pH relation approaches a linear Nernstian dependence.

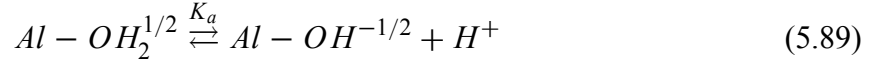
The  $pK_{\pm}$  values of various oxides can be found for example in Refs. [Davis, 1978] or [van Hal, 1995]. The best known example of an oxide surface with sub-Nernstian pH dependence is  $SiO_2$ , for which the site-binding model was successfully applied to describe the pH response around the point of zero charge [Bousse, 1983]. A value of  $\beta = 0.14$  was determined for the sensitivity factor and the  $pH_{pzc}$  was determined to 2.2. The sensitivity factor for  $Al_2O_3$  surfaces analyzed for comparison in the same paper was given as  $\beta = 4.8$  ( $pH_{pzc}=8.5$ ).

Bayer et al. have modeled the pH sensitivity of the  $Ga_xO_y$  surface of a GaN/AlGaIn/GaN SGFET by the site-binding model, and the best agreement with the result presented in Figure 5.37 was found for dissociation constants of  $K_- \approx 10^{-8}$  and  $K_+ \approx 10^{-6}$  and a point of zero charge of  $pH_{pzc} = 6.8$  [Bayer, 2005]. In the literature a  $pH_{pzc}$  of 8.47 is reported for  $Ga_2O_3$  surfaces [Xu & Schoonen, 2000]. With a total density of surface sites at the interface of  $N_S = 9 \times 10^{14} \text{ cm}^{-2}$ , a sensitivity factor  $\beta$  of around 50 is derived. Some analogies are observed between the pH response of the investigated  $Ga_xO_y$ - and the  $Al_2O_3$ -surfaces often used for ISFET devices. Both oxides exhibit a high and linear pH sensitivity, expressed by a high  $\beta$  value, show an immediate response to pH changes and a low cross sensitivity to other ions such as  $K^+$  and  $Na^+$  [Abe, 1979], [Bousse, 1983]. Dissociation constants of  $K_- \approx 10^{-10}$  and  $K_+ \approx 10^{-6}$  are given for  $Al_2O_3$  in the literature [van Hal, 1995].

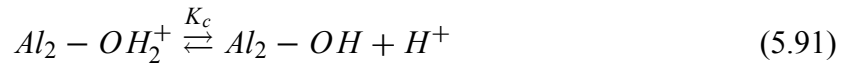
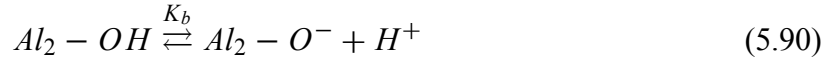
The pH-sensing properties of AlN films have been studied in the literature as well [Chiang, 2001]. For the modeling, again hydroxyl groups at the surface were assumed and the site-binding model was applied. Simulation and subsequent experimental studies yielded  $pK_- \approx 8.86$  and  $pK_+ \approx 7.68$ , resulting in a  $pH_{pzc}$  of 8.24 and a  $\beta$  factor larger than 100.

The given surface dissociation constants for metal oxides were obtained from titration data by the site-dissociation model, assuming a chemically homogeneous surface with only a single type of surface site associated with one or two protons. However, the number of metal ions coordinated to the surface oxygen can differ [Parfitt, 1975], resulting in various types of reactive surface groups with proton affinities expected to differ considerably [Hiemstra, 1989]. The multisite complexation (MUSIC) model developed by Hiemstra et al. considers singly, doubly and triply metal-coordinated oxygen and allows - in contrast to the site-binding model - an a priori estimation of the corresponding proton affinities from several physical parameters, including the valence of the metal ion, the number of metal ions coordinated with a ligand and the number of surrounding ligands [Hiemstra, 1989], [Hiemstra & Vanriemsdijk, 1991]. Van Hal and co-workers have applied the MUSIC model to  $Al_2O_3$ , assuming the aluminum ions to be in hexacoordination with six ligands [van Hal, 1996]. In their model, the formal charge of

a protonized singly coordinated surface oxygen group ( $Al - OH$ ) is estimated as  $-1/2$ . The proton dissociation reaction equations are given as



for a singly coordinated oxygen, and



for a doubly coordinated oxygen. As in general no surface groups with a total charge higher than one are present at a solid/liquid interface [van Hal, 1996], the second dissociation step for singly coordinated oxygen has been neglected. In the normal pH range, the doubly coordinated oxygen sites are neutral ( $K_b = 12.3$ ,  $K_c = -1.5$ ). The  $pH_{pzc}$  and the total surface charge are therefore determined by reaction (5.89), this means the dissociation of a singly coordinated surface oxygen group ( $pH_{pzc} = pK_a$ ) [van Hal, 1996].

Atomic hydrogen adsorption experiments monitored by high resolution electron energy loss spectroscopy (HREELS), as already applied to clean GaN surfaces [Tautz, 1999], could contribute to the identification of the H-adsorption sites on GaN surfaces with native and thermal oxide.

A possible reason for the small cross sensitivity of highly pH-sensitive surfaces like  $Al_2O_3$  or  $Ga_xO_y$  towards other ions such as  $K^+$ ,  $Na^+$ ,  $Ca^{2+}$ , or  $Cl^-$  is given in Ref. [Morrison, 1980]. The specific adsorption of ions different from protons or hydroxide is hindered by the loss of the solvation energy of the ion during the adsorption process as well as the hydroxylation energy of the surface, which is considerable for most ionic materials. However, some influence of various ions on the response of oxide surfaces was observed and considered in the site-binding model by counter ion adsorption [Yates, 1974] or the formation of surface complexes [Davis, 1978].

## 6. Biofunctionalization of III-Nitride Transducer Devices

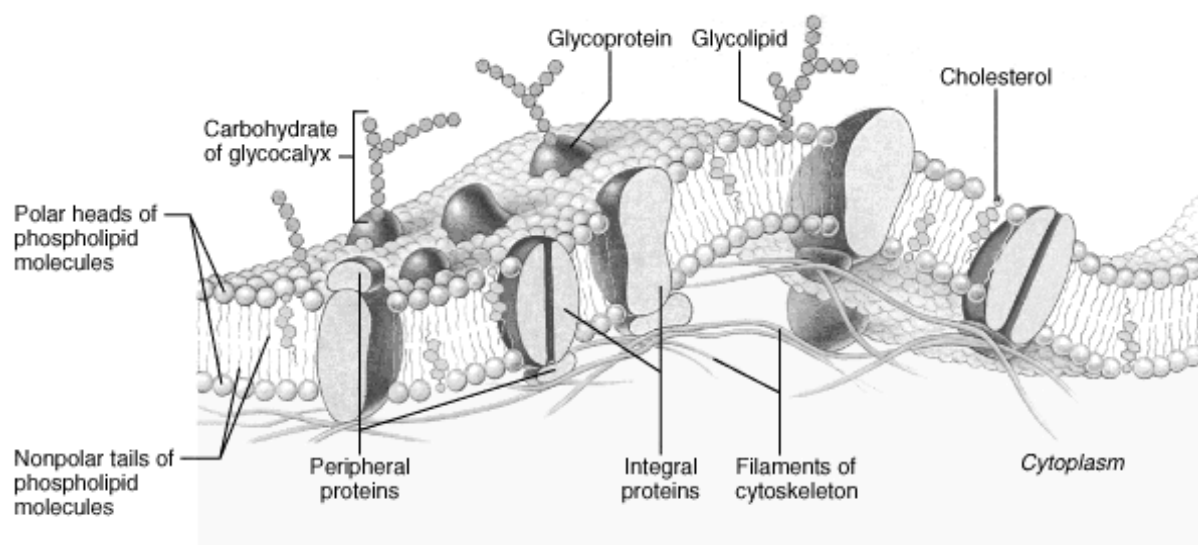
For an application of III-nitride-based transducer devices in biosensors or physiological research, a functional interface between biomaterials and inorganic device surface has to be established. Bioreceptors have to be immobilized without inhibiting their functionality or degrading of the transducer surface. In this chapter, three types of organic functionalizations of III-nitrides are discussed:

- (i) Artificial lipid bilayer cell membranes.
- (ii) Organic monolayers of silane molecules.
- (iii) Cardiac myocyte cell networks.

Optical and electrical analysis of the different types of biofunctionalization on GaN electrodes and AlGaN/GaN SGFETs are presented.

### 6.1. Supported Lipid Bilayer Membranes

One of the crucial structural elements of living cells is their enclosing plasma membrane, separating the interior of the cell from its outer environment. A schematic of the cell membrane is shown in Figure 6.1. In the generally accepted fluid mosaic model of the plasma cell membrane, introduced by Singer & Nicolson in 1972, it is described as a fluid bilayer matrix consisting mainly of phospholipids and cholesterol [Singer & Nicolson, 1972]. The phospholipids in a cell membrane are amphiphatic molecules composed of a hydrophilic polar phosphate containing headgroup and two hydrophobic non-polar fatty acid-derived hydrocarbon tails. The plasma membrane acts as a two-dimensional solvent for integral proteins and provides anchoring sites for peripheral proteins. The spontaneous formation of lipid bilayers in aqueous environment and the incorporation of integral proteins is driven by a self-organization process, as exclusion of water during the aggregation of the hydrophobic alkyl chains of the lipid molecules leads to a gain in free energy [Hoppe, 1983]. This hydrophobic interaction also induces the self-healing of bilayer membranes, as lipids spontaneously rearrange to minimize the contact of their hydrophobic tails to water, as caused by free edges and tears. Lipid membranes are highly impermeable to ions and water-soluble molecules, as for instance sugars or amino acids. Specialized transmembrane proteins such as carriers or channels mediate the exchange of these species between the cytoplasm and the cell exterior for the cell metabolism and allow the



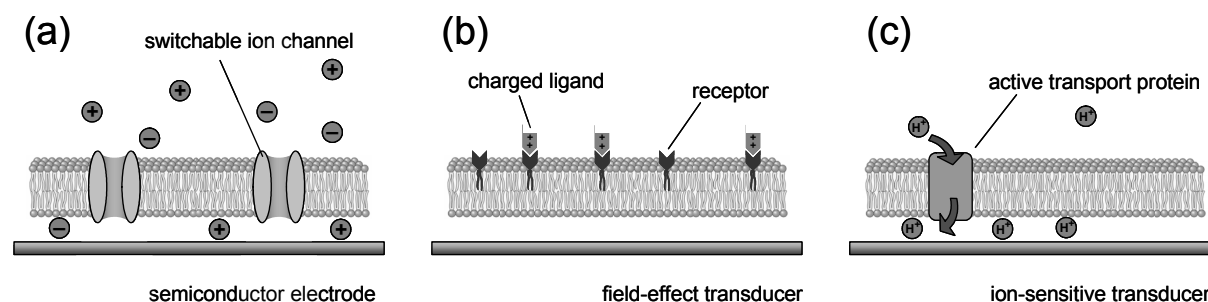
**Figure 6.1:** Schematic of the plasma membrane of a cell (from [Campbell, 1999]).

establishment of chemical or electrical gradients across the membrane. These gradients play an important role in many cellular processes (e.g. ATP synthesis) as well as in cell signaling processes in the intercellular communication [Alberts, 2002].

Phospholipid bilayers behave as two-dimensional crystals with two distinct phases. At temperatures below the melting temperature of the lipid,  $T_M$ , the membrane is in the gel phase, a closely packed crystalline array with highly ordered alkyl chains, little molecular motion and very slow lateral diffusion. For temperatures above  $T_M$ , the membrane is in the loosely packed liquid crystalline phase with highly disordered alkyl chains and fast lateral diffusion. The melting of a membrane is a sharp phase transition occurring over a temperature range of  $1 - 2^\circ\text{C}$ . Alkyl chain length, unsaturation, as well as the type of headgroup have a significant influence on the bilayer melting temperature  $T_M$ . Longer chains lead to higher melting temperatures due to increased Van der Waals interaction. The cis double bond of unsaturated alkyl chains produces a large drop in  $T_M$ , as the resulting kink in the unsaturated chain leads to less dense packaging in the gel phase and, therefore, to reduced interaction. The fluidity of a bilayer is a function of the ambient temperature and increasing with the temperature difference  $T - T_M$  to the melting temperature. Membranes of living cells are always in the liquid crystalline phase at physiological temperatures, as membrane fluidity is critical for the function of membrane proteins. In mammalian cells, the fluidity is generally controlled by the cholesterol content in membrane [Hoppe, 1983], [Alberts, 2002].

In order to investigate the electrical properties of membranes and membrane proteins, artificial membrane models such as spherical lipid vesicles [Sackmann, 1995], supported membranes, and free standing black lipid membranes [Müller & Rudin, 1968] have been established. Supported membranes are formed on a planar solid substrate by a self-organization process

## 6. Biofunctionalization of III-Nitride Transducer Devices



**Figure 6.2:** Biosensor designs based on a lipid bilayer membrane deposited on a semiconductor transducer device: (a) Switchable ion channels and measurement of membrane conductance, (b) field-effect detection of the specific binding of charged ligands to membrane-incorporated receptors, and (c) measurement of ionic concentration changes caused by active transport proteins.

[Kalb, 1992], [Nollert, 1995] and exhibit better mechanical and thermodynamical stability, as well as easier preparation compared to free standing membranes, while preserving the lateral bilayer fluidity [Tamm & McConnell, 1985]. Supported planar bilayers are suitable model systems for the study of, e.g., cell-cell recognition in the immune system [McConnell, 1986], binding of ligands to membrane-incorporated receptors [Kalb, 1990], or the electrical properties of membranes and ion-channels [Steinem, 1997], [Gritsch, 1998], [Raguse, 1998]. Further interest in solid supported membranes is attributed to their potential application in biosensors based on membrane incorporated receptors or selective ionophores [Kiefer, 1991], [Sackmann, 1996], [Cornell, 1997]. Depending on the solid substrate, either electrical or optical readout is possible.

Different biosensor concepts based on bilayer membranes deposited on semiconductor transducer devices have been proposed (Figure 6.2): (a) measurement of conductivity changes associated with the transport of ions through a lipid bilayer membrane deposited on a planar semiconductor electrode. The conductance of membrane transport proteins can be switched by a recognition event, e.g. the inhibition of ion channels by toxins [Cornell, 1997], [Sackmann & Tanaka, 2000]. (b) Potentiometric detection of the binding of charged ligands to membrane-incorporated receptors by a field effect device [Sackmann, 1996], [Hillebrandt, 2002]. (c) Monitoring changes in ionic concentration in the cleft between lipid membrane and solid surface, caused by active membrane transport proteins. Ottenbacher et al. have realized a lactose biosensor based on the cotransport of lactose and  $H^+$  through a lipid membrane containing lactose permease deposited on an ISFET-device. Changes in the lactose concentration resulted in a change in the pH at the transducer surface [Ottenbacher, 1992].

An important prerequisite for the realization of a membrane-based biosensor is the deposition of a fluid and stable lipid membrane on the surface of the transducer device. The lateral mobility of lipids and proteins in the membrane must be sufficient to allow the self-healing of defects and maintain the functionality of membrane-incorporated proteins. The bilayer must



be free of defects to ensure the intrinsically high electrical resistance of lipid membranes, which allows the built up of chemical and electrical gradients, as well as the detection of membrane resistance changes due to specific reaction of membrane channel proteins with the analyte [Tanaka & Sackmann, 2005]. Furthermore, defects act as strong binding sites for proteins and result in nonspecific protein binding [Stelzle, 1993].

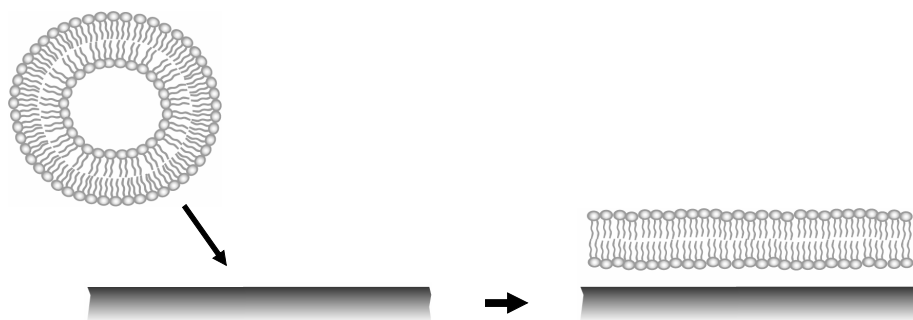
Apart from polymer supported bilayer membranes, where the lipid membrane is separated from the solid surface by a hydrated polymer cushion or tethered polymer spacers [Raguse, 1998], [Sackmann & Tanaka, 2000], [Tanaka & Sackmann, 2005], bilayers can be directly deposited on hydrophilic surfaces [Tamm & McConnell, 1985]. In this case, the thickness of the water film separating the lipid bilayer from the hydrophilic solid support was found to be approximately 20 Å by analysis of the frictional coupling between the bilayer and the thin water film [Merkel, 1989] and in nuclear magnetic resonance experiments [Bayerl & Bloom, 1990]. These results were confirmed by neutron reflectivity measurements [Johnson, 1991].

Solid supported membranes have been deposited directly on indium tin oxide (ITO) and p-type silicon electrodes and electrically characterized [Gritsch, 1998], [Wiegand, 2002], [Purrucker, 2001]. Due to the optical transparency of the ITO substrates to visible light ( $\lambda > 400$  nm), a combined electrical and optical characterization of the membrane properties was possible [Hillebrandt, 2002]. Membrane resistances up to  $100 \text{ k}\Omega \text{ cm}^2$  were achieved. For bilayers deposited on p-type silicon, even membrane resistances as high as  $1 \text{ M}\Omega \text{ cm}^2$  could be reached, which is in the range of free standing black lipid membranes [Montal & Müller, 1972]. Functional incorporation of gramicidin ion channels into supported membranes was demonstrated for both, ITO and p-type silicon electrodes, and a quantitative measurement of selective ion transport was shown [Gritsch, 1998], [Purrucker, 2001].

In this chapter, the realization of artificial cell membranes on hydrophilized group III-nitride surfaces by vesicle fusion and solvent exchange methods is described. Deposition of homogeneous, void free lipid membranes is confirmed by fluorescence microscopy, while the lateral diffusion of lipids is investigated by continuous bleaching analysis (see Section 2.3.2). Special emphasis is placed on the influence of electrostatic interactions between the lipid and the solid substrate on the lateral diffusion. Based on the results of the optical analysis, lipid bilayers and bilayer formation on hydrophilic III-nitride electrodes are electrically characterized by means of impedance spectroscopy. A final discussion of the results with respect to possible improvements concludes the chapter.

### 6.1.1. Preparation of Supported Membranes

For the deposition of lipid bilayers on III-nitride substrates two different methods have been applied: *vesicle fusion* and *solvent exchange* [Brian & McConnell, 1984], [Buboltz & Feigenson, 1999]. Both methods allow the formation of continuous, self-healing membranes with sufficient lateral mobilities on hydrophilic surfaces. Hydrophilization of the GaN-surface was obtained by means of thermal oxidation or wet chemical treatment in



**Figure 6.3:** Bilayer deposition by vesicle fusion on a hydrophilic substrate.

a  $\text{H}_2\text{SO}_4/\text{H}_2\text{O}_2$  3:1 mixture directly before membrane deposition (q.v. Section 3.2). The employed lipids and lipid compositions varied according to the particular experiment.

### Vesicle Fusion

The formation of a lipid bilayer by vesicle fusion is generally accepted to occur in three steps: (i) Vesicle adhesion, (ii) rupturing, and (iii) lateral spreading of the membrane patches and formation of a homogenous layer [Kalb, 1992], [Rädler, 1995] (q.v. Figure 6.3). Usually, small unilamellar vesicles in an aqueous solution are used. The method allows the suitable incorporation of membrane proteins into supported bilayers by the fusion of unilamellar vesicles, which contain the protein. Suspensions of liquid vesicles in buffer solutions were prepared as follows: An appropriate molar mixture of lipids was prepared from chloroform stock solutions in a glass flask. Evaporation of the chloroform under nitrogen atmosphere resulted in the formation of a thin lipid film on the walls of the glass flask. The flask was stored over night in vacuum to remove any traces of chloroform. Then, the dried lipids were dissolved in standard HEPES or PBS buffer to a total lipid concentration of  $1\ \mu\text{M}/\text{ml}$ , heated up to  $70\ ^\circ\text{C}$  and stored for 2 h at  $40\ ^\circ\text{C}$ . The lipid dispersion of multilamellar vesicles was sonicated with a titanium tip sonifier to obtain a clear suspension of unilamellar vesicles. The lipid suspension was centrifuged for 5 min at 5000 rpm to remove titanium particles from the tip sonifier. The resulting vesicle solution was spread on the substrate and incubated for at least 15 min at room temperature before thoroughly rinsing the surface with buffer solution to remove residual vesicles.

### Solvent Exchange

In case of membrane deposition by solvent exchange, a lipid bilayer forms at the hydrophilic substrate surface during the slow exchange of the solvent from alcohol to an aqueous solution (*lyotropic adsorption*) [Buboltz & Feigenson, 1999].

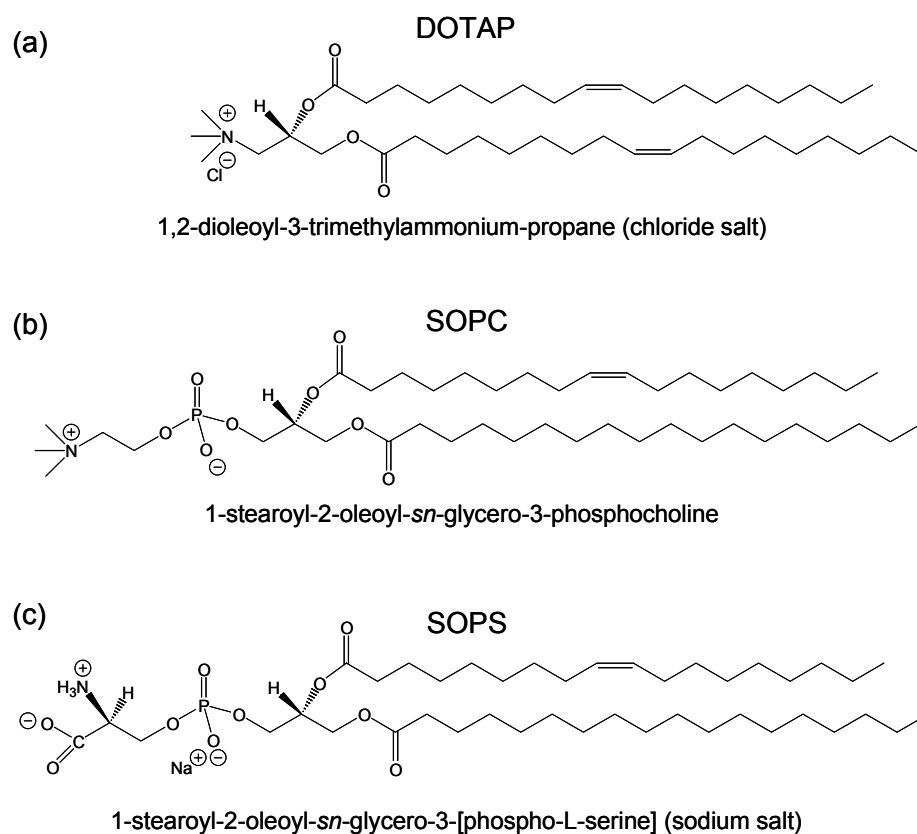
The appropriate amount of lipids from chloroform stock solutions were mixed in a glass flask, evaporated under nitrogen flow and subsequently dried by storage of the flask in a vacuum chamber over night. Isopropanol was added to obtain a total lipid concentration of about 1  $\mu\text{M}/\text{ml}$ . The lipid suspension was then injected into the flow chamber. The isopropanol was slowly exchanged by rinsing the flow chamber with degassed standard PBS buffer. After approximately 2 h, the chamber was extensively rinsed with buffer solution to remove residual lipids and isopropanol.

### 6.1.2 Optical Characterization of Supported Membranes on III-Nitrides

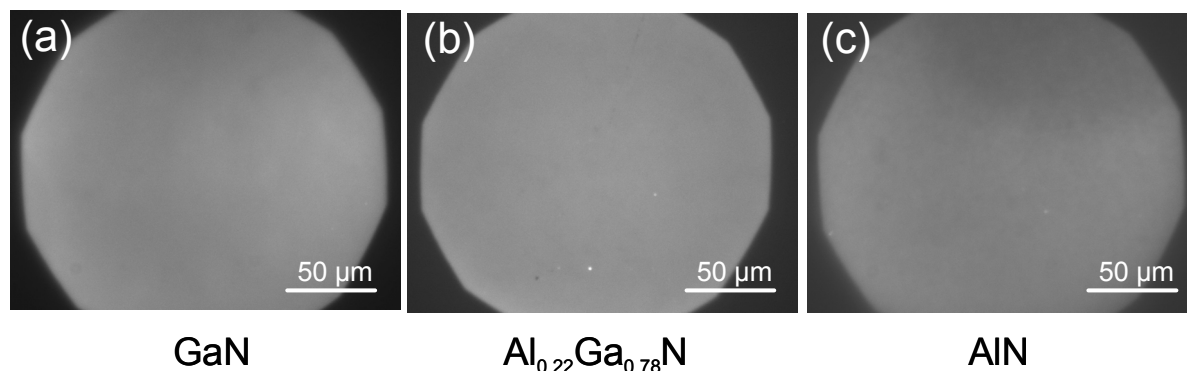
The functionality of solid supported artificial cell membranes regarding biosensor applications or the study of membrane proteins is strongly determined by the lateral fluidity of the membrane. The lateral diffusion of the lipids and proteins in the bilayer is (a) critical to the membrane protein functionality and (b) required to enable the spreading of homogeneous bilayers and the self-healing of membrane defects.

Some groups have reported about the important role of the electrostatic interaction between the membrane and the substrate for the formation of highly resistive supported membranes. Wiegand et al. have found a strong dependence of the bilayer resistance on the ratio of lipids with charged headgroups [Wiegand, 2002]. Further reports claim the necessity of electrostatic attraction between substrate and lipid for the formation of resistive bilayers on functionalized gold [Steinem, 1996] and silicon substrates [Purrucker, 2001].

To investigate the impact of electrostatic interactions at the interface on the membrane fluidity and homogeneity, diffusion constants of lipids with different net-charges of their polar headgroup were compared. For this purpose, bilayers of anionic, zwitterionic, and cationic lipids of equal chain length have been deposited on AlGaIn surfaces by vesicle fusion and examined by fluorescence microscopy. The lateral diffusion constants of lipids were determined by the continuous bleaching technique (see Section 2.3.2). As buffer solution for the vesicle preparation and the diffusion measurements, HEPES-buffer (10 mM HEPES, 50 mM NaCl) titrated to pH 7.5 was used. The chemical structure of the lipids at pH 7.5 is depicted in Figure 6.4. The headgroup of the anionic 1-stearoyl-2-oleoyl-sn-glycero-3-[phospho-L-serine] (SOPS) consists of a zwitterionic serine group and a negative phosphate in the headgroup, resulting in a total negative charge. SOPS has one saturated and one unsaturated fatty acid. The zwitterionic headgroup of the 1-stearoyl-2-oleoyl-sn-glycero-3-phosphocholine (SOPC) comprises a positive choline group and negative phosphate group. The lipid has one saturated and one unsaturated fatty acid. The total positive charge of the 1,2-dioleoyl-3-trimethylammonium-propane (DOTAP) is attributed to the positive trimethylammonium group. Both fatty acids of the DOTAP are unsaturated. The membranes were fluorescence labeled with NBD-PC (see Section 2.3.1). As the described lipids are all in a fluid state at room temperature, an influence on the diffusion properties from a phase transition could be excluded. All lipids were purchased from Avanti Polar Lipids Inc. (Alabama, USA).



**Figure 6.4:** Lipids with differently charged headgroups used for the determination of membrane diffusion constants.

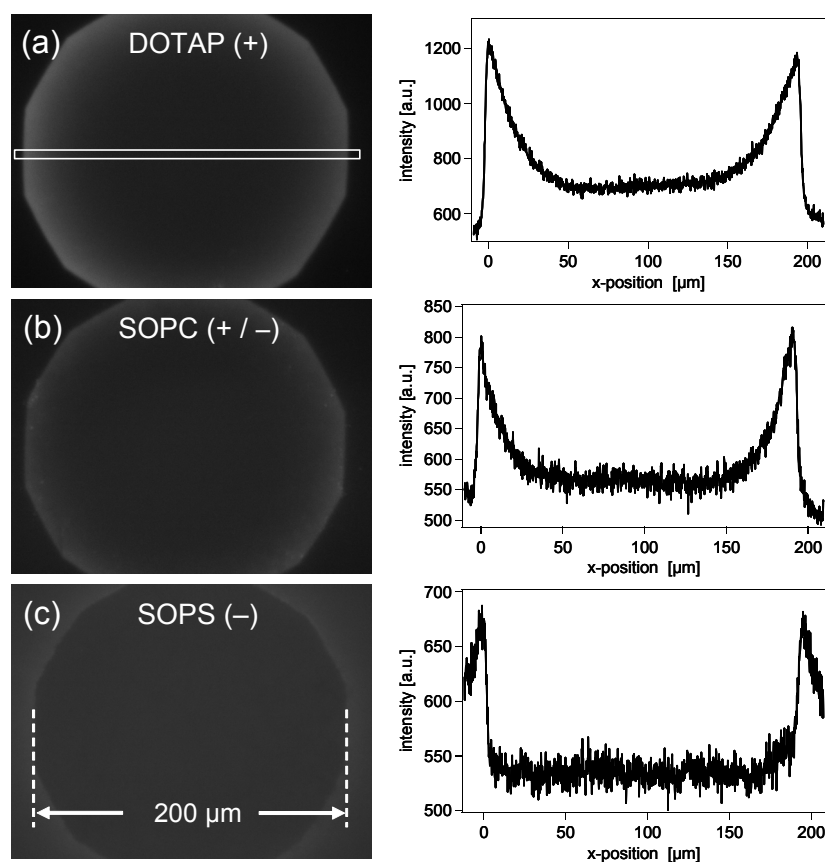


**Figure 6.5:** Fluorescence images of DOTAP membranes deposited on AlGaN surfaces with different aluminum contents.

AlGaN-films with different crystal polarities (Ga-face and N-face) and varying aluminum concentration  $x$  ( $x = 0, 0.22$ , and  $1$ ) have been used for the optical investigations of the lipid bilayer membranes and the interactions at the interface. The III-nitride films have been deposited on double-side-polished sapphire substrates by PAMBE to enable optical access from the backside. Prior to membrane deposition, the III-nitride surfaces have been hydrophilized by wet thermal oxidation for 2 h at  $650^\circ\text{C}$ , which resulted in contact angles of water smaller than  $10^\circ$  and a surface roughness of around  $1 - 1.5$  nm.

For all lipids, the formation of macroscopically large homogeneous membranes (typical area:  $5\text{ mm} \times 5\text{ mm}$ ) was observed. Figure 6.5 shows fluorescence images of membranes containing the cathodic lipid DOTAP deposited on AlGaN with varying aluminum content. No optical difference was observable due to the underlying substrate. Continuous illumination at  $460\text{ nm}$  resulted in bleaching of the fluorescence dyes. In Figure 6.6, fluorescence images after prolonged illumination and the corresponding fluorescence intensity profiles of bilayer membranes consisting of (a) cationic DOTAP, (b) zwitterionic SOPC, and (c) anionic SOPS deposited on Al<sub>0.22</sub>Ga<sub>0.78</sub>N surfaces are depicted. Within the experimental error, the fluorescence profiles appeared to be symmetric in arbitrary directions, indicating isotropic lateral diffusion of the fluorescence labels. A comparison of the extracted intensity line profiles from the left edge for the different lipids on Al<sub>0.22</sub>Ga<sub>0.78</sub>N surfaces, together with the monoexponential fits to derive the decay length  $\lambda$  is given in Figure 6.7. The calculated diffusion constants  $D$  of all investigated lipid membranes on the different III-nitride surfaces are summarized in Table 6.1. The exact determination of the low SOPS diffusion constant was limited by the measurement range of the adopted bleaching technique and not possible for all substrates.

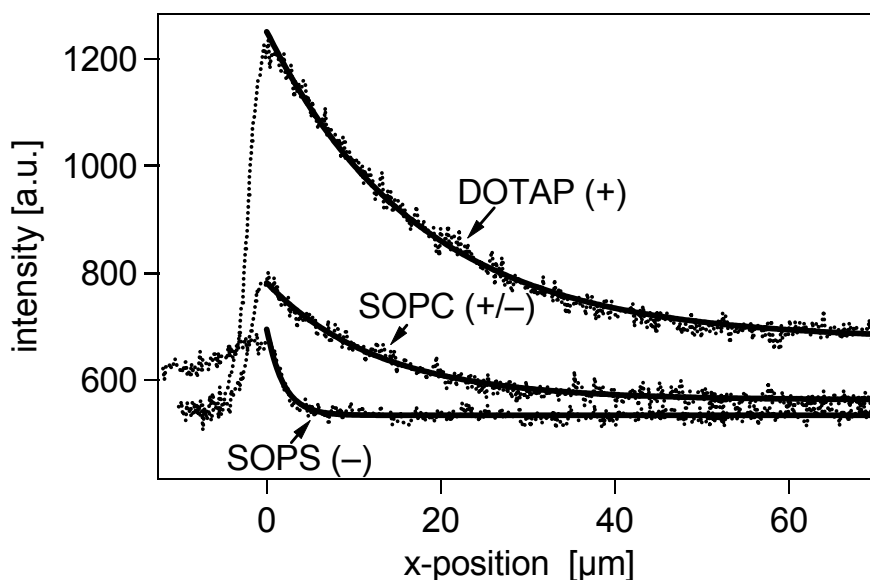
The anionic SOPS membranes exhibited significantly smaller diffusion constants than the other lipids. In contrast, cationic DOTAP membranes yielded the largest diffusion constants. The observed tendency ( $D_{\text{cationic}} > D_{\text{zwitterionic}} > D_{\text{anionic}}$ ) was independent of the chemical composition of the substrate. The supposition of a dominant role of electrostatic interactions



**Figure 6.6:** Continuous bleaching profiles and corresponding intensity profiles across the microscope aperture for membranes of lipids with differently charged headgroups formed on  $\text{Al}_{0.22}\text{Ga}_{0.78}\text{N}$  surfaces.

between the bilayer and the oxidized AlGaN surface on the frictional membrane-substrate coupling can be clearly rejected by measuring diffusion constants of cationic DOTAP on  $\text{c-Al}_2\text{O}_3$  and  $\text{SiO}_2$  substrates. Under the experimental conditions of pH 7.5, the  $\text{SiO}_2$  surface with a point of zero charge of  $\text{pH}_{pzc}=2.6$  [Huang & Stumm, 1973] obtains a negative surface charge, whereas the  $\text{Al}_2\text{O}_3$  surface ( $\text{pH}_{pzc}=8.5$ ) is positively charged [Bousse, 1983]. Nevertheless, no significant difference in DOTAP diffusion has been obtained (see Table 6.1), contradicting clearly the determination of the lateral membrane mobility by electrostatic interaction between charged lipid headgroups and the surface charge on the substrate.

The diffusion constants of the zwitterionic SOPC on AlGaN surfaces are comparable to values found in the literature of  $D_{SOPC} = 3.8 \mu\text{m}^2 \text{s}^{-1}$  for SOPC membranes on glass substrates with polymer cushions [Lee, 2002] or for the nearly identical 1-palmitoyl-2-oleoyl-sn-glycero-3-phosphocholine (POPC, see Appendix A.2) on quartz-slides  $D_{POPC} = 3.4 - 4.0 \mu\text{m}^2 \text{s}^{-1}$  [Kalb, 1992].



**Figure 6.7.:** Comparison of the intensity profiles and monoexponential fits for lipid membranes with different net-charges on hydrophilized  $\text{Al}_{0.22}\text{Ga}_{0.78}\text{N}$  surfaces after prolonged illumination.

In the case of anionic membranes (e.g. SOPS), the low diffusion constants compared to SOPC cannot be explained by the slightly higher melting temperature ( $T_M^{\text{SOPS}} = 12^\circ\text{C}$ ,  $T_M^{\text{SOPC}} = 3^\circ\text{C}$ ) only. Diffusion constants for bilayer membranes in the fluid state above the melting temperature of the lipid alkyl chains are generally of the order of  $\mu\text{m}^2\text{s}^{-1}$  [Tamm & McConnell, 1985]. There have been several reports postulating that traces of divalent cations ( $\text{Ca}^{2+}$ ) can cause not only strong ion bridges between the substrate and the proximal lipid layer [Stelzle, 1992], but also lateral lipid clustering [Feigson, 1986], resulting in inhibited diffusion.

Comparing the chemical structure of DOTAP and SOPC, not only the headgroups but also the alkyl chains are differing, as DOTAP contains two unsaturated alkyl chains in contrast to SOPC with one saturated and one unsaturated alkyl chain. Additional unsaturated chains lead to a significant drop in the membrane melting temperature ( $T_M^{\text{DOTAP}} \approx -20^\circ\text{C}$ ) and reduced interactions between the lipids. However, diffusion constants of  $4.0\mu\text{m}^2\text{s}^{-1}$  were found for the 1,2-dioleoyl-sn-glycero-3-phosphocholine (DOPC) on oxidized silicon [Tamm & McConnell, 1985]. DOPC and DOTAP have identical alkyl chains, but DOPC obtains the same zwitterionic headgroup as SOPC. Thus, a dominating influence of the second unsaturated alkyl chain on the increased DOTAP diffusion can be excluded. The fast lateral diffusion is therefore attributed to the compact TAP-headgroups without the bulky phosphate groups, which provide less sterical stress for lateral diffusion.

charge	DOTAP	SOPC	SOPS
	+	+ / -	-
AlN	7.8	4.2	< 0.1
AlGaN	14.4	3.1	0.16
GaN (0001)	7.3	6.3	< 0.1
GaN (000 $\bar{1}$ )	9.4	3.9	1.1
c-Al <sub>2</sub> O <sub>3</sub> (pH <sub>pzc</sub> 8.5)	6.8	-	-
SiO <sub>2</sub> (pH <sub>pzc</sub> 2.6)	9.9	-	-

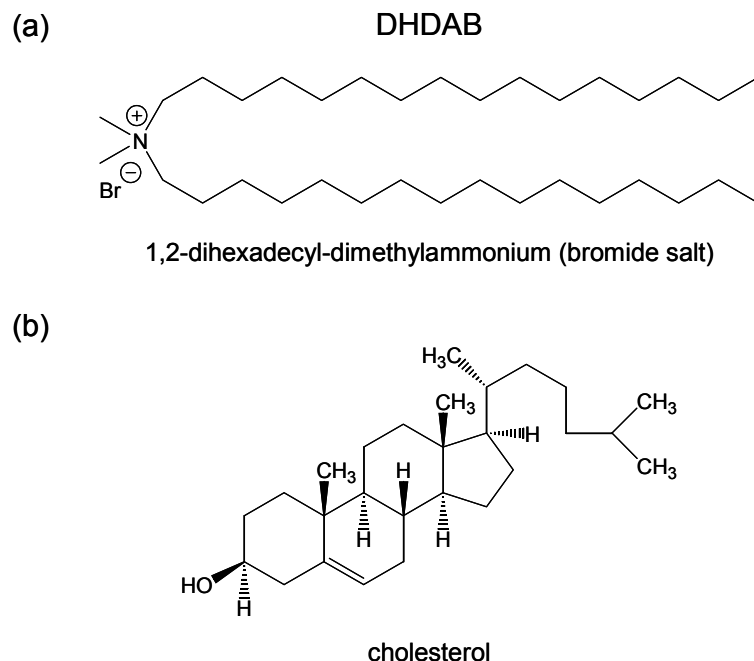
**Table 6.1:** Diffusion constants in [ $\mu\text{m}^2\text{s}^{-1}$ ] of different lipids on oxidized AlGaN, c-Al<sub>2</sub>O<sub>3</sub> and SiO<sub>2</sub> surfaces at pH 7.5, measured by continuous bleaching. The relative experimental error for the determination of the diffusion constants is about 25%.

### 6.1.3. Electrical Characterization of Supported Membranes and Membrane Formation on GaN

Formation of supported lipid membranes on GaN electrodes was observed by impedance spectroscopy on both, MOCVD and PAMBE grown GaN films on sapphire substrates. The electrical bilayer properties were quantified by means of equivalent circuits. Prior to membrane deposition, the GaN surfaces were hydrophilized by either (a) wet thermal oxidation for 2 h at 650 °C, (b) wet chemical surface treatment in H<sub>2</sub>SO<sub>4</sub>/H<sub>2</sub>O<sub>2</sub> (3:1), or (c) oxidation in an oxygen plasma at 500 °C for 2 h (Section 3.2). The bilayer deposition was carried out by the solvent exchange or the vesicle fusion method.

The optical membrane characterization in Section 6.1.2 revealed high diffusion constants for bilayers consisting of cationic or zwitterionic lipids, whereas anionic lipid membranes exhibited significantly lower lateral mobility. Thus, positively charged and neutral lipids (DHDAB, DOPC, DPPC, DPhPC, see Appendix A.2) were used for the studies of electrical membrane characteristics. To obtain the lipid bilayers in their fluid liquid crystalline phase at room temperature, they were mixed in different concentrations with cholesterol. Incorporation of cholesterol, which is a main component of most membranes in living cells, broadens or eventually eliminates the phase transition between the gel and liquid crystalline phase of lipid bilayers. Additionally, cholesterol increases the orientational order of the alkyl chains in fluid membranes and reduces their permeability to water and ions [Yeagle, 1985], [McMullen & McElhaney, 1996]. The enhanced membrane barrier properties with cholesterol incorporation, which go along with increased electrical membrane resistance, have been reported for native cell membranes, such as the eucaryotic plasma membrane [Yeagle, 1985], as well as for solid supported bilayer membranes on silicon or ITO substrates [Purrucker, 2001], [Wiegand, 2002].





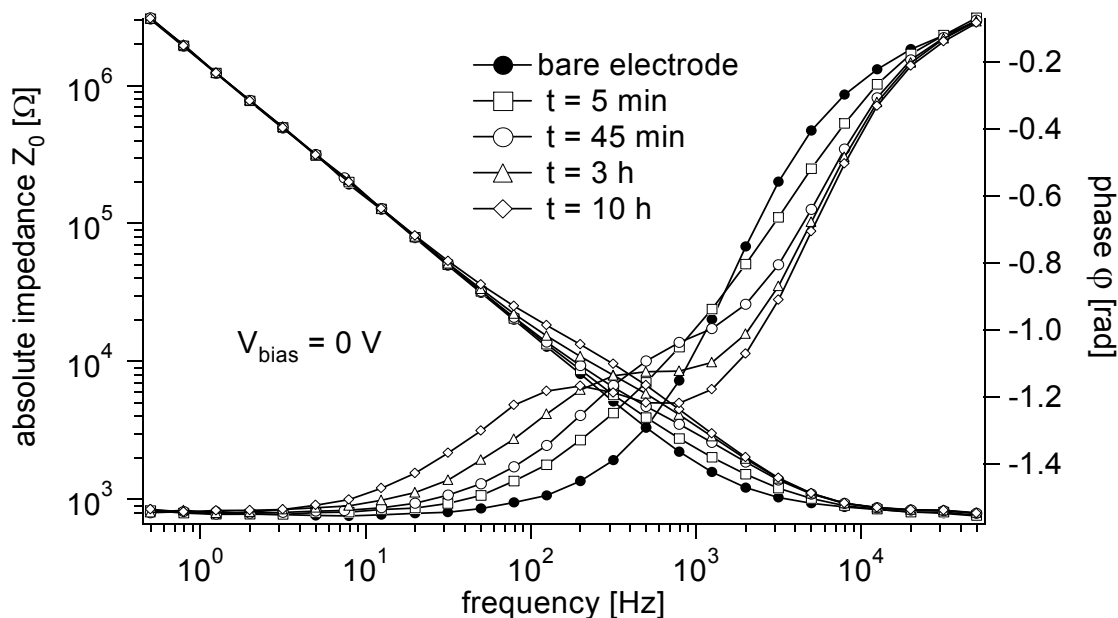
**Figure 6.8:** Chemical structure of (a) 1,2-dihexadecyl-dimethylammonium-bromide (DHDAB), and (b) cholesterol.

The most promising results regarding membrane resistivity were obtained for the cathodic lipid 1,2-dihexadecyl-dimethylammonium-bromide (DHDAB) in a 1:1 molar mixture with cholesterol. The chemical structures of both molecules are depicted in Figure 6.8. Experiments with other lipids and lipid mixtures (DHDAB, DOPC DPPC, DPhPC) in varying ratios with cholesterol were also performed and some bilayer formation could be observed by impedance spectroscopy. However, the obtained electrical membrane resistances were inferior to DHDAB/cholesterol mixtures by at least one order of magnitude. The electrical membrane characterizations presented in this work were solely obtained from supported DOTAP/cholesterol bilayers.

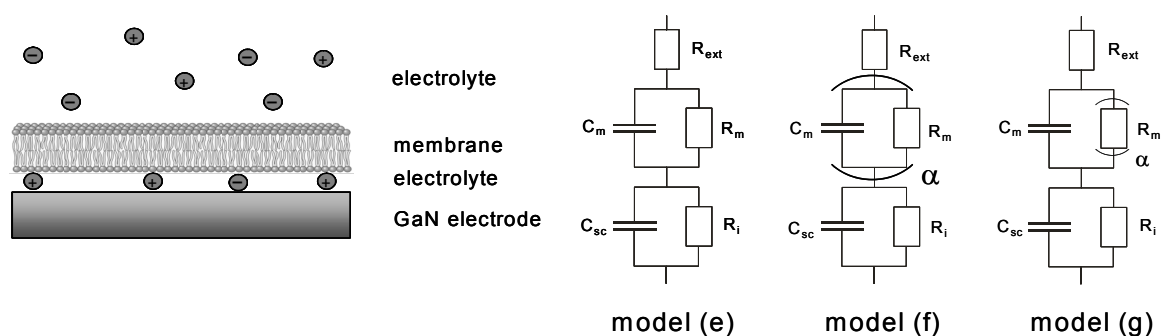
Membrane formation could be monitored in real time by sequential recording of impedance spectra at  $V_{bias} = 0$  V (vs. Ag/AgCl). Figure 6.9 shows the impedance spectra of a bare GaN electrode and at different times after the bilayer deposition by vesicle fusion. The measurements were started directly after the injection of the vesicle solution into the flow cell.

### Electrical Models for Solid Supported Lipid Membranes

Supported bilayer membranes are separated from the hydrophilic substrate surface by a thin water layer of approximately 20 Å thickness [Merkel, 1989]. The resulting electrolyte-membrane-electrolyte-semiconductor (EMES) system is depicted in Figure 6.10. In a simple model



**Figure 6.9.:** Impedance spectra of a bare GaN electrode obtained at  $V_{bias} = 0V$  at different times after the membrane deposition by vesicle fusion.



**Figure 6.10.:** Schematic of an electrolyte-membrane-electrolyte-semiconductor (EMES) structure (left). Equivalent circuit models representing an EMES structure. The membrane values are extracted by applying an ideal  $R_m C_m$  element in model (e) or an element of distributed time constants in model (f). In the equivalent circuit model (g), the ideal element of the membrane resistance was replaced by a constant phase element (right). An overview of all equivalent circuit models employed for the evaluation of impedance data in this work is given in Appendix A.5.

consisting only of ideal circuit elements, the EMES-structure can be electrically represented by an RC element accounting for the membrane, in series with the equivalent circuit of the semiconductor/electrolyte junction. The corresponding equivalent circuit model (e), which assumes the membrane as a homogeneous layer with low but finite conductance, is also given in Figure 6.10. The dielectric bilayer properties are described in terms of a membrane capacitance  $C_m$  and a membrane resistance  $R_m$ . In the following, a fit according to model (e) is denoted as *ideal element fit*. Lateral membrane inhomogeneities such as defects or domains can be considered in a parallel connection of multiple RC elements. However, this parallel connection is electrically equivalent to a single RC element with averaged values for membrane capacitance  $C_m$  and resistance  $R_m$ . Wiegand et al. have introduced the *model of distributed time constants* for supported bilayer membranes (*distributed  $\tau$  fit*) [Wiegand, 2002] to account for electrical heterogeneities across the lipid membrane, as each leaflet of the bilayer membrane can be divided into three layers with strongly varying dielectric properties: (i) the GCS-layer, (ii) the polar hydrophilic lipid headgroups, and (iii) the nonpolar hydrophobic alkyl chains [Sackmann, 1995]. Each layer is electrically represented by an independent RC element. The resulting linear array of six RC elements is replaced by a distribution of time constants with an average time constant  $\tau = R_m C_m$ , in order to reduce the number of free parameters (model (f) in Figure 6.10). The impedance is then expressed by

$$Z_{RC^\alpha} = \frac{R_m}{1 + (i\omega\tau)^\alpha}, \quad (6.1)$$

where  $\alpha$  ranges between 1 and 0, corresponding to an ideal RC element ( $\alpha = 1$ ) or an ideal resistor ( $\alpha = 0$ ). In model (g), the resistance of the RC element representing the lipid bilayer is replaced by a CPE (*CPE fit*) to test the ideality of model (e), in which the bilayer is described by ideal elements only.

The fits of the different equivalent circuit models (e), (f) and (g) to the impedance spectra of a supported bilayer membrane on a MOCVD GaN electrode after completed bilayer formation are depicted in Figure 6.11 (a). All three models lead to a good agreement with the impedance data. The respective values extracted by the different equivalent circuits are summarized in Table 6.2. The residuals in logarithmic absolute impedance obtained by fitting with the three models are presented in Figure 6.11 (b).

In contrast to the results of Wiegand et al. on ITO-electrodes [Wiegand, 2002], where substantially smaller residuals were reported for the model (f) of distributed time constants compared to the simple model (e) of ideal elements, only slightly smaller residuals were obtained by the distributed  $\tau$  fit. Furthermore, the extracted value for the exponent  $\alpha$  of 0.98 was much closer to the ideal value of  $\alpha = 1$  than the value of  $\alpha = 0.89$  found by [Wiegand, 2002], indicating a more ideal dielectric membrane behavior. Thus, accounting for the electrical heterogeneities along the axis of the lipid molecules by utilization of model (f) of distributed time constants does not lead to a considerable improvement of the data fit in comparison to the simple model (e). Apparently, the consideration of electrical heterogeneities in vertical membrane direction is of minor importance.

Exchange of the bilayer resistance of model (e) with a CPE element reduced the residuals by a factor of two, and the exponent  $\alpha$  was estimated to 0.08. Due to the good accordance of

the fit model (e) of ideal elements with the obtained impedance spectra and the only slight improvement of the fit quality by the introduction of non-ideal elements, which goes along with additional fit parameters, the equivalent circuit (e) was mainly used for the interpretation of the impedance data of solid-supported membranes on III-nitride substrates.

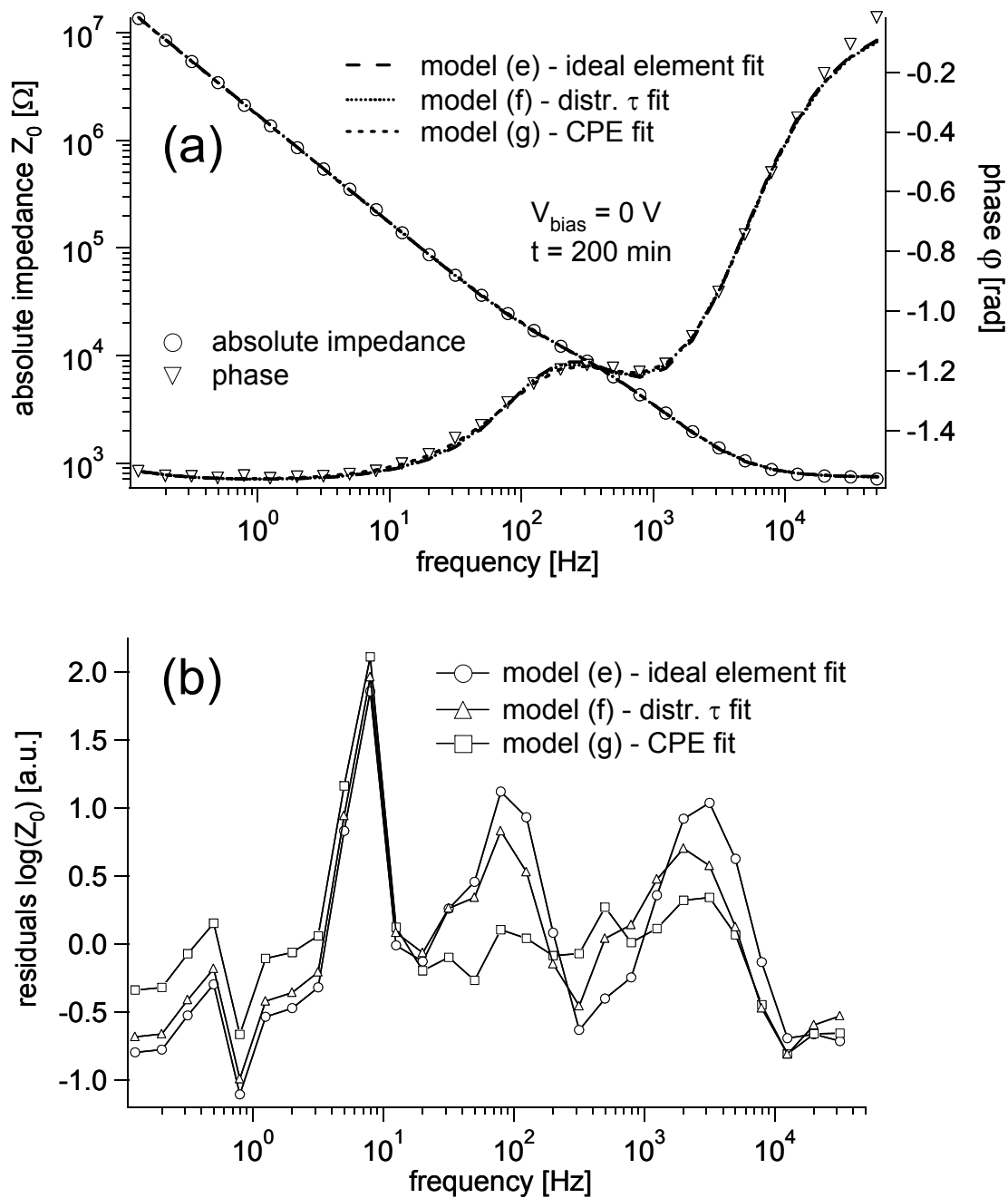
model	membr. resistance $R_m$ [k $\Omega$ cm $^2$ ]	membr. capacitance $C_m$ [ $\mu$ F cm $^{-2}$ ]	$\alpha$
(e) - ideal element fit	$0.73 \pm 0.02$	$0.71 \pm 0.01$	—
(f) - distr. $\tau$ fit	$0.77 \pm 0.03$	$0.74 \pm 0.02$	$0.98 \pm 0.01$
(g) - CPE fit	$1.3 \pm 0.1$	$0.67 \pm 0.02$	$0.08 \pm 0.01$

**Table 6.2:** Electrical properties of a supported bilayer membrane on a MOCVD GaN electrode extracted either by the ideal element fit model (e), the distributed  $\tau$  fit model (f), or the CPE fit model (g).

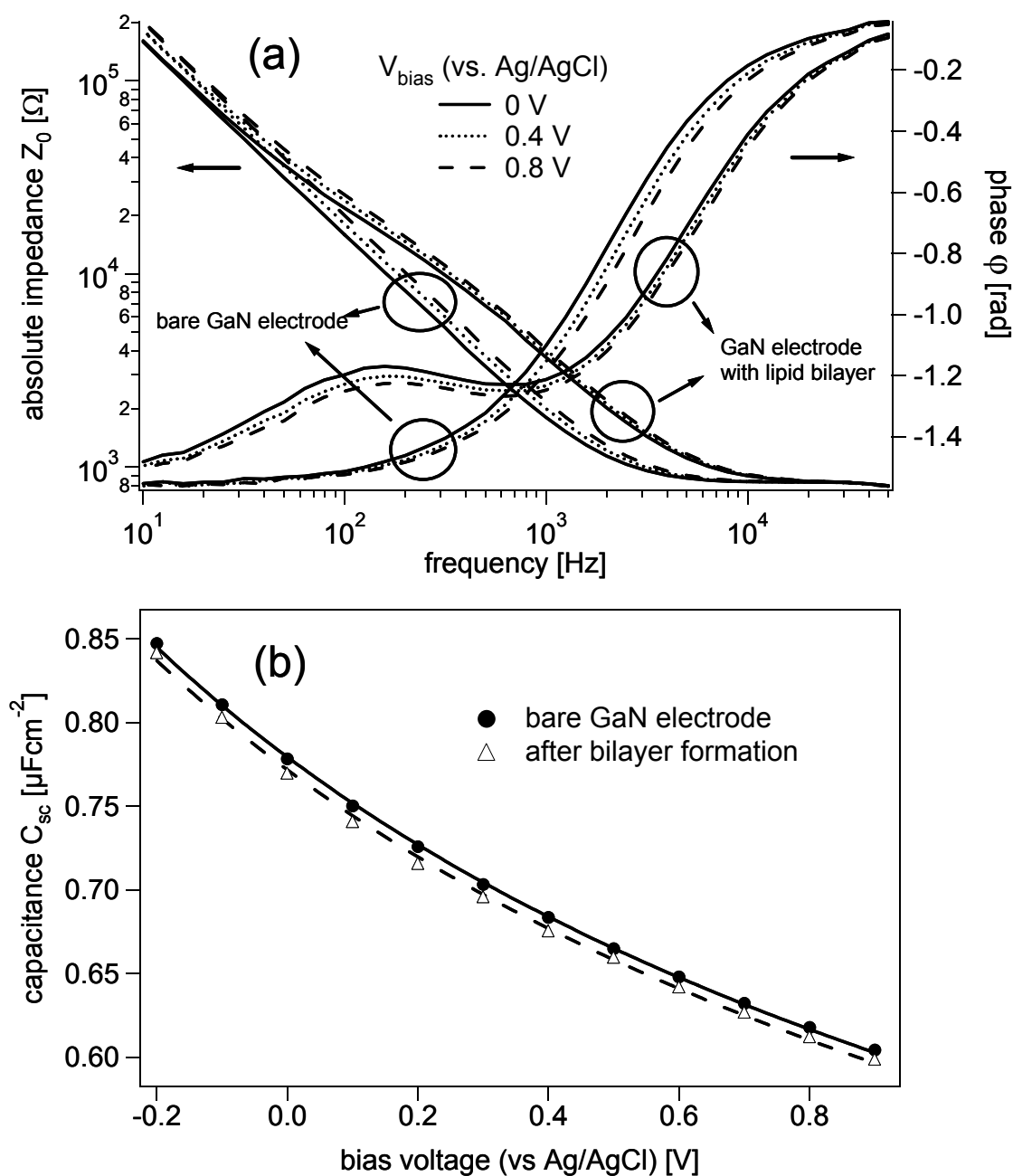
A further prerequisite for the accurate determination of the dielectric membrane properties from impedance data is the effective separation of various contributions to the total system impedance. In the used experimental setup, described in Section 2.2.1, the contribution of a bilayer with a capacitance between  $0.5 - 1 \mu\text{F cm}^{-2}$  can only be resolved for membrane resistances larger than  $50 \Omega \text{ cm}^2$ . For membranes with a higher resistance, application of the equivalent circuit model (e) provided an independent determination of the electrical parameters of the membrane and the subjacent GaN electrode. Figure 6.12 (a) shows impedance spectra of a GaN electrode before the membrane deposition and after completed bilayer formation, each for different applied bias potentials. The dependence of the electrode capacitance on the applied bias voltage, extracted by the equivalent circuit model (b) (e.g. Section 5.3.1) and (e) before and after membrane formation, is shown in Figure 6.12 (b). The behavior of a nearly ideal semiconductor depletion layer was found in both cases, and identical doping densities were derived by fitting with the Mott-Schottky model (Eq. (A.8)). A small shift in flatband voltage of 8 mV was obtained after the bilayer deposition. The described results clearly show the possible independent analysis of the various dielectric layers by impedance spectroscopy and fitting with the proposed equivalent circuit model.

### Electrical Bilayer Properties and Membrane Formation

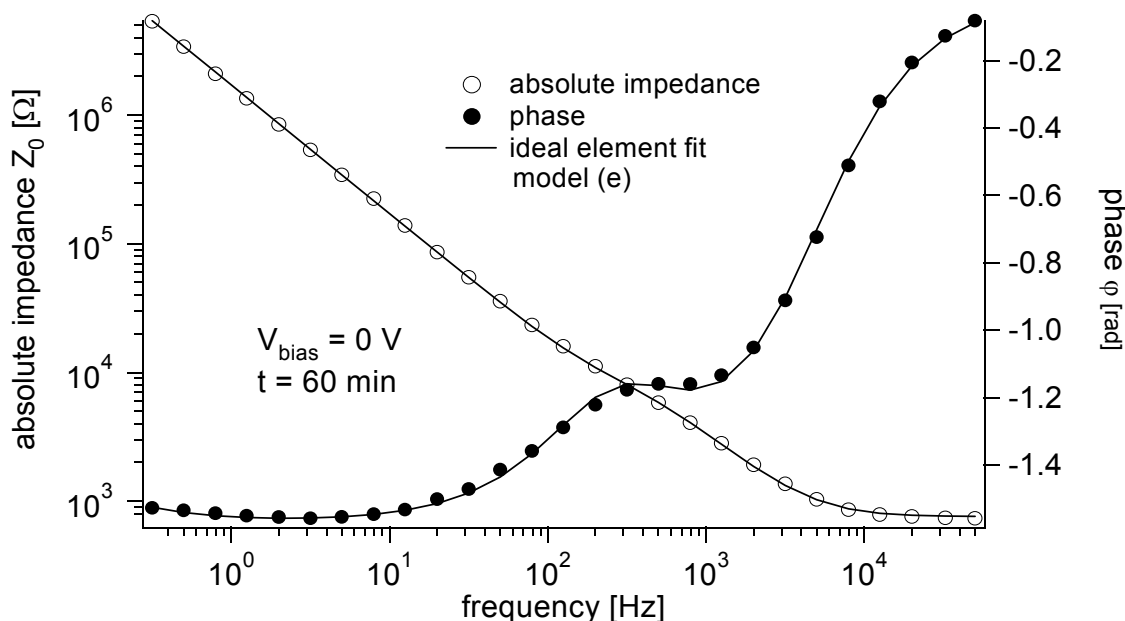
Figure 6.13 shows an impedance spectrum taken during the formation of a bilayer membrane on a MOCVD GaN electrode hydrophilized by wet chemical surface treatment. The solid line depicts a fit to the impedance data applying the ideal element fit. The self-healing process of the membrane can be monitored by extraction of the membrane capacitance  $C_m$  and the membrane resistance  $R_m$  as a function of incubation time. In Figure 6.14 (a), the time dependence of  $C_m$  and  $R_m$  obtained by the equivalent circuit (e) is shown. The extracted membrane resistance  $R_m$  increases over time up to a final value of around  $730 \Omega \text{ cm}^2$ , whereas the membrane capacitance  $C_m$  decreases to a constant value of approximately  $0.7 \mu\text{F cm}^{-2}$ . Both trends are discussed in



**Figure 6.11.:** (a) Impedance data and corresponding fits for a supported lipid bilayer on a GaN electrode. For fitting, the equivalent circuit models (e), (f), and (g) of Figure 6.10 have been applied. (b) Residuals in logarithmic absolute impedance  $Z_0(\omega)$  ( $\circ$ ,  $\triangle$ ,  $\square$ ) obtained by the fitting with the different equivalent models (e), (f), and (g), respectively.



**Figure 6.12:** (a) Impedance spectra of a bare GaN electrode and after completed membrane formation at different bias potentials. (b) Capacitance of the GaN electrode vs. the applied bias potential, extracted by the equivalent circuit models (b) and (e) before and after membrane formation. The solid (—) and dashed (---) lines represent the corresponding fits according to the Mott-Schottky equation of an idealized semiconductor depletion layer (Eq. (A.8)).

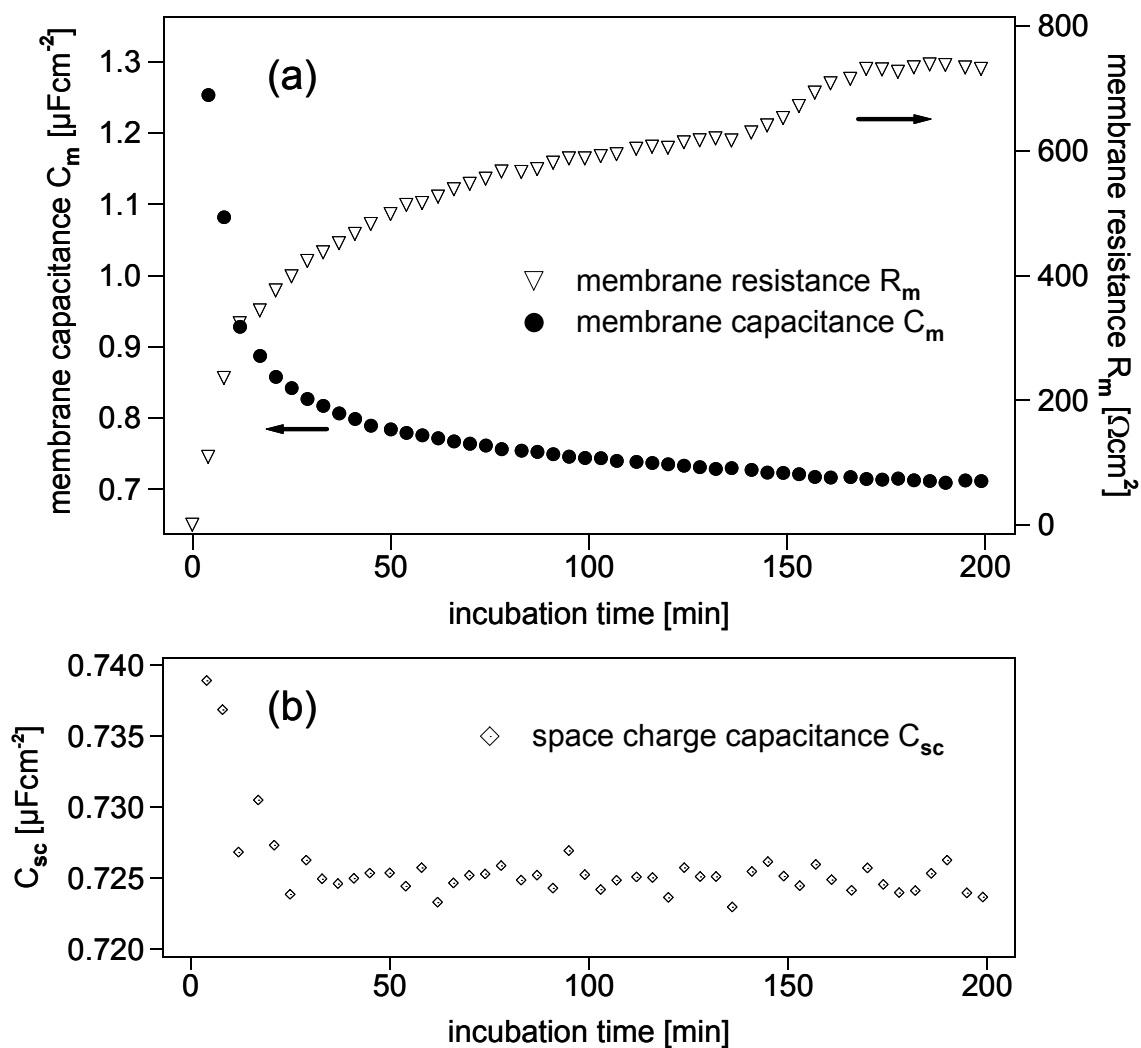


**Figure 6.13:** Impedance spectrum of a lipid membrane after an incubation time of 1 h. The solid lines (—) represent the fit of the impedance data by the equivalent circuit model (e).

the following sections. Directly after deposition of the bilayer, a small drop in the extracted capacitance of the GaN electrode  $C_{sc}$  is observable. Later during the bilayer growth,  $C_{sc}$  stays fairly constant at a value of  $0.725 \mu\text{F cm}^{-2}$ . The variations in the initial stage of the membrane formation result from the fast change of the system during the recording of a single impedance spectrum, which takes several minutes. The stability of the fitted capacitance of the GaN electrode and the continuity of the extract membrane properties over time confirm the accurate separation of the two time constants of the system, the time constant of the GaN electrode and that of the lipid membrane. Fitting of the time dependent impedance spectra with model (f) or (g) lead to different values for the extracted electrical parameters, but similar transient behavior.

### Bilayer Resistance and Membrane Defects

The continuous increase of the membrane resistance with increasing incubation time is a clear indication for the self healing process of the lipid bilayers deposited directly on GaN surfaces. However, the average final value for the membrane resistance of  $R_m \approx 1 \text{ k}\Omega \text{ cm}^2$  is far smaller than those values reported for solid-supported membranes on other semiconductor materials. On ITO and p-type silicon substrates, membrane resistances as high as  $100 \text{ k}\Omega \text{ cm}^2$  and  $1 \text{ M}\Omega \text{ cm}^2$  were achieved by comparable lipid mixtures [Gritsch, 1998], [Purrucker, 2001]. For bilayers deposited on gold surfaces functionalized by a SAM of mercaptopropionic acid, membrane resistances of  $0.46 \text{ M}\Omega \text{ cm}^2$  have been reported [Steinem, 1997]. Even higher resistances



**Figure 6.14:** (a) Formation of the lipid membrane as a function of incubation time. The membrane capacitance  $C_m$  (●) and resistance  $R_m$  (▽) were extracted by applying the equivalent circuit model (e). (b) Corresponding extracted values for the capacitance of the GaN space charge region (◇).



as high as  $1 - 5 \text{ M}\Omega \text{ cm}^2$  and  $7 \text{ M}\Omega \text{ cm}^2$  have been reached for tethered lipid bilayer membranes on gold electrodes by several groups [Raguse, 1998], [Terrettaz, 2003]. A discussion of possible reasons for the comparatively low membrane resistance reached here is given below.

Nevertheless, the membrane resistance of  $1 \text{ k}\Omega \text{ cm}^2$  is a clear indication for a bilayer with a low defect density and therefore preserved self healing properties. A simple estimation of the area ratio of the membrane defects can be made under the following assumptions: (i) The resistance of a defect free planar lipid bilayer is around  $10 \text{ M}\Omega \text{ cm}^2$  [Montal & Müller, 1972], [Hanke & Schlue, 1993]. Hence, the conductance of a low resistive membrane is dominated by bilayer defects. (ii) The membrane defects are of cylindrical shape and filled with electrolyte. The resistance of a defect is determined by the conductivity of the electrolyte  $\sigma_{el}$ , which is  $5.81 \cdot 10^{-3} \Omega^{-1} \text{ cm}^{-1}$  for the 50 mM NaCl solution used during the membrane deposition experiments. Hence, the resistance of a defect is calculated as

$$R_{def} = \frac{1}{\sigma_{el}} \cdot \frac{d_m}{A_{def}}, \quad (6.2)$$

with the membrane thickness  $d_m$  and the defect area  $A_{def}$ . The area normalized membrane resistance is then given by

$$R_{mem} = \frac{1}{\sigma_{el}} \cdot \frac{d_m}{x}, \quad (6.3)$$

with a defect area ratio  $x = \frac{A_{def}}{A_{ges}}$ . For a membrane thickness of  $30 - 40 \text{ \AA}$  and a membrane resistance of around  $1 \text{ k}\Omega \text{ cm}^2$ , a defect area ratio lower than  $10^{-7}$  is derived.

### Bilayer Capacitance and Estimated Bilayer Thickness

In this study, a decrease in the membrane capacitance with incubation time was observed, and final values of approximately  $0.7 \mu\text{F cm}^{-2}$  were extracted by the equivalent circuit model (e). Comparable values of  $C_m = 0.71 \mu\text{F cm}^{-2}$  for an identical lipid composition of DHDAB and cholesterol on p-type silicon substrates, which have been evaluated by the same equivalent circuit, were reported by Purruicker et al. [Purruicker, 2001]. A similar trend for the reduction of the membrane capacitance during membrane formation was observed. However, no explanation was given for this behavior. The data obtained by Steinem et al. for a lipid monolayer consisting only of DPPC, a phospholipid with identical alkyl chain length, show a DPPC bilayer capacitance of  $0.52 \mu\text{F cm}^{-2}$  [Steinem, 1996]. In general, membrane capacitances of  $0.5 - 1 \mu\text{F cm}^{-2}$  have been reported for solvent-free solid supported lipid bilayers on different substrates, depending on the lipid composition, the cholesterol content and the preparation technique [Lang, 1994], [Steinem, 1996], [Gritsch, 1998], [Raguse, 1998], [Steinem, 1998], [Purruicker, 2001], [Terrettaz, 2003].

The observed reduction of the membrane capacitance with incubation time cannot be explained by the healing of membrane defects. As pointed out in Section 6.1.3, the capacitance contribution of the bilayer is only notable for membrane resistances larger than  $50 \Omega \text{ cm}^2$ , which already

corresponds to a relative defect area as low as  $10^{-6}$ . Accordingly, the electrode surface is almost completely covered by a lipid bilayer already after several minutes of incubation, when the first spectra with perceptible bilayer contribution to the total impedance are recorded. The healing of membrane defects therefore has only a marginal influence on the total membrane capacitance. On the other hand, for membranes with high cholesterol content homogenization can cause a reduction of the membrane capacitance, as shown in the following.

The thickness  $d$  of the hydrophobic region of a lipid bilayer, which corresponds to the region of the hydrocarbon chains, can be evaluated from the experimentally obtained capacitances according to

$$d = \frac{\varepsilon_r \varepsilon_0}{C_m} \quad (6.4)$$

where  $C_m$  is the capacitance per unit area and  $\varepsilon_r$  the dielectric permittivity of the alkyl chains. Due to the considerably higher capacitance of the polar headgroup region of approximately  $30 \mu\text{F cm}^{-2}$  [Coster & Smith, 1974], their contribution to the total capacitance is generally neglected [Requena & Haydon, 1975]. By assuming an average value of 2.2 for the dielectric coefficient,  $\varepsilon_r$ , of long-chain hydrocarbons [Montal & Müller, 1972], [Requena & Haydon, 1975], a dielectric thickness of around  $28 \text{ \AA}$  can be estimated for the membrane hydrocarbon region. The assumption is justified by reports of Fettiplace et al., who found that the membrane dielectric constant is not significantly changed in the presence of cholesterol [Fettiplace, 1975]. Supposing all-*trans* conformation, the length of an unsaturated hydrocarbon chain consisting of 16 carbon atoms can be calculated to  $19 \text{ \AA}$ , assuming a C-C bond length of  $1.545 \text{ \AA}$  and  $110.5^\circ$  for the  $sp^3$ -hybrid bond angle. However, due to gauche defects the effective alkyl chain length is markedly reduced depending on the temperature [Hoppe, 1983]. From the average chain length of DMPC lipids obtained by NMR [Douliez, 1996], the average alkyl chain length of DHDAP can be estimated to  $14.6 \text{ \AA}$  at  $25^\circ\text{C}$ . Incorporation of cholesterol into a bilayer membrane has been shown to increase the order of the hydrocarbon chains due to the tendency to adopt more *trans*-configuration [Yeagle, 1985]. In DMPC membranes, the average number of gauche defects is reduced by about two gauche defects per chain (from  $\approx 3$  to  $\approx 1$ ) by the presence of 30 mol % cholesterol, therefore increasing the average alkyl chain length markedly by about  $3.5 \text{ \AA}$  per chain at  $25^\circ\text{C}$  [Douliez, 1996]. The resulting dielectric bilayer thickness of  $36 \text{ \AA}$  assuming a lipid alkyl chain length of 16 and a cholesterol content of 30 mol % is a bit larger than the derived dielectric membrane thickness of  $28 \text{ \AA}$  for a DHDAP/cholesterol 1 : 1 molar mixture, but still of the same order.

A slow homogenization of the cholesterol distribution in the bilayer during the membrane formation process could partly explain the observed time dependence of the membrane capacitance. Depending on the experimental conditions, cholesterol-rich and cholesterol-poor domains as well as the formation of pure cholesterol domains can be observed in bilayers with high cholesterol contents [McMullen & McElhaney, 1996]. Incorporation of cholesterol into the cholesterol-poor domains of a DHDAP would increase the bilayer thickness from  $29.2 \text{ \AA}$  to  $36.2 \text{ \AA}$ , resulting in a reduction of the membrane capacitance from  $0.67 \mu\text{F cm}^{-2}$  to  $0.52 \mu\text{F cm}^{-2}$ .

The obtained membrane capacitance of  $C_m = 0.71 \mu\text{F cm}^{-2}$  and the corresponding dielectric thickness of  $28 \text{ \AA}$  strongly suggest a solvent free bilayer, as a significant decrease in membrane capacitance to  $C_m = 0.4 \mu\text{F cm}^{-2}$  has been reported for the incorporation of an organic solvent such as n-decane into the membrane, which had lead to an increased thickness of the hydrophobic region of lipid bilayers [Montal & Müller, 1972]. Furthermore, the formation of a layered arrangement of various bilayers or bilayer patches, which could also be responsible for the increased membrane resistance can be excluded. A comparison of the obtained dielectric bilayer thickness with the estimated hydrocarbon length suggests the formation of a single bilayer membrane with increasing resistance due to the healing of membrane defects with incubation time.

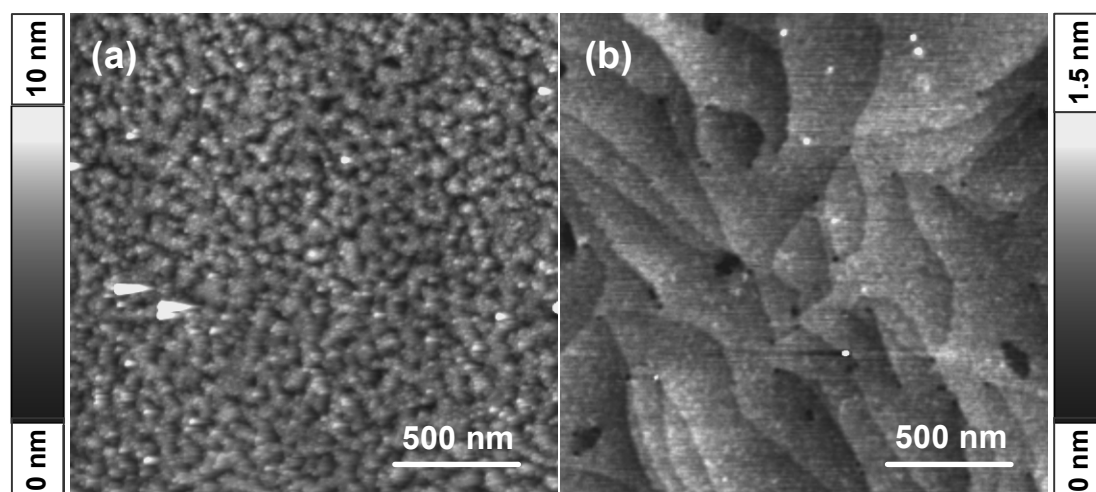
### Supported Membranes on PAMBE GaN Electrodes and the Influence of Surface Roughness

In addition to the electrical characterization of supported membranes on MOCVD GaN electrodes, bilayer formation could also be observed on GaN films grown by PAMBE on sapphire substrates. Due to their higher doping levels of  $3 \times 10^{19} \text{ cm}^{-3} - 1 \times 10^{20} \text{ cm}^{-3}$ , the PAMBE GaN electrodes exhibited a higher capacitance of approximately  $1 - 3 \mu\text{F cm}^{-2}$  at  $V_{bias} = 0 \text{ V}$  (vs. Ag/AgCl). The GaN layers deposited by the different growth methods and hydrophilized either by thermal oxidation or wet chemical treatment showed a significant difference in their surface morphology. The hydroxylated MOCVD surfaces exhibited a low roughness ( $< 0.5 \text{ nm rms}$ ) and terraces typical for two-dimensional growth (Figure 6.15 (b)), whereas the surface roughness of a thermally oxidized PAMBE surface as shown in Figure 6.15 (a) was significantly larger ( $1.5 \text{ nm rms}$ ). Despite the significantly higher surface roughness, the formation of bilayer membranes was also observed on PAMBE grown GaN films, and membrane resistances comparable to the values on MOCVD GaN were achieved. The dielectric membrane properties of a bilayer deposited by the vesicle fusion method on a PAMBE GaN electrode and calculated by the equivalent circuits (e), (f), and (g) are given in Table 6.3.

	membr. resistance $R_m$ [k $\Omega$ cm $^2$ ]	membr. capacitance $C_m$ [ $\mu\text{F cm}^{-2}$ ]	$\alpha$
(e) - ideal element fit	$0.65 \pm 0.04$	$0.86 \pm 0.04$	—
(f) - distr. $\tau$ fit	$0.83 \pm 0.05$	$1.04 \pm 0.06$	$0.88 \pm 0.02$
(g) - CPE fit	$3.4 \pm 0.5$	$0.66 \pm 0.03$	$0.23 \pm 0.02$

**Table 6.3:** Membrane resistance,  $R_m$ , and capacitance,  $C_m$ , for a lipid bilayer deposited by vesicle fusion on PAMBE grown GaN films.

The main difference in comparison to the results on MOCVD GaN are the much larger deviations of the distributed  $\tau$  and the CPE fit model with non-ideal elements from the fit by an ideal element circuit, reflected in the exponent  $\alpha$ . The value of  $\alpha = 0.88$  for the distributed  $\tau$  fit corresponds quite well to values of  $\alpha = 0.89$  for ITO-electrodes reported in Ref. [Wiegand, 2002].



**Figure 6.15:** AFM images of (a) a thermally oxidized PAMBE GaN surface (2 h at 650 °C), and (b) a hydroxylated MOCVD GaN surface, which exhibits the typical morphology due to two-dimensional growth.

Wiegand et al. have attributed the deviation from the behavior of an ideal circuit to electrical heterogeneities along the axis of the lipid molecules, caused by the different dielectric properties of the membrane layers (see Section 6.1.3). However, the results obtained on GaN electrodes strongly suggest a correlation of the ideality of the membrane reflected by the exponent  $\alpha$  and the roughness of the supporting solid substrate, as ITO-electrodes as well have been reported to exhibit rough surfaces with a rms value as high as 2.5 nm [Hillebrandt, 2001]. This conclusion is further corroborated by the results obtained by Purruicker et al. for supported bilayer membranes on smooth oxidized silicon substrates, as the circuit model (e) of ideal elements showed a high correlation with the recorded impedance data, and no introduction of non-ideal components was necessary [Purruicker, 2001].

Furthermore, it can be concluded that the surface roughness is not the limiting factor for the membrane resistance in the case of MOCVD grown GaN substrates, as equal membrane resistances were found for PAMBE grown films with significantly higher surface roughness.

### Membrane Deposition by Solvent Exchange

Membranes deposited by vesicle fusion and solvent exchange on PAMBE GaN electrodes were compared by impedance spectroscopy. A bilayer formation was also observable after a membrane preparation by solvent exchange, and the electrical parameters estimated by the equivalent circuits (e) - (g) are summarized in Table 6.4. No significant differences in the membrane capacitance due to the preparation method were obtained, and comparable membrane resistances around  $1 \text{ k}\Omega \text{ cm}^2$  were reached. Therefore, it can be concluded that the electrical

	membr. resistance $R_m$ [k $\Omega$ cm $^2$ ]	membr. capacitance $C_m$ [ $\mu$ F cm $^{-2}$ ]	$\alpha$
(e) - ideal element fit	$0.75 \pm 0.05$	$0.82 \pm 0.03$	—
(f) - distr. $\tau$ fit	$1.02 \pm 0.08$	$0.98 \pm 0.05$	$0.89 \pm 0.02$
(g) - CPE fit	$4.4 \pm 0.2$	$0.65 \pm 0.01$	$0.23 \pm 0.01$

**Table 6.4:** Membrane resistance,  $R_m$ , and capacitance,  $C_m$ , for a lipid bilayer deposited by solvent exchange on PAMBE grown GaN films.

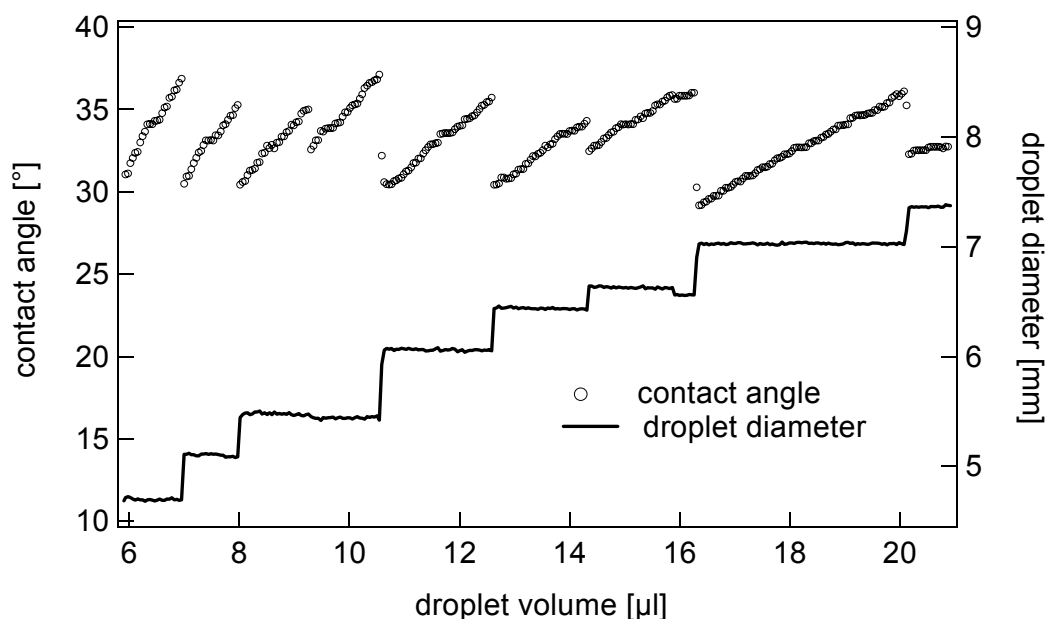
membrane parameters, particularly the resistance are independent of the preparation method but depend on the surface properties.

### Dynamic Contact Angle Experiments

In the previous sections it has been shown that the formation of lipid bilayer membranes on hydrophilized GaN surfaces is possible and membrane formation can be observed by impedance spectroscopy. Whereas the extracted membrane capacitance,  $C_m$ , is in good agreement with bilayer capacitances published for other semiconductor electrodes, the determined membrane resistance  $R_m$  is comparably small. A significant influence of the preparation method, either vesicle fusion or solvent exchange, or the surface roughness on the achievable membrane resistance was excluded. A possible explanation for this observation could be the formation of an inhomogeneous oxide with local pinning centers during the surface oxidation procedures.

By dynamic contact angle measurements, information about the lateral homogeneity of the oxidized surface and the wetting properties can be obtained. The contact angle of a liquid droplet of increasing volume on the surface is dependent on the velocity of the advancing edge of the droplet. Inhomogeneities lead to a local pinning of the droplet front, resulting in an increase in the contact angle until the adhesive force at the pinning center is exceeded. The described behavior results in a non-continuous increase of the wetted surface and excursive variations of the contact angle.

Figure 6.16 shows the contact angle and diameter of a water droplet on a hydroxylated MOCVD GaN surface for an increasing droplet volume. Abrupt rises of the droplet diameter, accompanied by jumps in the contact angle with increasing droplet volume are observed, indicating the stick-slip behavior described above for a pinning at local surface inhomogeneities. This inhomogeneities could also cause local defects in the deposited bilayer membranes, resulting in a significant reduction of its resistive properties.



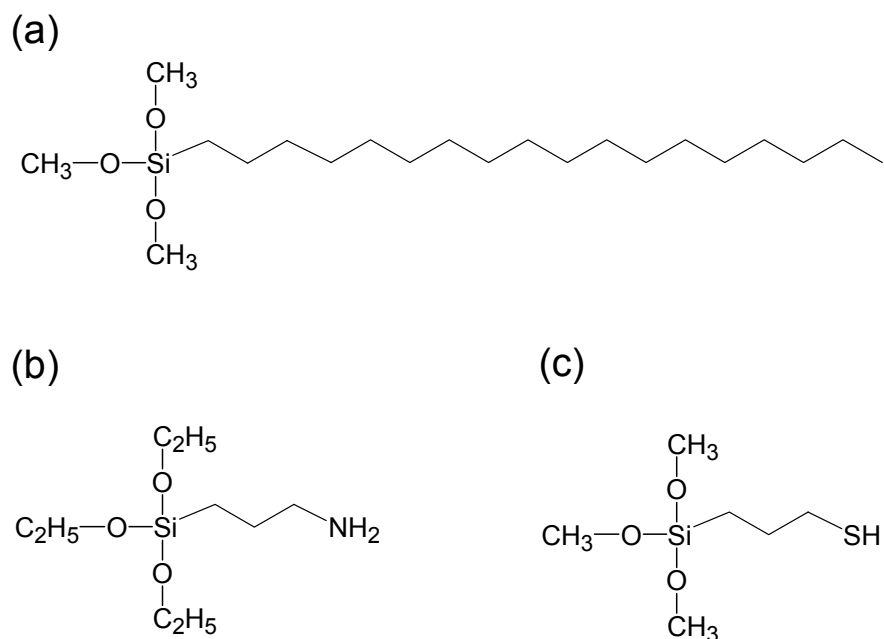
**Figure 6.16:** Contact angle and diameter of a water droplet with increasing volume on the surface of a hydroxylated MOCVD-grown GaN electrode with native oxide.

## 6.2 Organic Functionalization of GaN by Silane Monolayers

Organic functionalization of inorganic solid surfaces can be realized by deposition of self-assembled monolayers of organic molecules. These layers can provide a stable basis for subsequent coupling of functional biomolecules, like enzymes or specific receptors. Alkanethiol monolayers on Au surfaces are an intensely studied example for the establishment of a well controlled and stable organic/inorganic interface by covalent attachment of organic molecules in a self-organized process [Schreiber, 2000].

First studies on the adsorption of organic molecules on GaN surfaces have been carried out by Bermudez, who deposited anilines or octanethiols from the gas phase [Bermudez, 2003]. In this section, the covalent functionalization of GaN surfaces by SAMs of organosilanes, which is often simply referred to as silanization, is discussed with the main focus on their electrochemical properties.

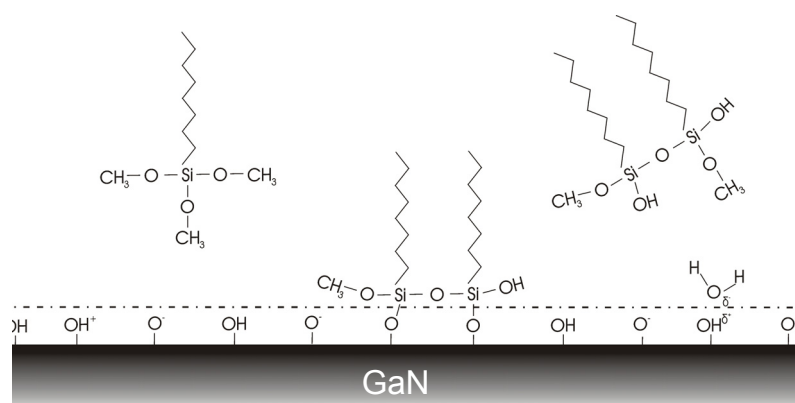
Silanization of glass or oxidized silicon surfaces has been thoroughly investigated and is discussed in various publications [Sagiv, 1980], [Parikh, 1994], [Bierbaum, 1995], [Rittner, 2005]. Linkage of biomolecules to silanized Si-based field-effect devices has been successfully used for the electronic detection of enzyme activity and DNA hybridization [Kharitonov, 2000], [Uslu, 2004]. For III-nitrides, a recent publication by the group of Pearton [Kang, 2005] presented the immobilization of proteins to AlGaIn/GaN transistors modified by aminopropyltriethoxysilane (APTES). However, neither formation of a monolayer, nor covalent immobilization of the APTES molecules was proven.



**Figure 6.17.:** Chemical structure of different alkyldimethylsilanes with a methyl, amino or thiol termination of their alkyl chain: (a) octadecyltrimethoxysilane (ODTMS), (b) aminopropyltriethoxysilane (APTES), and (c) (3-mercaptopropyl)trimethoxysilane (MP-TMS).

Alkyldimethylsilanes consist of a central Si atom surrounded by three active head groups and an unpolar alkyl chain, which is in some cases terminated with a functional end group like a methyl-, amino- or thiol-group. In Figure 6.17, the chemical structure of different alkyldimethylsilanes, exhibiting methoxy- or ethoxy-head groups and different terminations is presented. Depending on the nature of the functional end group, various strategies for the organic functionalization of the solid surface can be followed. Modification of oxidic surfaces by alkyldimethylsilane SAMs exhibiting a methyl termination, like octadecyltrimethoxysilane (ODTMS, Figure 6.17 (a)), results in hydrophobic surface properties due to the unpolar nature of the end group. After functionalization, these surfaces allow subsequent deposition of lipid monolayers [Lud, 2006], or polymer supported lipid membranes [Sackmann, 1996]. Reactive end groups like amino- or thiol-groups enable the linkage of biomolecules with corresponding terminations. Amino-terminated proteins can be immobilized via a glutaraldehyde linker and Schiff-base formation to the amino end group of APTES (Figure 6.17 (b)), or other amino-terminated silanes. Carboxyl-terminated molecules are attached to APTES via a peptide bond. Via a disulfide bridge, thiol-terminated proteins can be linked to SAMs of organosilanes with a thiol end group (Figure 6.17 (c)). Consequently, the whole diversity of proteins with thiol-terminations designed for grafting on Au surfaces [Schreiber, 2000] can be adopted to silanized GaN surfaces.

In the following section, an outline of the functionalization scheme for GaN surfaces by organosilane SAMs is given.



**Figure 6.18:** Silanization of a hydroxylated surface by ODTMS. The Si of the silane molecules form a covalent siloxyl bond with the OH-surface groups. During monolayer formation, the silanes are crosslinked by formation of Si-O-Si bridges.

### 6.2.1. Silanization of GaN Surfaces

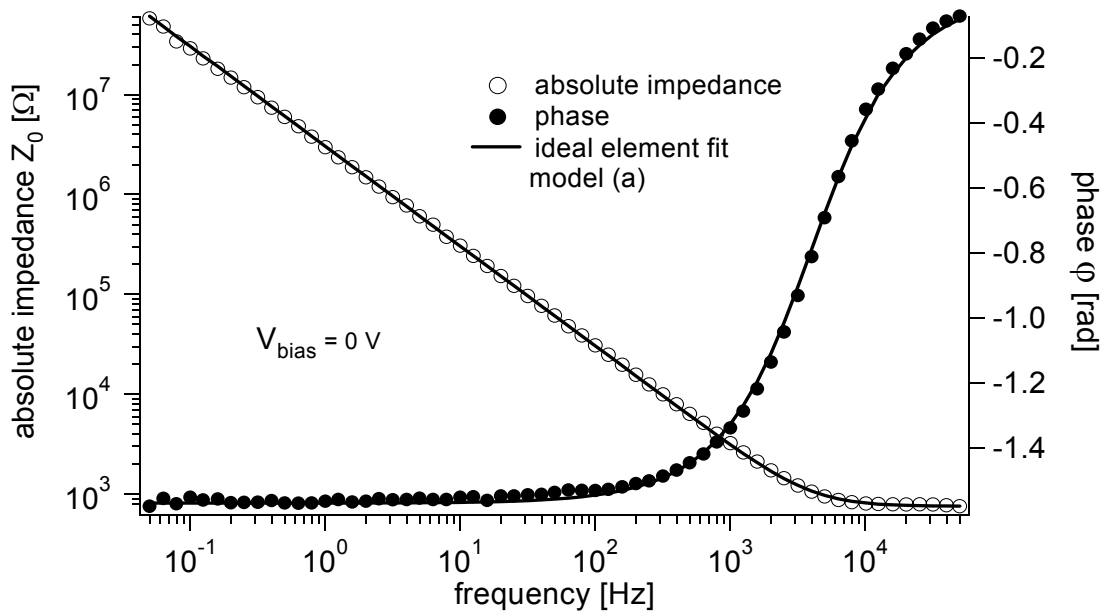
The silanes are solved in toluene and deposited on the hydroxylated GaN surface. By splitting off one or more head groups to the solution, the Si of the silane molecules can form a covalent siloxyl bond with the OH-surface group. Furthermore, the silanes are crosslinked by formation of Si-O-Si bonds, which is a basic requirement for the formation of a stable monolayer [Sung, 1999]. A detailed description of the silanization process for GaN and AlN surfaces can be found in [Baur, 2005].

For a self-assembly process, the entropy loss due to the ordered adsorption of molecules must be compensated by a gain in energy. This energy gain is achieved by the reaction of the head groups with the surface and the adjacent molecules, and the Van der Waals interaction between adjoining alkyl chains.

Furthermore, the water content and the reaction temperature are of major importance for the formation of a covalently bound monolayer. On the one hand, water in the organic solution results in blocking of the surface OH-groups, on the other hand, water is required to hydrolyze the surface groups to enable a reaction in the first place [Silberzan, 1991], [McGovern, 1994]. Depending on the alkyl chain length, the reaction temperature has to be thoroughly controlled. For too high reaction temperatures, gauche rotations of the alkyl chains impede an ordered assembly at the surfaces [Brzoska, 1992], [Parikh, 1994]. For a too low reaction temperature however, the silane molecules crystallize already in the solution.

The formation of a hydrophobic GaN surface by ODTMS-silanization with contact angles  $> 90^\circ$  was shown by Baur et al. [Baur, 2005]. No conglomeration of silane molecules or formation of several stacked silane layers was reported.





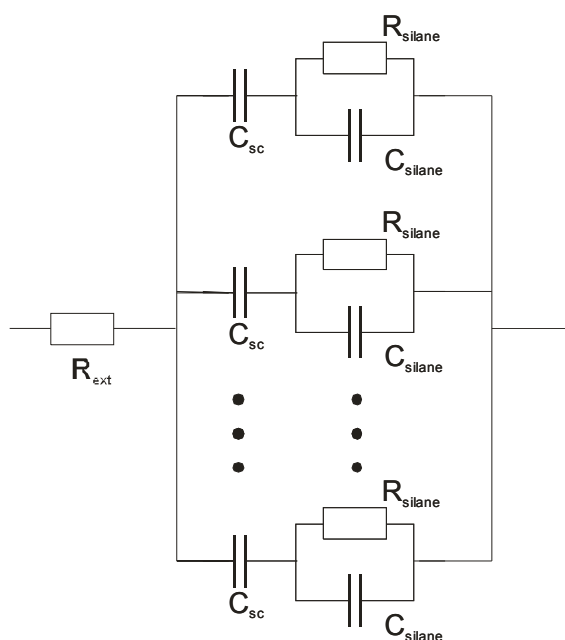
**Figure 6.19:** Impedance spectrum of an ODTMS-functionalized GaN electrode. Equivalent circuit model (a) was employed for the data analysis.

## 6.2.2 Electrical Characterization of Silane Monolayers on GaN

The electrical properties of ODTMS monolayers on hydroxylated GaN electrodes were characterized by impedance spectroscopy measurements. Impedance spectra were recorded directly after the hydroxylation of the GaN electrode, after the silanization with ODTMS and repeated over a time of 24 h, and after removal of the organosilane SAM by etching in diluted KOH and piranha etch.

Figure 6.19 shows the impedance spectrum of an ODTMS-modified GaN electrode for an applied bias voltage of  $V_{bias} = 0$  V.

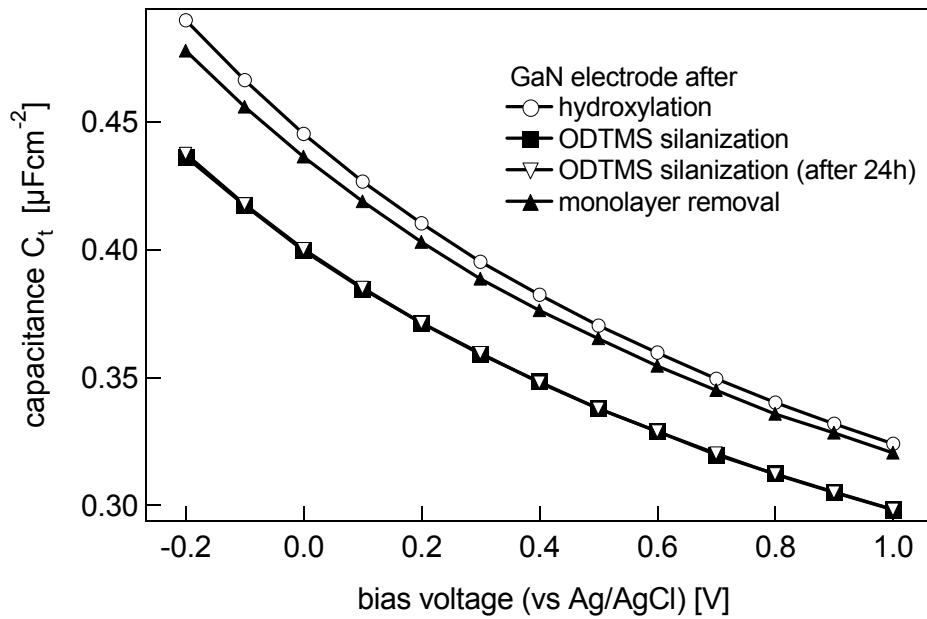
Based on the results for bare GaN electrodes of Section 5.3.1, the equivalent circuit (d) can be employed for modelling of a GaN electrode with an additional surface layer. The circuit model consists of a resistance  $R_{ext}$  in series with the interface capacitance  $C_{int}$  representing the GaN electrode, in series to a Randles circuit of  $C_L$  and  $R_L$  representing the organic functionalization layer. However, the interpretation of the individual circuit elements of the organic layer is different from the interpretation used for lipid bilayers in Section 6.1.3. Between a lipid bilayer and the electrode surface an intermediate layer of conducting electrolyte is present, resulting in an uniform potential on the electrode surface. The alkylsilanes, however, are covalently bound directly to the surface. As the alkylsilane layer is generally not conductive, the potential at the electrode surface cannot be regarded as uniform. For this reason, model (d) was modified according to Figure 6.20. The system is separated into parallel elements, each consisting of a



**Figure 6.20.:** Equivalent circuit model of a semiconductor electrode modified with a SAM of covalently bound alkylsilanes.  $C_{silane}$  and  $R_{silane}$  represent the local resistivity and capacitance of the silane layer, respectively.

space charge layer capacitance  $C_{sc}$  in series with the parallel capacitance  $C_{silane}$  and resistance  $R_{silane}$  of the silane layer. For the ideal case of defect-free and homogeneous SAMs, both models lead to identical results. However, significant differences are obtained for inhomogeneous functionalization layers with local defects. In the case of lipid double layer membranes, the membrane resistance is dominated by a few defects in an otherwise highly resistive membrane and reduced by some orders of magnitude, whereas the membrane capacitance remains basically unaffected. The total impedance of the Randles circuit representing the lipid double layer becomes negligibly small and the total system impedance is determined mainly by the serial capacitance of the space charge region,  $C_{sc}$ . For silane layers, local defects only reduce the local impedance of the functionalization layer, that is the impedance of only one of the parallel  $R_{silane}C_{silane}$ -elements. The total capacitance at this site is again determined by the space charge capacitance  $C_{sc}$  of the electrode. All parallel elements that represent the defect free regions remain unaffected. Hence, local defects only slightly change the total impedance of the system.

As a first approximation, the influence of local defects on the impedance spectra can be neglected for nearly closed silane layers due to their low surface area fraction. In practice, this allows the utilization of circuit model (d) for data analysis. The resistance  $R_L$ , however, is not interpreted as the total resistance of the functionalization layer, but the local microscopic resistance  $R_{silane}$  of the defect free regions of the silane layer. The extracted capacitance  $C_L$  can be directly identified with the silane layer capacitance  $C_{silane}$ . This interpretation is not



**Figure 6.21:** Total capacitances,  $C_t$ , versus bias voltage, extracted by the circuit model (a) from impedance spectra of a GaN electrode recorded before and after deposition of an ODTMS SAM and after removal of the monolayer.

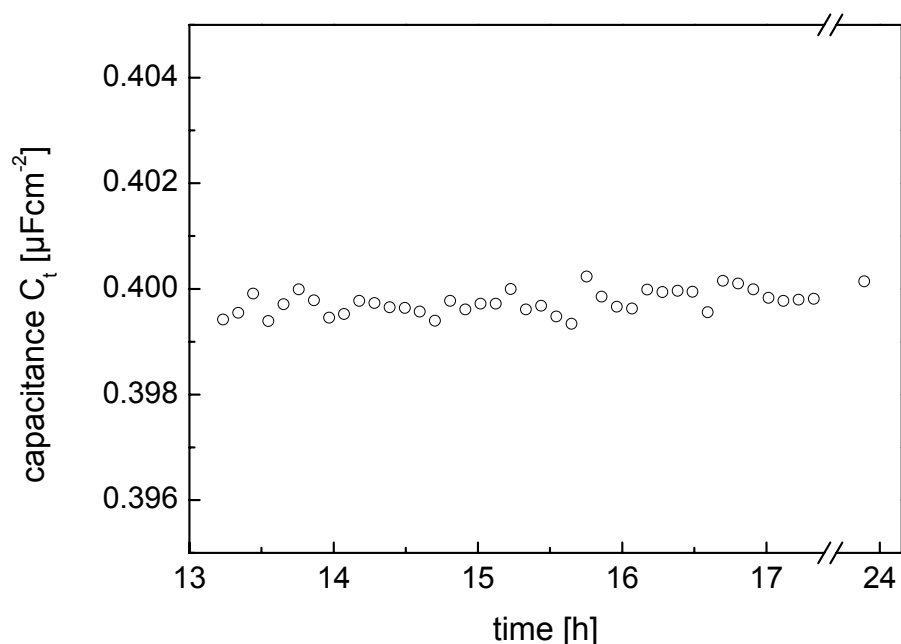
valid for low surface coverage, as the surface area fraction of defects can no longer be neglected in that case.

The impedance spectrum of the ODTMS-modified GaN electrode in Figure 6.19 shows no signature of a serial RC-element. However, a clear reduction of the system capacitance compared to measurements directly before the silanization is observed.

For this reason, the equivalent circuit model (a) was employed for analysis of the impedance spectra of both, hydroxylated and silanized GaN surfaces. Consequently, only one voltage dependent capacitance  $C_t(V_{bias})$  can be extracted from the impedance spectra, which corresponds to the voltage dependent capacitance of the space charge region  $C_{sc}(V_{bias})$  in series with the voltage independent capacitance  $C_{silane}$  of the silane layer.

In the investigated frequency range between 50 mHz and 50 kHz, no signature of the RC-element of the silane layer was observed. Under the assumption of a silane capacitance of  $C_{silane} = 2 \mu\text{F cm}^{-2}$  (see Section 6.2.2), a lower limit of  $1 \text{ M}\Omega \text{ cm}^2$  can be estimated for the local resistance  $R_{silane}$  of the ODTMS monolayer.

Figure 6.21 shows the total capacitance  $C_t$  extracted from the impedance spectra recorded at different bias potentials before and after silanization and after removal of the organic functionalization. The influence of the silane layer appears in the reduction of the total capacitance after silanization. After removal of the organic monolayer, the  $C_t - V_{bias}$  dependence approaches the initial behavior of a hydroxylated GaN electrode.



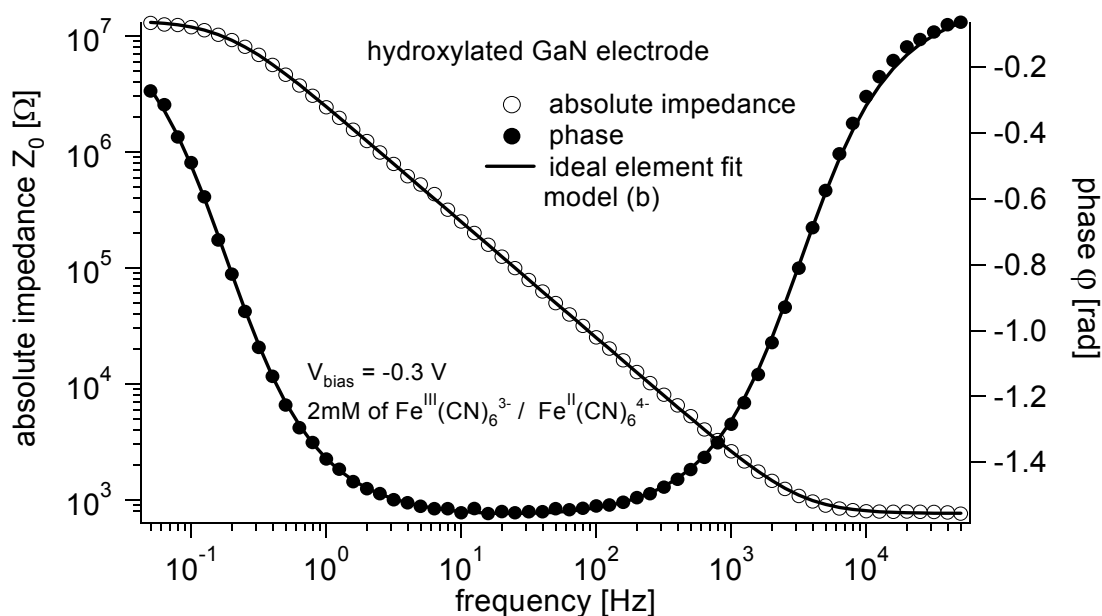
**Figure 6.22:** Total capacitance,  $C_t$ , of an ODTMS-modified GaN electrode at  $V_{bias} = 0$  V over a time interval of 10 h.

### Stability of the ODTMS Monolayer on GaN

The stability of the ODTMS functionalization on GaN electrodes in standard PBS buffer was checked by consecutive recording of impedance spectra over 24 h. The total capacitance,  $C_t$ , was extracted by circuit model (a) for each spectrum. No notable difference was observed between the  $C_t - V_{bias}$  dependence directly after silanization and after 24 h of continuous measurement (Figure 6.21). Figure 6.22 shows the total capacitance  $C_t$  obtained from spectra recorded over several hours at  $V_{bias} = 0$  V. The electrical properties of the ODTMS functionalized GaN electrode showed no variation over the investigated time interval of 10 h.

### Surface Coverage of the ODTMS Monolayer on GaN

One possible approach to obtain the surface coverage of a resistive monolayer by electrochemical methods is the comparison of the charge transfer to redox couples in the electrolyte for bare and modified electrodes, either by impedance spectroscopy or cyclic voltammetry experiments. Here, the following assumptions have to be made: (i) modification of the electrode surface by a resistive monolayer passivates the electrode, and (ii) charge transfer reactions occur only at



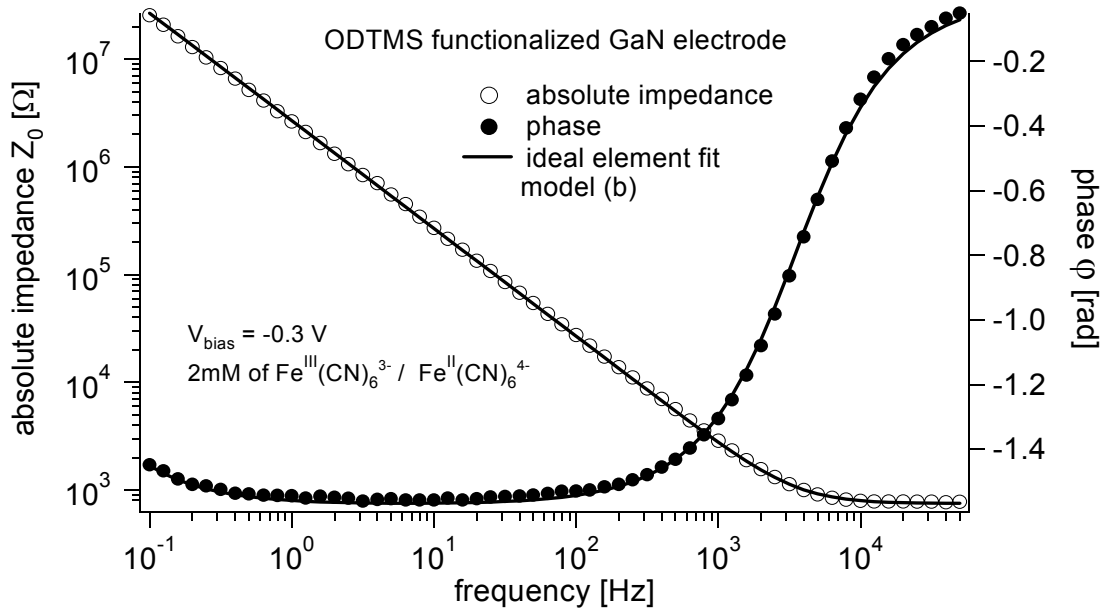
**Figure 6.23:** Impedance spectrum of a hydroxylated GaN electrode before functionalization with a monolayer of ODTMS. 2 mM of the iron-cyanide redox couple have been added to the measurement electrolyte.

defects in the passivation layer on the electrode surface. In that case, the fractional coverage of the electrode surface,  $\theta$ , is given by

$$\theta = 1 - \frac{R_{bare}}{R_{SAM}}, \quad (6.5)$$

where  $R_{bare}$  and  $R_{SAM}$  are the interface resistances for the bare electrode and after the deposition of the monolayer, respectively [Sabatani, 1993], [Janek, 1998]. Both interface resistances have to be obtained at the same bias voltage  $V_{bias}$ .

Because of its much higher accuracy compared to cyclic voltammetry, impedance spectroscopy is the preferable method for this purpose. For an increase of the charge transfer reactions at the GaN/electrolyte interface, 2 mM of the iron-cyanide redox couple (see Section 5.3.7) have been added to the standard PBS solution used for impedance spectroscopy experiments. Figures 6.23 and 6.24 show the impedance spectra of a hydroxylated GaN electrode recorded at  $V_{bias} = -0.3$  V, before and after modification with a monolayer of ODTMS, respectively. A significant increase of the absolute impedance at low measurement frequencies can be observed. The interface resistances  $R_i$  extracted by the equivalent circuit model (b) are given in the following table for the bare GaN electrode ( $R_{bare}$ ) and after deposition of the silane SAM ( $R_{SAM}$ ).



**Figure 6.24:** Impedance spectrum of a hydroxylated GaN electrode after functionalization with a monolayer of ODTMS. 2 mM of the iron-cyanide redox couple have been added to the measurement electrolyte.

$V_{bias} [V]$	$R_{bare} [\Omega \text{ cm}^2]$	$R_{SAM} [\Omega \text{ cm}^2]$	$\theta$
-0.2	$1.5 \times 10^7$	$1.6 \times 10^8$	91%
-0.3	$1.7 \times 10^6$	$2.8 \times 10^7$	94%

Although the obtained interface resistance varies about one order of magnitude between  $V_{bias} = -0.2 \text{ V}$  and  $-0.3 \text{ V}$ , similar values for the surface coverage around  $\theta = 92\% \pm 2\%$  have been extracted. The high defect area of about 10% justifies the assumption of charge transfer occurring only at the defect sites.

### Capacitance of the ODTMS Monolayer on GaN

As discussed above, the capacitances of the space charge region in the GaN electrode and the ODTMS functionalization layer cannot be separated by the impedance measurements due to their high parallel resistance. However, the additional capacitance of the silane layer can be extracted from the  $C_t - V$  behavior by means of the shift in flatband voltage under the following assumptions: (i) the SAM capacitance is voltage independent, (ii) the monolayer is homogeneous, and (iii) the obtained shift in flatband voltage is exclusively evoked by the additional serial capacitance of the ODTMS monolayer. Based on these assumptions, the capacitance of the silane SAM  $C_{silane}$  can be calculated by means of Eq. (5.68).

Under these assumptions, the additional serial capacitance  $C_{silane}$  was evaluated for ODTMS-modified GaN electrodes with different doping densities of  $2.9 \times 10^{18} \text{ cm}^{-3}$  and  $1.1 \times 10^{19} \text{ cm}^{-3}$  to  $1.5 \mu\text{F cm}^{-2}$  and  $2.4 \mu\text{F cm}^{-2}$ , respectively.

In X-ray reflectivity measurements, an ODTMS-layer thickness on GaN of  $d_{ODTMS} = 2.5 \text{ nm}$  was obtained [Baur, 2005]. By evaluating the ODTMS-layer capacitance according to

$$C_{ODTMS} = \frac{\epsilon_r \epsilon_0}{d_{ODTMS}}, \quad (6.6)$$

with the dielectric coefficient  $\epsilon_r = 2.2$  for long-chain hydrocarbons,  $C_{ODTMS} = 0.78 \mu\text{F cm}^{-2}$  is obtained.

Several reasons could be responsible for the difference in the capacitances evaluated either from the measured layer thickness by Eq. (6.6) or from the impedance measurements:

- The dielectric coefficient of the silane monolayer differs from the approximated value  $\epsilon_r$  for long-chain hydrocarbons. A higher dielectric constant could be caused by ions or water molecules in the silane layer.
- The layer thickness obtained by X-ray reflectivity measurement is not correct. A monolayer thickness  $d_{OTS} = 1.08 \text{ nm}$  was reported in [Rittner, 2005] for octadecyltrichlorosilane (OTS) monolayers on oxidized silicon. As the Si is directly bound to the surface, OTS and ODTMS SAMs have equal thicknesses,  $d_{OTS} = d_{ODTMS}$ . A corresponding capacitance of  $C_{ODTMS} = 1.8 \mu\text{F cm}^{-2}$  can be calculated by Eq. (6.6).
- The shift in  $V_{fb}$  caused by the additional serial capacitance of the monolayer is partly compensated due to a change in the surface chemistry.

## Conclusions

Hydroxylated GaN electrodes can be functionalized by organic monolayers of alkylsilanes in a self-assembly process. For hydroxylated GaN surfaces silanized by ODTMS, a surface coverage of 90 – 95% was evaluated by impedance spectroscopy with a redox electrolyte. The capacitance of the SAM was determined to  $C_{ODTMS} \approx 2 \mu\text{F cm}^{-2}$ , with a local resistance  $R_{silane}$  exceeding  $1 \text{ M}\Omega\text{cm}^2$ .

## 6.3. The Cell-Transistor Hybrid System

Recording the electrical activity of cells with planar device arrays is a promising approach for the study of biological networks as well as for the realization of whole-cell biosensors. A prerequisite for the understanding of information processing in neuronal networks is a multisite recording of cell signals at a cellular level [Fromherz, 1991]. In whole-cell biosensors, cells or

cell networks cultured on the device surface act as the biological receptor unit [Parce, 1989], [McConnell, 1992]. Such hybrid sensors benefit from the high sensitivity and selectivity of the specific receptors in the cellular membrane and the signal amplification in second messenger pathways of the cells. These cell-sensor hybrids are suitable for a variety of applications such as drug discovery and screening in pharmacology, detection of toxins, and environmental monitoring [Gross, 1985], [Yeung, 2001].

Most of these applications require a long-term multi-site recording of electrophysiological cell activity under physiological conditions. Intracellular recordings by the patch-clamp technique [Neher & Sakmann, 1976] exhibit a very high signal-to-noise ratio and even the function of single ion channels can be studied. However, this invasive method is not feasible for long-term measurements as the cells are subjected to a high degree of stress. Further, the observations are limited to only a few cells. The utilization of voltage sensitive dyes is also excluded, as they are toxic on illumination [Gritsch, 1998].

Extracellular monitoring of electrical cell activity can be performed by micro-electrode arrays [Thomas, 1972], [Gross, 1985], [Heer, 2004] or FET device arrays, as it was first reported for muscle fibers and neuronal slices by Bergveld et al. [Bergveld, 1976]. In 1991, Fromherz and co-workers succeeded in the recording of spontaneous and stimulated action potentials from the single Retzius neuron of a leech. Later, the capacitive stimulation of individual neurons with a silicon based integrated capacitor was shown to be possible [Fromherz & Stett, 1995], and a bidirectional interface between neuron and silicon microstructure was developed [Stett, 1997]. Zeck et al. have established a hybrid circuit of synaptically connected snail neurons and a silicon chip with noninvasive stimulation and recording [Zeck & Fromherz, 2001].

As a model cell system for the recording of action potentials with new transducer devices or device structures, myogenic cells like cardiac myocytes are suitable as they exhibit spontaneous action potentials and make external stimulation unnecessary. Because of the mechanical contraction, the spontaneous cell activity can be verified optically [Israel, 1984]. In this work, layers of heart muscle cells from embryonic E15 - E18 rats were used. Furthermore, hybrid systems of cardiac myocytes and AlGaIn/GaN SGFETs are interesting for various sensor applications based on detection of changes in beating frequency and shape of the extracellular signal [Offenhäusser & Knoll, 2001]. Dose-response curves of cardiac drugs like the cardiac stimulants (e.g. isoproterenol) or relaxants (e.g. verapamil) can be measured [Yeung, 2001], [Ingebrandt, 2001], and the detection of various channel blocking toxins was possible [Pancrazio, 1998].

In the following sections, the cultivation of cardiac myocyte cells on AlGaIn/GaN SGFET devices and the subsequent recording of their spontaneous activity is described. The cell-transistor coupling is discussed in the frame of the point-contact model.



### 6.3.1. Preparation of Cardiac Myocyte Cells

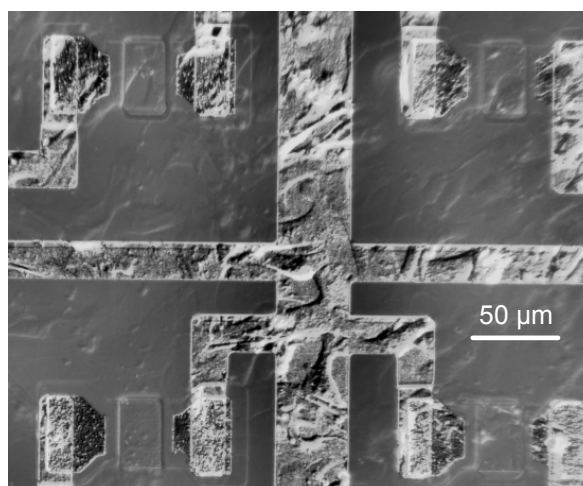
The preparation of the cardiac myocytes cell culture was adapted from previously published protocols [Denyer, 1999]. Briefly, hearts of embryonic Wistar rats (Charles River, Sulzbach, Germany), day 17, were removed, gently washed three times with ice-cold HBSS and minced. The chopped tissue was trypsinised for 8 min at 37 °C (0.5 g/l trypsin, 0.2 g/ml EDTA, Sigma-Aldrich, Munich, Germany). The supernatant was discarded and the remaining tissue was incubated at room temperature with 100 µl DNase II (10000 units/ml, Sigma-Aldrich). After 3 min, 2.5 ml Trypsin-EDTA were added and the suspension was incubated for 8 min at 37 °C. The supernatant was added to 4 ml blocking solution – Ham's F10 containing 33% fetal calf serum (FCS, Biochrom, Berlin, Germany) – to block the trypsinisation and kept on ice. The dissociation was repeated twice with the remaining tissue.

The cell suspension was centrifuged for 10 min at 200 g at 4 °C. The resulting pellet was resuspended in Ham's F10 medium containing 5% (v/v) FCS, 1% (v/v) Penicillin-Streptomycin (10000 units/ml penicillin and 10 mg/ml streptomycin, Sigma-Aldrich) and 0.5% (v/v) ITS (Sigma-Aldrich), adjusted to pH 7.2, and plated for 70 min on 35 mm dishes. During this differential adhesion [Denyer, 1999], the myocyte to fibroblast ratio was increased because fibroblasts have a higher adhesion rate than cardiomyocytes. Most of the fibroblasts adhered to the dish and the supernatant with the cardiomyocytes was centrifuged for 10 min at 200 g and room temperature. The pellet was resuspended in Ham's F10 medium.

The AlGaIn/GaN chips were cleaned for 30 min with 78% ethanol and coated for 30 min with 60 µl of 12.5 µg/ml fibronectin (Sigma-Aldrich) in HBSS at 37 °C. The surfaces were rinsed with PBS buffer solution (137 mM NaCl, 2.7 mM KCl, 4.3 mM Na<sub>2</sub>HPO<sub>4</sub>, 1.4 mM NaH<sub>2</sub>PO<sub>4</sub>, pH 7.3) before plating the cells. The cells were plated onto the chips at densities of 5000–12000 cells per chip (effective surface: 6.2 mm<sup>2</sup>). The chips were kept at 37 °C and 5% CO<sub>2</sub> in a humidified chamber. The medium was replaced several times. After 5 to 6 days in culture, a confluent monolayer of cells (syncytium) developed on the sensor surface, which exhibited spontaneous rhythmic activity. Figure 6.25 shows a cardiac myocyte syncytium on the device surface of an AlGaIn/GaN SGFET array.

### 6.3.2. Recording of Action Potentials

For recording of extracellular cell potentials, cardiac myocytes were cultivated as described above on 4 × 4 AlGaIn/GaN SGFET arrays. The preparation and characterization of the readout devices is described in Section 3.3.2 and Chapter 4. For the recordings, the culture medium was replaced by a solution containing 145 mM NaCl, 3 mM KCl, 2 mM MgCl<sub>2</sub>, 3 mM CaCl<sub>2</sub>, 10 mM HEPES, 8 mM glucose, and adjusted to pH 7.3 with NaOH as extracellular medium. The setup used for transistor control, signal amplification, and data extraction during the measurements is briefly described in Section 4.1. An Ag/AgCl wire was used as a reference electrode.



**Figure 6.25.:** Syncytium of cardiac myocyte cells cultivated on the device surface of an AlGaN/GaN SGFET array.

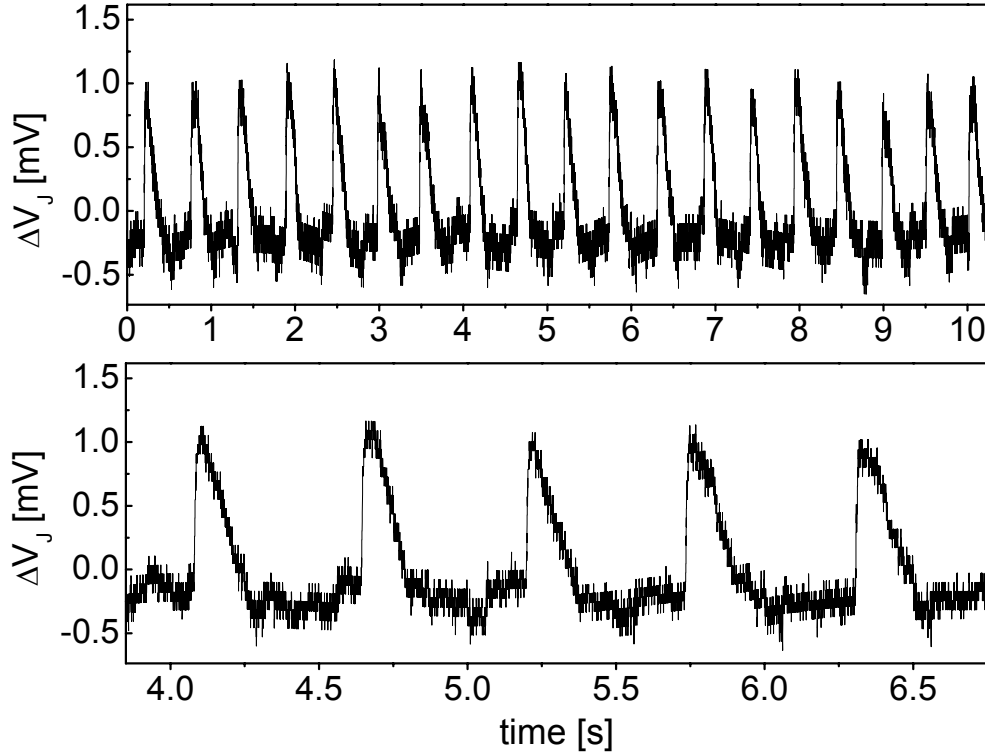
Measurements of the extracellular membrane voltage were performed with a confluent monolayer of rat heart muscle cells after 5 to 6 days in culture. The cells were beating spontaneously with a stable frequency and the electrical activity of the cells was recorded by means of the voltage  $V_J$  in the junction area between cell and transistor gate. An extracted 10 s time sequence of the measurement is shown in Figure 6.26.

The monitored transistor signals were 100 ms – 150 ms in duration, occurring with a stable frequency of around 2 Hz for several minutes. Signal amplitudes between 1.2 mV – 1.4 mV were recorded.

Action potentials of fully developed cultured cardiac cells are mainly generated by ionic fluxes of sodium, calcium, and potassium across the cellular membrane. The initial fast-rising action potential is triggered by an influx of sodium ions. The action potential is retarded by an inward directed calcium flux leading to a plateau phase. The following potassium efflux repolarizes the cell.

A first approximation to describe the coupling of an electrically active cell to a planar sensor is the point contact model introduced by Regehr et al. for micro-electrode arrays [Regehr, 1989], and later applied to transistors [Fromherz, 1991], [Sprössler, 1999]. Figure 6.27 shows the schematic illustration of a cell-transistor junction including the idealized equivalent circuit. The electrical contact between cell and transistor is approximated by a single contact point. The cell is separated from the transistor gate by an extended cleft of electrolyte with a height of 60 – 110 nm, depending on the surface coating and type of cell [Braun & Fromherz, 1998]. The cleft represents a seal resistor with a seal conductance  $g_J$ . The cell membrane has a capacitance of  $c_M$ .

Mainly two contributions to the electrical signal have to be considered: First, changes of the

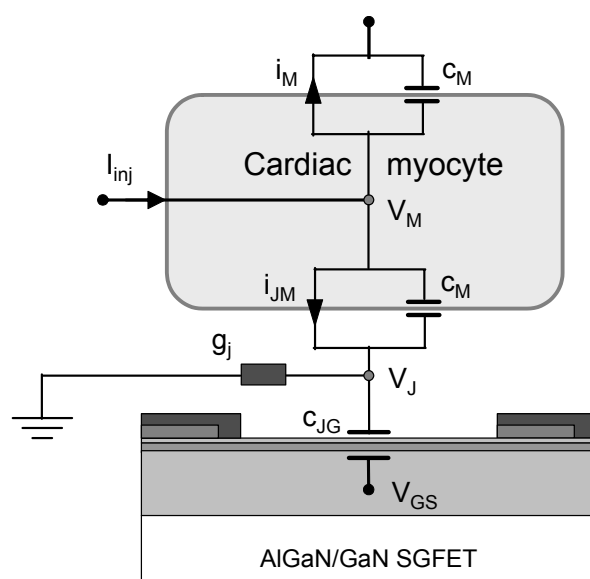


**Figure 6.26:** Extracellular potential of a spontaneously beating cardiac myocyte syncytium recorded with an AlGaIn/GaN SGFET. The cells were cultivated on the device surface.

intracellular potential  $V_M$  lead to capacitive currents across the attached part of the cellular membrane into the contact point. Secondly, the ionic currents through ion channels in the attached part of the membrane - which are summarized in  $i_{JM}$  - have to be considered. Both currents are forced to flow along the small cleft formed by the cellular membrane and the sensor surface. This leads to a voltage change at the sensor surface and both contributions have to be taken into account for the interpretation of the recorded signal shape. Under the assumption  $V_J \ll V_M$ , the extracellular voltage  $V_J$  can be expressed by Kirchhoff's law as

$$V_J = \frac{1}{g_J} \left( c_M \frac{dV_M}{dt} + i_{JM} \right). \quad (6.7)$$

The signal shapes recorded by the AlGaIn/GaN transistors seem to consist mainly out of the potassium signal part [Sprössler, 1999], [Ingebrandt, 2001]. Based on the available measurements, the exact origin of this signal shape could not be completely clarified. The shape resembles the "B-type" signal described in Ref. [Sprössler, 1999] for a syncytium of comparable cells. For the kind of cell-transistor junction resulting in "B-type" signals, the capacitive current is negligible and the junction voltage  $V_J$  is mainly determined through the ratio  $R_J/R_{JM}$  between



**Figure 6.27.:** Point contact model of the electrical coupling between a cell and a SGFET device.

the seal resistance  $R_J$  of the cleft and the membrane resistance  $R_{JM}$  at the junction. However, the extracellular voltages reported for "B-type" signals in the literature are significantly larger [Sprössler, 1999].

In conclusion, arrays of AlGaIn/GaN SGFET are suitable devices for the monitoring of extracellular cell potentials, as demonstrated for the spontaneous action potentials of a confluent layer of cardiac myocytes cultivated on the device surface. The presented data provide the first cell action potentials recordings performed by a non-silicon-based FET. The optical transparency of the substrate further permits optical analysis from the backside simultaneous to the electrical measurements. Based on the presented cell-transistor hybrid system, the realization of various whole-cell biosensor concepts for drug screening, detection of toxins, or environmental monitoring is possible.

## 7. Summary and Outlook

In the present work, the application potential of the AlGaN alloy system in biochemical sensors is evaluated. Biochemical sensors based on a biological recognition element and a semiconductor field-effect transducer are suitable devices for sensitive and specific analytical detection, and can be integrated with electronic circuits for on-chip signal amplification and processing. As biochemical sensors are operated in aqueous liquids, investigation of the physical chemistry of GaN/electrolyte interfaces, including the charge- and potential distribution, charge transfer processes, or the dependence of the interface potential on ionic concentrations was one of the main aspects. Various methods for an organic functionalization of AlGaN surfaces were investigated, and possible biosensor concepts are discussed. Furthermore, a novel device for recording of extracellular cell signals based on AlGaN/GaN heterostructure transistors was developed, and successfully applied to the recording of spontaneous action potentials of a cardiac myocyte syncytium.

AlGaN/GaN solution-gate field-effect transistors and transistor arrays were implemented and analyzed regarding an application as transducers in biochemical sensors. The transistor channel current was controlled by the potential applied to the solution gate contact, analogous to a Schottky metal gate contact. Stable operation with negligible leakage current over the electrolytic gate was observed. To avoid excessive heat development at the gate surface, the transistors were operated in the linear regime at  $V_{DS} \leq 0.5$  V, and a maximum transconductance of 0.2 mS was obtained.

Measurements of the low-frequency noise between 1 Hz and 1 kHz exhibited a  $1/f$  noise behavior, and a Hooge parameter of  $5 \times 10^{-3}$  was determined. The equivalent gate input noise  $S_{V_{GS}}$  showed a minimum for the gate voltage  $V_{GS}$  of maximum transconductance, hence chosen as the operation point for further sensor applications. However, strong variations in the low frequency noise have been obtained, which are assumed to be caused by the non-optimized ohmic contacts. The best tested devices exhibited a peak-to-peak noise level of 25  $\mu$ V, which is one order of magnitude smaller than for common silicon-based devices, and comparable to buried-channel silicon SGFETs suitable for the recording of mammalian neuron activity.

The surface chemistry of native and thermally oxidized GaN was analyzed by XPS. As-grown GaN surfaces show the immediate formation of a native oxide or oxynitride layer after exposure to atmosphere. For dry thermal oxidation at temperatures between 600 °C and 800 °C, the formation of a gallium oxide was observed. Island growth of gallium oxide, preferentially at threading dislocations was confirmed by cross sectional transmission electron microscopy micrographs for a 2 h dry oxidation at 700 °C in Ref. [Weidemann, 2005].

## 7. Summary and Outlook

---

Electrochemical analysis of the GaN/electrolyte interface was performed by impedance spectroscopy and cyclic voltammetry. For external potentials afar from the flatband voltage ( $V_{bias} - V_{fb} > 1$  V), n-type GaN electrodes exhibit an ideally polarizable interface, and can be electrically described by a capacitance in series to a resistor. Closer to the flatband condition, Faradaic contributions could be observed. An additional resistor in parallel to the capacitor gave a fair approximation of the electrical properties. The extracted interface capacitance,  $C_i$ , followed the behavior of an ideal semiconductor depletion region. The band edges at the interface are almost "pinned" with respect to the solution redox levels, and have been determined to  $E_{C,S} = 0.91$  eV and  $E_{V,S} = -2.69$  eV relative to the  $H^+/H_2$  redox level from the flatband voltages of  $V_{fb} = -1.12$  V (vs. Ag/AgCl) for an n-type and of  $V_{fb} = 2.27$  V (vs. Ag/AgCl) for a p-type GaN electrode. The flatband voltage was evaluated from the Mott-Schottky plots of the depletion layer capacitance extracted from impedance spectroscopy measurements. The doping dependence of the determined  $V_{fb}$  was attributed to the capacitive contribution of an additional surface layer ( $C_L \approx 2 \mu\text{F cm}^{-2}$ ). For the investigated AlGaIn electrodes with Al molar ratios  $x$  ranging from 0 to 0.5, the valence band edge at the interface to the solution,  $E_{V,S}$ , was found to be independent of the Al-concentration.

GaN/AlGaIn/GaN SGFETs with either native or dry thermal surface oxide exhibited a high and linear pH sensitivity of  $\approx 56.0$  mV/pH, close to the theoretical Nernstian limit. The pH sensitivity was discussed in terms of the site-dissociation model and the MUSIC-model. A resolution better than 0.05 pH could already be reached without an optimization of the device geometry and layer structure. Further, only a low cross sensitivity towards  $Na^+$ ,  $K^+$ ,  $Ca^{2+}$ , and  $Cl^-$  ions was observed in the range between  $10^{-5}$  M and  $2 \times 10^{-3}$  M at pH 7.

The deposition of fluid and stable lipid membranes on the surface of AlGaIn electrodes was demonstrated. The lateral mobility of lipids was analyzed by photobleaching experiments and is sufficient to allow self-healing of defects during the membrane formation process and to maintain the functionality of membrane-incorporated proteins. The anionic SOPS membranes exhibited significantly smaller diffusion constants than the zwitterionic SOPC, or the cationic DOTAP membranes. The observed tendency ( $D_{cationic} > D_{zwitterionic} > D_{anionic}$ ) was independent of the chemical composition of the substrate. An influence of the surface charge on the lateral mobility was excluded by a comparison to sapphire and glass substrates, which exhibit opposite surface charge at pH 7.

Formation of supported lipid membranes - containing DHDAB in a 1:1 molar mixture with cholesterol - on GaN electrodes was monitored by impedance spectroscopy. The parallel connection of an ideal resistor and capacitor already provides a fair approximation of the electrical membrane properties. A membrane resistance of around  $1 \text{ k}\Omega \text{ cm}^2$  was observed after membrane formation, corresponding to a defect area ratio lower than  $10^{-7}$ . It was shown that the observed decrease of the membrane capacitance,  $C_m$ , during membrane formation is likely to be caused by a slow homogenization of the cholesterol concentration in the bilayer. Final values of approximately  $0.7 \mu\text{F cm}^{-2}$  were extracted by means of the equivalent circuit model, comparable to values of  $C_m = 0.71 \mu\text{F cm}^{-2}$  for an identical lipid composition on p-type silicon substrates.

Thus, biosensors based on the potentiometric detection of the binding of charged ligands

---

to membrane-incorporated receptors [Sackmann, 1996], [Hillebrandt, 2002] can be realized. However, the attained membrane resistances of the order of  $1 \text{ k}\Omega \text{ cm}^2$  are not sufficient to allow the formation of chemical and electrical gradients, or the detection of membrane resistance changes due to the specific reaction of membrane channel proteins with the analyte [Tanaka & Sackmann, 2005].

A possible explanation for this observation, which is supported by dynamic contact angle measurements, is the presence of local pinning centers due to an inhomogeneous surface oxide. Hence, further improvement of the GaN crystallinity and an improvement of the surface oxidation is expected to reduce the defect density in deposited lipid membranes.

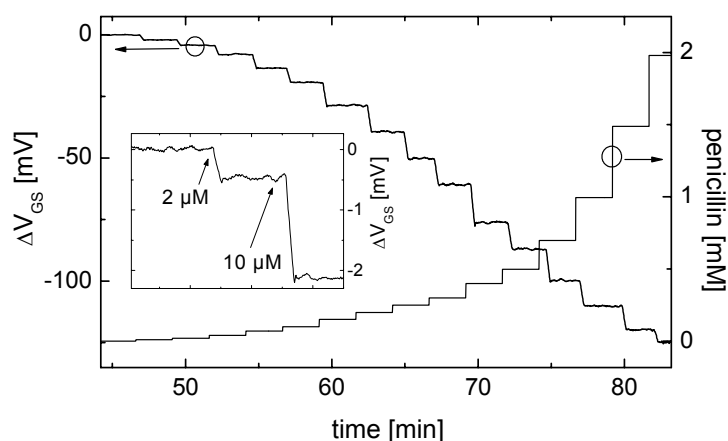
Functionalization of GaN by an ODTMS monolayer was shown [Baur, 2005], and the electrical monolayer parameters were evaluated to  $C_{\text{silane}} = 2 \mu\text{F cm}^{-2}$  and  $R_{\text{silane}} > 1 \text{ M}\Omega \text{ cm}^2$  by impedance spectroscopy. The silanization process resulted in a surface coverage of around  $\theta = 92\% \pm 2\%$ .

For the first time, the recording of electrophysiological cell signals with AlGaN/GaN SGFET arrays has been demonstrated in this work. The spontaneous action potentials of the examined muscle cells of embryonic rat hearts could be detected with an amplitude in the range of 1 mV. However, the analysis of neuronal networks usually requires the detection of considerably smaller extracellular action potentials in the range of  $100 \mu\text{V}$  [Vassanelli & Fromherz, 1998], and only a few tested devices exhibited the required resolution. Optimization of the contact technology is expected to generally reduce the low frequency noise, allowing the routinely recording of mammalian neuron activity.

In conclusion, the suitability of AlGaN based transducer devices for biochemical sensor applications is demonstrated by the investigations performed on GaN electrodes and AlGaN/GaN SGFETs. A wide range of chemical and biological applications is conceivable based on the presented results.

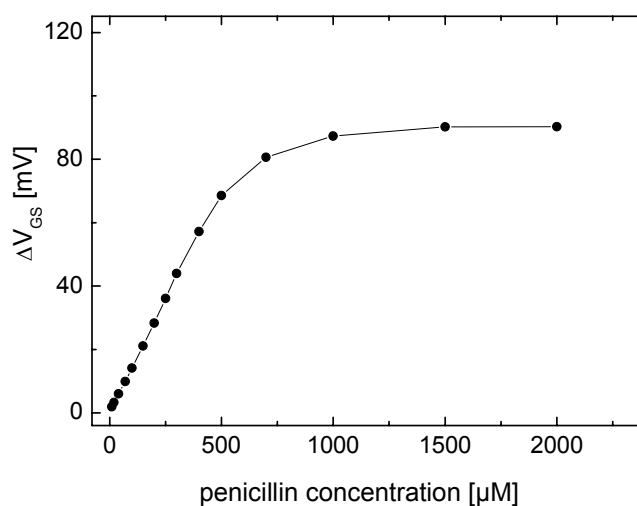
As an example, functionalization with a monolayer of APTES or other amino-terminated silanes enables the immobilization of amino-terminated proteins via a glutaraldehyde linker and Schiff-base formation. By means of this method, amino-terminated DNA single strands can be immobilized at the surface of a III-nitride SGFET [Baur, 2005], and a label free detection of DNA hybridization events by potentiometric detection of the intrinsic charge associated with the target DNA is imaginable [Fritz, 2002], [Uslu, 2004], [Song, 2006].

The high and linear pH sensitivity of GaN/AlGaN/GaN SGFETs allows the realization of EnFET devices, where the catalytic conversion of the analyte by enzymes immobilized at the transistor surface results in a local change of the solution pH [Caras & Janata, 1980]. Depending on the enzyme, the analyte concentrations of e.g. urea, glucose, or penicillin can be measured [Kharitonov, 2000], [Poghossian, 2001], [Pijanowska, 2003]. Immobilization of the enzyme layer on the transistor surface is possible either by physisorption or covalent linkage via Schiff-base formation. For the latter, the GaN transistor surface is modified with a monolayer of APTES prior to enzyme linkage. After functionalization with APTES and glutaraldehyde, the pH sensitivity is unchanged at  $\approx 56 \text{ mV/pH}$  [Baur, 2006]. Based on the AlGaN/GaN SGFETs developed in this work, EnFET devices were realized by immobilizing penicillinase or urease



**Figure 7.1:** Transient response of an AlGaIn/GaN EnFET with covalently linked penicillinase to changes of the penicillin G concentration in the buffer solution, according to [Baur, 2006].

on the GaN gate area, and successfully applied to the measurement of analyte concentrations of penicillin and urea [von Ribbeck, 2006], [Baur, 2006]. Figure 7.1 shows the transient response of an AlGaIn/GaN EnFET with covalently linked penicillinase enzymes to changes of the penicillin G concentration in the buffer solution. The calibration curve of such a device towards penicillin G is presented in Figure 7.2. Investigation of the penicillinase enzyme kinetics as well as the influence of the immobilization process on the enzyme functionality by means of AlGaIn/GaN EnFETs are interesting topics of current research. By expanding the principle to



**Figure 7.2:** Calibration curve of an AlGaIn/GaN EnFET with covalently immobilized penicillinase enzymes towards penicillin G, according to [Baur, 2006].



---

other enzymes, sensor arrays sensitive and selective to a multitude of analytes can be realized based on the presented devices.

Apart from the realization of field-effect transducer devices for biochemical sensors, AlGaN is a suitable alloy system for the fabrication of optical transducers. Recently, efficient room-temperature luminescence of self-assembled quantum dots (QD) in an AlN matrix has been demonstrated [Widmann, 1998], [Brown, 2001], [Gogneau, 2004]. The utilization of GaN QDs for chemical sensors with optical readout, based on the recording of chemically induced changes in the luminescence characteristics, is imaginable, and would take advantage of the optical transparency of both, sapphire substrate and AlN. Investigation of these devices is a promising and exciting topic for future research activities in the field of AlGaN based biochemical sensors.

## A. Appendix

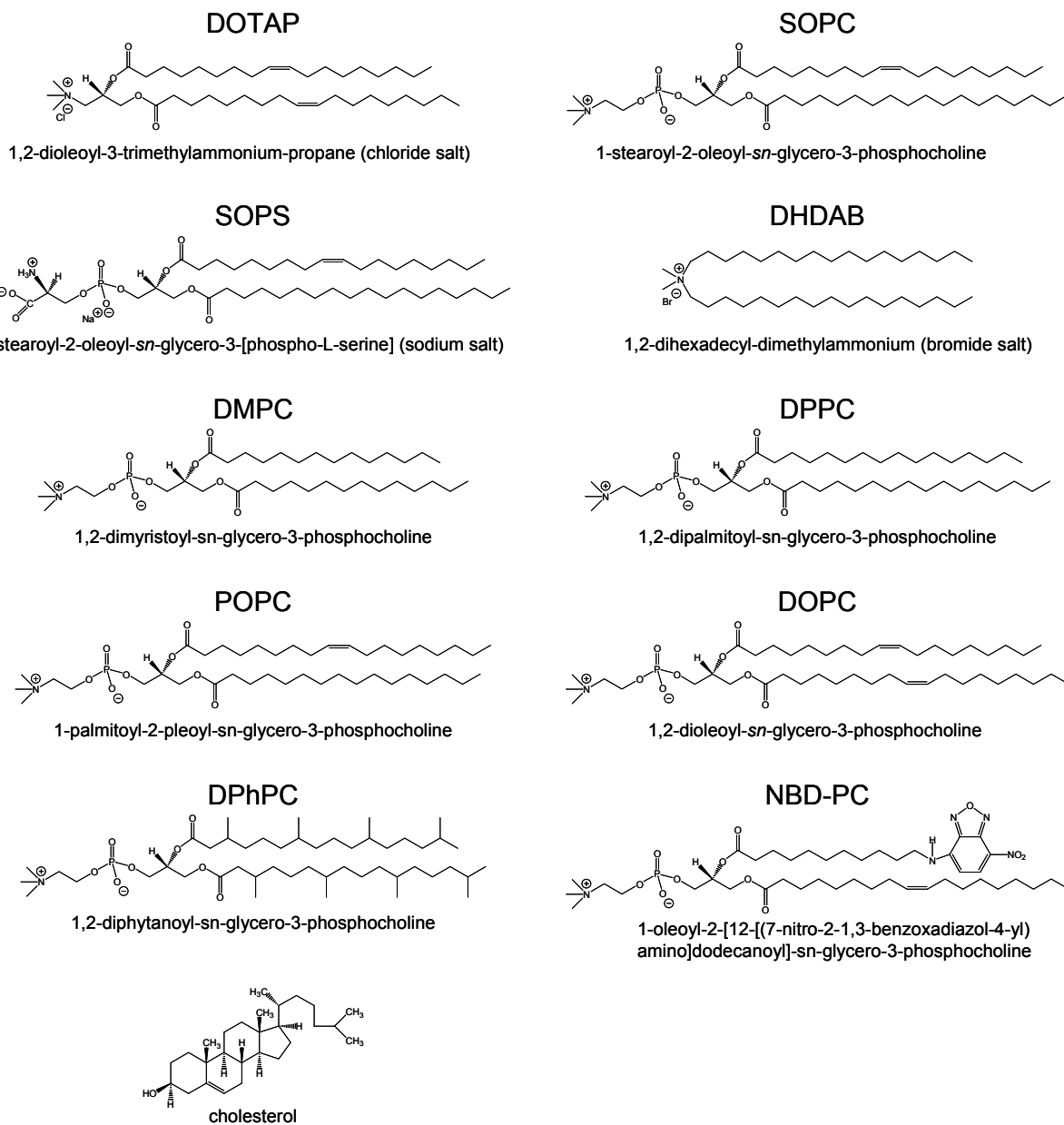
### A.1. Abbreviations

2DEG	two-dimensional electron gas
AFM	atomic force microscope
APTES	aminopropyltriethoxysilane
CPE	constant phase element
DHDAB	1,2-dihexadecyl-dimethylammonium-bromide
DMPC	1,2-dimyristoyl-sn-glycero-3-phosphocholine
DOPC	1,2-dioleoyl-sn-glycero-3-phosphocholine
DOTAP	1,2-dioleoyl-3-trimethylammonium-propane
DPhPC	1,2-diphytanoyl-sn-glycero-3-phosphocholine
DPPC	1,2-dipalmitoyl-sn-glycero-3-phosphocholine
ELISA	enzyme-linked immunosorbent assay
EMES	electrolyte-membrane-electrolyte-semiconductor
EnFET	enzyme-modified field-effect transistor
FWHM	full width at half maximum
FET	field-effect transistor
GCS	Gouy-Chapman-Stern
GOD	glucose oxidase
HEMT	high electron mobility transistor
HEPES	N-2-hydroxyethylpiperazine-N'-2-ethanesulfonic acid
HREEL	high resolution electron energy loss
IHP	inner Helmholtz plane
ISFET	ion-sensitive field-effect transistor
ISE	ion-sensitive electrode
ML	monolayer
MOCVD	metal organic chemical vapor deposition
MP-TMS	(3-mercaptopropyl)trimethoxysilane
MUSIC	multisite complexation
NADP	nicotinamide adenine dinucleotide phosphate

---

NBD-PC	1-oleoyl-2-[12-[(7-nitro-2-1,3-benzoxadiazol-4-yl)amino]dodecanoyl]-sn-glycero-3-phosphocholine
ocp	open circuit potential
ODTMS	octadecyltrimethoxysilane
OHP	outer Helmholtz plane
PBS	phosphate buffered saline
PDI	potential determining ions
PAMBE	plasma-assisted molecular beam epitaxy
POPC	1-palmitoyl-2-oleoyl-sn-glycero-3-phosphocholine
pzc	point of zero charge
QCM	quartz crystal microbalance
QD	quantum dot
SAM	self-assembled monolayer
SCE	standard calomel electrode
SGFET	solution-gate field-effect transistor
SHE	standard hydrogen electrode
SOPC	1-stearoyl-2-oleoyl-sn-glycero-3-phosphocholine
SOPS	1-stearoyl-2-oleoyl-sn-glycero-3-[phospho-L-serine]
SPR	surface plasmon resonance
TRIS	tris(2-carboxyethyl)phosphine hydrochloride
XPS	X-ray photoelectron spectroscopy
XRD	X-ray diffraction

## A.2 Lipids



**Figure A.1:** Chemical structures of the used lipids, fluorescence dye tracers, and cholesterol.

### A.3. The Semiconductor Space Charge Layer

A semiconductor space charge layer is formed under most experimental conditions due to several reasons:

- In vacuum, free electrons or holes from the semiconductor bulk are captured in surface states and a space charge of uncompensated ionized donors or acceptors is built up in the semiconductor.
- In contact with an electrolyte solution, free carriers of the semiconductor can additionally be transferred to redox ions with appropriate energy levels in the solution to compensate for an initial difference in the Fermi levels  $E_F$  between the two phases.
- Application of an external bias voltage between the semiconductor and the electrolyte.

A detailed discussion of the theory of the semiconductor space charge layer can be found for example in [Sze, 1981]. The potential and charge distribution,  $\phi(x)$  and  $\rho(x)$ , in the space charge layer are related by the Poisson equation (5.28), where  $\varepsilon_{sc}$  is the permittivity of the semiconductor, and  $x$  the distance from the surface. Assuming uniform doping, the absence of surface states and complete ionization of the donor and acceptor atoms, the total charge density is given by

$$\rho(x) = e [N_D - N_A - n(x) + p(x)] \quad (\text{A.1})$$

with the donor and acceptor densities  $N_D$  and  $N_A$ , respectively. The electron and hole densities,  $n(x)$  and  $p(x)$ , depend on the potential at the distance  $x$  according to

$$n(x) = n_0 \exp\left(\frac{e\phi}{kT}\right) \quad (\text{A.2})$$

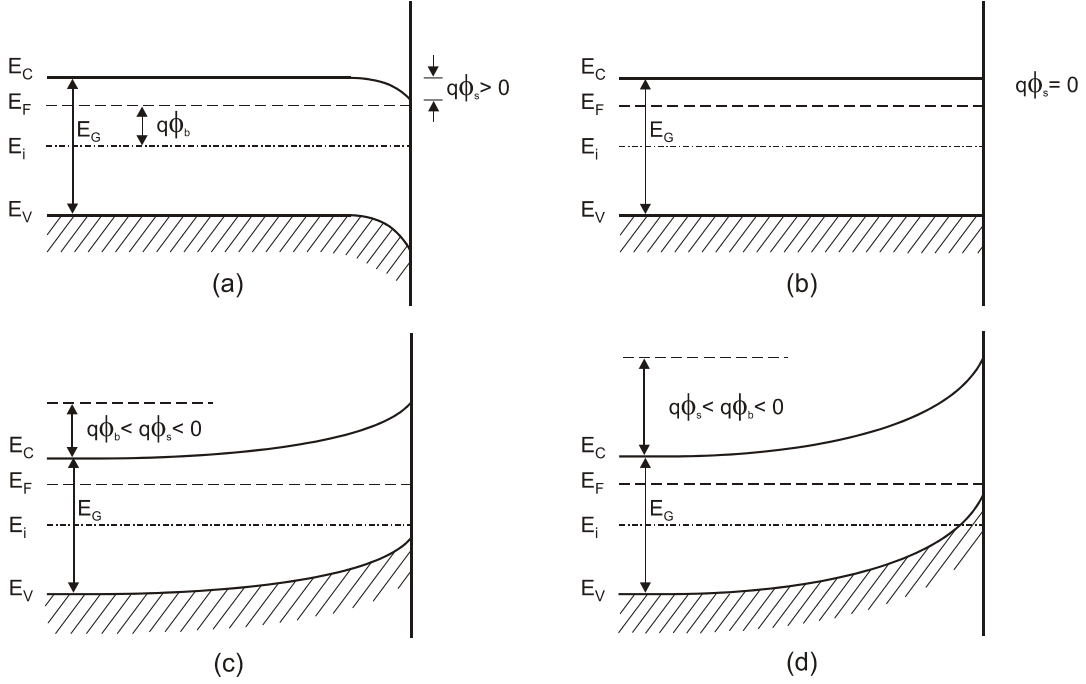
and

$$p(x) = p_0 \exp\left(-\frac{e\phi}{kT}\right) \quad (\text{A.3})$$

where  $n_0$  and  $p_0$  are the equilibrium densities of electrons and holes in the bulk of the semiconductor. The potential  $\phi$  at a distance  $x$  is measured with respect to the bulk potential ( $\phi(\infty) = 0$ ) and corresponds to the band bending at this point. Thus, the potential at the surface  $\phi(x = 0)$  denotes the total potential drop across the space charge layer,  $\phi_S$ . In the following, an n-type semiconductor is considered. For p-type semiconductors, similar considerations can be made by changing the polarity of the voltage.

Solving the Poisson equation, the total space charge per unit area in the space charge layer,  $\sigma_{sc}$ , can be calculated to

$$\sigma_{sc} = \mp \sqrt{2\varepsilon_{sc}\varepsilon_0 kT N_D} \left[ \frac{p_0}{n_0} (e^{-\beta\phi_S} + \beta\phi_S - 1) + (e^{\beta\phi_S} - \beta\phi_S - 1) \right]^{\frac{1}{2}} \quad (\text{A.4})$$



**Figure A.2:** Band diagrams for an n-type semiconductor under the following conditions: (a) accumulation, (b) flatband condition, (c) depletion, and (d) inversion or deep depletion.

with positive sign for  $\phi_S < 0$  and negative sign for  $\phi_S > 0$ .  $\beta$  is defined as

$$\beta = \frac{e}{kT}. \quad (\text{A.5})$$

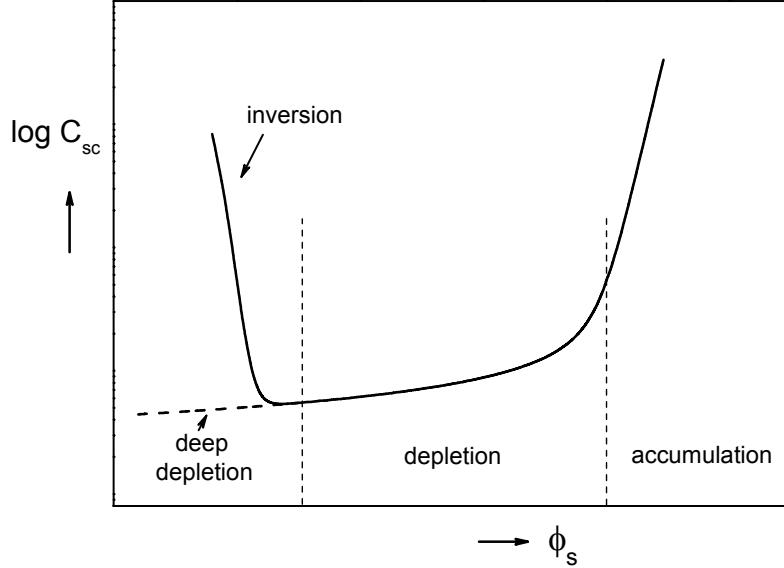
From A.4 the differential capacitance  $C_{sc}$  of the space charge region is derived by differentiation:

$$C_{sc} = \left( \frac{e^2 N_D \epsilon_{sc} \epsilon_0}{2kT} \right)^{\frac{1}{2}} \frac{\left| \frac{p_0}{n_0} (1 - e^{-\beta\phi_S}) + (e^{\beta\phi_S} - 1) \right|}{\left[ \frac{p_0}{n_0} (e^{-\beta\phi_S} + \beta\phi_S - 1) + (e^{\beta\phi_S} - \beta\phi_S - 1) \right]^{\frac{1}{2}}}. \quad (\text{A.6})$$

Figure A.2 illustrates the typical band situations that can be obtained at an n-type semiconductor surface depending on the surface potential  $\phi_S$ . The corresponding space charge layer capacitance  $C_{sc}$  is shown as a function of the surface potential in Figure A.3. For the following discussion it is useful to introduce  $\phi_b$ , the potential difference between the Fermi level  $E_F$  and the intrinsic Fermi level  $E_i$  ( $e\phi_b = E_F - E_i$ ) in the bulk (see Figure A.2).

### Accumulation

For positive surface potentials,  $\phi_S > 0$ , the conduction band is bent downwards closer to



**Figure A.3:** Differential capacitance of the semiconductor space charge layer under different conditions.

$E_F$  and the electron density at the surface  $n_s$  becomes larger than the bulk electron density  $n_0$  (Eq. (A.2)). Majority carriers are accumulated close to the surface. The capacitance of the accumulation layer can be approximated by

$$C_{sc}^{acc} = \left( \frac{e^2 N_D \epsilon_{sc} \epsilon_0}{2kT} \right)^{\frac{1}{2}} (e^{\beta \phi_s})^{\frac{1}{2}} \quad (\text{A.7})$$

from Eq. (A.6) and increases exponentially with increasing surface potential (Figure A.3).

### Flatband condition

The surface potential is zero,  $\phi_s = 0$ . There is no band bending or voltage drop in the semiconductor.

### Depletion

For small negative surface potentials ( $\phi_b < \phi_s < 0$ ) the bands are bent upwards and majority carriers are depleted from the surface region, resulting in a depletion region of uncompensated ionized donors. The depletion layer capacitance can be approximated by the Mott-Schottky equation,

$$C_{sc}^{dep} = \left( \frac{e^2 N_D \epsilon_{sc} \epsilon_0}{2kT} \right)^{\frac{1}{2}} [-1 - \beta \phi_s]^{-\frac{1}{2}} \quad (\text{A.8})$$

and a plot of  $1/C_{sc}^2$  vs.  $\phi_S$  yields a straight line, whose slope is determined by the donor concentration  $N_D$  in the depletion region. Under the approximation that the potential drop occurs completely over the depletion region and the charge density is equal to the donor density in the depletion region ( $\rho(x \leq W) = N_D$ ) and zero elsewhere ( $\rho(x > W) = 0$ ), the depletion layer width  $W$  and the total semiconductor space charge  $\sigma_{sc}$  per unit area are given by

$$W = \frac{\epsilon_s c \epsilon_0}{C_{sc}^{dep}} = \sqrt{\frac{2\epsilon_s \epsilon_0}{e N_D} \left( -\phi_S - \frac{kT}{e} \right)} \quad (\text{A.9})$$

and

$$\sigma_{sc} = e N_D W. \quad (\text{A.10})$$

### Inversion and deep depletion

For larger negative surface potentials ( $\phi_S < \phi_b$ ), the equilibrium minority carrier (hole) density at the surface becomes larger than the majority carrier (electron) density. Under equilibrium conditions, a space charge layer of inversion carriers is formed close to the surface and the capacitance increases exponentially with increasing negative  $\phi_S$ . However, under experimental conditions an inversion layer is not always formed. Either, the minority carrier generation time is large compared to the timescale of the experiment. This is of particular importance for wide bandgap semiconductors, where the thermal generation of minority carriers can almost be excluded. Or, generated minority carriers that reach the inversion layer are immediately consumed in a redox reaction taking place at the semiconductor surface. In both situations, the formation of an inversion layer is inhibited and the non-equilibrium configuration of deep depletion is reached. Eqs. (A.8) to (A.10) hold as well for the deep depletion case.

## A.4. Site-Binding Model

Under the assumptions made in Section 5.4.2 for the description of the electrical double layer at the interface between an oxide and an aqueous electrolyte by the site-binding model, the relation between the surface potential,  $\phi_S$ , the surface charge,  $\sigma_S$ , and the pH of the bulk electrolyte can be calculated based on the following equations:

$$K_+ = \frac{[A - OH] \cdot [H^+]_S}{[A - OH_2^+]} \quad (\text{A.11})$$

$$K_- = \frac{[A - O^-] \cdot [H^+]_S}{[A - OH]} \quad (\text{A.12})$$

$$\sigma_S = e \cdot ([A - OH_2^+] - [A - O^-]) \quad (\text{A.13})$$

$$N_S = [A - OH] + [A - OH_2^+] + [A - O^-] \quad (\text{A.14})$$



$$[H^+]_S = [H^+] \exp\left(\frac{-e\phi_S}{kT}\right) \quad (\text{A.15})$$

The fraction  $\alpha_S$  of the surface charge density  $\sigma_S$  relative to the total density of surface sites  $N_S$  is given by:

$$\alpha_S = \frac{\sigma_S}{eN_S} = \frac{[A - OH_2^+] - [A - O^-]}{[A - OH] + [A - OH_2^+] + [A - O^-]} \quad (\text{A.16})$$

Inserting the Eqs. (A.11), (A.12), and (A.15) yields:

$$\alpha_S = \frac{K_+^{-1} \cdot [A - OH][H^+] \exp(-\beta\phi_S) - K_- \cdot [A - OH][H^+]^{-1} \exp(\beta\phi_S)}{[A - OH] + K_+^{-1} \cdot [A - OH][H^+] \exp(-\beta\phi_S) + K_- \cdot [A - OH][H^+]^{-1} \exp(\beta\phi_S)}, \quad (\text{A.17})$$

with  $\beta = \frac{e}{kT}$ . Conversion and multiplication by  $[H^+]$  leads to a quadratic equation in  $[H^+]$ :

$$(\alpha_S - 1)K_+^{-1} \exp(-\beta\phi_S) \cdot [H^+]^2 + \alpha_S \cdot [H^+] + (\alpha_S + 1)K_- \exp(\beta\phi_S) = 0, \quad (\text{A.18})$$

with the solutions

$$[H^+]_{1/2} = \frac{-\alpha_S \pm \sqrt{\alpha_S^2 - 4(\alpha_S - 1)K_-/K_+}}{2(\alpha_S - 1) \exp(-\beta\phi_S) / K_+}. \quad (\text{A.19})$$

As negative concentrations are physically not reasonable, only the second solution is of physical relevance. Together with the abbreviation  $\delta = 2\sqrt{K_-/K_+}$  introduced in Section 5.4.2, the remaining solution is given by

$$[H^+] = \sqrt{K_-K_+} \exp(\beta\phi_S) \frac{\alpha_S/\delta + \sqrt{(\alpha_S/\delta)^2 \cdot (1 - \delta^2) + 1}}{1 - \alpha_S} \quad (\text{A.20})$$

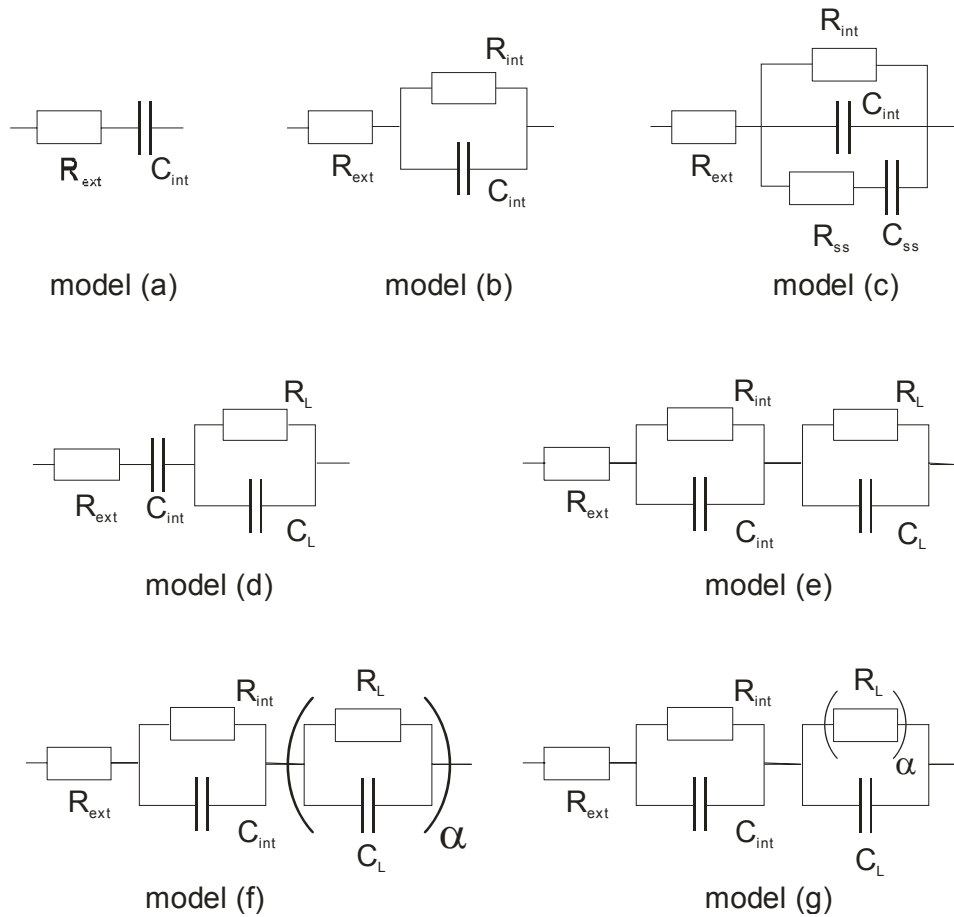
According to [Bousse, 1983]  $\delta^2 \ll 1$  can be assumed for oxidic surfaces. Thus, taking the logarithm yields

$$\log [H^+] = \log \sqrt{K_-K_+} + \beta\phi_S + \sinh^{-1}(\alpha_S/\delta) - \log(1 - \alpha_S). \quad (\text{A.21})$$

Note that

$$\sinh^{-1}(\alpha_S/\delta) = \log \alpha_S/\delta + \sqrt{(\alpha_S/\delta)^2 + 1}. \quad (\text{A.22})$$

## A.5. Equivalent Circuits



**Figure A.4.:** Equivalent circuit models utilized for the analysis of the impedance spectra in this work. Model (a) - (e) consist of ideal elements only. Model (d) - (g) are suitable circuits to describe an electrode with additional surface layer. The electrical properties of the surface layer are described either by a Randles circuit (model (d) and (e)), an element of distributed time constants with  $Z_{RC^\alpha} = \frac{R_m}{1+(i\omega\tau)^\alpha}$  and  $\tau = R_m C_m$  (model (f)), or a capacitor in parallel to a constant phase element (CPE) with  $Z_{CPE}(\omega) = K \cdot (i\omega)^{-\alpha}$  (model (g)).

## Bibliography

- [Abe, 1979] H. Abe, M. Esashi, and T. Matsuo, "ISFETs Using Inorganic Gate Thin-Films", *IEEE Transactions on Electron Devices* **26** (12), 1939-1944 (1979).
- [Alberts, 2002] B. Alberts, *Molecular biology of the cell*, 4th ed. (Garland Science, New York, 2002).
- [Alifragis, 2005] Y. Alifragis, G. Konstantinidis, A. Georgakilas, and N. Chaniotakis, "Anion selective potentiometric sensor based on gallium nitride crystalline membrane", *Electroanalysis* **17** (5-6), 527-531 (2005).
- [Ambacher, 1998] O. Ambacher, "Growth and applications of Group III nitrides", *Journal of Physics D-Applied Physics* **31** (20), 2653-2710 (1998).
- [Ambacher, 1999] O. Ambacher, J. Smart, J. R. Shealy, N. G. Weimann, K. Chu, M. Murphy, W. J. Schaff, L. F. Eastman, R. Dimitrov, L. Wittmer, M. Stutzmann, W. Rieger, and J. Hilsenbeck, "Two-dimensional electron gases induced by spontaneous and piezoelectric polarization charges in N- and Ga-face AlGaN/GaN heterostructures", *Journal of Applied Physics* **85** (6), 3222-3233 (1999).
- [Axelrod, 1976] D. Axelrod, D. E. Koppel, J. Schlessinger, E. Elson, and W. W. Webb, "Mobility Measurement by Analysis of Fluorescence Photobleaching Recovery Kinetics", *Biophysical Journal* **16** (9), 1055-1069 (1976).
- [Balandin, 1998] A. Balandin, S. Cai, R. Li, K. L. Wang, V. R. Rao, and C. R. Viswanathan, "Flicker noise in GaN/Al<sub>0.15</sub>Ga<sub>0.85</sub>N doped channel heterostructure field effect transistors", *IEEE Electron Device Letters* **19** (12), 475-477 (1998).
- [Bansal & Turner, 2000] A. Bansal, and J. A. Turner, "Suppression of band edge migration at the p-GaInP<sub>2</sub>/H<sub>2</sub>O interface under illumination via catalysis", *Journal of Physical Chemistry B* **104** (28), 6591-6598 (2000).
- [Bard, 1986] A. J. Bard, J. A. Crayston, G. P. Kittlesen, T. V. Shea, and M. S. Wrighton, "Digital-Simulation of the Measured Electrochemical Response of Reversible Redox Couples at Microelectrode Arrays - Consequences Arising from Closely Spaced Ultramicroelectrodes", *Analytical Chemistry* **58** (11), 2321-2331 (1986).
- [Bard & Faulkner, 2001] A. J. Bard, and L. R. Faulkner, *Electrochemical methods : fundamentals and applications*, 2nd ed. (John Wiley, New York, 2001).

- [Barsoukov & Macdonald, 2005] E. Barsoukov, and J. R. Macdonald, *Impedance spectroscopy: theory, experiment, and applications*, 2nd ed. (Wiley-Interscience, Hoboken, N.J., 2005).
- [Baumann, 1999] W. H. Baumann, M. Lehmann, A. Schwinde, R. Ehret, M. Brischwein, and B. Wolf, "Microelectronic sensor system for microphysiological application on living cells", *Sensors and Actuators B-Chemical* **55** (1), 77-89 (1999).
- [Baur, 2005] B. Baur, G. Steinhoff, J. Hernando, O. Purruicker, M. Tanaka, B. Nickel, M. Stutzmann, and M. Eickhoff, "Chemical functionalization of GaN and AlN surfaces", *Applied Physics Letters* **87** (26), 263901 (2005).
- [Baur, 2006] B. Baur, J. Howgate, H. G. von Ribbeck, Y. Gawlina, V. Bandalo, G. Steinhoff, M. Stutzmann, and M. Eickhoff, "Catalytic activity of enzymes immobilized on AlGaIn/GaN solution gate field-effect transistors", *Applied Physics Letters* **89** (18), 183901 (2006).
- [Bayer, 2005] M. Bayer, C. Uhl, and P. Vogl, "Theoretical study of electrolyte gate AlGaIn/GaN field effect transistors", *Journal of Applied Physics* **97** (3), 033703 (2005).
- [Bayerl & Bloom, 1990] T. M. Bayerl, and M. Bloom, "Physical-Properties of Single Phospholipid-Bilayers Adsorbed to Micro Glass-Beads - a New Vesicular Model System Studied by H-2-Nuclear Magnetic-Resonance", *Biophysical Journal* **58** (2), 357-362 (1990).
- [Beach, 2003] J. D. Beach, R. T. Collins, and J. A. Turner, "Band-edge Potentials of n-type and p-type GaN", *Journal of the Electrochemical Society* **150** (7), A899-A904 (2003).
- [Bergveld, 1970] P. Bergveld, "Development of an Ion-Sensitive Solid-State Device for Neurophysiological Measurements", *IEEE Transactions on Biomedical Engineering* **BM17** (1), 70-71 (1970).
- [Bergveld, 1972] P. Bergveld, "Development, Operation, and Application of Ion-Sensitive Field-Effect Transistor as a Tool for Electrophysiology", *IEEE Transactions on Biomedical Engineering* **BM19** (5), 342-351 (1972).
- [Bergveld, 1976] P. Bergveld, J. Wiersma, and H. Meertens, "Extracellular Potential Recordings by Means of a Field-Effect Transistor without Gate Metal, Called OSFET", *IEEE Transactions on Biomedical Engineering* **23** (2), 136-144 (1976).
- [Bergveld, 1978] P. Bergveld, N. F. Derooij, and J. N. Zemel, "Physical Mechanisms for Chemically Sensitive Semiconductor-Devices", *Nature* **273** (5662), 438-443 (1978).
- [Berman & Hébert, 1974] H. J. Berman, and N. C. Hébert, *Ion-selective microelectrodes*. (Plenum Press, New York, 1974).
- [Bermudez, 1996] V. M. Bermudez, "Study of oxygen chemisorption on the GaN(0001)-(1x1) surface", *Journal of Applied Physics* **80** (2), 1190-1200 (1996).

- [Bermudez, 2003] V. M. Bermudez, "Adsorption of 1-octanethiol on the GaN(0001) surface", *Langmuir* **19** (17), 6813-6819 (2003).
- [Bierbaum, 1995] K. Bierbaum, M. Kinzler, C. Woll, M. Grunze, G. Hahner, S. Heid, and F. Effenberger, "A near-Edge X-Ray-Absorption Fine Structure Spectroscopy and X-Ray Photoelectron-Spectroscopy Study of the Film Properties of Self-Assembled Monolayers of Organosilanes on Oxidized Si(100)", *Langmuir* **11** (2), 512-518 (1995).
- [Birner, 2006] S. Birner, S. Hackenbuchner, M. Sabathil, G. Zandler, J. A. Majewski, T. Andlauer, T. Zibold, R. Morschl, A. Trellakis, and P. Vogl, "Modeling of semiconductor nanostructures with nextnano<sup>3</sup>", *Acta Physica Polonica A* **110** (2), 111-124 (2006).
- [Bilitewski & Turner, 2000] U. Bilitewski, and A. P. F. Turner, *Biosensors for environmental monitoring*. (Harwood Academic Publishers, Amsterdam, the Netherlands, 2000).
- [Bockris & Reddy, 1970] J. O. M. Bockris, and A. K. N. Reddy, *Modern electrochemistry*, (Plenum Press, New York, 1970).
- [Boddy, 1965] P. J. Boddy, "Structure of Semiconductor-Electrolyte Interface", *Journal of Electroanalytical Chemistry* **10** (3), 199-244 (1965).
- [Boddy, 1968] P. J. Boddy, "Oxygen Evolution on Semiconducting TiO<sub>2</sub>", *Journal of the Electrochemical Society* **115** (2), 199 (1968).
- [Bousse, 1983] L. Bousse, N. F. DeRooij, and P. Bergveld, "The influence of counter-ion adsorption on the  $\psi_0$ /pH characteristics of insulator surfaces", *Surface Science* **135**, 479-496 (1983).
- [Bousse, 1994] L. Bousse, S. Mostarshed, B. Vanderschoot, and N. F. Derooij, "Comparison of the Hysteresis of Ta<sub>2</sub>O<sub>5</sub> and Si<sub>3</sub>N<sub>4</sub> pH-Sensing Insulators", *Sensors and Actuators B-Chemical* **17** (2), 157-164 (1994).
- [Brattain & Garrett, 1954] W. H. Brattain, and C. G. B. Garrett, "Electrical Properties of the Interface between a Germanium Single Crystal and an Electrolyte", *Physical Review* **94** (3), 750-750 (1954).
- [Braun & Fromherz, 1998] D. Braun, and P. Fromherz, "Fluorescence interferometry of neuronal cell adhesion on microstructured silicon", *Physical Review Letters* **81** (23), 5241-5244 (1998).
- [Brian & McConnell, 1984] A. A. Brian, and H. M. McConnell, "Allogeneic Stimulation of Cyto-Toxic T-Cells by Supported Planar Membranes", *Proceedings of the National Academy of Sciences of the United States of America-Biological Sciences* **81** (19), 6159-6163 (1984).
- [Briggs & Grant, 2003] D. Briggs, and J. T. Grant, *Surface analysis by Auger and X-ray photoelectron spectroscopy*. (IMPublications, Manchester, 2003).

- [Brown, 2001] J. Brown, C. Elsass, C. Poblenz, P. M. Petroff, and I. S. Speck, "Temperature dependent photoluminescence of MBE grown gallium nitride quantum dots", *physica status solidi (b)* **228** (1), 199-202 (2001).
- [Brunner, 1997] D. Brunner, H. Angerer, E. Bustarret, F. Freudenberg, R. Hopler, R. Dimitrov, O. Ambacher, and M. Stutzmann, "Optical constants of epitaxial AlGa<sub>N</sub> films and their temperature dependence", *Journal of Applied Physics* **82** (10), 5090-5096 (1997).
- [Brzoska, 1992] J. B. Brzoska, N. Shahidzadeh, and F. Rondelez, "Evidence of a Transition-Temperature for the Optimum Deposition of Grafted Monolayer Coatings", *Nature* **360** (6406), 719-721 (1992).
- [Buboltz & Feigenson, 1999] J. T. Buboltz, and G. W. Feigenson, "A novel strategy for the preparation of liposomes: rapid solvent exchange", *Biochimica Et Biophysica Acta-Biomembranes* **1417** (2), 232-245 (1999).
- [Butler, 1977] M. A. Butler, "Photoelectrolysis and Physical-Properties of Semiconducting Electrode WO<sub>3</sub>", *Journal of Applied Physics* **48** (5), 1914-1920 (1977).
- [Campbell, 1999] N. A. Campbell, J. B. Reece, and L. G. Mitchell, *Biology*, 5th ed. (Benjamin Cummings, Menlo Park, Calif., 1999).
- [Caras & Janata, 1980] S. Caras, and J. Janata, "Field-Effect Transistor Sensitive to Penicillin", *Analytical Chemistry* **52** (12), 1935-1937 (1980).
- [Carin, 1990] R. Carin, J. P. Deville, and J. Werckmann, "An XPS Study of GaN Thin-Films on GaAs", *Surface and Interface Analysis* **16** (1-12), 65-69 (1990).
- [Cardon & Gomes, 1978] F. Cardon, and W. P. Gomes, "Determination of Flat-Band Potential of a Semiconductor in Contact with a Metal or an Electrolyte from Mott-Schottky Plot", *Journal of Physics D - Applied Physics* **11** (4), L63-L67 (1978).
- [Chaniotakis, 2004] N. A. Chaniotakis, Y. Alifragis, G. Konstantinidis, and A. Georgakilas, "Gallium nitride-based potentiometric anion sensor", *Analytical Chemistry* **76** (18), 5552-5556 (2004).
- [Chaniotakis, 2005] N. A. Chaniotakis, Y. Alifragis, A. Georgakilas, and G. Konstantinidis, "GaN-based anion selective sensor: Probing the origin of the induced electrochemical potential", *Applied Physics Letters* **86** (16), 164103 (2005).
- [Chiang, 2001] J. L. Chiang, Y. C. Chen, and J. C. Chou, "Simulation and experimental study of the pH-sensing property for AlN thin films", *Japanese Journal of Applied Physics* **40** (10), 5900-5904 (2001).
- [Clark & Lyons, 1962] L. C. Clark, and C. Lyons, "Electrode Systems for Continuous Monitoring in Cardiovascular Surgery", *Annals of the New York Academy of Sciences* **102** (1), 29-45 (1962).

- [Cohen, 2004] A. Cohen, M. E. Spira, S. Yitshaik, G. Borghs, O. Shwartzglass, and J. Shapir, "Depletion type floating gate p-channel MOS transistor for recording action potentials generated by cultured neurons", *Biosensors & Bioelectronics* **19** (12), 1703-1709 (2004).
- [Cornell, 1997] B. A. Cornell, V. L. B. BraachMaksvytis, L. G. King, P. D. J. Osman, B. Raguse, L. Wiczorek, and R. J. Pace, "A biosensor that uses ion-channel switches", *Nature* **387** (6633), 580-583 (1997).
- [Coster & Smith, 1974] H. G. L. Coster, and J. R. Smith, "The Molecular Organization of Biomolecular Lipid Membranes. A Study of the Low Frequency Maxwell-Wagner Impedance Dispersion", *Biochimica Et Biophysica Acta* **373**, 151-164 (1974).
- [Cowley & Sze, 1965] A. M. Cowley, and S. M. Sze, "Surface States and Barrier Height of Metal-Semiconductor Systems", *Journal of Applied Physics* **36** (10), 3212-3220 (1965).
- [Davis, 1978] J. A. Davis, R. O. James, and J. O. Leckie, "Surface Ionization and Complexation at Oxide-Water Interface. 1. Computation of Electrical Double-Layer Properties in Simple Electrolytes", *Journal of Colloid and Interface Science* **63** (3), 480-499 (1978).
- [de Gennes, 1985] P. G. de Gennes, "Wetting - Statics and Dynamics", *Reviews of Modern Physics* **57** (3), 827-863 (1985).
- [De Gryse, 1975] R. De Gryse, W. P. Gomes, F. Cardon, and J. Vennik, "Interpretation of Mott-Schottky Plots Determined at Semiconductor-Electrolyte Systems", *Journal of the Electrochemical Society* **122** (5), 711-712 (1975).
- [Delevie, 1989] R. Delevie, "On the Impedance of Electrodes with Rough Interfaces", *Journal of Electroanalytical Chemistry* **261** (1), 1-9 (1989).
- [Denyer, 1999] M. C. T. Denyer, M. Riehle, J. Hayashi, M. Scholl, C. Sprössler, S. T. Britland, A. Offenhäusser, and W. Knoll, "Bioassay development: The implications of cardiac myocyte motility in vitro", *In Vitro Cellular & Developmental Biology-Animal* **35** (6), 352-356 (1999).
- [Dewald, 1960] J. F. Dewald, "The Charge Distribution at the Zinc Oxide-Electrolyte Interface", *Journal of Physics and Chemistry of Solids* **14**, 155-161 (1960).
- [Dietrich & Tampé, 1995] C. Dietrich, and R. Tampé, "Charge Determination of Membrane Molecules in Polymer-Supported Lipid Layers", *Biochimica Et Biophysica Acta-Biomembranes* **1238** (2), 183-191 (1995).
- [Dietrich, 1997] C. Dietrich, R. Merkel, and R. Tampé, "Diffusion measurement of fluorescence-labeled amphiphilic molecules with a standard fluorescence microscope", *Biophysical Journal* **72** (4), 1701-1710 (1997).
- [Dilger, 1979] J. P. Dilger, S. G. A. McLaughlin, T. J. McIntosh, and S. A. Simon, "The Dielectric Constant of Phospholipid Bilayers and the Permeability of Membranes to Ions", *Science* **206** (7), 1196 - 1198 (1979).

- [Dimitrov, 2000] R. Dimitrov, M. Murphy, J. Smart, W. Schaff, J. R. Shealy, L. F. Eastman, O. Ambacher, and M. Stutzmann, "Two-dimensional electron gases in Ga-face and N-face AlGa<sub>N</sub>/Ga<sub>N</sub> heterostructures grown by plasma-induced molecular beam epitaxy and metalorganic chemical vapor deposition on sapphire", *Journal of Applied Physics* **87** (7), 3375-3380 (2000).
- [Dörfler, 1994] H.-D. Dörfler, *Grenzflächen- und Kolloidchemie*. (VCH, Weinheim, 1994).
- [Douliez, 1996] J. P. Douliez, A. Leonard, and E. J. Dufourc, "Conformational order of DMPC sn-1 versus sn-2 chains and membrane thickness: An approach to molecular protrusion by solid state H-2-NMR and neutron diffraction", *Journal of Physical Chemistry* **100** (47), 18450-18457 (1996).
- [Duh & Van der Ziel, 1985] K. H. Duh, and A. Van der Ziel, "Hooge Parameters for Various FET Structures", *IEEE Transactions on Electron Devices* **32** (3), 662-666 (1985).
- [Eggins, 2002] B. R. Eggins, *Chemical sensors and biosensors*. (John Wiley, New York, 2002).
- [Eickhoff, 2000] M. Eickhoff, *Piezowiderstandsmechanismen in Halbleitern mit großer Bandlücke*, (Dissertation Technische Universität München 2000).
- [Eickhoff, 2003] M. Eickhoff, J. Schalwig, G. Steinhoff, O. Weidemann, L. Görgens, R. Neuberger, M. Hermann, B. Baur, G. Müller, O. Ambacher, M. Stutzmann, *physica status solidi (c)* **0** (6), 1908-1918 (2003).
- [Elsner, 1998] J. Elsner, R. Gutierrez, B. Hourahine, R. Jones, M. Haugk, and T. Frauenheim, "A theoretical study of O chemisorption on GaN (0001)/(000 $\bar{1}$ ) surfaces", *Solid State Communications* **108** (12), 953-958 (1998).
- [Ennaoui, 1993] A. Ennaoui, S. Fiechter, C. Pettenkofer, N. Alonsovante, K. Buker, M. Bronold, C. Hopfner, and H. Tributsch, "Iron Disulfide for Solar-Energy Conversion", *Solar Energy Materials and Solar Cells* **29** (4), 289-370 (1993).
- [Esashi & Matsuo, 1978] M. Esashi, and T. Matsuo, "Integrated Micro Multi Ion Sensor Using Field-Effect of Semiconductor", *IEEE Transactions on Biomedical Engineering* **25** (2), 184-192 (1978).
- [Feigson, 1986] G. W. Feigson, "On the nature of calcium ion binding between phosphatidylserine lamellae", *Biochemistry* **25** (19), 5819-5825 (1986).
- [Fettiplace, 1975] R. Fettiplace, L. Gordon, S. B. Hladky, J. Requena, H. P. Zingsheim, and D. A. Haydon, in "*Methods in membrane biology*", edited by E. D. Korn (Plenum Press, New York, 1975), Vol. 4, pp. 1-75.
- [Finklea, 1988] H. O. Finklea, *Semiconductor electrodes*. (Elsevier, Amsterdam; New York, 1988).



- [Fleig & Maier, 1996] J. Fleig, and J. Maier, "The impedance of imperfect electrode contacts on solid electrolytes", *Solid State Ionics* **85** (1-4), 17-24 (1996).
- [Fritz, 2002] J. Fritz, E. B. Cooper, S. Gaudet, P. K. Sorger, and S. R. Manalis, "Electronic detection of DNA by its intrinsic molecular charge", *Proceedings of the National Academy of Sciences of the United States of America* **99** (22), 14142-14146 (2002).
- [Fromherz, 1991] P. Fromherz, A. Offenhäusser, T. Vetter, and J. Weis, "A Neuron-Silicon Junction - a Retzius Cell of the Leech on an Insulated-Gate Field-Effect Transistor", *Science* **252** (5010), 1290-1293 (1991).
- [Fromherz & Stett, 1995] P. Fromherz, and A. Stett, "Silicon-Neuron Junction - Capacitive Stimulation of an Individual Neuron on a Silicon Chip", *Physical Review Letters* **75** (8), 1670-1673 (1995).
- [Fujimoto, 1993] K. Fujimoto, M. Minato, H. Tadokoro, and Y. Ikada, "Platelet Deposition onto Polymeric Surfaces During Shunting", *Journal of Biomedical Materials Research* **27** (3), 335-343 (1993).
- [Fujishima & Honda, 1972] A. Fujishima, and K. Honda, "Electrochemical Photolysis of Water at a Semiconductor Electrode", *Nature* **238** (5358), 37-38 (1972).
- [Fung, 1986] C. D. Fung, P. W. Cheung, and W. H. Ko, "A Generalized Theory of an "Electrolyte-Insulator-Semiconductor Field-Effect Transistor", *IEEE Transactions on Electron Devices* **33** (1), 8-18 (1986).
- [Gärtner, 1959] W. W. Gärtner, "Depletion-Layer Photoeffects in Semiconductors", *Physical Review* **116** (1), 84-87 (1959).
- [Garrido, 1998] J. A. Garrido, F. Calle, E. Muñoz, I. Izpura, J. L. Sanchez-Rojas, R. Li, and K. L. Wang, "Low frequency noise and screening effects in AlGaIn/GaN HEMTs", *Electronics Letters* **34** (24), 2357-2359 (1998).
- [Garrido, 2000a] J. A. Garrido, B. E. Foutz, J. A. Smart, J. R. Shealy, M. J. Murphy, W. J. Schaff, L. F. Eastman, and E. Muñoz, "Low-frequency noise and mobility fluctuations in AlGaIn/GaN heterostructure field-effect transistors", *Applied Physics Letters* **76** (23), 3442-3444 (2000).
- [Garrido, 2000b] J. A. Garrido Ariza, *Fabricación, Caracterización y Modelado de Transistores de Heterounión de Efecto Campo Basados en AlGaIn/GaN*, (Dissertation Universidad Politécnica de Madrid 2000).
- [Garrido, 2005] J. A. Garrido, A. Härtl, S. Kuch, M. Stutzmann, O. A. Williams, and R. B. Jackmann, "pH sensors based on hydrogenated diamond surfaces", *Applied Physics Letters* **86** (7), 073504 (2005).

- [Gerischer, 1960] H. Gerischer, "Über den Ablauf von Redoxreaktionen an Metallen und an Halbleitern I. Allgemeines zum Elektronenübergang zwischen einem Festkörper und einem Redoxelektrolyten", *Zeitschrift Für Physikalische Chemie Neue Folge* **26**, 223-247 (1960).
- [Gerischer, 1961] H. Gerischer, "Über den Ablauf von Redoxreaktionen an Metallen und an Halbleitern III. Halbleiterelektroden", *Zeitschrift Für Physikalische Chemie Neue Folge* **27**, 48-79 (1961).
- [Gerischer, 1966] H. Gerischer, "Electrochemical Behavior of Semiconductors under Illumination", *Journal of the Electrochemical Society* **113** (11), 1174-1181 (1966).
- [Gerischer, 1969] H. Gerischer, "Charge Transfer Processes at Semiconductor-Electrolyte Interfaces in Connection with Problems of Catalysis", *Surface Science* **18** (1), 97-122 (1969).
- [Götz, 1999] W. Götz, R. S. Kern, C. H. Chen, H. Liu, D. A. Steigerwald, and R. M. Fletcher, "Hall-effect characterization of III-V nitride semiconductors for high efficiency light emitting diodes", *Materials Science and Engineering B-Solid State Materials for Advanced Technology* **59** (1-3), 211-217 (1999).
- [Gogneau, 2004] N. Gogneau, F. Fossard, E. Monroy, S. Monnoye, H. Mank, and B. Daudin, "Effects of stacking on the structural and optical properties of self-organized GaN/AlN quantum dots", *Applied Physics Letters* **84** (21), 4224-4226 (2004).
- [Gomer & Tryson, 1977] R. Gomer, and G. Tryson, "Experimental-Determination of Absolute Half-Cell Emfs and Single Ion Free-Energies of Solvation", *Journal of Chemical Physics* **66** (10), 4413-4424 (1977).
- [Gomes & Cardon, 1982] W. P. Gomes, and F. Cardon, "Electron-Energy Levels in Semiconductor Electrochemistry", *Progress in Surface Science* **12** (2), 155-215 (1982).
- [Grahame, 1947] D. C. Grahame, "The Electrical Double Layer and the Theory of Electrocapillarity", *Chemical Reviews* **41** (3), 441-501 (1947).
- [Grinvald, 1985] A. Grinvald, "Real-Time Optical Mapping of Neuronal-Activity - from Single Growth Cones to the Intact Mammalian Brain", *Annual Review of Neuroscience* **8**, 263-305 (1985).
- [Gritsch, 1998] S. Gritsch, P. Nollert, F. Jahnig, and E. Sackmann, "Impedance spectroscopy of porin and gramicidin pores reconstituted into supported lipid bilayers on indium-tin-oxide electrodes", *Langmuir* **14** (11), 3118-3125 (1998).
- [Gross, 1985] G. W. Gross, W. Y. Wen, and J. W. Lin, "Transparent Indium Tin Oxide Electrode Patterns for Extracellular, Multisite Recording in Neuronal Cultures", *Journal of Neuroscience Methods* **15** (3), 243-252 (1985).
- [Gross, 1995] G. W. Gross, B. K. Rhoades, H. M. E. Azzazy, and M. C. Wu, "The Use of Neuronal Networks on Multielectrode Arrays as Biosensors", *Biosensors & Bioelectronics* **10** (6-7), 553-567 (1995).

- [Gurevich & Pleskov, 1986] Y. Y. Gurevich, and Y. V. Pleskov, *Semiconductor photoelectrochemistry*. (Consultants Bureau, New York, 1986).
- [Härtl, 2004] A. Härtl, E. Schmich, J. A. Garrido, J. Hernando, S. C. R. Catharino, S. Walter, P. Feulner, A. Kromka, D. Steinmüller, and M. Stutzmann, "Protein-modified nanocrystalline diamond thin films for biosensor applications", *Nature Materials* **3** (10), 736-742 (2004).
- [Hanke & Schlue, 1993] W. Hanke, and W. R. Schlue, *Planar lipid bilayers: methods and applications*. (Academic Press, London ; New York, 1993).
- [Hart, 1997] J. P. Hart, R. M. Pemberton, R. Luxton, and R. Wedge, "Studies towards a disposable screen-printed amperometric biosensor for progesterone", *Biosensors & Bioelectronics* **12** (11), 1113-1121 (1997).
- [Hashizume, 2001] T. Hashizume, S. Ootomo, S. Oyama, M. Konishi, and H. Hasegawa, "Chemistry and electrical properties of surfaces of GaN and GaN/AlGaIn heterostructures", *Journal of Vacuum Science & Technology B* **19** (4), 1675-1681 (2001).
- [Healy, 1977] T. W. Healy, D. E. Yates, L. R. White, and D. Chan, "Nernstian and Non-Nernstian Potential Differences at Aqueous Interfaces", *Journal of Electroanalytical Chemistry* **80** (1), 57-66 (1977).
- [Healy & White, 1978] T. W. Healy, and L. R. White, "Ionizable Surface Group Models of Aqueous Interfaces", *Advances in Colloid and Interface Science* **9** (4), 303-345 (1978).
- [Heer, 2004] F. Heer, W. Franks, A. Blau, S. Taschini, C. Ziegler, A. Hierlemann, and H. Baltes, "CMOS microelectrode array for the monitoring of electrogenic cells", *Biosensors & Bioelectronics* **20** (2), 358-366 (2004).
- [Hiemstra, 1989] T. Hiemstra, W. H. Vanriemsdijk, and G. H. Bolt, "Multisite Proton Adsorption Modeling at the Solid-Solution Interface of (Hydr)Oxides - a New Approach. 1. Model Description and Evaluation of Intrinsic Reaction Constants", *Journal of Colloid and Interface Science* **133** (1), 91-104 (1989).
- [Hiemstra & Vanriemsdijk, 1991] T. Hiemstra, and W. H. Vanriemsdijk, "Physical-Chemical Interpretation of Primary Charging Behavior of Metal (Hydr)Oxides", *Colloids and Surfaces* **59**, 7-25 (1991).
- [Hillebrandt, 2001] H. Hillebrandt, *Design of polymer supported lipid membranes on indium-tin-oxide (ITO) semiconductor electrodes for biosensoric applications*, (Dissertation Technische Universität München 2001).
- [Hillebrandt, 2002] H. Hillebrandt, M. Tanaka, and E. Sackmann, "A novel membrane charge sensor: Sensitive detection of surface charge at polymer/lipid composite films on indium tin oxide electrodes", *Journal of Physical Chemistry B* **106** (2), 477-486 (2002).

- [Hollinger, 1994] G. Hollinger, R. Skheytakabbani, and M. Gendry, "Oxides on GaAs and InAs Surfaces - an X-Ray-Photoelectron-Spectroscopy Study of Reference Compounds and Thin Oxide Layers", *Physical Review B* **49** (16), 11159-11167 (1994).
- [Hooge, 1972] F. N. Hooge, "Discussion of Recent Experiments on 1/f Noise", *Physica* **60** (1), 130-144 (1972).
- [Hooge, 1981] F. N. Hooge, T. G. M. Kleinpenning, and L. K. J. Vandamme, "Experimental Studies on 1/f Noise", *Reports on Progress in Physics* **44** (5), 479-532 (1981).
- [Hooge & Tacano, 1993] F. N. Hooge, and M. Tacano, "Experimental Studies of 1/f Noise in n-GaAs", *Physica B* **190** (2-3), 145-149 (1993)
- [Hooge, 1994] F. N. Hooge, "1/F Noise Sources", *IEEE Transactions on Electron Devices* **41** (11), 1926-1935 (1994).
- [Hoppe, 1983] W. Hoppe, W. Lohmann, H. Markl, and H. Ziegler, *Biophysics*. (Springer-Verlag, Berlin ; New York, 1983).
- [Huang & Stumm, 1973] C. P. Huang, and W. Stumm, "Specific adsorption of cations on hydrous  $\gamma$ -Al<sub>2</sub>O<sub>3</sub>", *Journal of Colloid and Interface Science* **43** (2), 409-420 (1973).
- [Huygens, 2000] I. M. Huygens, K. Strubbe, and W. P. Gomes, "Electrochemistry and photoetching of n-GaN", *Journal of the Electrochemical Society* **147** (5), 1797-1802 (2000).
- [Ibbetson, 2000] J. P. Ibbetson, P. T. Fini, K. D. Ness, S. P. DenBaars, J. S. Speck, and U. K. Mishra, "Polarization effects, surface states, and the source of electrons in AlGaIn/GaN heterostructure field effect transistors", *Applied Physics Letters* **77** (2), 250-252 (2000).
- [Ingebrandt, 2001] S. Ingebrandt, C. K. Yeung, M. Krause, and A. Offenhäusser, "Cardiomyocyte-transistor-hybrids for sensor application", *Biosensors & Bioelectronics* **16** (7-8), 565-570 (2001).
- [Ingebrandt, 2003] S. Ingebrandt, C. K. Yeung, W. Staab, T. Zetterer, and A. Offenhäusser, "Backside contacted field effect transistor array for extracellular signal recording", *Biosensors & Bioelectronics* **18** (4), 429-435 (2003).
- [Israel, 1984] D. Israel, W. H. Barry, D. J. Edell, and R. G. Mark, "An Array of Microelectrodes to Stimulate and Record from Cardiac-Cells in Culture", *American Journal of Physiology* **247** (4), H669-H674 (1984).
- [Jakobson, 1998] C. Jakobson, I. Bloom, and Y. Nemirovsky, "1/f noise in CMOS transistors for analog applications from subthreshold to saturation", *Solid-State Electronics* **42** (10), 1807-1817 (1998).
- [Janata, 1989] J. Janata, *Principles of chemical sensors*. (Plenum Press, New York, 1989).

- [Janek, 1998] R. P. Janek, W. R. Fawcett, and A. Ulman, "Impedance spectroscopy of self-assembled monolayers on Au(111): Sodium ferrocyanide charge transfer at modified electrodes", *Langmuir* **14** (11), 3011-3018 (1998).
- [Janzen, 1999] O. Janzen, C. Hahn, and W. Mönch, "Oxidation of GaN{0001}-1 x 1 surfaces at room temperature", *European Physical Journal B* **9** (2), 315-321 (1999).
- [Jena, 2000] D. Jena, A. C. Gossard, and U. K. Mishra, "Dislocation scattering in a two-dimensional electron gas", *Applied Physics Letters* **76** (13), 1707-1709 (2000).
- [Jogai, 2003] B. Jogai, "Influence of surface states on the two-dimensional electron gas in AlGaIn/GaN heterojunction field-effect transistors", *Journal of Applied Physics* **93** (3), 1631-1635 (2003).
- [Johnson, 1991] S. J. Johnson, T. M. Bayerl, D. C. Mcdermott, G. W. Adam, A. R. Rennie, R. K. Thomas, and E. Sackmann, "Structure of an Adsorbed Dimyristoylphosphatidylcholine Bilayer Measured with Specular Reflection of Neutrons", *Biophysical Journal* **59** (2), 289-294 (1991).
- [Kalb, 1990] E. Kalb, J. Engel, and L. K. Tamm, "Binding of Proteins to Specific Target Sites in Membranes Measured by Total Internal-Reflection Fluorescence Microscopy", *Biochemistry* **29** (6), 1607-1613 (1990).
- [Kalb, 1992] E. Kalb, S. Frey, and L. K. Tamm, "Formation of Supported Planar Bilayers by Fusion of Vesicles to Supported Phospholipid Monolayers", *Biochimica Et Biophysica Acta* **1103** (2), 307-316 (1992).
- [Kang, 2005] B. S. Kang, F. Ren, L. Wang, C. Lofton, W. H. W. Tan, S. J. Pearton, A. Dabiran, A. Osinsky, and P. P. Chow, "Electrical detection of immobilized proteins with ungated AlGaIn/GaN high-electron-mobility transistors", *Applied Physics Letters* **87** (2), 023508 (2005).
- [Kampen & Mönch, 1997] T. U. Kampen, and W. Mönch, "Barrier heights of GaN Schottky contacts", *Applied Surface Science* **117**, 388-393 (1997).
- [Katz & Willner, 2003] E. Katz, and I. Willner, "Probing biomolecular interactions at conductive and semiconductive surfaces by impedance spectroscopy: Routes to impedimetric immunosensors, DNA-Sensors, and enzyme biosensors", *Electroanalysis* **15** (11), 913-947 (2003).
- [Keller, 2001] M. Keller, J. Schilling, and E. Sackmann, "Oscillatory magnetic bead rheometer for complex fluid microrheometry", *Review of Scientific Instruments* **72** (9), 3626-3634 (2001).
- [Kiefer, 1991] H. Kiefer, B. Klee, E. John, Y. D. Stierhof, and F. Jähnig, "Biosensors Based on Membrane-Transport Proteins", *Biosensors & Bioelectronics* **6** (3), 233-237 (1991).

- [Kim, 1996] W. Kim, A. Salvador, A. E. Botchkarev, O. Aktas, S. N. Mohammad, and H. Morcoc, "Mg-doped p-type GaN grown by reactive molecular beam epitaxy", *Applied Physics Letters* **69** (4), 559-561 (1996).
- [Kim, 2001] H. Kim, S. J. Park, and H. S. Hwang, "Thermally oxidized GaN film for use as gate insulators", *Journal of Vacuum Science & Technology B* **19** (2), 579-581 (2001).
- [King, 1998] S. W. King, J. P. Barnak, M. D. Bremser, K. M. Tracy, C. Ronning, R. F. Davis, and R. J. Nemanich, "Cleaning of AlN and GaN surfaces", *Journal of Applied Physics* **84** (9), 5248-5260 (1998).
- [Kharitonov, 2000] A. B. Kharitonov, M. Zayats, A. Lichtenstein, E. Katz, and I. Willner, "Enzyme monolayer-functionalized field-effect transistors for biosensor applications", *Sensors and Actuators B-Chemical* **70** (1-3), 222-231 (2000).
- [Kocha, 1995] S. S. Kocha, M. W. Peterson, D. J. Arent, J. M. Redwing, M. A. Tischler, and J. A. Turner, "Electrochemical investigation of the gallium nitride-aqueous electrolyte interface", *Journal of the Electrochemical Society* **142** (12), L238-L240 (1995).
- [Kösslinger, 1995] C. Kösslinger, E. Uttenthaler, S. Drost, F. Aberl, H. Wolf, G. Brink, A. Stanglmaier, and E. Sackmann, "Comparison of the QCM and the SPR Method for Surface Studies and Immunological Applications", *Sensors and Actuators B-Chemical* **24** (1-3), 107-112 (1995).
- [Koide, 1987] Y. Koide, H. Itoh, M. R. H. Khan, K. Hiramatu, N. Sawaki, and I. Akasaki, "Energy Band-Gap Bowing Parameter in an  $\text{Al}_x\text{Ga}_{1-x}\text{N}$  Alloy", *Journal of Applied Physics* **61** (9), 4540-4543 (1987).
- [Kohn, 1999] E. Kohn, P. Gluche, and M. Adamschik, "Diamond MEMS - a new emerging technology", *Diamond and Related Materials* **8** (2-5), 934-940 (1999).
- [Koley & Spencer, 2005] G. Koley, and M. G. Spencer, "On the origin of the two-dimensional electron gas at the AlGaIn/GaN heterostructure interface", *Applied Physics Letters* **86** (4), 042107 (2005).
- [Krötz, 1999] G. H. Krötz, M. H. Eickhoff, and H. Möller, "Silicon compatible materials for harsh environment sensors", *Sensors and Actuators A-Physical* **74** (1-3), 182-189 (1999).
- [Kroll, 1994] P. Kroll, *Wetting in 25. IFF-Ferienkurs Komplexe Systeme zwischen Atomen und Festkörpern* (Forschungszentrum Jülich GmbH, 1994).
- [Lambacher & Fromherz, 1996] A. Lambacher, and P. Fromherz, "Fluorescence interference-contrast microscopy on oxidized silicon using a monomolecular dye layer", *Applied Physics a-Materials Science & Processing* **63** (3), 207-216 (1996).
- [Lang, 1994] H. Lang, C. Duschl, and H. Vogel, "A New Class of Thiolipids for the Attachment of Lipid Bilayers on Gold Surfaces", *Langmuir* **10** (1), 197-210 (1994).

- [Lee, 2002] J. C. M. Lee, M. Santore, F. S. Bates, and D. E. Discher, "From membranes to melts, rouse to entangled: Diffusion in polymersome versus lipid bilayers", *Biophysical Journal* **82** (1), 551a-551a (2002).
- [Levinshtein, 1998] M. E. Levinshtein, F. Pascal, S. Contreras, W. Knap, S. L. Rumyantsev, R. Gaska, J. W. Yang, and M. S. Shur, "Low-frequency noise in GaN/GaN heterojunctions", *Applied Physics Letters* **72** (23), 3053-3055 (1998).
- [Licht & Peramunage, 1990] S. Licht, and D. Peramunage, "Efficient Photoelectrochemical Solar-Cells from Electrolyte Modification", *Nature* **345** (6273), 330-333 (1990).
- [Lin, 2000] Y. J. Lin, C. D. Tsai, Y. T. Lyu, and C. T. Lee, "X-ray photoelectron spectroscopy study of  $(\text{NH}_4)_2\text{S}_x$ -treated Mg-doped GaN layers", *Applied Physics Letters* **77** (5), 687-689 (2000).
- [Link, 2004] A. Link, *Zweidimensionale Elektronen- und Löchergase in GaN/AlGaN Heterostrukturen*, (Dissertation Technische Universität München 2004).
- [Liu, 1985] S. H. Liu, "Fractal Model for the AC Response of a Rough Interface", *Physical Review Letters* **55** (5), 529-532 (1985).
- [Lloyd Spetz, 1997] A. Lloyd Spetz, A. Baranzahi, P. Tobias, and I. Lundström, "High temperature sensors based on metal-insulator-silicon carbide devices", *physica status solidi (a)* **162** (1), 493-511 (1997).
- [Lohmann, 1967] F. Lohmann, "Fermi-Niveau Und Flachbandpotential Von Molekülkristallen Aromatischer Kohlenwasserstoffe", *Zeitschrift Für Naturforschung A* **22** (5), 843-844 (1967).
- [Lud, 2006] S. Q. Lud, M. G. Nikolaidis, I. Haase, M. Fischer, and A. R. Bausch, "Field effect of screened charges: Electrical detection of peptides and proteins by a thin-film resistor", *Chemphyschem* **7** (2), 379-384 (2006).
- [Luther, 1999] B. P. Luther, S. D. Wolter, and S. E. Mohny, "High temperature Pt Schottky diode gas sensors on n-type GaN", *Sensors and Actuators B-Chemical* **56** (1-2), 164-168 (1999).
- [Lyklema & Overbeek, 1961] J. Lyklema, and J. T. Overbeek, "Electrochemistry of Silver Iodide - Capacity of Double Layer at Silver Iodide-Water Interface", *Journal of Colloid Science* **16** (6), 595-608 (1961).
- [Macdonald, 1987] J. R. Macdonald, *Impedance spectroscopy: emphasizing solid materials and systems*. (Wiley, New York, 1987).
- [Madou & Morrison, 1989] M. J. Madou, and S. R. Morrison, *Chemical sensing with solid state devices*. (Academic Press, Boston, 1989).

- [Maruska & Tietjen, 1969] H. P. Maruska, and J. J. Tietjen, "Preparation and Properties of Vapor-Deposited Single-Crystalline GaN", *Applied Physics Letters* **15** (10), 327-329 (1969).
- [Matsuo & Wise, 1974] T. Matsuo, and K. D. Wise, "Integrated Field-Effect Electrode for Biopotential Recording", *IEEE Transactions on Biomedical Engineering* **BM21** (6), 485-487 (1974).
- [McCaldin, 1976a] J. O. McCaldin, T. C. McGill, and C. A. Mead, "Schottky Barriers on Compound Semiconductors - Role of Anion", *Journal of Vacuum Science & Technology* **13** (4), 802-806 (1976).
- [McCaldin, 1976b] J. O. McCaldin, T. C. McGill, and C. A. Mead, "Correlation for III-V Semiconductors and II-VI-Semiconductors of Au Schottky-Barrier Energy with Anion Electronegativity", *Physical Review Letters* **36** (1), 56-58 (1976).
- [McConnell, 1986] H. M. McConnell, T. H. Watts, R. M. Weis, and A. A. Brian, "Supported Planar Membranes in Studies of Cell-Cell Recognition in the Immune-System", *Biochimica Et Biophysica Acta* **864** (1), 95-106 (1986).
- [McConnell, 1992] H. M. McConnell, J. C. Owicki, J. W. Parce, D. L. Miller, G. T. Baxter, H. G. Wada, and S. Pitchford, "The Cytosensor Microphysiometer - Biological Applications of Silicon Technology", *Science* **257** (5078), 1906-1912 (1992).
- [McGovern, 1994] M. E. McGovern, K. M. R. Kallury, and M. Thompson, "Role of Solvent on the Silanization of Glass with Octadecyltrichlorosilane", *Langmuir* **10** (10), 3607-3614 (1994).
- [McMullen & McElhaney, 1996] T. P. W. McMullen, and R. N. McElhaney, "Physical studies of cholesterol-phospholipid interactions", *Current Opinion in Colloid & Interface Science* **1** (1), 83-90 (1996).
- [McWhorter, 1957] A. L. McWhorter, "1/f Noise and Germanium Surface Properties" in *Semiconductor Surface Physics*, edited by R. H. Kingston, (University of Pennsylvania Press, Philadelphia, 1957), pp. 207-228
- [Memming & Schwandt, 1968] R. Memming, and G. Schwandt, "Electrochemical Properties of Gallium Phosphide in Aqueous Solutions", *Electrochimica Acta* **13** (6), 1299-1310 (1968).
- [Memming, 2001] R. Memming, *Semiconductor electrochemistry*. (Wiley-VCH, Weinheim; New York, 2001).
- [Merkel, 1989] R. Merkel, E. Sackmann, and E. Evans, "Molecular Friction and Epitactic Coupling between Monolayers in Supported Bilayers", *Journal De Physique* **50** (12), 1535-1555 (1989).
- [Meyburg, 2006] S. Meyburg, M. Goryll, J. Moers, S. Ingebrandt, S. Bocker-Meffert, H. Lüth, and A. Offenhäusser, "N-Channel field-effect transistors with floating gates for extracellular recordings", *Biosensors & Bioelectronics* **21** (7), 1037-1044 (2006).



- [Michaelis & Menten, 1913] L. Michaelis, and M. L. Menten, "The kinetics of the inversion effect." *Biochemische Zeitschrift* **49**, 333-369 (1913).
- [Mizokawa, 1988] Y. Mizokawa, O. Komoda, and S. Miyase, "Long-Time Air Oxidation and Oxide Substrate Reactions on GaSb, GaAs and GaP at Room-Temperature Studied by X-Ray Photoelectron-Spectroscopy", *Thin Solid Films* **156** (1), 127-143 (1988).
- [Mjamlin & Pleskov, 1967] V. A. Mjamlin, and J. V. Pleskov, *Electrochemistry of semiconductors*. (Plenum Press, New York, 1967).
- [Montal & Müller, 1972] M. Montal, and P. Müller, "Formation of Biomolecular Membranes from Lipid Monolayers and a Study of Their Electrical Properties", *Proceedings of the National Academy of Sciences of the USA* **69** (2), 3561-3566 (1972).
- [Morrison & Freund, 1967] S. R. Morrison, and T. Freund, "Chemical Role of Holes and Electrons in ZnO Photocatalysis", *Journal of Chemical Physics* **47** (4), 1543-1551 (1967).
- [Morrison, 1969] S. R. Morrison, "Electron Capture by Ions at ZnO/Solution Interface", *Surface Science* **15** (3), 363-379 (1969).
- [Morrison, 1971] S. R. Morrison, "Surface Phenomena Associated with the Semiconductor/Electrolyte Interface", *Progress in Surface Science* **1**, 106-154 (1971).
- [Morrison, 1977] S. R. Morrison, *The chemical physics of surfaces*. (Plenum Press, New York, 1977).
- [Morrison, 1980] S. R. Morrison, *Electrochemistry at semiconductor and oxidized metal electrodes*. (Plenum Press, New York, 1980).
- [Moulder & Chastain, 1992] J. F. Moulder, and J. Chastain, *Handbook of X-ray photoelectron spectroscopy : a reference book of standard spectra for identification and interpretation of XPS data*. (Perkin-Elmer Corp., Eden Prairie, Minn., 1992).
- [Müller & Rudin, 1968] P. Müller, and D. Rudin, "Action potentials induce in bimolecular lipid membranes", *Nature* **217**, 713-719 (1968).
- [Murphy, 1999] M. J. Murphy, K. Chu, H. Wu, W. Yeo, W. J. Schaff, O. Ambacher, L. F. Eastman, T. J. Eustis, J. Silcox, R. Dimitrov, and M. Stutzmann, "High-frequency AlGaIn/GaN polarization-induced high electron mobility transistors grown by plasma-assisted molecular-beam epitaxy", *Applied Physics Letters* **75** (23), 3653-3655 (1999).
- [Muth, 1997] J. F. Muth, J. H. Lee, I. K. Shmagin, R. M. Kolbas, H. C. Casey, B. P. Keller, U. K. Mishra, and S. P. DenBaars, "Absorption coefficient, energy gap, exciton binding energy, and recombination lifetime of GaN obtained from transmission measurements", *Applied Physics Letters* **71** (18), 2572-2574 (1997).

- [Myszka, 1997] D. G. Myszka, T. A. Morton, M. L. Doyle, and I. M. Chaiken, "Kinetic analysis of a protein antigen-antibody interaction limited by mass transport on an optical biosensor", *Biophysical Chemistry* **64** (1-3), 127-137 (1997).
- [Nakamura, 1997] S. Nakamura, in "*GaN and related materials*", edited by S. J. Pearton (Gordon and Breach, Amsterdam, 1997).
- [Naumann, 2002] R. Naumann, T. Baumgart, P. Graber, A. Jonczyk, A. Offenhäusser, and W. Knoll, "Proton transport through a peptide-tethered bilayer lipid membrane by the H<sup>+</sup>-ATP synthase from chloroplasts measured by impedance spectroscopy", *Biosensors & Bioelectronics* **17** (1-2), 25-34 (2002).
- [Neher & Sakmann, 1976] E. Neher, and B. Sakmann, "Single-Channel Currents Recorded from Membrane of Denervated Frog Muscle-Fibers", *Nature* **260** (5554), 799-802 (1976).
- [Neuberger, 2001] R. Neuberger, G. Müller, O. Ambacher, and M. Stutzmann, "High-electron-mobility AlGa<sub>N</sub>/Ga<sub>N</sub> transistors (HEMTs) for fluid monitoring applications", *physica status solidi (a)* **185** (1), 85-89 (2001).
- [Neuberger, 2003] R. T. Neuberger, *AlGa<sub>N</sub>/Ga<sub>N</sub>-Heterostrukturen als chemische Sensoren in korrosiven Medien*, (Dissertation Technische Universität München 2003).
- [Nicollian & Goetzberger, 1965] E. H. Nicollian, and A. Goetzberger, "MOS Conductance Technique for Measuring Surface State Parameters (SiO<sub>2</sub>-Si E)", *Applied Physics Letters* **7** (8), 216-219 (1965).
- [Nicollian & Goetzberger, 1967] E. H. Nicollian, and A. Goetzberger, "Si-SiO<sub>2</sub> Interface - Electrical Properties as Determined by Metal-Insulator-Silicon Conductance Technique", *Bell System Technical Journal* **46** (6), 1055-1133 (1967).
- [Nissen, 1999] J. Nissen, S. Gritsch, G. Wiegand, and J. O. Rädler, "Wetting of phospholipid membranes on hydrophilic surfaces - Concepts towards self-healing membranes", *European Physical Journal B* **10** (2), 335-344 (1999).
- [Nollert, 1995] P. Nollert, H. Kiefer, and F. Jahnig, "Lipid Vesicle Adsorption Versus Formation of Planar Bilayers on Solid-Surfaces", *Biophysical Journal* **69** (4), 1447-1455 (1995).
- [Nowak, 2001] G. Nowak, X. H. Xia, J. J. Kelly, J. L. Weyher, and S. Porowski, "Electrochemical etching of highly conductive Ga<sub>N</sub> single crystals", *Journal of Crystal Growth* **222** (4), 735-740 (2001).
- [Nozik, 1978] A. J. Nozik, "Photoelectrochemistry - Applications to Solar-Energy Conversion", *Annual Review of Physical Chemistry* **29**, 189-222 (1978).
- [Nozik & Memming, 1996] A. J. Nozik, and R. Memming, "Physical chemistry of semiconductor-liquid interfaces", *Journal of Physical Chemistry* **100** (31), 13061-13078 (1996).

- [Offenhäusser, 1997] A. Offenhäusser, C. Sprössler, M. Matsuzawa, and W. Knoll, "Field-effect transistor array for monitoring electrical activity from mammalian neurons in culture", *Biosensors & Bioelectronics* **12** (8), 819-826 (1997).
- [Offenhäusser & Knoll, 2001] A. Offenhäusser, and W. Knoll, "Cell-transistor hybrid systems and their potential applications", *Trends in Biotechnology* **19** (2), 62-66 (2001).
- [O'Regan & Grätzel, 1991] B. O'Regan, and M. Grätzel, "A Low-Cost, High-Efficiency Solar-Cell Based on Dye-Sensitized Colloidal TiO<sub>2</sub> Films", *Nature* **353** (6346), 737-740 (1991).
- [Ottenbacher, 1992] D. Ottenbacher, R. Kindervater, P. Gimmel, B. Klee, F. Jahnig, and W. Göpel, "Developing Biosensors with pH-ISFET Transducers Utilizing Lipid Bilayer-Membranes with Transport Proteins", *Sensors and Actuators B* **6** (1-3), 192-196 (1992).
- [Owicki & Parce, 1992] J. C. Owicki, and J. W. Parce, "Biosensors Based on the Energy-Metabolism of Living Cells - the Physical-Chemistry and Cell Biology of Extracellular Acidification", *Biosensors & Bioelectronics* **7** (4), 255-272 (1992).
- [Pancrazio, 1998] J. J. Pancrazio, P. P. Bey, D. S. Cuttino, J. K. Kusel, D. A. Borkholder, K. M. Shaffer, G. T. A. Kovacs, and D. A. Stenger, "Portable cell-based biosensor system for toxin detection", *Sensors and Actuators B-Chemical* **53** (3), 179-185 (1998).
- [Parce, 1989] J. W. Parce, J. C. Owicki, K. M. Kercso, G. B. Sigal, H. G. Wada, V. C. Muir, L. J. Bousse, K. L. Ross, B. I. Sikic, and H. M. McConnell, "Detection of Cell-Affecting Agents with a Silicon Biosensor", *Science* **246** (4927), 243-247 (1989).
- [Parfitt, 1975] R. L. Parfitt, R. J. Atkinson, and R. S. C. Smart, "Mechanism of Phosphate Fixation by Iron Oxides", *Soil Science Society of America Journal* **39** (5), 837-841 (1975).
- [Parikh, 1994] A. N. Parikh, D. L. Allara, I. B. Azouz, and F. Rondelez, "An Intrinsic Relationship between Molecular-Structure in Self-Assembled N-Alkylsiloxane Monolayers and Deposition Temperature", *Journal of Physical Chemistry* **98** (31), 7577-7590 (1994).
- [Peng, 1998a] L. H. Peng, C. W. Chuang, J. K. Ho, C. N. Huang, and C. Y. Chen, "Deep ultraviolet enhanced wet chemical etching of gallium nitride", *Applied Physics Letters* **72** (8), 939-941 (1998).
- [Peng, 1998b] L. H. Peng, C. W. Chuang, Y. C. Hsu, J. K. Ho, C. N. Huang, and C. Y. Chen, "Hydration effects in the photoassisted wet chemical etching of gallium nitride", *IEEE Journal of Selected Topics in Quantum Electronics* **4** (3), 564-569 (1998).
- [Pijanowska, 2003] D. G. Pijanowska, M. Dawgul, and W. Torbicz, "Comparison of urea determination in biological samples by EnFETs based on pH and pNH<sub>4</sub> detection", *Sensors* **3** (6), 160-165 (2003).
- [Poghossian, 2001] A. Poghossian, M. J. Schoning, P. Schroth, A. Simonis, and H. Lüth, "An ISFET-based penicillin sensor with high sensitivity, low detection limit and long lifetime", *Sensors and Actuators B-Chemical* **76** (1-3), 519-526 (2001).

- [Ponce, 1996] F. A. Ponce, D. P. Bour, W. Gotz, N. M. Johnson, H. I. Helava, I. Grzegory, and J. Jun, "Homoepitaxy of GaN on polished bulk single crystals by metalorganic chemical vapor deposition", *Applied Physics Letters* **68** (7), 917-919 (1996).
- [Pleskov, 1980] J. V. Pleskov, "The Double Layer" in *Comprehensive treatise of electrochemistry*, edited by J. O. M. Bockris, (Plenum Press, New York, 1980).
- [Prabhakaran, 1996] K. Prabhakaran, T. G. Andersson, and K. Nozawa, "Nature of native oxide on GaN surface and its reaction with Al", *Applied Physics Letters* **69** (21), 3212-3214 (1996).
- [Purrucker, 2001] O. Purrucker, H. Hillebrandt, K. Adlkofer, and M. Tanaka, "Deposition of highly resistive lipid bilayer on silicon-silicon dioxide electrode and incorporation of gramicidin studied by ac impedance spectroscopy", *Electrochimica Acta* **47** (5), 791-798 (2001).
- [Py & Buehlmann, 1996] M. A. Py, and H. J. Buehlmann, "Evidence for screening effects on the 1/f current noise in GaAs/AlGaAs modulation doped field effect transistors", *Journal of Applied Physics* **80** (3), 1583-1593 (1996).
- [Raguse, 1998] B. Raguse, V. Braach-Maksvytis, B. A. Cornell, L. G. King, P. D. J. Osman, R. J. Pace, and L. Wiczorek, "Tethered lipid bilayer membranes: Formation and ionic reservoir characterization", *Langmuir* **14** (3), 648-659 (1998).
- [Rädler, 1995] J. Rädler, H. Strey, and E. Sackmann, "Phenomenology and Kinetics of Lipid Bilayer Spreading on Hydrophilic Surfaces", *Langmuir* **11** (11), 4539-4548 (1995).
- [Razeghi & Rogalski, 1996] M. Razeghi, and A. Rogalski, "Semiconductor ultraviolet detectors", *Journal of Applied Physics* **79** (10), 7433-7473 (1996).
- [Readinger, 1999] E. D. Readinger, S. D. Wolter, D. L. Waltemyer, J. M. Delucca, S. E. Mohney, B. I. Prenitzer, L. A. Giannuzzi, and R. J. Molnar, "Wet thermal oxidation of GaN", *Journal of Electronic Materials* **28** (3), 257-260 (1999).
- [Rebien, 2002] M. Rebien, W. Henrion, M. Hong, J. P. Mannaerts, and M. Fleischer, "Optical properties of gallium oxide thin films", *Applied Physics Letters* **81** (2), 250-252 (2002).
- [Regehr, 1989] W. G. Regehr, J. Pine, C. S. Cohan, M. D. Mischke, and D. W. Tank, "Sealing Cultured Invertebrate Neurons to Embedded Dish Electrodes Facilitates Long-Term Stimulation and Recording", *Journal of Neuroscience Methods* **30** (2), 91-106 (1989).
- [Requena & Haydon, 1975] J. Requena, and D. A. Haydon, "Van Der Waals Forces in Oil-Water Systems from the Study of Thin Lipid Films. II. The Dependence of the Van Der Waals Free Energy of Thinning on Film Composition and Structure", *Proceedings of the Royal Society of London* **347** (1649), 161-177 (1975).
- [Revesz, 1977] A. G. Revesz, "Mechanism of Ion Sensitive Field-Effect Transistor", *Thin Solid Films* **41** (2), L43-L47 (1977).

- [Rhoderick & Williams, 1988] E. H. Rhoderick, and R. H. Williams, *Metal-semiconductor contacts*, 2nd ed. (Clarendon Press, Oxford, 1988).
- [Rittner, 2005] M. Rittner, M. S. Martin-Gonzalez, A. Flores, H. Schweizer, F. Effenberger, and M. H. Pilkuhn, "Nanostructural and electrical properties of functionally terminated self-assembled monolayers on silicon surfaces", *Journal of Applied Physics* **98** (5), 054312 (2005).
- [Rizzi, 1999] A. Rizzi, R. Lantier, F. Monti, H. Lüth, F. Della Sala, A. Di Carlo, and P. Lugli, "AlN and GaN epitaxial heterojunctions on 6H-SiC(0001): Valence band offsets and polarization fields", *Journal of Vacuum Science & Technology B* **17** (4), 1674-1681 (1999).
- [Robbins & Joanny, 1987] M. O. Robbins, and J. F. Joanny, "Contact-Angle Hysteresis on Random Surfaces", *Europhysics Letters* **3** (6), 729-735 (1987).
- [Römer & Steinem, 2004] W. Römer, and C. Steinem, "Impedance analysis and single-channel recordings on nano-black lipid membranes based on porous alumina", *Biophysical Journal* **86** (2), 955-965 (2004).
- [Rotter, 2000] T. Rotter, D. Mistele, J. Stemmer, F. Fedler, J. Aderhold, J. Graul, V. Schwegler, C. Kirchner, M. Kamp, and M. Heuken, "Photoinduced oxide film formation on n-type GaN surfaces using alkaline solutions", *Applied Physics Letters* **76** (26), 3923-3925 (2000).
- [Rumyantsev, 2000a] S. Rumyantsev, M. E. Levinshtein, R. Gaska, M. S. Shur, J. W. Yang, and M. A. Khan, "Low-frequency noise in AlGaIn/GaN heterojunction field effect transistors on SiC and sapphire substrates", *Journal of Applied Physics* **87** (4), 1849-1854 (2000).
- [Rumyantsev, 2000b] S. L. Rumyantsev, N. Pala, M. S. Shur, R. Gaska, M. E. Levinshtein, M. A. Khan, G. Simin, X. Hu, and J. Yang, "Effect of gate leakage current on noise properties of AlGaIn/GaN field effect transistors", *Journal of Applied Physics* **88** (11), 6726-6730 (2000).
- [Rumyantsev, 2001] S. L. Rumyantsev, N. Pala, M. S. Shur, R. Gaska, M. E. Levinshtein, M. A. Khan, G. Simin, X. Hu, and J. Yang, "Low frequency noise in GaN metal semiconductor and metal oxide semiconductor field effect transistors", *Journal of Applied Physics* **90** (1), 310-314 (2001).
- [Sabatani, 1993] E. Sabatani, J. Cohenboulakia, M. Bruening, and I. Rubinstein, "Thioaromatic Monolayers on Gold - a New Family of Self-Assembling Monolayers", *Langmuir* **9** (11), 2974-2981 (1993).
- [Sackmann, 1995] E. Sackmann, "Physical Basis of Self-Organization and Function of Membranes: Physics of Vesicles" in *Handbook of Biological Physics, volume 1*, 213-305. (Elsevier Science B. V.: Amsterdam, 1995).
- [Sackmann, 1996] E. Sackmann, "Supported membranes: Scientific and practical applications", *Science* **271** (5245), 43-48 (1996).

- [Sackmann & Tanaka, 2000] E. Sackmann, and M. Tanaka, "Supported membranes on soft polymer cushions: fabrication, characterization and applications", *Trends in Biotechnology* **18** (2), 58-64 (2000).
- [Sagiv, 1980] J. Sagiv, "Organized Monolayers by Adsorption. 1. Formation and Structure of Oleophobic Mixed Monolayers on Solid-Surfaces", *Journal of the American Chemical Society* **102** (1), 92-98 (1980).
- [Satpathy, 2004] S. Satpathy, Z. S. Popovic, and W. C. Mitchel, "Theory of the composition dependence of the band offset and sheet carrier density in the GaN/Al<sub>x</sub>Ga<sub>1-x</sub>N heterostructure", *Journal of Applied Physics* **95** (10), 5597-5601 (2004).
- [Schalwig, 2002a] J. Schalwig, G. Müller, M. Eickhoff, O. Ambacher, and M. Stutzmann, "Gas sensitive GaN/AlGaN-heterostructures", *Sensors and Actuators B-Chemical* **87** (3), 425-430 (2002).
- [Schalwig, 2002b] J. Schalwig, G. Müller, M. Eickhoff, O. Ambacher, and M. Stutzmann, "Group III-nitride-based gas sensors for combustion monitoring", *Materials Science and Engineering B-Solid State Materials for Advanced Technology* **93** (1-3), 207-214 (2002).
- [Schalwig, 2002c] J. Schalwig, G. Müller, U. Karrer, M. Eickhoff, O. Ambacher, M. Stutzmann, L. Gorgens, and G. Dollinger, "Hydrogen response mechanism of Pt-GaN Schottky diodes", *Applied Physics Letters* **80** (7), 1222-1224 (2002).
- [Skena, 2000] M. Skena, *DNA microarrays : a practical approach*. (Oxford University Press, Oxford ; New York, 2000).
- [Schienle, 2004] M. Schienle, C. Paulus, A. Frey, F. Hofmann, B. Holzapfl, P. Schindler-Bauer, and R. Thewes, "A fully electronic DNA sensor with 128 positions and in-pixel A/D conversion", *IEEE Journal of Solid-State Circuits* **39** (12), 2438-2445 (2004).
- [Schmitz, 1996] A. C. Schmitz, A. T. Ping, M. A. Khan, Q. Chen, J. W. Yang, and I. Adesida, "Schottky barrier properties of various metals on n-type GaN", *Semiconductor Science and Technology* **11** (10), 1464-1467 (1996).
- [Schreiber, 2000] F. Schreiber, "Structure and growth of self-assembling monolayers", *Progress in Surface Science* **65** (5-8), 151-256 (2000).
- [Shalish, 2001] I. Shalish, Y. Shapira, L. Burstein, and J. Salzman, "Surface states and surface oxide in GaN layers", *Journal of Applied Physics* **89** (1), 390-395 (2001).
- [Shirley, 1972] D. A. Shirley, "High-Resolution X-Ray Photoemission Spectrum of Valence Bands of Gold", *Physical Review B* **5** (12), 4709-4714 (1972).
- [Shockley & Read, 1952] W. Shockley, and W. T. Read, "Statistics of the Recombinations of Holes and Electrons", *Physical Review* **87** (5), 835-842 (1952).

- [Sigal, 1998] G. B. Sigal, M. Mrksich, and G. M. Whitesides, "Effect of surface wettability on the adsorption of proteins and detergents", *Journal of the American Chemical Society* **120** (14), 3464-3473 (1998).
- [Silberzan, 1991] P. Silberzan, L. Léger, D. Ausserré, and J. J. Benattar, "Silanation of Silica Surfaces - a New Method of Constructing Pure or Mixed Monolayers", *Langmuir* **7** (8), 1647-1651 (1991).
- [Singer & Nicolson, 1972] S. Singer, and G. Nicolson, "The fluid mosaic model of the structure of cell membranes", *Science* **175**, 720-731 (1972)
- [Siu & Cobbold, 1979] W. M. Siu, and R. S. C. Cobbold, "Basic Properties of the Electrolyte-SiO<sub>2</sub>-Si System - Physical and Theoretical Aspects", *IEEE Transactions on Electron Devices* **26** (11), 1805-1815 (1979).
- [Song, 2006] K. S. Song, G. J. Zhang, Y. Nakamura, K. Furukawa, T. Hiraki, J. H. Yang, T. Funatsu, I. Ohdomari, and H. Kawarada, "Label-free DNA sensors using ultrasensitive diamond field-effect transistors in solution", *Physical Review E* **74** (4), 041919 (2006)
- [Sprössler, 1998] C. Sprössler, D. Richter, M. Denyer, and A. Offenhäusser, "Long-term recording system based on field-effect transistor arrays for monitoring electrogenic cells in culture", *Biosensors & Bioelectronics* **13** (6), 613-618 (1998).
- [Sprössler, 1999] C. Sprössler, M. Denyer, S. Britland, W. Knoll, and A. Offenhäusser, "Electrical recordings from rat cardiac muscle cells using field-effect transistors", *Physical Review E* **60** (2), 2171-2176 (1999).
- [Steinem, 1996] C. Steinem, A. Janshoff, W. P. Ulrich, M. Sieber, and H. J. Galla, "Impedance analysis of supported lipid bilayer membranes: A scrutiny of different preparation techniques", *Biochimica Et Biophysica Acta-Biomembranes* **1279** (2), 169-180 (1996).
- [Steinem, 1997] C. Steinem, A. Janshoff, F. Hohn, M. Sieber, and H. J. Galla, "Proton translocation across bacteriorhodopsin containing solid supported lipid bilayers", *Chemistry and Physics of Lipids* **89** (2), 141-152 (1997).
- [Steinem, 1998] C. Steinem, A. Janshoff, K. von dem Bruch, K. Reihls, J. Goossens, and H. J. Galla, "Valinomycin-mediated transport of alkali cations through solid supported membranes", *Bioelectrochemistry and Bioenergetics* **45** (1), 17-26 (1998).
- [Stelzle, 1992] M. Stelzle, R. Miehlich, and E. Sackmann, "2-Dimensional Microelectrophoresis in Supported Lipid Bilayers", *Biophysical Journal* **63** (5), 1346-1354 (1992).
- [Stelzle, 1993] M. Stelzle, G. Weissmüller, and E. Sackmann, "On the Application of Supported Bilayers as Receptive Layers for Biosensors with Electrical Detection", *Journal of Physical Chemistry* **97** (12), 2974-2981 (1993).

- [Stern, 1924] O. Stern, "Zur Theorie der Elektrolytischen Doppelschicht", *Zeitschrift für Elektrochemie und Angewandte Physikalische Chemie* **30**, 508-516 (1924).
- [Stett, 1997] A. Stett, B. Müller, and P. Fromherz, "Two-way silicon-neuron interface by electrical induction", *Physical Review E* **55** (2), 1779-1782 (1997).
- [Stumm, 1970] W. Stumm, C. P. Huang, and S. R. Jenkins, "Specific Chemical Interaction Affecting Stability of Dispersed Systems", *Croatica Chemica Acta* **42** (2), 223-& (1970).
- [Sung, 1999] M. M. Sung, G. J. Kluth, and R. Maboudian, "Formation of alkylsiloxane self-assembled monolayers on  $\text{Si}_3\text{N}_4$ ", *Journal of Vacuum Science & Technology a-Vacuum Surfaces and Films* **17** (2), 540-544 (1999).
- [Swank, 1967] R. K. Swank, "Surface Properties of II-VI Compounds", *Physical Review* **153** (3), 844-849 (1967).
- [Sze, 1981] S. M. Sze, *Physics of semiconductor devices*, 2nd ed. (Wiley, New York, 1981).
- [Tachiki, 2003] M. Tachiki, Y. Kaibara, Y. Sumikawa, M. Shigeno, T. Banno, K. S. Song, H. Umezawa, and H. Kawarada, "Diamond nanofabrication and characterization for biosensing application", *physica status solidi (a)* **199** (1), 39-43 (2003).
- [Tamm & McConnell, 1985] L. K. Tamm, and H. M. McConnell, "Supported Phospholipid-Bilayers", *Biophysical Journal* **47** (1), 105-113 (1985).
- [Tanaka & Sackmann, 2005] M. Tanaka, and E. Sackmann, "Polymer-supported membranes as models of the cell surface", *Nature* **437** (7059), 656-663 (2005).
- [Tautz, 1999] F. S. Tautz, S. Sloboshanin, U. Starke, and J. A. Schaefer, "Reactivity and morphology of  $(10\overline{12})$ -faceted and  $(3\times 3)$ -reconstructed GaN $(000\overline{1})$  epilayers grown on sapphire $(0001)$ ", *Journal of Physics-Condensed Matter* **11** (41), 8035-8048 (1999).
- [Terrettaz, 2003] S. Terrettaz, M. Mayer, and H. Vogel, "Highly electrically insulating tethered lipid bilayers for probing the function of ion channel proteins", *Langmuir* **19** (14), 5567-5569 (2003).
- [Thevenot, 1999] D. R. Thevenot, K. Toth, R. A. Durst, and G. S. Wilson, "Electrochemical biosensors: Recommended definitions and classification - (Technical Report)", *Pure and Applied Chemistry* **71** (12), 2333-2348 (1999).
- [Thomas, 1972] C. A. Thomas, P. A. Springer, L. M. Okun, Berwaldn.Y, and G. E. Loeb, "Miniature Microelectrode Array to Monitor Bioelectric Activity of Cultured Cells", *Experimental Cell Research* **74** (1), 61-66 (1972).
- [Tougaard, 1997] S. Tougaard, "Universality classes of inelastic electron scattering cross-sections", *Surface and Interface Analysis* **25** (3), 137-154 (1997).



- [Trasatti, 1977] S. Trasatti, "Temperature-Coefficient of Water Dipole Contribution to Electrode Potential", *Journal of Electroanalytical Chemistry* **82** (1-2), 391-402 (1977).
- [Tung, 2001] R. T. Tung, "Recent advances in Schottky barrier concepts", *Materials Science & Engineering R-Reports* **35** (1-3), 1-138 (2001).
- [van Hal, 1995] R. E. G. Van Hal, J. C. T. Eijkel, and P. Bergveld, "A Novel Description of ISFET Sensitivity with the Buffer Capacity and Double-Layer Capacitance as Key Parameters", *Sensors and Actuators B-Chemical* **24** (1-3), 201-205 (1995).
- [van Hal, 1996] R. E. G. van Hal, J. C. T. Eijkel, and P. Bergveld, "A general model to describe the electrostatic potential at electrolyte oxide interfaces", *Advances in Colloid and Interface Science* **69**, 31-62 (1996).
- [van Regenmortel, 1998] M. H. V. Van Regenmortel, D. Altschuh, J. Chatellier, L. Christensen, N. Rauffer-Bruyere, P. Richalet-Secordel, J. Witz, and G. Zeder-Lutz, "Measurement of antigen-antibody interactions with biosensors", *Journal of Molecular Recognition* **11** (1-6), 163-167 (1998).
- [Vassanelli & Fromherz, 1998] S. Vassanelli, and P. Fromherz, "Transistor records of excitable neurons from rat brain", *Applied Physics a-Materials Science & Processing* **66** (4), 459-463 (1998).
- [Vassanelli & Fromherz, 1999] S. Vassanelli, and P. Fromherz, "Transistor probes local potassium conductances in the adhesion region of cultured rat hippocampal neurons", *Journal of Neuroscience* **19** (16), 6767-6773 (1999).
- [Völker & Fromherz, 2005] M. Völker, and P. Fromherz, "Signal transmission from individual mammalian nerve cell to field-effect transistor", *Small* **1** (2), 206-210 (2005).
- [von Ribbeck, 2006] H.-G. von Ribbeck, *Elektrochemische Charakterisierung von biofunktionalisierten Gallium-Nitrid-Oberflächen*, (Diplomarbeit Technische Universität München 2006).
- [Vurgaftman & Meyer, 2003] Vurgaftman, and J. R. Meyer, "Band parameters for nitrogen-containing semiconductors", *Journal of Applied Physics* **94** (6), 3675-3696 (2003).
- [Updike & Hicks, 1967] S. J. Updike, and G. P. Hicks, "Enzyme Electrode", *Nature* **214** (5092), 986-988 (1967).
- [Uslu, 2004] F. Uslu, S. Ingebrandt, D. Mayer, S. Bocker-Meffert, M. Odenthal, and A. Offenhäuser, "Labelfree fully electronic nucleic acid detection system based on a field-effect transistor device", *Biosensors & Bioelectronics* **19** (12), 1723-1731 (2004).
- [Waldrop & Grant, 1996] J. R. Waldrop, and R. W. Grant, "Measurement of AlN/GaN (0001) heterojunction band offsets by X-ray photoemission spectroscopy", *Applied Physics Letters* **68** (20), 2879-2881 (1996).

- [Watkins, 1999] N. J. Watkins, G. W. Wicks, and Y. L. Gao, "Oxidation study of GaN using X-ray photoemission spectroscopy", *Applied Physics Letters* **75** (17), 2602-2604 (1999).
- [Weidemann, 2005] O. Weidemann, E. Monroy, E. Hahn, M. Stutzmann, and M. Eickhoff, "Influence of thermal oxidation on the electronic properties of Pt Schottky contacts on GaN grown by molecular-beam epitaxy", *Applied Physics Letters* **86** (8), 083507 (2005).
- [Westall & Hohl, 1980] J. Westall, and H. Hohl, "Comparison of Electrostatic Models for the Oxide-Solution Interface", *Advances in Colloid and Interface Science* **12** (4), 265-294 (1980).
- [Westmeyer, 2006] A. N. Westmeyer, S. Mahajan, K. K. Bajaj, J. Y. Lin, H. X. Jiang, D. D. Koleske, and R. T. Senger, "Determination of energy-band offsets between GaN and AlN using excitonic luminescence transition in AlGaIn alloys", *Journal of Applied Physics* **99** (1), 013705 (2006).
- [Widmann, 1998] F. Widmann, B. Daudin, G. Feuillet, Y. Samson, J. L. Rouviere, and N. Pelekanos, "Growth kinetics and optical properties of self-organized GaN quantum dots", *Journal of Applied Physics* **83** (12), 7618-7624 (1998).
- [Wiegand, 2000] G. Wiegand, K. R. Neumaier, and E. Sackmann, "Fast impedance spectroscopy: General aspects and performance study for single ion channel measurements", *Review of Scientific Instruments* **71** (6), 2309-2320 (2000).
- [Wiegand, 2002] G. Wiegand, N. Arribas-Layton, H. Hillebrandt, E. Sackmann, and P. Wagner, "Electrical properties of supported lipid bilayer membranes", *Journal of Physical Chemistry B* **106** (16), 4245-4254 (2002).
- [Williams & Bube, 1960] R. Williams, and R. H. Bube, "Photoemission in the Photovoltaic Effect in Cadmium Sulfide Crystals", *Journal of Applied Physics* **31** (6), 968-978 (1960).
- [Wolf, 1998] B. Wolf, M. Brischwein, W. Baumann, R. Ehret, T. Henning, M. Lehmann, and A. Schwinde, "Microsensor-aided measurements of cellular signalling and metabolism on tumor cells - The cell monitoring system (CMS (R))", *Tumor Biology* **19** (5), 374-383 (1998).
- [Wolter, 1997] S. D. Wolter, B. P. Luther, D. L. Waltemyer, C. Onneby, S. E. Mohny, and R. J. Molnar, "X-ray photoelectron spectroscopy and X-ray diffraction study of the thermal oxide on gallium nitride", *Applied Physics Letters* **70** (16), 2156-2158 (1997).
- [Wolter, 2000] S. D. Wolter, J. M. DeLucca, S. E. Mohny, R. S. Kern, and C. P. Kuo, "An investigation into the early stages of oxide growth on gallium nitride", *Thin Solid Films* **371** (1-2), 153-160 (2000).
- [Xu & Schoonen, 2000] Y. Xu, and M. A. A. Schoonen, "The absolute energy positions of conduction and valence bands of selected semiconducting minerals", *American Mineralogist* **85** (3-4), 543-556 (2000).

- [Yang, 2002] W. S. Yang, O. Auciello, J. E. Butler, W. Cai, J. A. Carlisle, J. Gerbi, D. M. Gruen, T. Knickerbocker, T. L. Lasseter, J. N. Russell, L. M. Smith, and R. J. Hamers, "DNA-modified nanocrystalline diamond thin-films as stable, biologically active substrates", *Nature Materials* **1** (4), 253-257 (2002).
- [Yasuda, 1994] T. Yasuda, T. Okuno, and H. Yasuda, "Contact-Angle of Water on Polymer Surfaces", *Langmuir* **10** (7), 2435-2439 (1994).
- [Yates, 1974] D. E. Yates, S. Levine, and T. W. Healy, "Site-Binding Model of Electrical Double-Layer at Oxide-Water Interface", *Journal of the Chemical Society-Faraday Transactions I* **70**, 1807-1818 (1974).
- [Yeagle, 1985] P. L. Yeagle, "Cholesterol and the cell membrane", *Biochimica Et Biophysica Acta* **822**, 267 - 287 (1985).
- [Yeung, 2001] C. K. Yeung, S. Ingebrandt, M. Krause, A. Offenhäusser, and W. Knoll, "Validation of the use of field effect transistors for extracellular signal recording in pharmacological bioassays", *Journal of Pharmacological and Toxicological Methods* **45** (3), 207-214 (2001).
- [Yim, 1973] W. M. Yim, E. J. Stofko, P. Zanzucchi, J. I. Pankove, M. Ettenber, and S. L. Gilbert, "Epitaxially Grown AlN and its Optical Band Gap", *Journal of Applied Physics* **44** (1), 292-296 (1973).
- [Yu & Cardona, 1996] P. Y. Yu, and M. Cardona, *Fundamentals of semiconductors: physics and materials properties*. (Springer, Berlin ; New York, 1996).
- [Zaus, 2004] E. S. Zaus, *Chemische und elektrochemische Herstellung von Gruppe III-Nitrid Mikrostrukturen*, (Diplomarbeit Technische Universität München 2004).
- [Zeck & Fromherz, 2001] G. Zeck, and P. Fromherz, "Noninvasive neuroelectronic interfacing with synaptically connected snail neurons immobilized on a semiconductor chip", *Proceedings of the National Academy of Sciences of the United States of America* **98** (18), 10457-10462 (2001).
- [Zisman, 1964] W. Zisman, in *Contact Angle, Wettability and Adhesion*, edited by F. M. Fowkes, *Advances in Chemistry Series* **43**. (American Chemical Society, Washington D.C., 1964).
- [Zywietz, 1999] T. K. Zywietz, J. Neugebauer, and M. Scheffler, "The adsorption of oxygen at GaN surfaces", *Applied Physics Letters* **74** (12), 1695-1697 (1999).